Università Politecnica delle Marche
Scuola di Dottorato di Ricerca in Scienze dell'Ingegneria
Corso di Dottorato in Ingegneria Industriale
--------------------------------------------------------------------------------------

# Development of a thermomechanical and metallurgical model in order to design a predictive in line control system for rolling process.

Ph.D. Dissertation of:

**Alberto Nardini**

Supervisor:

**Prof. Mohamad El Mehtedi**

Ph.D. Course coordinator:

**Prof. F. Mandorli**

XXX Cycle edition

Università Politecnica delle Marche
*Dipartimento di Ingegneria Meccanica*
Via Brecce Bianche — 60131 - Ancona, Italy

# Abstract

This project wants to build up a model which is able to predict mechanical properties achieved depending on parameters governing the inline thermal treatment developed by Siemens Metals Technologies between multiple rolling stages.

Such technologies consists in a specific treatment of quenching and tempering processes, like the Rail Head Hardening System that is actually the new evolutional technology to increase the performances in terms of safety and wear of the high speed train railways.

In order to guarantee a model which could be considered as more flexible as possible, the results want to be exploitable even in case of necessity to model other thermal processes.

The model will be developed in order to achieve the exact simulation for thermal treatment proposed by Siemens Metals Technologies, but it will be simply adjustable in order to allow predictions even in case of other thermal processes.

The approach which is going to be followed is the result of the compromise among the trial to develop a model on the state of the art, the in-field results offered by Siemens Metals Technologies and the experimental validation executable into the laboratories.

# Contents

# Chapter 1

# 1.  Introduction

## 1.1  Preface

During the last 50 years, economic and technical demands have forced the steel industry to develop innovative processes to supply the transportation, energy and construction market with high strength, high toughness and cost-effective steels. While high strength can be easily achieved through the addition of solute strengthening or precipitation hardening elements, toughness cannot be significantly improved by alloy additions, but can be only achieved through the control of the final microstructure.

In particular in the present demanding SBQ and rail market, producers ask for high quality materials and high productivity at the lowest possible transformation costs. The plant suppliers' challenge is to provide quality bars and rail producers with the most advanced and flexible technology available in order to match the market requirements and to move to an evolution of the product.

Since 1950, it was known that the refinement of microstructure improves both resistance to brittle fracture and strength of materials. Therefore research and development activities were focused on understanding how steels respond to hot processing and in-line cooling conditions and how that response can be altered by alloying, because the final microstructure after the phase transformation depends on the microstructure and composition of austenite just before the phase transformation and the evolution on the final metallurgical phases.

This has led to advances in both process and product metallurgy: the joint development of thermomechanical processes (TMP) and microalloyed steels (MA steels). While the aim of thermomechanical processing is the refinement of the austenitic grain size, the addition of microalloyed elements permits to better control the evolution of microstructure during processing.

In conventional hot rolling (CHR) both roughing and finishing pass are given to the material at the highest possible temperature in order to optimize productivity without taking into account the as-rolled mechanical properties and delegating the final balance between strength and toughness to subsequent heat treatments.

On the other hand TMPs can achieve a fine austenitic grain size either by lowering the temperature in roughing and finishing passes,

producing highly deformed austenite as in conventional controlled rolling (CCR), or by controlling the evolution of microstructure, producing a fine fully recrystallized austenite as in recrystallization controlled rolling (RCR).

From an industrial point of view the main drawback of CCR is that it is not always applicable to rolling schedules because the power needed by mills to deform the materials raises as the temperature is lowered. The temperature involved in RCR, instead, can be sufficiently high to avoid excessive loads. RCR, therefore, can be a profitable way to balance processing needs with final product requirements.

However, in order to design a RCR rolling schedule it is necessary to have detailed models describing the recrystallization kinetics and evolution of the size of recrystallized and unrecrystallized austenite grains of steels during and between each deformation pass. Moreover, to be industrially effective, these models have to be coupled with Finite Element Modelling (FEM) that is widely used to calculate power, forces etc. needed by rolling mill and in tools design.

Microstructural models deeply changed in the last 25 years, evolving from empirical models to more physically based ones. However the growth of models complexity has been accompanied by a reduction of their applicability, since there is a lack of highly reliable data for the physical variables that are used in the calculations. Moreover physically based models are not industrially used because, when coupled to FEM, the computational time become excessive.

Up to now, from and industrial point of view, only empirical models have proved to give satisfactory results, but these rely on a huge quantity of parameters that have to be calibrated by ad-hoc laboratory tests. Especially production of high quality bars and rails requires an accurate alloys design, rolling processes and thermal treatment strategies.

Therefore, the aim of this research is to develop an innovative in-line hardening flexible system applied for rails, named idRHa+®, able to enhance the mechanical properties desired and consequently increase service life up to three times compared to non-treated rails.

The work and the thesis have been organized as follows:

- Chapter 2 retraces the motivations of this research work birth, starting from the geopolitical analysis of the industrial rail market, passing through the technical aspects and the production technologies in use, until it comes to its economic analysis.
- Chapter 3 is oriented to the description of the process technology.
- Chapter 4 is devoted to a literary review about the thermomechanical and metallurgical processes controlling the

steel microstructural evolution, the mechanical properties and their characterization methodologies used in this work.

- Chapter 5 is focused on the describing of the process control system developed.
- Chapter 6 presents the results obtained by the system through a pilot plant.
- In the end, Chapter 7 provides the general conclusions of this research activity.

# Chapter 2

# 2. Business Analysis

## 2.1 Introduction

Transport is crucial for economic growth and poverty reduction. Almost nothing can be produced or consumed unless people, raw materials, commodities, fuel, and finished products can be moved to and from different locations. In many countries, railways are an important part of the transport network. With growing environmental concerns, and increasing congestion from personal vehicles, today many governments and organizations, see railways as a critical element of greener transportation and development.

Railways have a huge potential to contribute to developing country green growth agendas. There are several reasons for this:

- Railways are clean: Within the transport sector, rail accounts for 2% of $CO_2$ emissions and rail is 3 to 10 times less GHG(greenhouse gas) intensive than other modes of transport.
- Railways are efficient: In some market segments (e.g. bulk freight over 800km, or passengers for up to four-hour trips) railways are the most efficient mode of transportation.
- Railways integrate easily with other modes of transport: Many cities have integrated public transport ticketing systems; rail stations are hubs for interchange with other modes - bus, taxi, car, cycle, and pedestrian; new advances in containers allow for more integrated freight transport with shipping and air transport.
- Railways continue to innovate: Today's electric rail transport is free of direct local air pollution while innovative thinking in public-private partnerships is transforming many railways into modern, efficient, and revenue-generating enterprises.
- Railways take less space: Railway infrastructure occupies 2-3 times less land per passenger or freight unit than other modes of transport.
- Railways are safe: Although railways are not free of accidents, disproportionately more people die on world roads every year.

## 2.2   Rail Market

The production of rails in the world has reached a stable volume over 12 million tons/p.a., sustained by demographic, economic/political and technological drivers. The production plants overall capacity is quickly expected to approach the 15 million tons/p.a. and there are strong indications for a further push of growth towards 20 million/p.a. tons by the next decade.  A network density close or higher than 0,05 km/km² is currently installed only in some limited areas of the world (fig.2.1), but represents a possible medium-term target for many other areas in most of the continents.
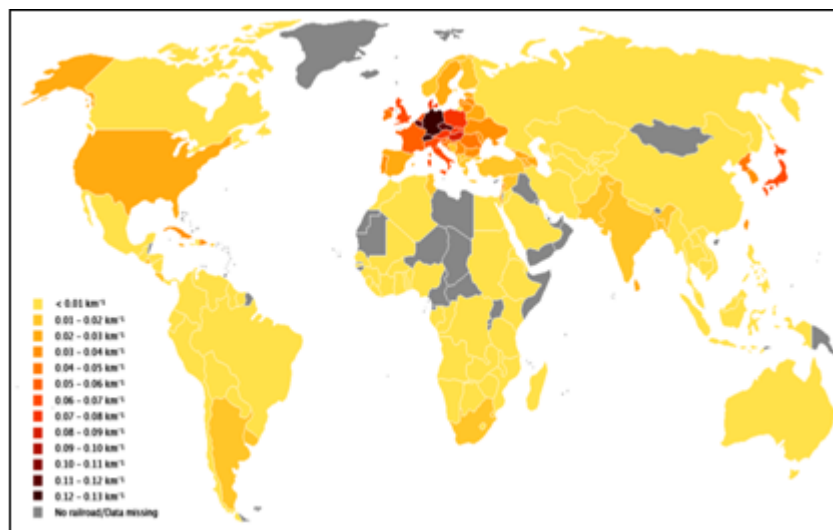


*Figure 2.1 Rail Network density*

Beside such network extension, there is then an arising tendency for the installation of higher quality tracks, mainly linked to the developments of high-speed or/and heavy-haul transport lines.
As known, the technical and the quality requirements of the rails are indicated in the relevant country or clusters Standards; the quick impulse of development of the rail technical qualities and performances, has therefore determined a parallel need of updating for many Standards.
A clear example of this trend of updating of the International Standards, are the new European EN 13674-1:2011-04, the American ASTM A1-2010, the Russian GOST 51685-2011 (part of overall Technical Specification TU 0921 231 01124323-2007), the Indian IRS T12-2009 and the Chinese TB/T 2344-2012.
It can be noted that all Standards of the countries where the rails production poles are (figure 2.2) have been updated during the last 3-4 years, a clear indication of the dynamism of the strong technological evolution. In some cases (i.e. GOST ДТ350-НН rail grade for extreme low-temperature applications), the Standards specify demanding features

even higher than those industrially obtainable with the current production technologies and requiring processes still in consolidation or even in study.
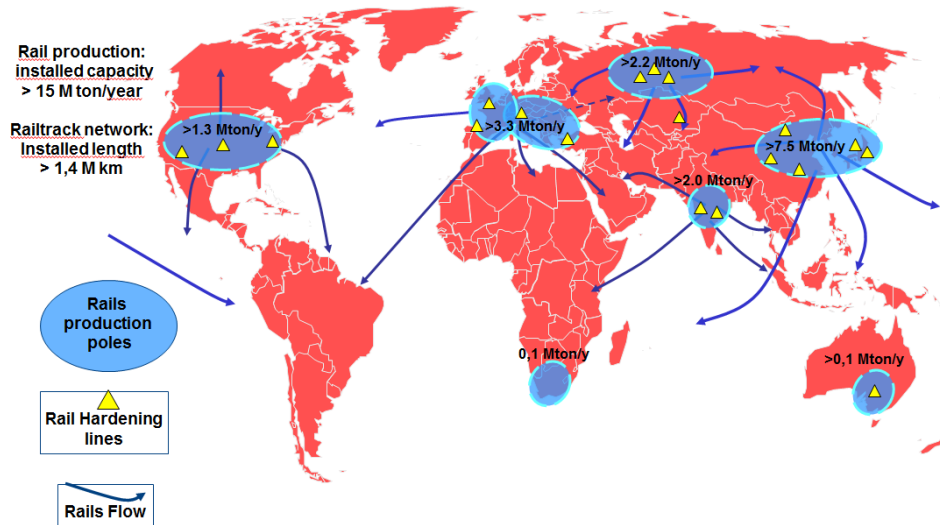


*Figure 2.2 Rail production map and network worldwide*

Figure 2.3 represents graphically some typical rail technical requirements: the green bubbles are for standard not-alloyed/ not treated low strength pearlitic rails (about 80÷85% of the overall market) and the yellow bubbles for hard rails (10÷15% of the market, trend to increase), both alloyed and thermal treated. The red bubbles are instead relevant to some new-generation of rail grades which are currently in a study or prototyping phase.
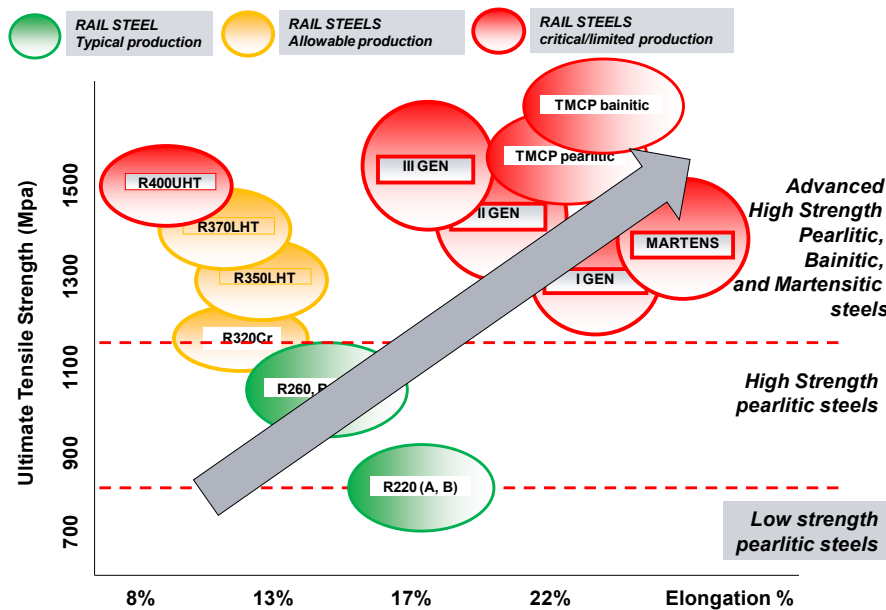


*Figure 2.3 Rail steels (present and future market)*

It has to be highlighted that the requirements are quite distant and scattered in the graph, depending on the application and of the life-cycle, The figure 2.4 lists the major process technologies nowadays available to produce rails; the capability for a rail plant to produce efficiently a wide range of grades-sizes-lengths with quick automatic setup operations, self-adaptability of use governed by an intelligent process control system and at sustainable cost, is becoming more and more a must to be flexible and reactive in the world market scenario.
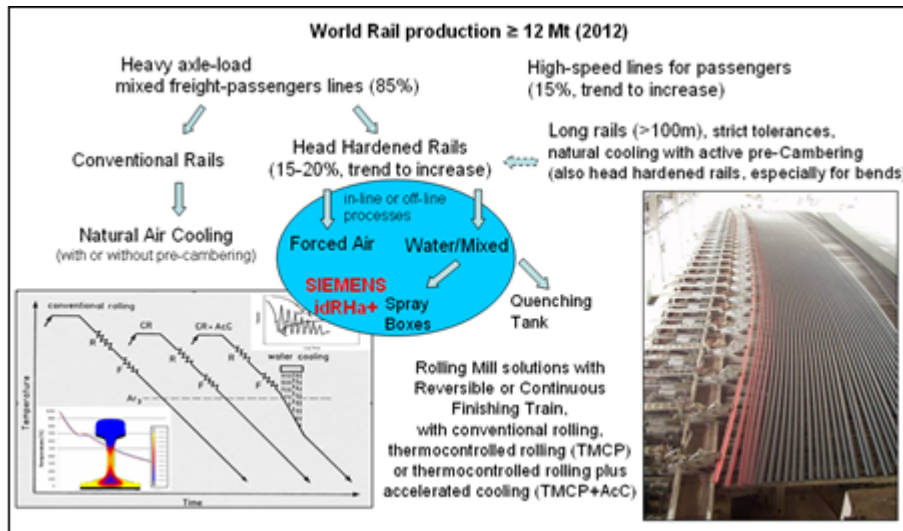


*Figure 2.4 Major process production rails technologies available*

This fast progression of the technical and economical requirements of the rails, challenges the capabilities of the Plant-makers to evolve their portfolio of solutions with incremental innovations..

The most modern solutions applicable in a rolling mill for rails can drive to a significant containment of the operational cost (i.e.-20÷30%) while producing products of superior quality (i.e. narrow size tolerances, consistency and uniformity of technical and metallurgical features) with higher added value; considering for instance the production of in-line thermal treated hardened rail, the price paid by market is, depending on countries, 8 to 20% higher than that of a standard untreated rail and with an estimated saving in production cost by at least 10%.

## 2.2.1   Problems and Improvements

Nowadays, the rapid rise in weight and speed of trains, has inevitably enhanced the rails wear rate, in terms of loss of material due to the abrasion between wheel and rail, and therefore an increasing of hardness has been required in order to reduce wear. With the increase of hardness

also the resistance to cracks damage and failure, therefore the susceptibility to rolling contact fatigue (RCF), has been improved.

RCF is, by definition, damage of components that arises because of repeated loading associated with rolling contacts. A percentage of these cycles, under conditions of high friction and high contact stress, deforms the wheel and rail metal in the direction of the applied stress. The accumulating increments of deformation "ratchet" the surface layer. Although the effective strength of the material is increasing progressively because of strain hardening, it cannot strain indefinitely.
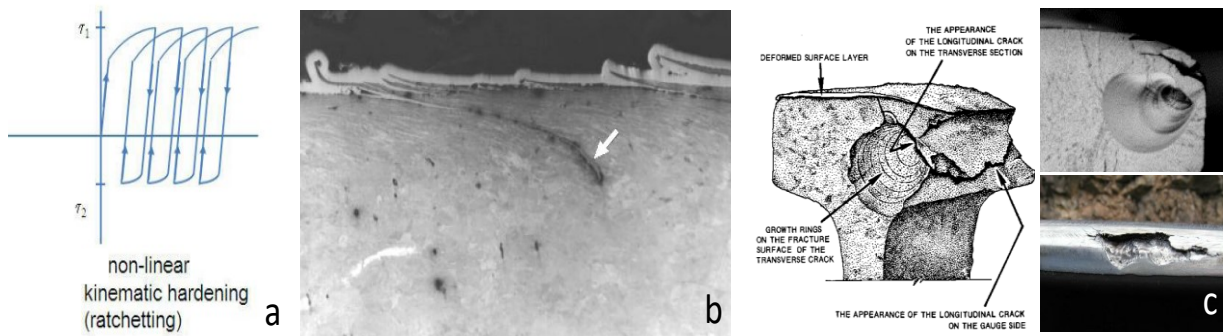


*Figure 2.5(a) Kinematic Hardening, (b) Ratcheting in Rail Steels Associated with Contact Fatigue and (c) crack propagations.*

Figure 1.6 shows an exemplification diagram of the necessity for a new apparatus able to improve rail steels mechanical properties.
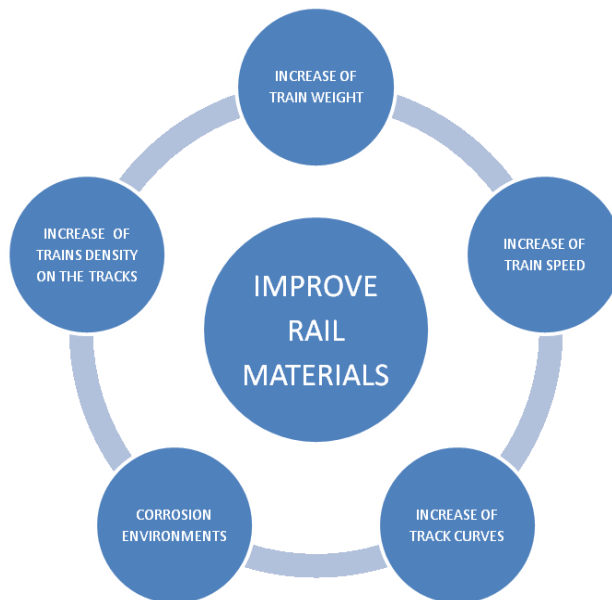


*Figure 1.6 Reasons for the search of new materials for rails*

Conventional rail steels primarily contain nearly eutectoid pearlitic microstructure. Pearlite is an important feature of the microstructure

because it possesses good wear resistance, hence, making carbon an essential alloying element in rail steels. However, it is not only the amount of pearlite that is important but also its morphology, which means the shape and the distance between the cementite lamellae. The finer the structure of pearlite, the higher is its strength whilst still retaining reasonable toughness. Therefore the development of pearlitic rail steels has been focused on the refinement of pearlite.

The strength of rail steels increases with a pearlite structure refinement whilst still retaining sufficient toughness. Therefore, the development of pearlitic rail steels has been focused on the refinement of pearlite. Two types of manufacturing processes have been applied to produce high strength pearlitic rail steels with fine lamellar spacing. One is to make the as-rolled high strength alloy steel rails whose hardenability is increased by the addition of alloying elements. The other one is to make a eutectoid carbon steel rail whose head is hardened by off-line or in-line heat treatment. The wear resistance of above-mentioned fine pearlitic rail steels has proved to be sufficient in practical use. However, with the extension of the rail life, rail surface damage by rolling contact fatigue came out as new challenge. In order to solve this new problem, the applicability of some bainitic steels was studied from literature results.

The bainitic rail steels have high tensile strength and large elongation. Both fracture toughness and absorbed energy are much higher than those of head-hardened pearlitic rails. The wear resistance is nearly the same as in head-hardened pearlitic rails. Very long life span before shelling was also observed. The developed bainitic rails are expected to exhibit excellent performance in heavy haul railroads.

Pearlite comprises a mixture of relatively soft ferrite and a hard, brittle iron carbide called cementite, taking the form of roughly parallel plates. It achieves a good resistance to wear because of the hard carbide and some degree of toughness as a result of the ferrite's ability to flow in an elastic/plastic manner. Figure 2.7 (a) shows the microstructure of a pearlitic rail steel. The cementite is white and the ferrite is black. The interlamellar spacing is about 0.3 microns.

Correct choice of alloys and a correct cooling rate can produce a bainitic structure. This structure, like pearlite, normally contains ferrite and carbide, but in this case the ferrite is semi-coherent with the high temperature austenite phase from which it was formed. Alloying additions are made to prevent the formation of carbides, resulting in very fine interlath films of austenite which are retained between the ferrite plates. The structure is composed largely of low carbon carbide free bainite with some retained austenite. Figure 2.7 (b) shows the microstructure of a bainitic rail steel. The resulting bainitic rail steel has a high tensile strength of about 1400 MPa, and a large elongation. Both fracture toughness and absorbed energy by Charpy impact test are twice as high as those of head-hardened pearlitic rails. Wear resistance is nearly

the same than high strength pearlitic rails. Very long life span before shelling was also observed, about twice as long as that of high strength pearlitic rails.
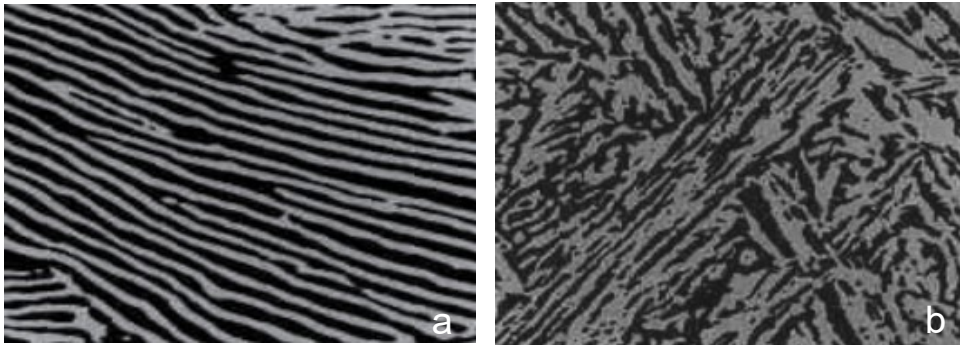


*Figure 2.7 Microstructures of (a) pearlitic and (b) bainitic rail steels*

At present, the situation for thermal treatments is different. There are only two means used to cool the rails: air or water. The water is typically used as liquid in a tank or sprayed with nozzles.

Air is typically compressed through nozzles. None of these arrangements allows producing all the rail microstructures with the same plant. In particular, a thermal treatment plant tuned for the treatment of pearlitic rails can hardly treat bainitic rails. Further present solution are not so flexible about possibility to treat the whole rail section or portions of the rail section in differentiated ways (head, web, foot).

The present invention overcomes the constraints previously mentioned by means of the flexibility of multi-means controlled cooling devices.
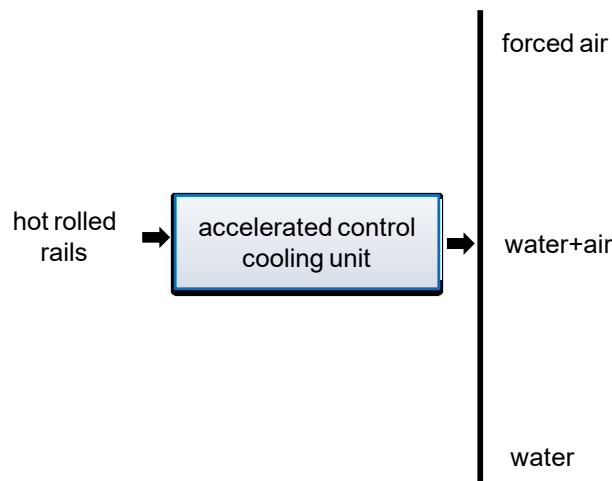


*Figure 2.8 Accelerated control cooling unit-multi-means*

The flexible system allows to obtain both high performance fine bainitic, pearlitic and hypereutectoid final microstructures by means of the same plant. Figure 2. show the different microstructure that can be created with the apparatus.
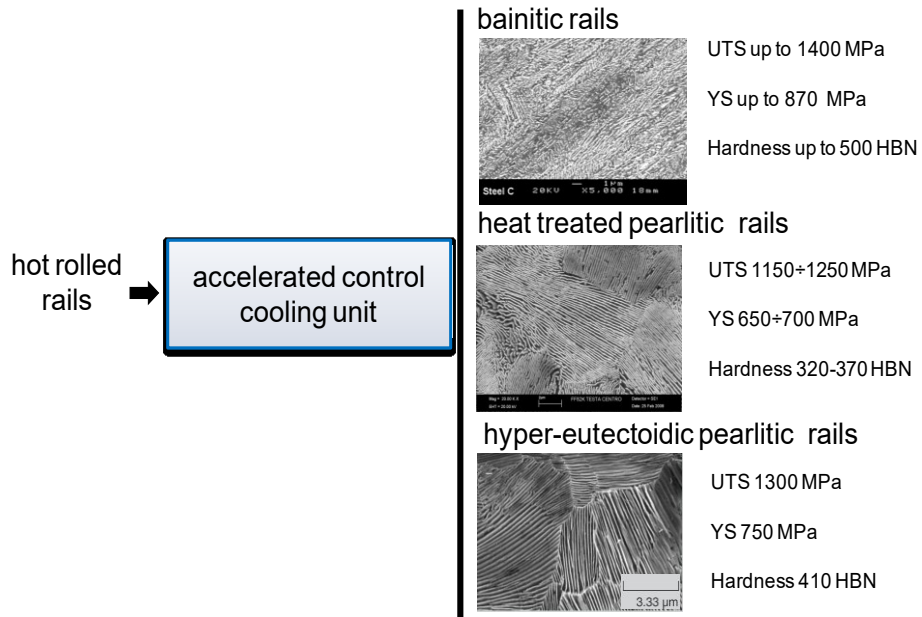
*Figure 2.9 Accelerated control cooling unit – different microstructures*

# Chapter 3

# 3. Task Description

## 3.1 Introduction

The final characteristics of a steel rail in terms of geometrical profiles and mechanical properties are obtained through a sequence of thermo-mechanical processes: a hot rail rolling process followed by a thermal treatment and a straightening step. The hot rolling process profiles the final product according to the designed geometrical shape and provides the pre-required metallurgical microstructure for the following treatment.
In particular, this step allows the achievement of the fine microstructure which, through the following treatments, will guarantee the high level of requested mechanical properties

## 3.2 Concept design of the heat treatment system

At present, two main hot rolling processes, performed in two typologies of plant, reversible and continuous mills, are available (figure 3.1). The final properties of a rail produced by both of these hot rolling processes can be assumed as quite similar and comparable. In fact, bainitic, pearlitic and hypereutectoidic rails are commonly obtained at industrial level through both these kinds of plant.
Whereas the design of the hot rolling line is in some extent neutral to the quality of rails, the standard available solutions for the rail hardening treatment are not recognized so flexible and suitable to process efficiently all range of grades and selectively the whole rail section or portions of the rail section in differentiated ways (head, web, foot).
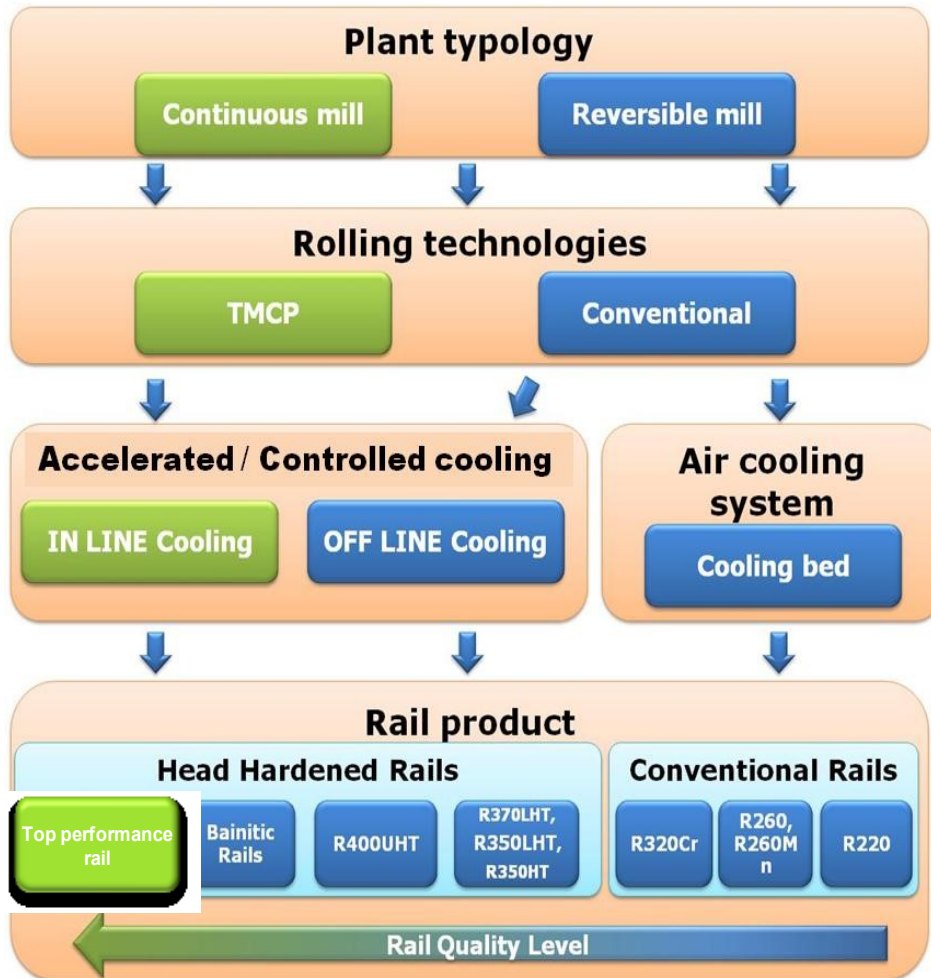
*Figure 3.1 Best mechanical properties can be reached adopting strategies/apparatus put in the green blocks*

Furthermore, in all the present industrial apparatus for thermal treatment of rails, most of the transformation of austenite occurs outside the cooling apparatus itself due to a number of technical and economic constraints, like space availability, process flow and productivity, cost of cooling media, outdated process controls. This means that the austenite transformation is not completely controlled, in particular when the austenite decomposition occurs, with an unrepressed increase of rail temperature due to the latent heat transformation. In this case, the temperature of austenite transformation is higher than the optimal one, with final mechanical characteristics lower than those potentially obtainable by finer and more homogeneous microstructures (fig. 3.2). This uncontrolled temperature profile is also critical for the bainitic rails, where the ideal path of transformation to obtain an homogeneous structure in the whole rail section (head, web and foot) is very narrow.
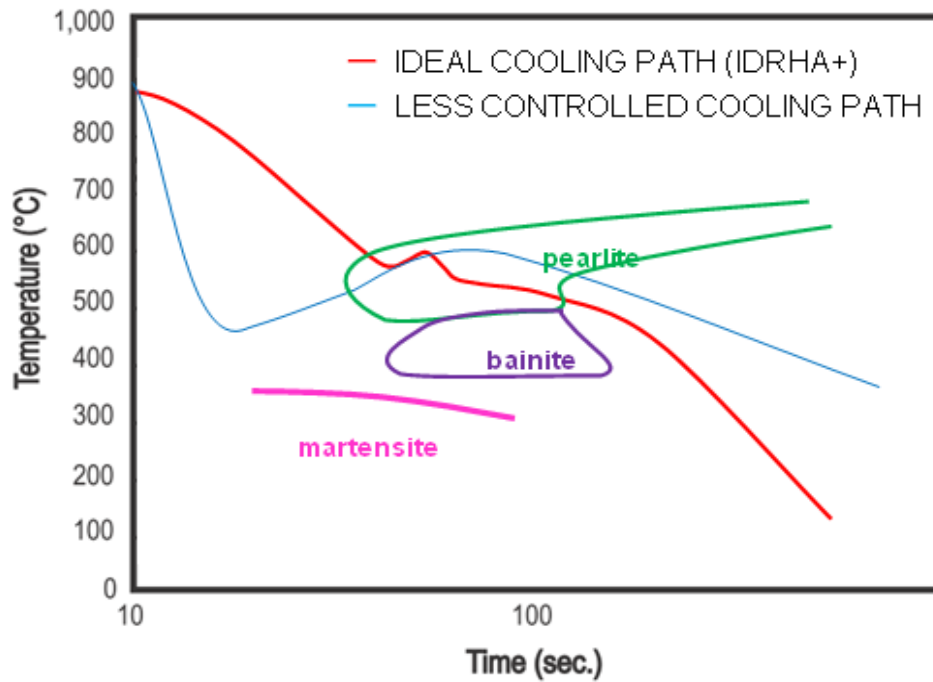
*Figure 3.2 Comparison between the correct/ideal cooling path and less controlled cooling process*

Moreover, due to the real thermal profile of the rail along the length, a not or partially controlled thermal treatment unable to apply selective and variable cooling, can conduct to heterogeneous microstructures also along the length.

The design of idRHa+®, injector dual-phase Rail Hardening as the thermomechanical system is called, overcomes the limits previously mentioned by means of a more controlled thermal treatment, active on the rail until a significant amount of austenite is transformed (at least 50% on the rail surface and not less than 20% at the rail head core) This means that the austenite transformation temperature is maintained within a narrow ideal band thus avoiding any risk to produce secondary undesired structures: martensite for bainitic rails and martensite/bainite for pearlitic rails. The strict control of austenite transformation temperature is obtained by a dedicated flexible apparatus of suitable length equipped with multi-means controlled cooling devices, governed by an active process control system.

### 3.2.1 Process design of idRHa+

The process can be operated in-line or off-line in continuous or non-continuous rail process route. The essential feature of the in line heat treating process is the ability to transform the high temperature austenitic structure that exists immediately following the hot rolling process to the

desired room temperature structure without the normal intermediate steps of cooling to room temperature and then reheating (resolutionizing) prior to accelerated cooling.

Figure 3.3 (a) illustrates a schematic continuous cooling transformation of rail steel. Air cooling of conventional (no hardened) rail steel corresponds to path 1. Cooling along path 2 will produce a much finer pearlite but below point (d) on path 2, bainite and then untempered martensite will be produced instead of pearlite. The bainite and untempered martensite are not preferred transformation products when formed with pearlite. Ideally, cooling along path 3 would be preferred because only a very fine pearlite would be produced. The dashed line on path 3 is nearly isothermal indicating that the pearlite will be of uniform interlamellar spacing as opposed to the varying spacing achieved between points (a) and (b) on path 1. The key issue will be to produce such an isothermal type of transformation in a bainitic region of the transformation diagram. Figure 3.3 (b) shows the intermitted quenching action good for obtains homogeneous pearlite or bainite structures.
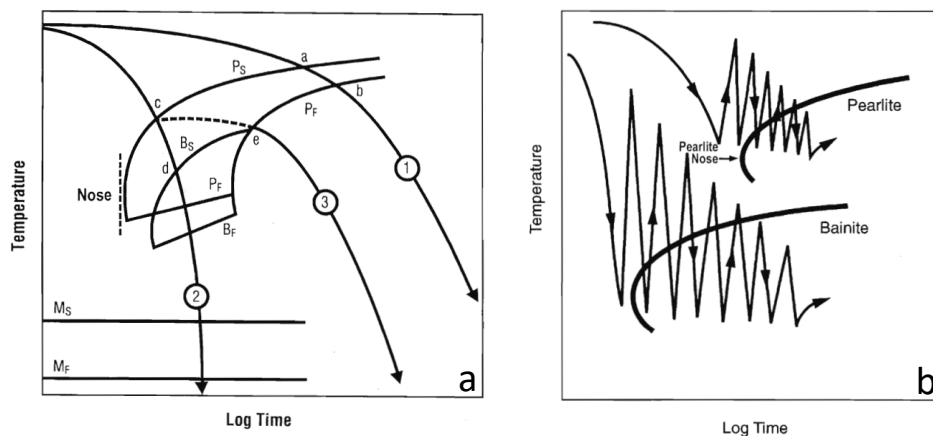


*Figure 3.3 (a) Schematic Representation of a Continuous Cooling Transformation diagram and (b) Conceptual Illustration of Bainite Compared to Pearlite Surface Cooling Paths*

The intermittent quenching action is achieved with water, air or air+water sprays applied to the head, web, and base of the rail.

A system of heating from room temperature, in case of off-line process or a system of heating to equalize the rail temperature after hot rolling, in case of in-line process, is adopted (fig. 3.4).
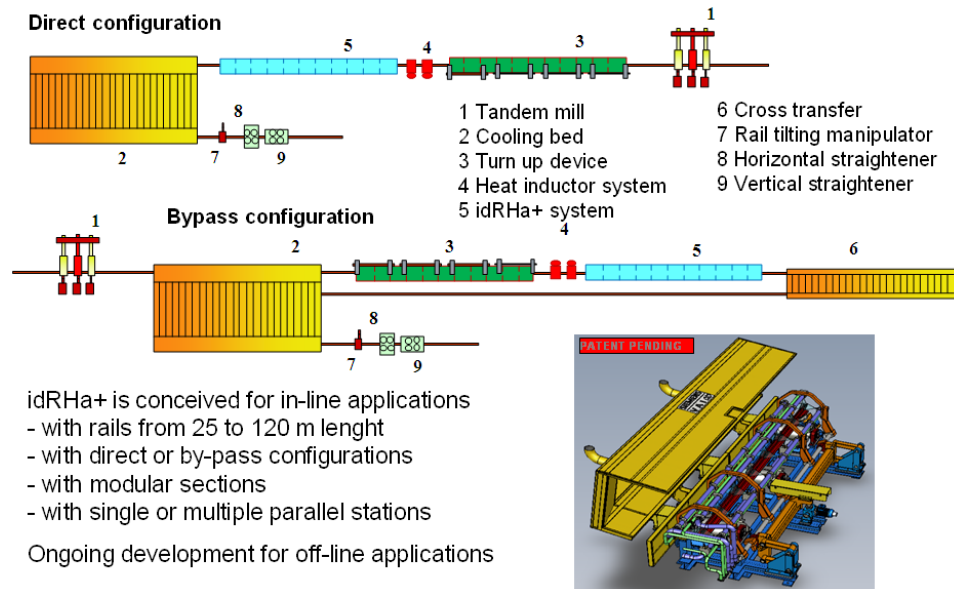
*Figure 3.4 Schematic plant lay-out for in-line process and bypass configuration for off-line system.*

The heating is applied with a series of high-power induction modules, with split top and bottom coils fed with individually powered IGBT converters. Some peculiar design features of the induction modules are hereby described.

The flexible thermal treatment apparatus is composed by modules, whose number and relative position depend on plant productivity, rail length/sizes and grades to be produces. Each module is equipped with a set of interchangeable cooling devices (spraying nozzles with mist-atomizers or air-jet blades). The rail entry temperature is kept in the range of 750÷1000°C measured on the running surface. The cooling is adjustable in the range of 0.5÷40°C/s (figure 3.5) as function of desired microstructure and final mechanical characteristics.  The rail temperature at the apparatus exit is in the range of 300÷ 650°C depending on the treated grade.
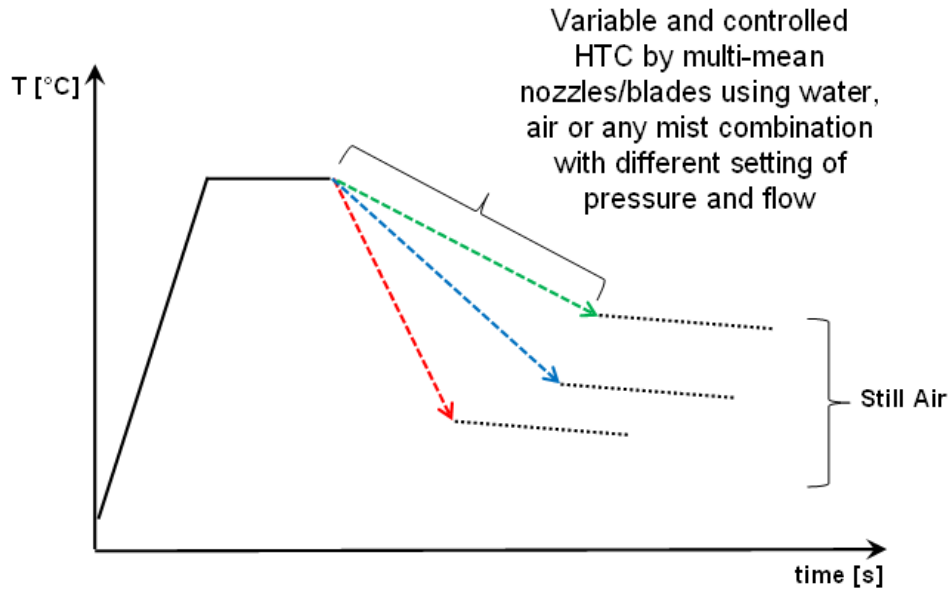
*Figure 3.5 Cooling rate capabilities depending on microstructure and final mechanical properties desired.*

Any module can be controlled and managed alone or coupled with one or more modules. The process strategy (e.g. heating rate, cooling rate, temperature profile) is pre-defined as a function of the final product properties. The process control system uses several embedded thermal, mechanical and metallurgical models: i.e. models for austenite decomposition with microstructure prediction, for precipitation behavior, for thermal evolution with transformation heat calculation, for mechanical properties prediction, for deformation behavior (see figures 3.6 a-b).



- Heat transfer coefficient [H( x, y, z, T, t)]
- TTT diagram and Prior Austenite Grain Size (PAGS)
- Thermo-physical and mechanical properties of metallurgical constituents
- Initial strain field [$\sigma_{ij}^0(r, t)$, $\varepsilon_{ij}^0(r, t)$] and initial temperature field [$T_0(r)$]

- Chemical composition
- Temperature field [r, T(t)]
- Average Particle Size
- Precipitate Volume Fraction

**Thermo-Microstructural-Mechanical Model**

**Mechanical Model**

- Temperature field [(r, T(t)]
- Microstructural field [$f_V(r, t)$]
- Stress and strain field [$\sigma_{ij}(r, t)$, $\varepsilon_{ij}(r, t)$]

- Ultimate Tensile Strength
- Yield Strength
- Hardness

*Figure 3.6 Process control system scheme about thermo-mechanical and microstructural model*

By means of above models, the control system manages and predicts the process and the product parameters according to:

- rail grade chemical composition;
- rail grade mechanical characteristics (e.g. hardness, strength)
- hot rolling mill setup and procedures
- expected rail temperature in defined  profile points (head, web and foot) and along the length (head, center, tail)
- expected austenite decomposition rate and transformation temperature.

The pre-set cooling strategy is then fine-tuned taking into account the actual parameters, measured or predicted with integrative data during the rail process route.

The use of the most suitable cooling mean and its working parameters (e.g. pressure, flow rate) are determined for each module according to the optimized process strategy suggested by the process models. This guarantees the application of an ideal cooling path all along the rail length and through each position in the transverse rail section. Very strict characteristic variation can be obtained avoiding formation of zone with too high or too low hardness and avoiding any undesired microstructure. The basis of the process control scheme is shown in figures 3.7.
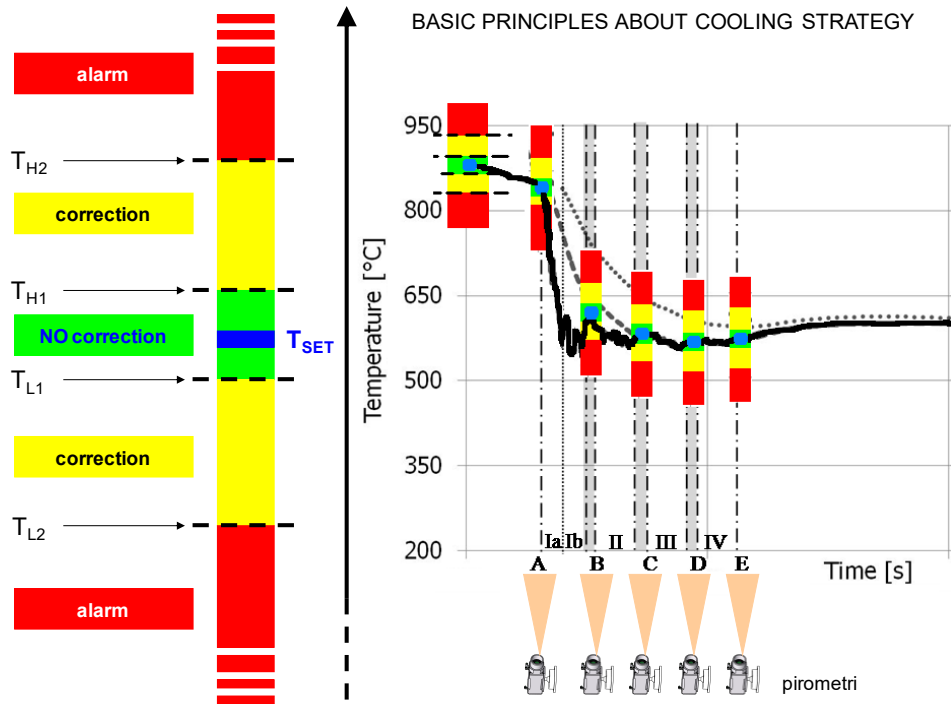
*Figure 3.7 Process control system scheme for automation procedures*

After the measurement of the rail temperatures in different peculiar positions, the process control system takes into account also the actual chemistry of the rail, the target microstructure and the target mechanical characteristic. The temperature measuring devices, pyrometers or thermoscan cameras, keep the temperature continuously monitored: this set of data is used by the process control system to impose the fine regulation to the automation system in terms of selective use of cooling modules, cooling media flux, running speed of the rail in order to correct dynamically any recognized thermal heterogeneity along the rail length and across the rail section. The embedded process models define the cooling strategies in terms of heat to be removed selectively from the profile and along the length of the rail. A specific temperature drop in function of time is proposed in order to transform the austenite at the exit of the flexible apparatus in a percentage not lower than 50% on rail surface and not lower than 20% at rail head core.

## 3.2.2 Mechanical design of idRHa+

The idRHa+ rail hardening system is composed by a group of integrated devices, each with a specific functional and technological purpose.
The system is fully modular so that it can be assembled in several configurations according to the process needs, to the required level of productivity and to the existing plant constraints.

The figure 3.8 shows a typical layout of an in-line idRHa+ system with its functional units.
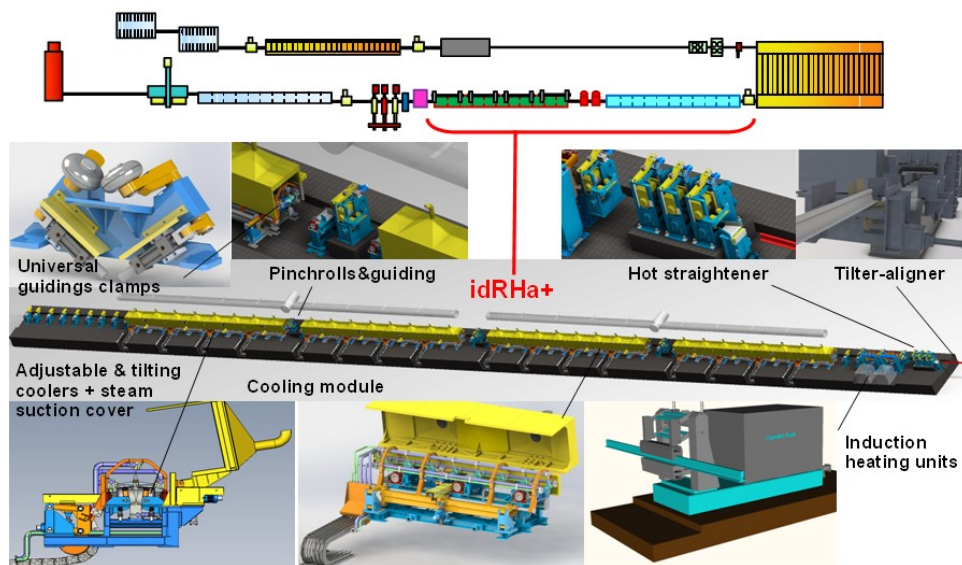


*Figure 3.8 Typical layout of an in-line idRHa+ system with its functional units.*

For in-line applications, after leaving the finishing stand or downstream the cooling bed, the rail is lifted in vertical position by a rail turning system whose center of rotation can be adjusted laterally to have any size of rail in the right upstream position to feed the idRHa+ line. The hot rail could be bent or have some waved parts along its length, especially in the first meters at its ends. It is therefore very useful to have a hot-straightening unit placed before the treatment line in order to recover a suitable straightness of the rail by soft plastic deformation applied by a group of vertically adjustable pinch-rolls.

A set of induction heating units, at least two, provide thermal energy to the rail to equalize the temperature along the length and adjust the suitable temperature distribution across the rail section; in order to have a sufficient buffer of integrative energy to recover the temperature gradients in the rail section and along its length, a typical installed power for an in-line idRHa+ treatment system is 30÷35 kW per ton of rolled rails, meaning that for a productivity of 150 tons/hours the installed power is about 5 MW. The setting of the induction units is pre-defined by a FEM modelling analysis and then dynamically tuned during operations depending on the detected evolution of the temperature profile. In fig. 3.9 an example of the results of the FEM analysis showing the temperature profile expected at the entry of the induction units and the corrected profile at the exit.
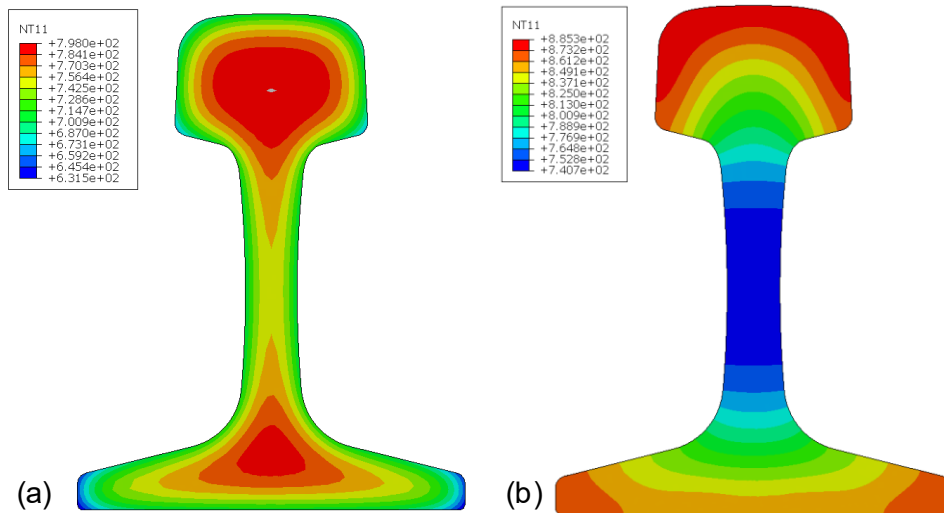
*Figure 3.9 Thermal profile entry section HF(a) and exit section HF(b)*

The design of the induction heaters is of extreme importance to grant a selective and efficient transfer of high power density to the rail in a short time and in a limited space. The induction heaters (coils) are split for the head and the foot of the rail and are fed by individual power converters designed with IGBT (insulated gate bipolar transistor) technology for maximum efficiency and control at optimized consumption (figure 3.10).
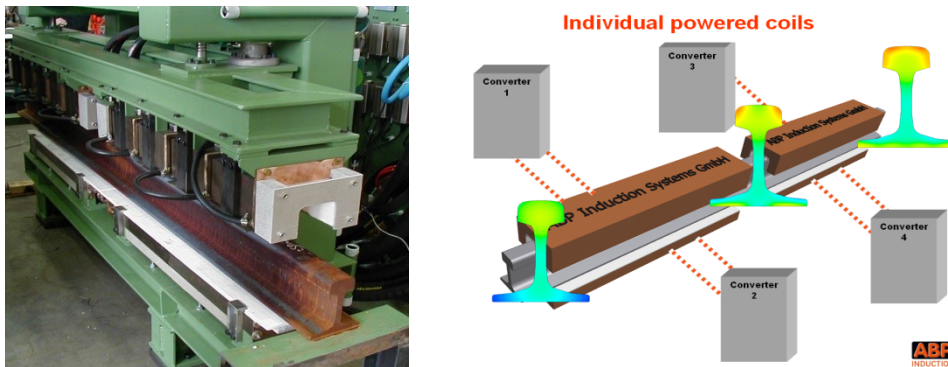


*Figure 3.10 Inductor heaters with IGBT Technology*

The induction heaters are adjustable on the vertical and on the horizontal axis to follow the possible out-of-straightness of the rail and to adapt to the various processed sizes and shapes of rails, including asymmetric rails.
The rail is kept guided through the inductors by horizontal and vertical pinch-rolls while the risk of contact of the rail against the ceramic walls is prevented by means of a contour-follower device with rollers (figure 3.11).
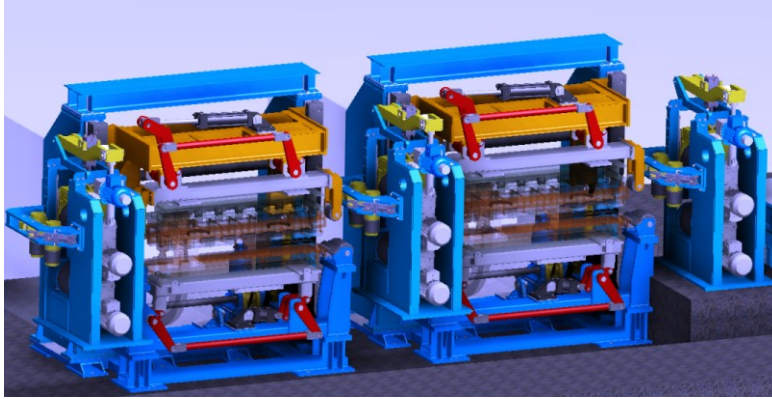
*Figure 3.11 Inductor heaters assembly*

After being heated by the induction units, the rail enters in the cooling area, the core of the idRHa+ technology. As said before, the line is composed by several cooling modules assembled in sequence for a total length granting a sufficient time to have in the rail head most of the austenite (>50% on the surface, 20% in the core) transformed.

Each module is equipped with a set of cooling ramps acting selectively on a part of the rail in order to grant the proper heat transfer coefficient as necessary to reach the desired features; they have also the function to keep balanced the temperature gradients in the rail section to contain excessive deformations. The coolers can be atomizing-mist nozzles, adjustable at different mix of media, and air-jet blades; the proper combination of the coolers along the line and their full interchangeability grant an absolute flexibility of use to match any different process requirements. The position of the coolers is adjustable by means of a cam-system to maintain the proper distance from the rail necessary for an optimized cooling effect and to adapt to the different treated rail sizes, including asymmetric rails. The coolers are mounted on hydraulically tiltable ramps to facilitate the accessibility for the  maintenance operations. The modules are sealed with covers and equipped with a suction system to evacuate the produced steam; also the covers are hydraulically openable to give access to the cooling module (fig. 3.12).
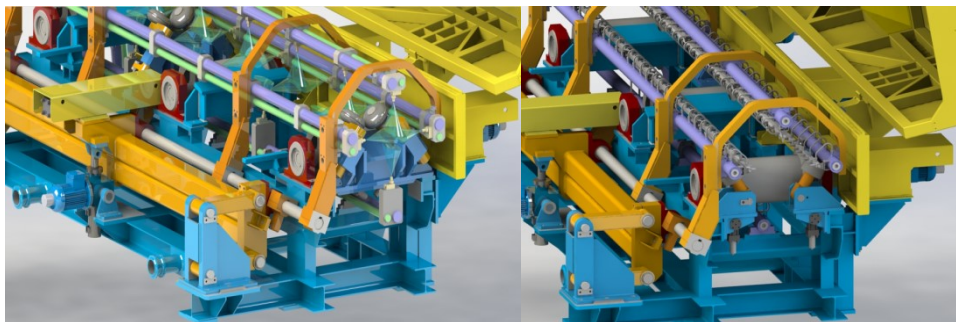


*Figure 3.12 Cooling module assembly*

Each module is equipped with a set of swinging hydraulic pinch-rolls to keep the rail laterally clamped and guided while moving through the coolers; the particular design of this device makes it adaptable to any size and shape of rail (figures 3.13 a-b).
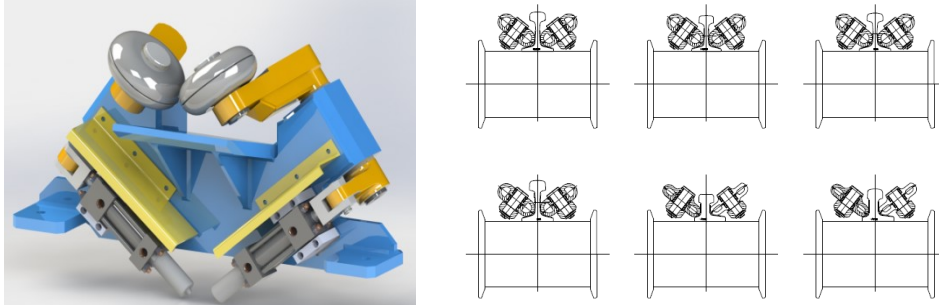


*Figure 3.13 Swinging hydraulic pinch-rolls system (a), different shape configuration (b)*

In between the modules, there are a number of horizontal pinch-rolls equipped with vertical idle rollers to keep the rail centered and guided all along its length without distortion.

### 3.2.3 Main technical features

Downstream the cooling bed, the rail shall be turned in vertical position by a rail turning system. A set of induction heating units of variable power depending on productivity and rail temperature profile provides thermal energy to the rail to equalize the temperature along the length and adjust the suitable temperature distribution across the rail section. At the entry of the induction units, there are some devices to align/center the rail and also to apply a soft hot-straightening to recover anomalous bending of the rail. The rail head could also be cut before entering the induction units to remove abnormally bent part. A set of guiding pinch-rolls ensures a constant speed under the cooling section. After the heating phase the rail enters the cooling line, where it is cooled down following a dedicated cooling strategy in order to achieve the proper microstructure. The rails is then transferred by a transfer machine to cooling table entry way and then straightened.
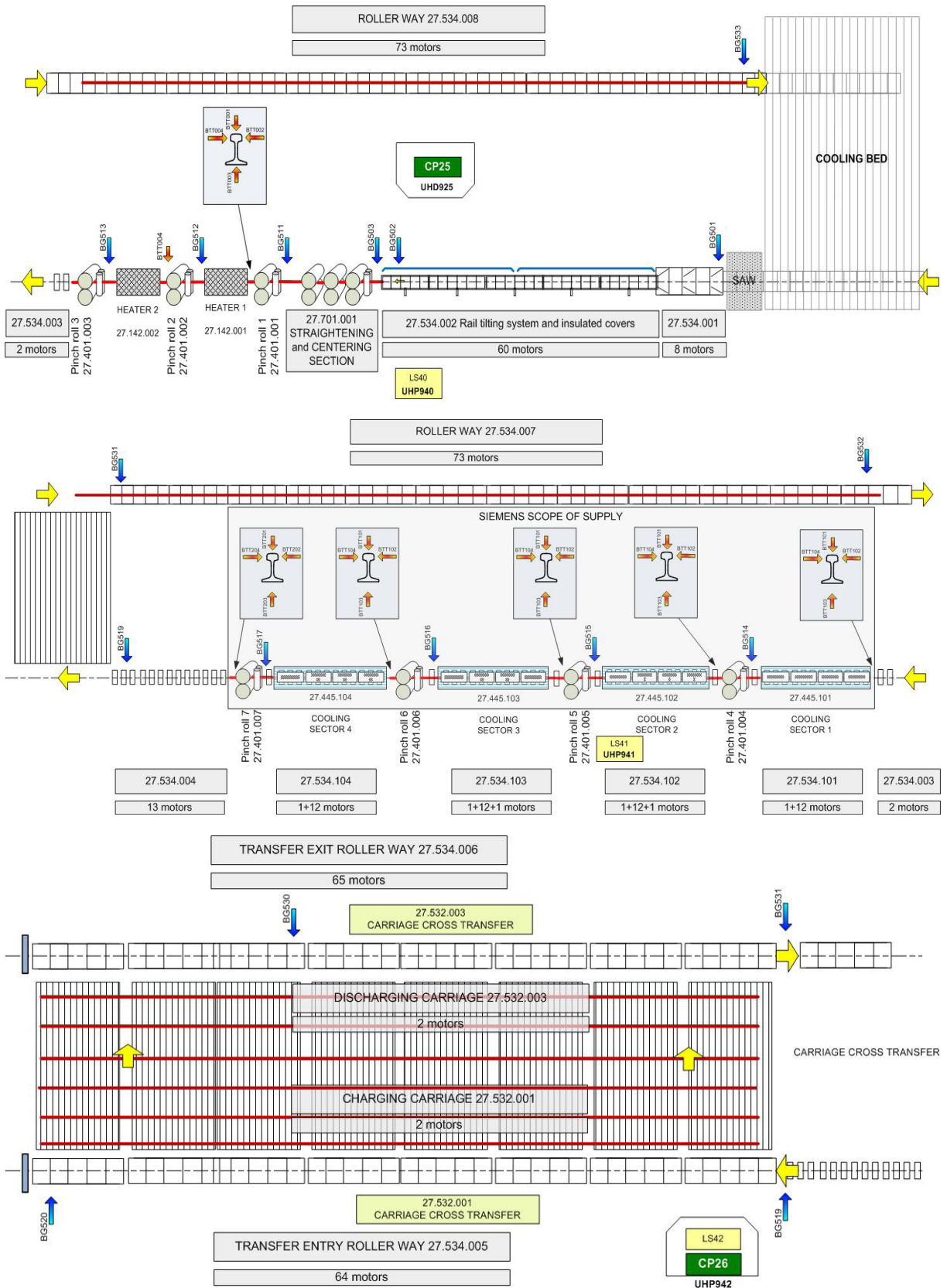
*Figure 3.14 the general layout of the Flexible Rail Hardening System*

### 3.2.3.1  Straightener

The straightening and centering system is used to align/center the rail before sending it into the induction heaters. It applies soft hot-straightening to recover anomalous bending of the rail.

It is equipped with a hydraulic system that is used for opening and closing the top rolls, lifting and lowering the bottom rolls, opening and closing the vertical rolls, and 3 sets of AC motors controlled by single drives for the rollers rotation motion.

Another set of 3 AC motors, connected to a screw jack, is used to adjust the closing distance of the top rollers that is controlled by absolute encoders.

By adjusting different heights of the three rollers, it is possible to straighten the rail when it is passing.
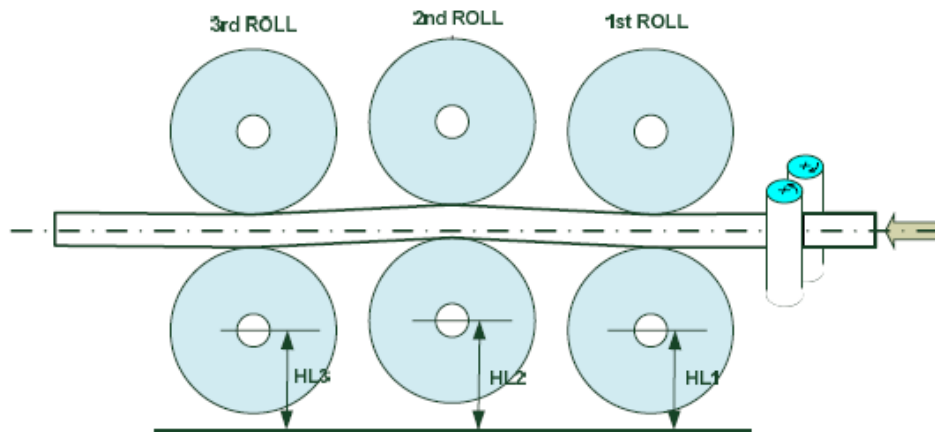


*Figure 3.15 Straightener concept*

The automatic cycle is enabled only when the actual values for the position adjustments all correspond to the set-point values.

As soon as the rail is ready after tilting, the rollers start running at the requested speed and the entry roller way delivers the rail to the straightening machine. The downstream process will then take control for the speed reference and decelerate or accelerate according to the hardening process.

### 3.2.3.2  Induction Heater

The Induction Rail Heater is located on the entry of the Flexible Rail Hardening System to raise the rails temperature to the target value before the cooling process.

To maximize the efficiency of the induction heating, the coils must be as close as possible to the rail, therefore the rail must necessarily has a suitable controlled profile in its length; the rail straightness can be

detected by mechanical (contact rollers) systems to allow the induction units to adjust their position (in vertical and in horizontal planes) to follow the contour of the incoming rail. Reasonable deviation can be tolerated otherwise the induction units are opened to avoid damages by contact with the protecting layer of the coils.

The heater is composed of two inductors, one on the top a another on the bottom of the rail pass line. The top inductor closing gap adjustment is done by an AC motor, controlled by an absolute encoder, that drives a jack screw. The top inductor can be lifted and lowered by means of a proportional hydraulic valve, in order to control the lowering phase with acceleration and deceleration in time. The top inductor's actual position is monitored by two end position sensors, to detect the UP or DOWN position. The bottom inductor can be lifted and lowered by means of a double solenoid hydraulic valve. The top inductor's actual position is monitored by two end position sensors, to detect the UP or DOWN position.

The automatic cycle is enabled only when the actual values for the top inductor height adjustment corresponds to the set-point value.
The induction heater waits for the rail's head with the top inductor in the UP position and the bottom inductor in the DOWN position. The rail enters the heater area pushed by the upstream pinch roll, that also has the function to center it with the vertical rollers. After the heater there is the downstream pinch roll that will receive the rail head, and close on the rail. As soon as the rail is pinched with the two pinch rolls, the inductors "close" on the rail by lifting the bottom inductor and lowering the top inductor.
The actual temperature of the rail is measured on the entry side of the Heater, and this value is sent to the Induction Heater Automation System, as well as the actual Rail speed.
Heater performance:
- Temperature variation along the rail length = ±20 °C
- Rail top target temperature after heating > 850°C (reheating of 100°C)
- Rail foot target temperature after heating > 800°C (reheating of 100°C)

Temperatures are detected by the in-line pyrometers installed ahead of the first induction unit and after the second induction unit.
The measured temperatures will be averaged on a period of 3 seconds.
The stress for the converter is calculated according to the following equation:

$$U = k_1 \cdot \sqrt{k_2 \cdot (T_0 - T_{in}) \cdot \frac{T_{ref}}{T_{ref0}} \cdot \frac{m}{m_0} \cdot \frac{v}{v_0}} + U_{corr}$$

(3.1)

Where:

| | |
|---|---|
| *K1* | *Proportional factor for all temperatures* |
| *K2* | *Proportional factor for low temperatures* |
| *T0* | *Theoretical temperature where the reference stress for the converter is 0 - affects mostly high Temperatures* |
| *Tin* | *Inlet Temperature of the head of the rail* |
| *Tref* | *Reference temperature at end of heater* |
| *Tref0* | *Reference temperature for calculations* |
| *M* | *Mass of rail* |
| *m0* | *Reference mass of rail for calculation ( 60 kg/m )* |
| *V* | *Rail Speed* |
| *v0* | *Reference rail speed ( 1000 mm/s)* |
| *Ucorr* | *Stress bias* |
| *Yui* | *Upper inductor relative position to rail head* |

### 3.2.3.3 Temperature measurement

The temperature of the rail is measured in 4 points on the entrance of the cooling sector.

One pyrometer placed on top of the rail measures the top temperature, another two measure the side temperatures and a fourth one the foot temperature.
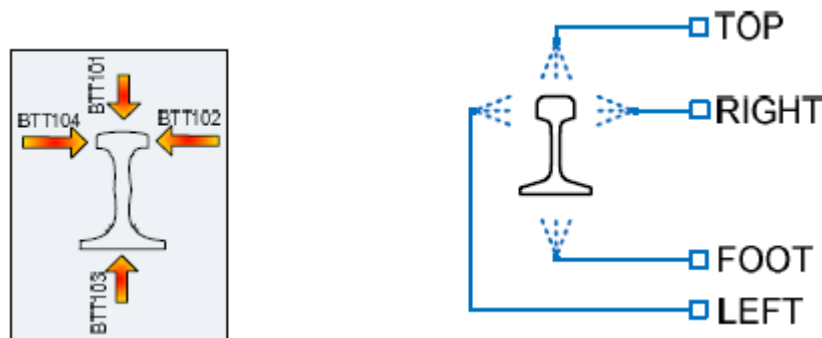


*Figure 3.16 Pyrometers positions*

### 3.2.3.4 Water & Air pressure control

The cooling process control is common for each pair of 2 air/mist modules. It is divided into four individual systems for the TOP, LEFT SIDE, RIGHT SIDE and FOOT cooling regulation for water, and three for AIR ( the left and right air control are a common system).

Each pair of modules has 7 closed loop regulators, 4 for water and 3 for air

pressure control. The three systems are separate for the TOP, SIDE and FOOT part of the rail.

Each pair of modules have in common:
- A set of 4 proportional controlled water pressure regulation valves;
- A set of 4 water pressure transducers;
- 4 water draining valves for fine control of flow for low set points;
- A set of 3 proportional controlled air pressure regulation valves;
- A set of 3 air pressure transducers

In the case of only air module is used for cooling, every module use independent air pressure control valves and a feedback transducers.
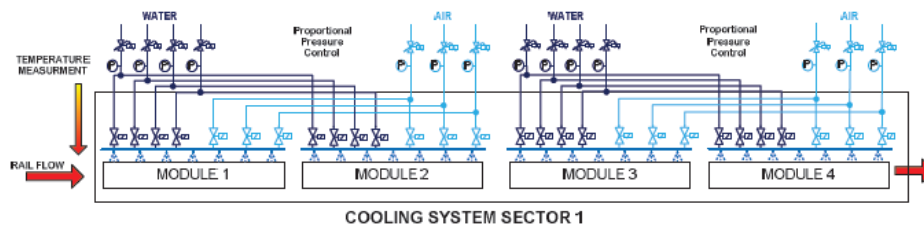


*Figure 3.17 One sector of Cooling system*

# Chapter 4

# 4. Literature review

## 4.1 Metallurgical model

Modeling and simulation of microstructure evolution is one of the most important ways to improve the quality of the final product. In order to optimize thermomechanical parameters for achieving the desired mechanical properties of the product, understanding and modeling microstructure evolution is a key issue for designers of metal forming processes (hot rolling, forging, and extrusion).

### 4.1.1 Transformation kinetics

A variety of phase transformations are important in the processing of materials and usually they involve some alteration of the microstructure. It is possible to identify three different kind of transformations:

1. Simple diffusion-dependent transformations and recrystallization, in which there is no change in either the number or composition of the phases present. These include solidification of a pure metal, allotropic transformations and recrystallization and grain growth;

2. Diffusion-dependent transformation governed by the presence of some alteration in phase compositions and often in the number of phases present;

3. Diffusion less transformation, wherein a metastable phase is produced.

Due to the fact that in present work I will deal with transformation which involves only solid phases, the present section is going to be devoted to solid-state transformations. As Johnson and Mehl originally observed, phase transformations are usually the result of simultaneous process of nucleation and growth. Transformation progress is usually ascertained by either microscopic examination or measurement of some physical properties (such as electrical conductivity) whose magnitude is distinctive of the new phase. As it will be following proposed, data are usually plotted as the fraction of transformed material versus time as reported in fig. 4.1. Nucleation and growth stage are reported.
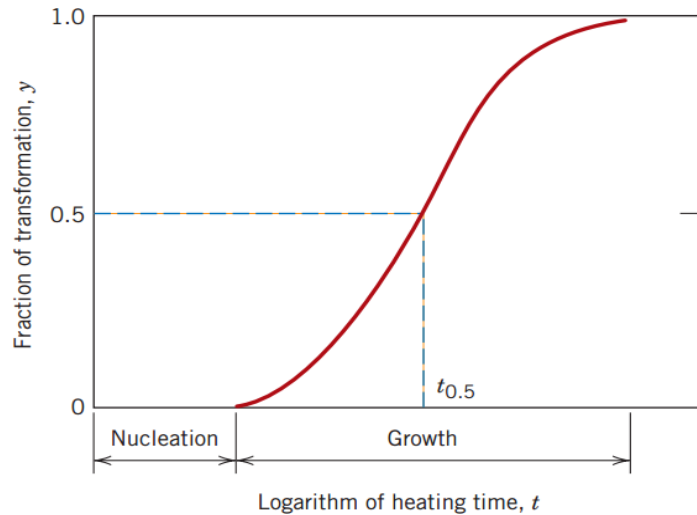
*Figure 4.1 Fraction reacted versus the logarithm of time typical of many solid-state transformations in which temperature is held  constant*

### 4.1.2   Isothermal transformation  kinetics

For  an isothermal diffusional or reconstructive transformation i.e.  for which  T  (t)  =  constant,  the  Johnson-Mehl-Avrami-Kolgomorov  or "JMAK" equation is often used for the analysis of the experimental kinetic data:

$$f(t, T) = 1 - exp\left[-k(T)t^n\right] \qquad (4.1)$$

where f (t, T ) is the fraction transformed and t is the transformation time and n is the exponent, k is the reaction rate constant. It is given by:

$$k(T) = k_0 \cdot e^{-\frac{Q}{RT}} \qquad (2.2)$$

where Q is the activation energy for the transformation. The JMAK equation can be derived assuming constant nucleation and growth rates. The sigmoidal shape is a consequence of the small number of nuclei available for short times, the growth of many nuclei at intermediate times and  impingement  at  longer  times.  The  JMAK  equation  may  be generalized to include an incubation time:

$$X(t, T) = 1 - exp\left[-k(T)(t - \tau_{inc})^n\right] \qquad (4.3)$$

The factors that influence f(t,T) are:
- the nucleation rate, which is function of the undercooling;
- the growth rate, which is temperature dependent in diffusion controlled transformations;
- the number of nucleation sites;
- the distribution of nucleation sites.

The rate of transformation is given by:

$$\frac{dX(t,T)}{dt} = nkt^{n-1}(1-X) = nk(1-X)\left[-\frac{\ln(1-X)}{k}\right]^{\frac{n-1}{n}} \quad (4.4)$$

In the isothermal case, the JMAK equation has a typical sigmoidal or S-shaped time dependence as the one reported in fig.4.1. The JMAK equation can be derived theoretically and the $k$ and $n$ value can be shown to have a clear physical meaning. It is assumed that nucleation starts at $t = \tau$ and the nuclei are spherical. Assuming the radius $r$ of the phase product has a linear rate of increase, i.e. its growth rate G is described by $G = dr/dt$ , the volume of a single sphere of product phase nucleated at time $\tau$ is, at time $t$, given by:

$$\frac{4}{3}\pi r^3 = \frac{4}{3}\pi\left[\frac{dr}{dt}(t-\tau)\right]^3 = \frac{4}{3}\pi G^3(t-\tau)^3 \quad (4.5)$$

If constant rate of nucleation $N$ is assumed, equal to the number of nuclei generated per time unit in a unit volume, the number of nuclei generated in a time interval $dt$ results to be $N \cdot dt$. Therefore, the volume of product phase formed in a unit volume within a time interval $dt$ is given by:

$$N\frac{4}{3}\pi G^3(t-\tau)^3 dt \quad (4.6)$$

Taking the "overlap or impingement error" into account, the actual total volume of untransformed phase volume is given by the "extended volume fraction": $V_{tot}(1-f)$, where $V_{tot}$ is the total volume of transforming phase and $f$ is the fraction of phase, which has already transformed. This connection recognizes that a nucleus can only grow into a given volume of the untransformed material. The increase $df$ in transformed fraction within a time interval $dt$ is given by:

$$df = \frac{1}{V_{tot}}(1-f)NG^3\frac{4}{3}\pi(t-\tau)^3 dt \quad (4.7)$$

and hence:

$$\frac{df}{1-f} = \frac{4}{3}NG^3\pi(t-\tau)^3 dt \quad (4.8)$$

This equation can be integrated to yield:

$$\int_0^f \frac{df}{1-f} = N\frac{4}{3}\pi G^3\int_0^t (t-\tau)^3 dt = \frac{\pi}{3}NG^3(t-\tau)^4 \quad (4.9)$$

Rearranging:

$$f = 1 - exp(-N\frac{\pi}{3}G^3(t-\tau)^4) \quad (4.10)$$
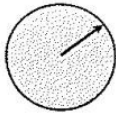
*Figure 4.2 The transformation-geometry dependent n values at constant nucleation rate N and growth rate G for spherical, plate and needle type growth of new phase.*

When the nucleation rate goes to 0, only pre-existing nuclei grow and no new nuclei are generated during the transformation: this leads to a reduction of the n-value

This equation has the same general form as the JMAK equation. This deviation can be modified to show that the coefficient $n$ is related to particular types of transformation growth geometries as depicted in fig.4.2. The coefficients $k$ and $n$ can be calculated based on theoretical transformation models. Both can be also determined experimentally by means of measured isothermal transformation kinetics using dilatometric data. Constant $k$ depends on both the nucleation rate and the growth rate. It is therefore very sensitive to the temperature. The activation energy $Q$, is determined experimentally as follows. As the parameter k is given by eq.4.2, for two isothermal transformation measurements at $T_1$ and $T_2$ it is possible to write:

$$\ln(k_1) = \ln(k_0) - \frac{Q}{RT_1}$$

$$\ln(k_2) = \ln(k_0) - \frac{Q}{RT_2}$$

and subtracting each term:

$$\ln(k_1) - \ln(k_2) = -\frac{Q}{RT_1} + \frac{Q}{RT_2} \rightarrow ln\left(\frac{k_1}{k_2}\right) = \frac{Q}{R}\left(\frac{1}{T_2} - \frac{1}{T_1}\right) \qquad (4.11)$$

Rearranging:

$$Q = \frac{R ln\left(\frac{k_1}{k_2}\right)}{\left(\frac{1}{T_2} - \frac{1}{T_1}\right)} \qquad (4.12)$$

The above mentioned procedure is represented schematically in fig.4.3.
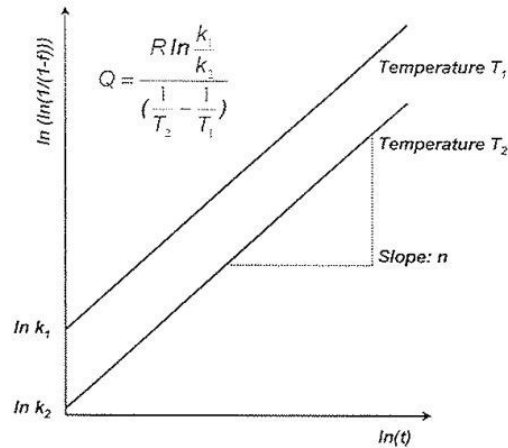
*Figure 4.3 Schematic showing the method to determine k and n in the JMAK equation*

### 4.1.3   Nucleation kinetics

Some important transformations that occur in steels, e.g. the formation of ferrite and perlite, are of "nucleation and growth" type, and the nucleation stage plays an essential role in the initial stages of the transformation. The nucleation of ferrite in austenite in pure *Fe* can be very fast. It is usually heterogeneous, which implies that the $\alpha$–*Fe* nuclei are formed on low energy sites, usually grain boundaries or inclusions in the parent $\gamma$–*Fe* phase. The rate of nucleation, *I*, i.e. the number of $\alpha$–*Fe* nuclei that form per unit of volume and per unit of time in $\gamma$–*Fe*, is described by the following equation:

$$I = Zn_{total}\, e^{-\frac{\Delta G^*}{kT}} \omega e^{-\frac{Q}{kT}} \left( 1 - e^{\frac{t}{\tau}} \right) \tag{4.13}$$

where:

- *Z* is the Zeldovitch factor, which takes into account the fact that only a fraction of critical-sized embryos become nuclei.

- $n^* = n_{total}\, e^{-\frac{\Delta G^*}{kT}}$ is the number of $\alpha$–*Fe* nuclei that have reached the critical size, assuming the total number of potential nucleation sites in $\gamma$–*Fe* is given by $n_{total}$.

This factor depends of the free energy variation $\Delta G^*$ associated with the formation of a heterogeneous critical nucleus of diameter *r*. This situation is illustrated in fig.4.4, where it is shown a lens-shaped $\alpha$–*Fe* nucleus with radius *r* on a grain boundary in $\gamma$–*Fe*, which has surmounted the free energy barrier $\Delta G^*$. A shape factor is used in order to take into account the geometry of the nucleus. In this case, it is equal to $\frac{(2+\cos\theta)(1-\cos\theta)^2}{2}$, with $\theta$ the contact angle.

- $\beta = \omega e^{-\frac{Q}{kT}}$ is the rate at which Fe atoms jump from the $\gamma$ to the $\alpha$ phase. $\omega$ is the jump frequency to a suitable position in the nucleus.

- $e^{-\frac{\tau}{t}}$, is a factor which takes into account the fact that an incubation time *tau* may pass before the nucleation starts. Schematic representation is reported in fig.4.4. At lower temperatures the nucleation process is fully-diffusion controlled. The activation energy for diffusion entering into the calculation for the nucleation rate is not necessarily the activation energy for bulk diffusion. Grain boundary diffusion may have a much lower activation barrier. The TTT diagram of diffusional transformation transformations will usually have a "nose" or "C" shape which is indicative of the fact that the rate of transformation is highest at an intermediate undercooling below the equilibrium transformation temperature. At temperatures close to the equilibrium transformation temperature the driving force for transformation is small and both nucleation and growth rates are low. At greater undercooling the transformation is again delayed due to the slow diffusion rates. Heating transformations, such as austenite formation from ferrite, exhibit a monotonic increase in kinetics with temperature because there is no "trade-off" between driving force and diffusivity in heating transformations. Transformations in steel are complicated due to the fact that these are multicomponent systems requiring diffusion of different species. In general, the nucleation rate and the growth rate are functions of temperature as depicted in fig.4.5.
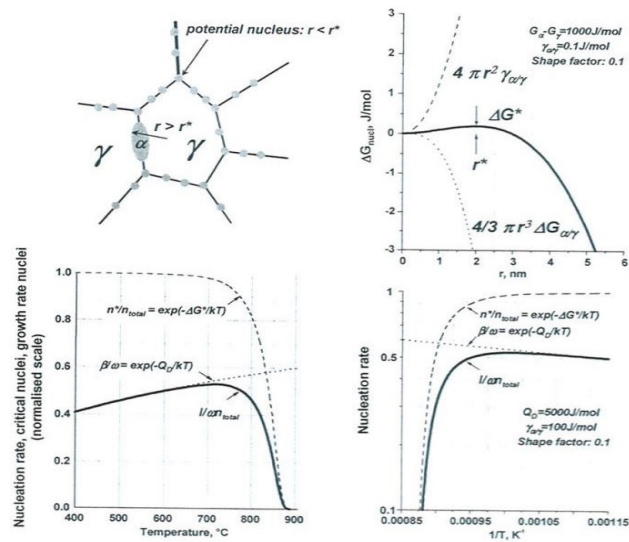


*Figure 4.4 Scheme of the fundamental aspects that play a role during the nucleation process in solid state transformations in ferrous alloys. Nucleation of ferrite at austenite grain boundaries. Calculation of the critical free energy and critical size for nuclei. Determination of nucleation rate.*

### 4.1.4 Empirical Methods

Simple empirical methods have been proposed to describe the transformation kinetics for steels based on parameters determined using non-linear least squares regression analysis of experimental data from a large number of steels. The temperature dependence of k, the reaction rate constant, is described by means of a modified Gaussian function:

$$k = P_1 \, exp\left[-\left(\frac{T-P_2}{P_3}\right)^{P_4}\right] \qquad (4.14)$$
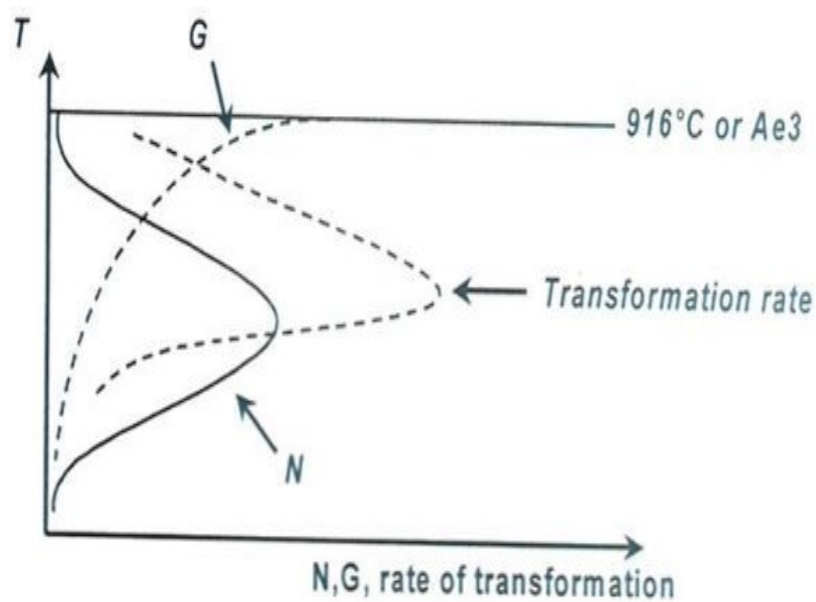


*Figure 4.5 Schematic of the temperature dependence of the nucleation rate N and the growth rate G, and the overall rate of transformation*

TTT curves can easily be plotted if the $P_i$ parameters are known. $P_i$ parameters have the following meaning:

- $P_1$: the maximum value of k;

- $P_2$: the temperature of the nose;

- $P_3$: the width of the k function;

- $P_4$: a parameter related to the sharpness of the $k$ function;

- $A_{e3}$: temperature under which the existence of the ferrite becomes thermodynamically possible. It can be simply evaluated such as:

  $A_{e3} = 911 - 29\%Mn - 10\%Cr + 70\%Si - (418 - 32\%Mn + 86\%Si + 1\%Cr) \cdot \%C + 232\%C^2$

  where all the percentages are expressed in terms of weight percentage;

Considering the austenite grain size $d_\gamma$ in $\mu m$, the $P_i$ parameters can be evaluated as:

- For ferrite:

$$P_1 = \frac{2}{d_\gamma \left(\%C + \%\frac{Mn}{6}\right)}$$

$$P_2 = Ae_3 - 210 - 170\%$$

$$P_3 = 67$$

$$P_4 = 1.9$$

$$n = 1.5 \tag{4.15}$$

- For pearlite:

$$P_1 = \frac{213}{d_\gamma}$$

$$P_2 = A_{e_1} - 60 + \frac{400}{d_\gamma} - 470\%C$$

$$P_3 = 47$$

$$P_4 = 2.2$$

$$n = 1 \tag{4.16}$$

For a hypo-eutectoid steel, there is an additional complication in the sense that pro-eutectoid ferrite can form.

### 4.1.5   Martensite transformation kinetics

The $\gamma \rightarrow \alpha'$ martensitic transformation in ferrous alloys is most often athermal, i.e. the fraction transformed is controlled by temperature changes rather than being time dependent. In TTT diagrams the extent of martensitic transformation is therefore represented as a series of parallel lines representing the transformed austenite fraction. The transformation kinetics can be described by an empirical time independent equation such as:

$$f_{\alpha'} = 1 - exp\left(-\alpha \left(M_s - T\right)^n\right) \tag{4.17}$$

where $f_{\alpha'}$ is the fraction of austenite that has transformed to martensite, $M_s$ is the martensite start temperature and T is the temperature to which the steel is quenched. According to Koinstinen and Marburger, the coefficients α and n are 0.011 and 1 respectively. It is necessary to underline that this is not the unique formula proposed to described

martensitic formation. Further equations, even of different shape (linear or exponential) exist. There are several formulas available in literature in order to determine the Ms temperature depending on chemical composition. According to:

$$M_s = 521 - 353\%C - 26\%Mo - 22\%Si - 24\%Mn - 17\%Ni - 8\%Cu + 18\%Cr$$

$$(4.18)$$

### 4.1.6 Consideration on the use of JMAK equation

When JMAK equation is adopted, it is very important to take into account which hypothesis are assumed. In particular it is necessary to remark, as Humphreys noted that, the hypothesis at the basis of JMAK model are:

- random nucleation sites dispersed in the parent phase;

- the growth rate of the new phase is constant and not dependent on the extend of transformation;

- growth occurs at the same rate in all directions.

Depending if the nucleation rate will be constant or not during the whole transformation, the coefficient n can assume different values:

- $n$ = 4: if the nucleation rate during the whole transformation is constant;

- $n$ = 3: id the nucleation occurs only at the beginning of the transformation.
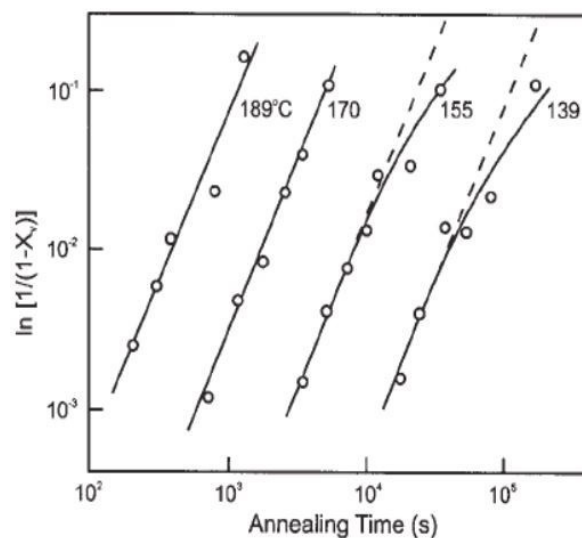


*Figure 4.6 Example of Avrami plot for an aluminum alloy deformed by rolling*

Humphreys noted that is very unusual to find experimental data with very good agreement with JMAK model. The Avrami exponent $n$ is measured on the $ln(ln(1/(1 - X)))$ against $ln(t)$ plot (the so called Avrami plot) where it is represented by the slope of a straight line as reported in fig.4.6. However, it is frequent to find out some deviations from the linearity that indicate some non-modelled slowdown.
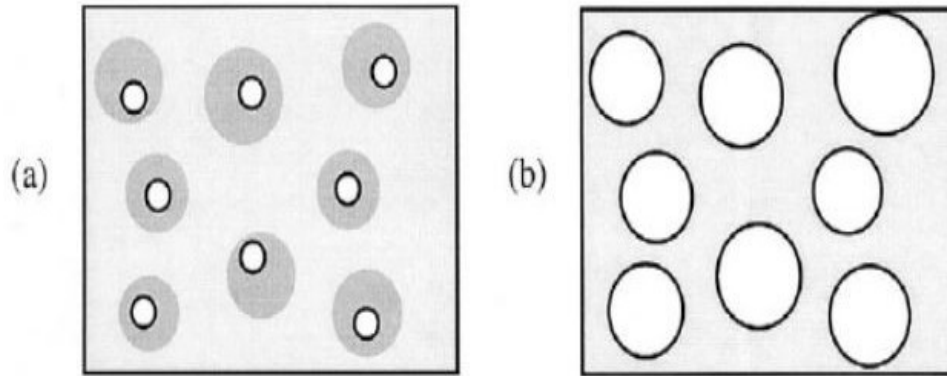


*Figure 4.7 Example of inhomogeneities in the distribution of the stored energy*

In real materials, the nucleation occurs in preferential sites and there are evidences that the growth rate of new grains is not a constant in the volume of the sample and during the recrystallization. Another justification for the typical trend of experimental Avrami plot is based on a not homogeneous distribution of the stored energy and can be used both for high and low stacking fault materials. As reported in fig.4.7, there are some regions (dark shaded) with high energy stored, resulting for example from local straining, dispersed into a matrix with lower energy values. New grains will nucleate inside or close to these regions and their growth will be initially fast but will decrease when regions with high energy stored are consumed. This ex- plains the non-random distribution of nucleation sites and the decreasing of growth rate with time. These complex phenomena cannot be fully predicted and because of this reason approximations achieved by JMAK model is univocally achieved by literature. Some authors proposed modifications, such as Khanna and Taylor arbitrarily did proposing a correction to the original JMAK equation. In particular, the correction proposed for the transformed fraction was:

$$X = 1 - exp(-Bt^k) \rightarrow X = 1 - exp(-(At)^k) \qquad (4.19)$$

However Marangoni proved that Avrami equation should be used in its original form and the use of "modified" version must be abandoned.

## 4.1.7   Non-isothermal transformation kinetics

In many practical situations, the temperature which governs a transformation of phase is not constant during the process. This is the case of many industrial processes. During heat treatments for steel, the transformation associated with austenite decomposition occur conditions of continuous cooling rather than isothermal conditions and the cooling rates may be different in different places as a result of the geometry of the part which has to treated. However, if the isothermal transformation kinetics are known, i.e. if the *n*-parameters and *k*-parameters of the JMAK equation for isothermal transformation are available, the transformation kinetics during continuous cooling can be estimated. The cooling path $T$ (*t*) is therefore replaced by consecutive isothermal steps as represented in fig.4.8. In the original version, the *n*-parameter is assumed to be temperature independent while the *k*-parameter is assumed to be temperature dependent.
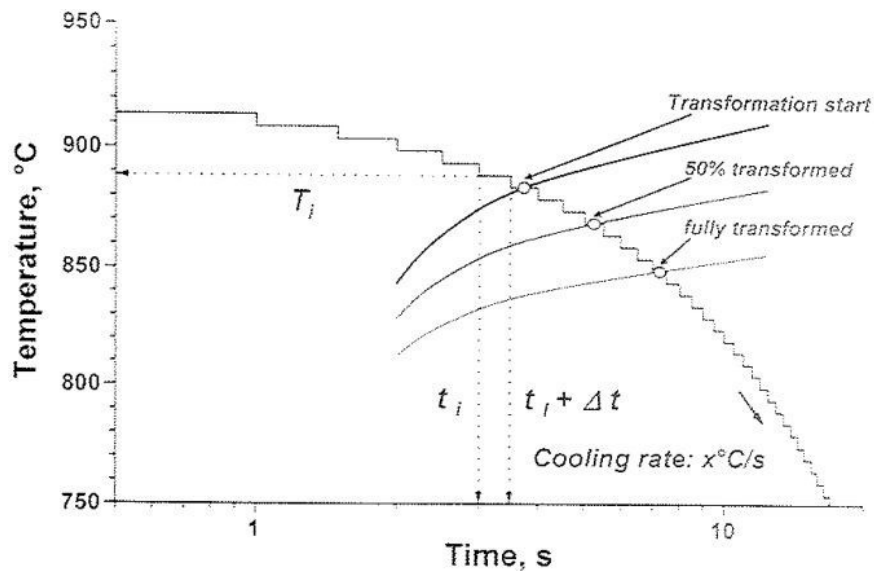


*Figure 4.8 Schematic show in the equivalence of a continuous cooling curve T(t) and a succession of small isothermal steps*

The method is known as "Additivity rule" originally proposed by Scheil. The mathematics of the additivity principle are rather simple. Say one replaces the continuous $T(t)$ by a succession of isothermal steps lasting for a time $\Delta t$ at $T_1$, $T_2$..., $T_i$,. The first short isothermal hold at $T_1$ will result in a ferrite fraction equal to $f_1$:

$$f_1 = 1 - e^{-k_1 \delta t^n} \tag{4.20}$$

For the isothermal transformation at T2, a time $t_2^*$ is defined:

$$t_2^* = \sqrt[n]{\frac{ln(1-f_1)}{-k_2}} \tag{4.21}$$

$t_2^*$ is the time to form a ferrite fraction equal to $f_1$ if the transformation takes place at a temperature $T_2$, i.e. with kinetic parameters n and $k_2$. The ferrite fraction formed after the second small isothermal step at $T_2$ is then given by:

$$f_2 = 1 - e^{-k_2(t_2^* - \Delta t)^n} \tag{4.22}$$

If the same procedure is repeated for the full succession of isothermal steps, the transformation kinetics can be obtained for a specific cooling rate. In other words, the time $t_i$ at a certain temperature $T_i$ divided by the isothermal time $\tau_i$, which is required to start the transformation, can be considered as representative for the fraction of total incubation time elapsed. Scheil, postulate that for non-isothermal treatment, the transformation can start when the summation of the incubation times is identically unitary:

$$\sum_{i=1}^n \frac{t_i}{\tau_i} = 1 \tag{4.23}$$

The summation is performed on each step exploited to described the non-isothermal cooling between the equilibrium temperature and the temperature at which the transformation started. Because of this reason, the total time necessary to complete the transformation can be obtained summing all the fractions of time necessary to achieve at final stage through isothermal way, up to the moment in which their sum is identically unitary.

Generalizing:

$$\int_{t0}^t \frac{dt}{t_i(T)} = 1 \tag{4.24}$$

So, the transformation process (incubation) will be completed when the sum of the fractional increment of the events will achieve the unit. In this way, a mathematical relation between the non-isothermal path and an isothermal one is achieved. Integrating with respect to temperature instead time, it is possible to write down:

$$\int_{T0}^{Ti} \frac{1}{t_i(T)} \frac{dt}{dT} dT = 1 \tag{4.25}$$

where $t_i(T)$ is the time for a temperature $Ti$ at which a part of transformation is completed, $T_0$ is the temperature is the starting temperature. Let us note that $dt/dT$ is the reciprocate of the cooling temperature, con- firming that the mathematical deal takes into account non-isothermal effects. Repeating the calculation for different cooling rates, results in the full CCT diagram for the non-isothermal $\gamma \rightarrow a$ transformation. In practice, transformation data are most often obtained using dilatometry. In general, transformation data are obtained using non-standardized techniques. In order to increase the reliability of transformation data for various production processes, clear procedures have been established.

### 4.1.8 Criteria for additivity

Cahn examined the possibility to exploit additivity rule during transformation processes and he was able to state a criterion to identify an additivity reaction. In particular, if the reaction rate depends exclusively on instantaneous temperature and on the transformed fraction, the reaction can be considered additive.

Mathematically:

$$\frac{dX}{dt} = F(T, X) \qquad (4.26)$$

where $X$ is the transformed fraction, $t$ and $T$ are respectively time and temperature of the reaction.

Afterwards, Christian modified the criterion and proved that additivity principle holds if the transformation rate can be expressed as following:

$$\frac{dX}{dt} = \frac{G(T)}{H(X)} \qquad (4.27)$$

where $G(T)$ and $H(X)$ depend exclusively on temperature and transformed fraction respectively. An additive reaction requires that the reaction rate depends exclusively on the final state and not on the path followed in order to achieve that state.

### 4.1.9 Further ways to model microstructure evolution

Even if the theory described up to now still remains the theoretical basin for microstructure's evolution which happens during cooling phase and it will be adopted in present work, in order to have a full overview of the state of the art it is necessary to mention even further theory which have been developed. Orend et al. proposed a full overview of major approaches for modeling recrystallization and described their feasibility for process control application.

#### 4.1.9.1 Constitutive models

Constitutive models provide a simple way of describing the microstructure evolution mostly by closed form equations, which make it possible to use them even in simple spread sheet applications. Sellars and Whiteman proposed such a model designed for the application of the simulation of the microstructure evolution during hot rolling. These models use the temperature $T$, the strain $s$ and the strain rate $\dot{s}$ of each deformation step, the initial average grain size $d_0$ and the time $t$ after the prior deformation as input parameters. The output parameters are the recrystallized volume fraction $X$ and the average austenite grain size d after deformation. Constitutive microstructure evolution models distinguish between different recrystallization phenomena like dynamic,

metadynamic and static recrystallization (DRX, MDRX and SRX) and grain growth that are modeled separately by closed form formulations based on physical considerations. Chen et al. recently investigated in deeper detail the three mechanisms of recrystallization above mentioned on structure of 30Cr2Ni4MoV ultra-super-critical rotor steel during hot deformation. In order to perform a full characterization of material through the adoption of SRX, MDRX, and DRX crystallization uniaxial hot compression tests using a computer-controlled servo-hydraulic Gleeble thermo-mechanical simulator are required. The effects of thermomechanical parameters and deformation history on microstructural evolution and grain size were discussed by integrating the thermomechanical coupled finite element method. Furthermore, based on FE software DEFORM, a three-dimension thermomechanical analysis system for the closed-die hot forging was established.
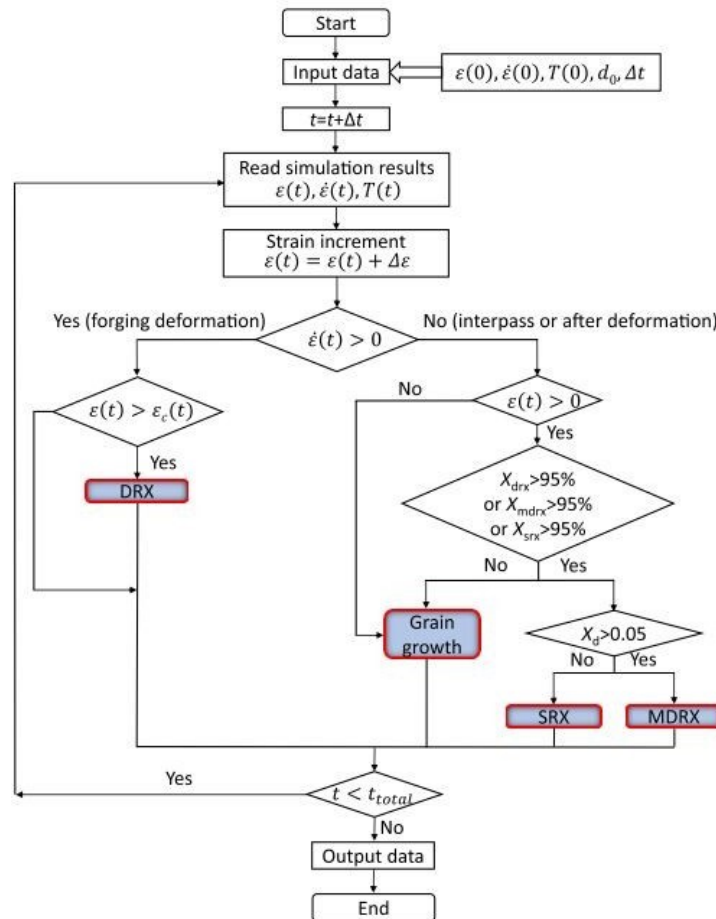


*Figure 4.9 Numerical analysis procedure to predict the microstructural evolution*

These models are very demanding in terms of equipment required and number of experiments which must be performed. However, they show good agreement with experimental results.

### 4.1.9.2    Mean field theory (MFT)

The mean field theory (MFT) is a general method for the approximation of many body problems, where one element interacts with every other element in a system. The main idea of the MFT is to transform the many body problem into a one body problem. This is done by the introduction of a representative element describing the average state of all individual elements. The interactions between each element are then simplified to the interactions of each element with the representative one. Montheillet et Al. used the MFT to model the evolution of a set of spherical grains during dynamic recrystallization. Each grain is described by a dislocation density $\rho_i$ and its diameter $D_i$. It is assumed that individual grains grow or shrink only due to their difference in dislocation density. Montheillet et al. show that this approach coupled with a suitable formulation of the evolution of the dislocation density and the nucleation of new grains is able to describe various phenomena of DRX.

### 4.1.9.3    Cellular Automata (CA)

A CA consists of a set of cells that are commonly ordered in a lattice. Each cell has a state described by a set of variables and is related to a defined set of cells that are called neighborhood. The transition of one state to another is defined by a set of rules that is applied at each evolution step. These rules can only rely on the state of one cell and its neighborhood at the previous evolution step. In particular Kugler and Turk use a 2-D CA with a rectangular grid for the simulation of multistage deformations. To describe a virtual microstructure the state of one cell consists of four variables including one variable for the dislocation density and the crystal orientation. A model of this kind can describe the transition from SRX to MDRX without introducing submodels or special case handling for each recrystallization process as it is necessary for the constitutive models described earlier.

### 4.1.9.4    Monte Carlo Potts method

Similar to CA models a lattice is used as representation of the microstructure. Each of the cells, called Monte Carlo Units (MCU), has a state $Q$ that indicates the misorientation and the affiliation of the cell to one specific grain. Neighboring cells with different values of $Q$ define a grain boundary. A basic algorithm for the simulation of grain growth has been described by Zollner and Streitenberger.

### 4.1.9.5    Vertex models

Vertex models also use a spatial description of the microstructure. In contrast to CA models, these ones do not use a lattice. Instead, the shape of

the grains is only described by a set of geometrical features like vertices which mark the grain boundary. This reduces the needed amount of memory and allows the simulation of larger grain ensembles compared to the CA method. The free energy of the model is then reduced by either optimizing the angles at the connection junctions or by using the variation principle.

### 4.1.9.6    Creusot-Loire system

Creusot and Loire systematically studied the impacts of chemical composition and austeniting conditions on the CCT of carbon steel and low alloy steel; by comparing workpieces' critical quenching speed and its limited cooling speed, and employing the interpolation method to determine the workpiece's structure, they got the limited cooling speed model represented in fig.4.10. The main limited cooling speed at 700 °C were:
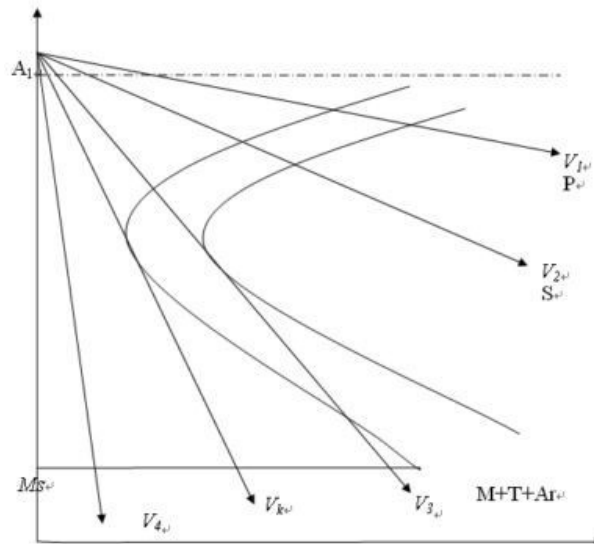


*Figure 4.10 Evaluation of critical cooling speed on IT diagram*

$$log(v_k) = 9.81 - (4.62C + 1.05Mn + 0.54Ni + 0.5Cr + 0.66Mn + 0.00183P_A)$$
$$(4.28)$$

$$log(v_3) = 10.17 - 3.83C + 1.07Mn + 0.7Ni + 0.57Cr + 1.58Mo + 0.0032P_A$$
$$(4.29)$$

$$log(v_1) = 6.36 - 0.43C + 0.49Mn + 0.78Ni + 0.27Cr + 0.38Mo + 2\sqrt{Mo} +$$
$$+ 0.0019P_A \quad (4.30)$$

Where

$$P_A = \left| \frac{1}{T_A} + \frac{nR}{\Delta H} \log(t) \right|$$

$$T_A = austeniting\ temperature\ [K]$$
$$n = \log(10) = 2.3026$$
$$R = 8.31 \frac{J}{K \cdot mol}$$
$$t = time(h)$$

The approach is acceptable if the material of interest satisfy following requirements:

- carbon content: $0.2\% \leq C \leq 0.5\%$

- silicon content: $Si \leq 1\%$

- manganese content: $Mn \leq 2\%$

- nickel content: $Ni \leq 4\%$

- chromium content: $Cr \leq 3\%$

- molybdenum content: $Mn \leq 1\%$

- vanadium content: $V \leq 0.2\%$

Depending on cooling speed governing the process, through proper interpolation it is possible to predict the phases formed during cooling simple knowing the chemical composition

## 4.2 Mechanical model

Once a metallurgical model able to predict the microstructure of the treated part will be developed, it will be necessary to provide a model able to convert the microstructural feature into mechanical properties. Because of this reason, the necessity to develop a mechanical model is usually straightforward in industrial application. In steels and cast irons, the microstructural constituents have the names ferrite, pearlite, bainite, martensite, cementite, and austenite. The microstructure plays the primary role in providing the properties desired for each application. One can see how material properties can be tailored by microstructural manipulation or alteration. Knowledge about microstructure is thus paramount in component design and alloy development. Each microstructural constituent will be described with particular reference to the properties that can be developed by appropriate manipulation of the microstructure through deformation (e.g., hot and cold rolling) and heat treatment.

### 4.2.1 Scientific approach

Researchers invested a lot of effort in order to correlate the microstructure with the mechanical properties achieved. The present section wants to provide some examples of the very detailed models which have been realized.

### 4.2.1.1 Ferrite

Ferrite is essentially a solid solution of iron containing carbon or one or more alloying elements such as silicon, chromium, manganese, and nickel. There are two types of solid solutions: interstitial and substitutional. In an interstitial solid solution, elements with small atomic diameter, for example, carbon and nitrogen, occupy specific interstitial sites in the body-centered cubic (bcc) iron crystalline lattice. These sites are essentially the open spaces between the larger iron atoms. In a substitutional solid solution, elements of similar atomic diameter replace or substitute for iron atoms. The two types of solid solutions impart different characteristics to ferrite. For example, interstitial elements like carbon and nitrogen can easily diffuse through the open bcc lattice, whereas substitutional elements like manganese and nickel diffuse with great difficulty. Therefore, an interstitial solid solution of iron and carbon responds quickly during heat treatment, whereas substitutional solid solutions behave sluggishly during heat treatment, such as in homogenization. Exploitation of solid-solution elements strongly affects the yield strength achieved.

In fig.4.11 it is possible to check the strongly effect obtained by increasing in carbon content. Nitrogen, also an interstitial element, has a similar effect. Phosphorus is also a ferrite strengthener. the substitutional solid solution elements of silicon, copper, manganese, molybdenum, nickel, aluminum, and chromium are shown to have far less effect as ferrite strengtheners than the interstitial elements. In fact, chromium, nickel, and aluminum in solid solution have very little influence on the strength of ferrite.
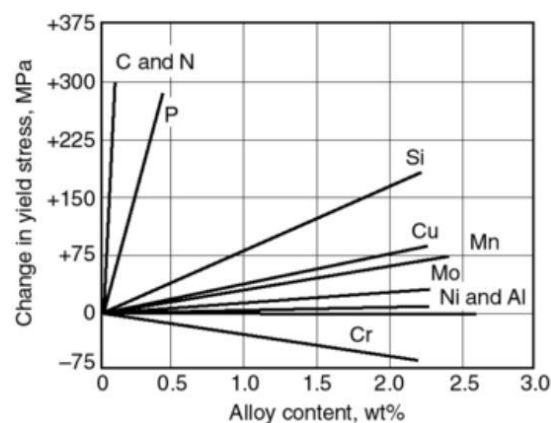


*Figure 4.11 Influence of solid-solution elements on the changes in yield stress of low-carbon ferritic steels*

In addition to carbon and other solid-solution elements, the strength of a

ferritic steel is also determined by its grain size according to the Hall-Petch relationship:

$$\sigma_y = \sigma_0 + k_y d^{-0.5} \tag{4.31}$$

where $\sigma_y$ is the yield strength in MPa, $\sigma_0$ and $k_y$ are constants and $d$ is the grain diameter (in mm). An example is graphically reported in fig.4.12.
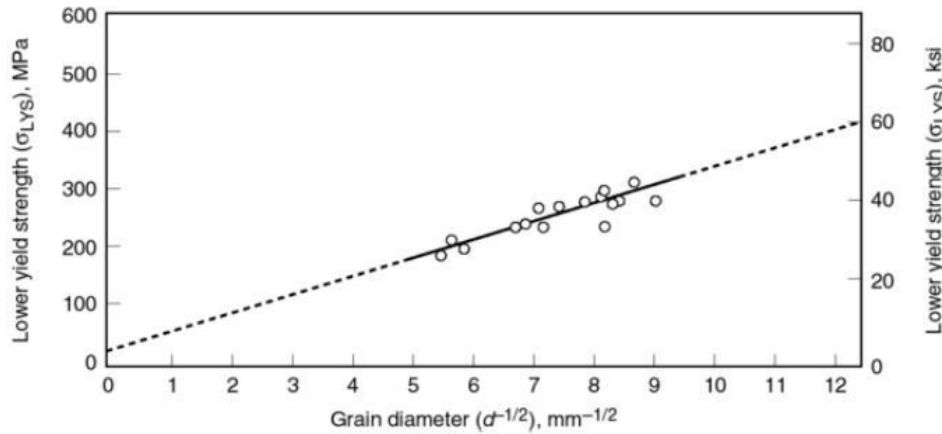


*Figure 4.12 Hall-Petch relationship in low-carbon ferritic steels*

### 4.2.1.2 Pearlite

As the carbon content of steel is increased beyond the solubility limit (0.02% C) on the iron-carbon binary phase diagram, a constituent called pearlite forms. Pearlite is formed by cooling the steel through the eutectoid temperature (727 ∘C) by the following reaction:

$$austenite \leftrightarrow cementite + ferrite$$

The cementite and ferrite form as parallel plates called lamellae. The properties of fully pearlitic steels are determined by the spacing between the ferrite-cementite lamellae, a dimension called the interlamellar spacing, $\lambda$, and the colony size. A simple relationship for yield strength has been developed by Heller as follows:

$$\sigma_y = -85.9 + 8.3(\lambda)^{-0.5} \tag{4.32}$$

where $\sigma_y$ is the 0.2% offset yield strength (in MPa) and the $\lambda$ is the interlamellar spacing (in mm). It has also been shown by Hyzak and Bernstein that strength is related to interlamellar spacing, pearlite colony size, and prior-austenite grain size, according to the following relationship:

$$YS = 52.3 + 2.18(\lambda)^{-0.5} - 0.4(d_c)^{-0.5} - 2.88d^{-}0.5 \tag{4.33}$$

where $YS$ is the yield strength (in MPa), $d_c$ is the pearlite colony size (in mm), and $d$ is the prior-austenite grain size (in mm). The thickness of the cementite lamellae can also influence the properties of pearlite. Fine cementite lamellae can be deformed, compared with coarse lamellae, which tend to crack during deformation. Although fully pearlitic steels have high strength, high hardness, and good wear resistance, they also have poor ductility and toughness for pearlite, strength is controlled by interlamellar spacing, colony size, and prior-austenite grain size, and toughness is controlled by colony size and prior-austenite grain size. To determine interlamellar spacing, a scanning electron microscope (SEM), or a transmission electron microscope (TEM) is needed in order to resolve the spacing.

### 4.2.1.3 Ferrite-pearlite

The most common structural steels produced have a mixed ferrite-pearlite microstructure. Their applications include beams for bridges and high-rise buildings, plates for ships, and reinforcing bars for roadways. These steels are relatively inexpensive and are produced in large tonnages. They also have the advantage of being able to be produced with a wide range of properties. In most ferrite-pearlite steels, the carbon content and the grain size determine the microstructure and resulting properties. For example, fig.4.13 shows the effect of carbon on tensile and impact properties. The ultimate tensile strength steadily increases with increasing carbon content. This is caused by the increase in the volume fraction of pearlite in the microstructure, which has a strength much higher than that of ferrite.
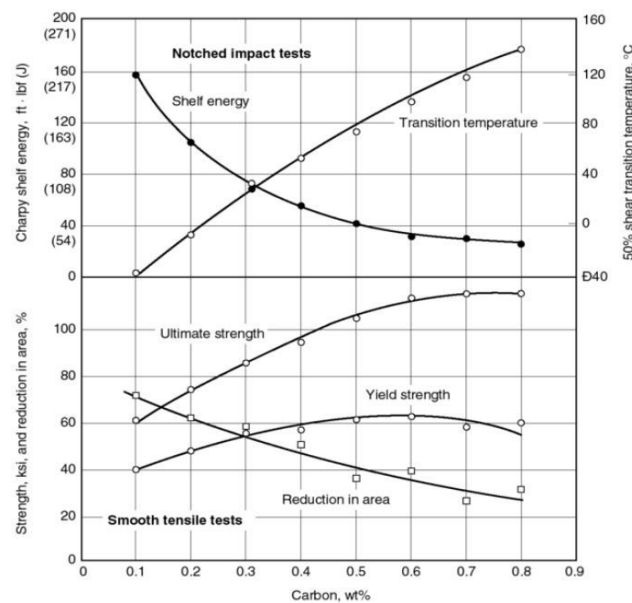


*Figure 4.13 Mechanical properties of ferrite-pearlite steels as a function of carbon content*

Thus, increasing the volume fraction of pearlite has a profound effect on increasing tensile strength. However the yield strength is relatively un-affected by carbon content, rising from about 275 MPa (40 ksi) to about 415 MPa (60 ksi) over the range of carbon content shown. This is because yielding in a ferrite-pearlite steel is controlled by the ferrite matrix, which is generally considered to be the continuous phase (matrix) in the microstructure. Therefore, pearlite plays only a minor role in yielding behavior. Even in case of ferrite-pearlite steel, much work has been done to develop empirical equations that relate mechanical properties and microstructure. One such equation for ferrite-pearlite steels with 0.25% C was provided by Pickering:

$$YS = 53.9 + 32.34Mn + 83.2Si + 354.2N_f + 17.7d^{-0.5} \qquad (4.34)$$

where $Mn$ is the manganese content (%wt), $Si$ is the silicon content (%wt), $N_f$ is the free nitrogen content (%wt) and $d$ is the ferrite grain size (in mm).

### 4.2.1.4 Bainite

Like pearlite, bainite is a composite of ferrite and cementite. Unlike pearlite, the ferrite has an acicular morphology and the carbides are discrete particles. Because of these morphological differences, bainite has much different property characteristics than pearlite. In general, bainitic steels have high strength coupled with good toughness, whereas pearlitic steels have high strength with poor toughness. It is common to find out the division among upper and lower bainite. Upper bainite formed isothermally in the temperature range of 400 to 550°C, while lower bainite formed isothermally in the temperature range of 250 to 400°C. In order to quantify bainite mechanical properties, attempts have been made to quantitatively relate the microstructural features of bainite to mechanical properties. Honeycombey proposed the relationship:

$$YS = -194 + 17.4d^{-0.50} + 15n^{0.25} \qquad (4.35)$$

where YS is the 0.2% offset yield strength (in MPa), d is the bainite lath size (mean linear intercept in mm) and $n$ is the number of carbides per $mm^2$ in the plane section.
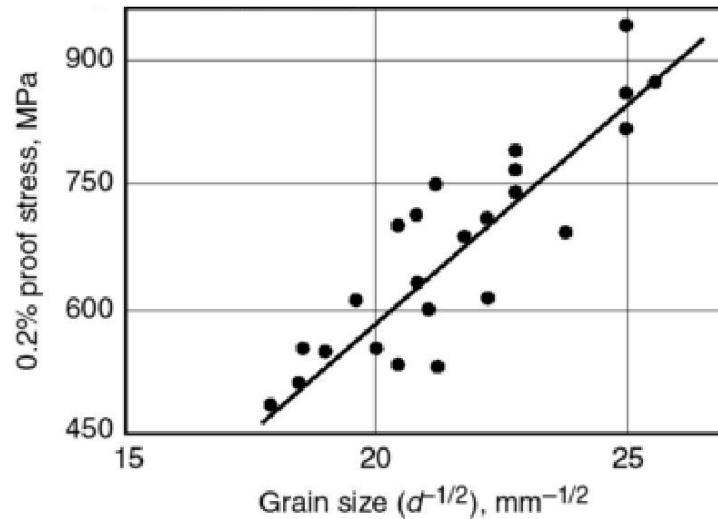
*Figure 4.14 Relationship between bainite lath width (grain size) and yield strength*

### 4.2.1.5  Martensite

Martensite is essentially a supersaturated solid solution of carbon in iron. The amount of carbon in martensite far exceeds that found in solid solution in ferrite. Because of this, the normal body-centered cubic (bcc) lattice is distorted in order to accommodate the carbon atoms. The distorted lattice becomes body-centered tetragonal (bct). In plain-carbon and low-alloy steels, this supersaturation is generally produced through very rapid cooling from the austenite phase region (quenching in water, iced-water, brine, iced-brine, oil or aqueous polymer solutions) to avoid forming ferrite, pearlite, and bainite. Some highly alloyed steels can form martensite upon air cooling. Depending on carbon content, martensite in its quenched state can be very hard and brittle, and, because of this brittleness, martensitic steels are usually tempered to restore some ductility and increase toughness. Plain- carbon and low-alloy martensitic steels are rarely used in the as-quenched state because of poor ductility. To increase ductility, these martensitic steels are tempered (reheated) to a temperature below 650∘C. During tempering, the carbon that is in supersaturated solid solution precipitates on preferred crystallographic planes of the martensitic lattice.
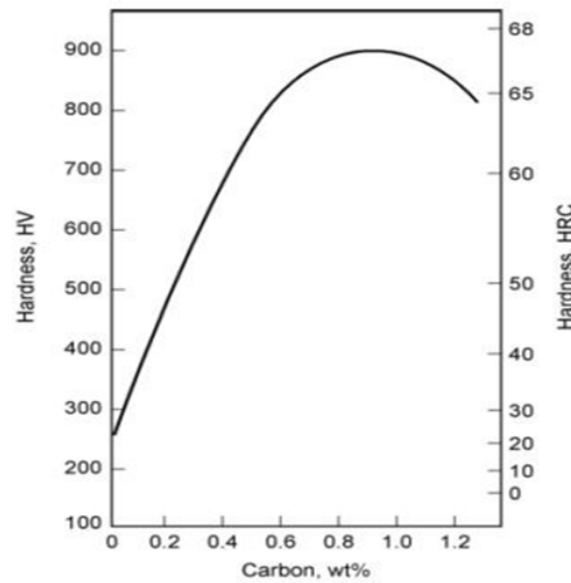
*Figure 4.15 Effect of carbon content on the hardness of martensite*

The hardness of martensite is determined by its carbon content, as shown fig. 4.15. The reason that the hardness does not monotonically increase with carbon is that retained austenite is found when the carbon content is above about 0.4% (austenite is much softer than martensite). Effort to predict the yield strength has been carried out. For untempered low-carbon martensite:

$$YS(MPa) = 413 + 17.2 \cdot 10^5 \cdot (C)^{0.5} \qquad (4.36)$$

However, in order to recover at least a small percentage of ductility, martensitic steel are never used in as quenched state, but instead after tempering process. Hardnesses of quenched-and-tempered (Q&T) steels can be estimated by a method established by Grange et al. The general equation for hardness is:

$$HV = HV_C + \Delta HV_{Mn} + \Delta HV_P + \Delta HV_{Si} + \Delta HV_{Ni} + \Delta HV_{Cr} + \Delta HV_{Mo} + \Delta HV_V \qquad (4.37)$$

In order to exploit eq.2.37, some graphs are provided. For example, in fig.4.16 is reported the graphs which must be exploited in order to determine the first term $\Delta HV_C$ in eq.2.37.
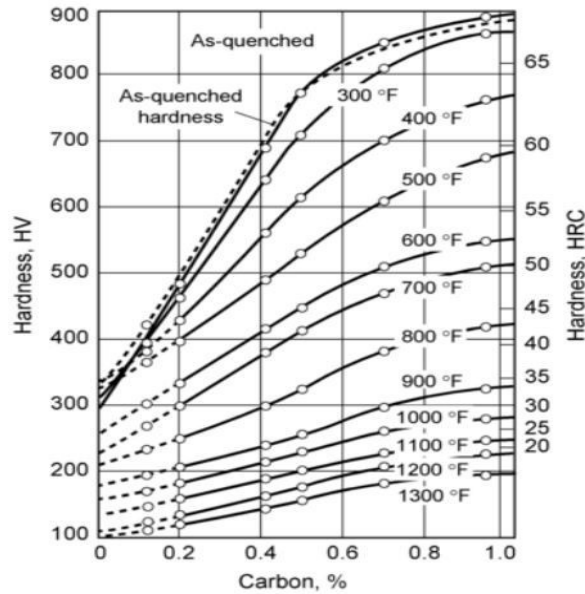
*Figure 4.16 Relationship between hardness of tempered martensite with carbon content at various tempering temperatures*

Then the effect of each alloying element must be taken into account exploiting diagrams as the one reported in fig.4.17:
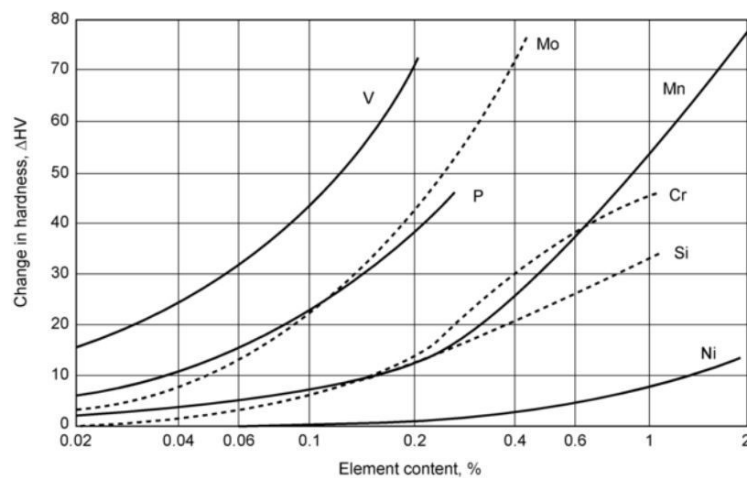


*Figure 4.17 Effect of alloying elements on the retardation or softening during tempering at 540°C relative to iron-carbon alloys*

With graphs like the one reported in fig.4.17, all the remaining terms in eq.2.37 are predicted. Thus, this method can be used to estimate a specific hardness value after a quenching and tempering heat treatment for a low-alloy steel. Also an approximation for the tensile stress has been proposed according to:

$$TS\,(MPa) = -42.3 + 3.6HB \qquad (4.38)$$

#### 4.2.1.6   Conclusions about scientific approach

From these last paragraphs, it is quite clear that microstructure achieved strongly affects the mechanical properties of the steel. A big effort has been provided in literature in order to correlate the microstructure with the yield strength or with the hardness, being these two mechanical properties strongly correlated among them. However, even if from a scientific point of view very good results have been obtained considering the model which have been reported up to now, in industrial application they found out just a very small exploitation resulting unemployable and requiring a lot of measurements especially with scanning electron microscope (SEM) and requiring some measurements on-situ which difficulty could be promptly provided. Because of this reason, industrial world necessary had the necessity to switch towards further approaches. Often, these ones result less academic and even less detailed from a scientific point of view. However, the compromise has been a requirement. In further sections, I will provide some examples about the most spread applications.

### 4.2.2   Industrial Approach

Steels whose data are not available in literature are not rare events in industrial application. Also the project work developed in this thesis will have to front with material quite unknown in literature collection. Because of this reason, two different approaches could be exploited: on one hand a full characterization of the subject material should be performed in laboratory, while, on the other hand, the possibility to trust in statistical analysis and develop new numerical approach is the most spread and even economic approach. Clearly, the results will be approximated and uncertainties depend on the ability of the engineer to select a proper amount of data and to provide a correct interpolation of data available. The possibility to base on model which could extended to new materials just relying on chemical composition and on the parameters governing the heat treatment which the material will have to support is a very useful tool to be employed even in case of depth economic ambiguities. In particular, exploiting the tools developed in this way, it could be possible to predict which would be the results achieved employing new materials combined with the technology already available and evaluate the choice first of all in terms of mechanical results which could be achieved and secondary, but surely not less important, from an economical point of view. In this context, regression analysis on data recollected in literature becomes the primary statistical tool which must be exploited in terms of statistical analysis. Adopting this kind of approach, the unique requirements necessary for a precise design will be a correct numerical and statistical analysis supported by sufficient computational power. Even if at the beginning the results could be not satisfying at all, and model will have to

be fine-tuned, once this kind of tool will be optimized it will offer an enormous saving in terms of time and money.

### 4.2.2.1 Hardness prediction during cooling phase

Creusot-Loire exploiting non-linear statistical analysis developed some formulas in order to predict hardness depending on material and thermal cycle which the part must front. The approach is acceptable if the material of interest satisfy following requirements:

- carbon content: $0.2\% \leq C \leq 0.5\%$

- silicon content: $Si \leq 1\%$

- manganese content: $Mn \leq 2\%$

- nickel content: $Ni \leq 4\%$

- chromium content: $Cr \leq 3\%$

- molybdenum content: $Mn \leq 1\%$

- vanadium content: $V \leq 0.2\%$

In order to take into account the material, all the formulas developed present dependence on chemical composition, while in order to consider also the thermal cycle, the term $dT/dt$ representing the mean cooling rate is inserted. The empirical regression formulas for Vickers hardness (HV) versus composition and cooling rate developed by Creusot-Loire for martensite (M), bainite (B), and ferrite-pearlite (FP) are:

$$HV_M = 127 + 949C + 27Si + 11Mn + 8Ni + 16Cr + 21\log_{10}\frac{dT}{dt} \qquad (4.39)$$

$$HV_B = -323 + 185C + 330Si + 153Mn + 65Ni + 144Cr + 191Mo$$
$$+(89 + 53C - 55Si - 22Mn - 10Ni\,20Cr - 33Mo)\log_{10}\frac{dT}{dt} \quad (4.40)$$

$$HV_{FP} = 42 + 223C + 53Si + 30Mn + 13Ni + 7Cr + 19Mo + (10 - 19Si +$$
$$4Ni + 8Cr + 130V)\log_{10}\frac{dT}{dt} \quad (4.41)$$

Clearly, the approach could be applied in case of continuous cooling transformation, it means in case of constant cooling rate. When the cooling rate is not constant, instead, a proper numerical adaptation will be required. Clearly, this procedure rest on the possibility to have sufficient hardware capability in order to front the higher expense in terms of computational requirements.

Once the hardness of each phase is computed, the necessity of a weighted averaging taking into account the fraction of each phased formed during cooling process is necessary. To satisfy this requirement, "Rule of mixtures" grew up and so, considering even the percentage of phase formed it is

possible to write down:

$$HV_{mix} = \sum_{1}^{i} HV_i \cdot X_i \qquad (4.42)$$

where $HV_i$ represents the Vickers hardness of each individual constituent while $X_i$ the fraction formed of each one. The relation it is written referring to Vickers hardness in order to be coherent with the approach described by Creusot-Loire but it could be simply extended to each other mechanical property.

### 4.2.2.2 Further approaches

One of the most important factors for efficient simulation of hardening is the good selection of representative of the cooling phenomena that is relevant for phase transformation. It implies that sometimes, even if we are not able to monitor closely a precise quantity we can trust in monitoring another one and then reconstruct the quantity of our direct interest. Characteristic cooling time, relevant for phase transformation in most structural steels is the time of cooling from 800 to 500°C: time $t_{8/5}$. The above mentioned quantity must be considered during a Jominy test. Each location of distance from the quenched end of Jomini-specimen(=Jomini distance) must be compared with the cooling time $t_{8/5}$. An example is reported in fig.4.18.
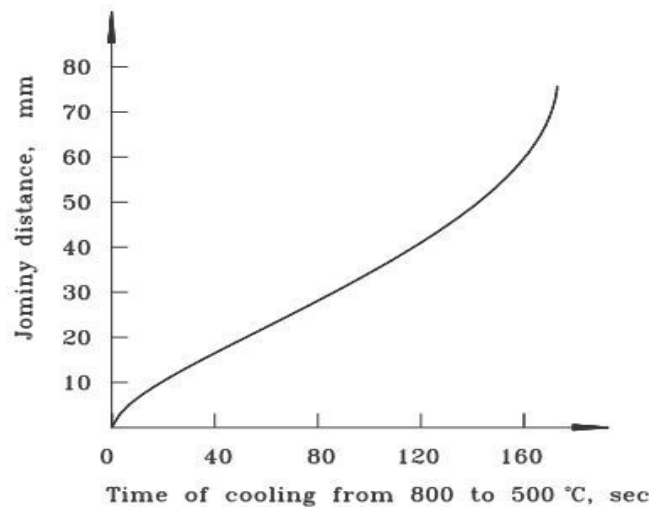


*Figure 4.18 Distance from the quenched end of Jominy-specimen vs. cooling time from 800 to 500 °C*

The hardness at grid-points can be estimated by the conversion of cooling time $t_{8/5}$ results to hardness by using both, the relation between cooling time and distance from the quenched end of Jominy specimen and the Jominy hardenability curve. According to Smoljan, if other heat treatment parameters are constant, the austenite decomposition results in some

location of a cooled specimen will depend only on the time $t_{8/5}$. It could be written for Jominy test that phase hardness depends of chemical composition ($CC$) and cooling rate parameter ($CRP$) that corresponds to actual distance ($d$) of Jominy specimen quenched end. It was adopted that $CRP = log(t_{8/5})^d$.

It could be written:

$$HV_d^M = f_M(CC, CRP) = HV_{max}^M - K_M log \frac{t_{8/5_d}^M}{t_{8/5_{max}}^M} \qquad (4.43)$$

$$HV_d^B = f_B(CC, CRP) = HV_{max}^B - K_B log \frac{t_{8/5_d}^B}{t_{8/5_{max}}^B} \qquad (4.44)$$

$$HV_d^{P+F} = f_{P+F}(CC, CRP) = HV_{max}^{P+F} - K_{P+F} log \frac{t_{8/5_d}^{P+F}}{t_{8/5_{max}}^{P+F}} \qquad (4.45)$$

where $N$ is normalizing, $B_{max}$ is lower bainite. Characteristic value of $HV$, $K$, and $t_{8/5}$ has to be evaluated on chemical composition for investigated steel combined by Jominy test results. Once the estimation of hardness is available for each component, once again "Rule of mixtures described" in previous paragraphs can be applied concluding:

$$HV_{mix} = \sum_1^i HV_i \cdot X_i \qquad (4.46)$$

### 4.2.2.3  Hardness prediction during tempering

Components usually have a ferrite–pearlite microstructure at the core and a tempered martensitic rim. A property prediction model is deemed necessary to maintain consistent mechanical properties. The strength depends on the thickness of the rim as well as on the distribution of various phases inside the part treated. Prediction of the strength or hardness of the tempered martensitic rim is not very simple, primarily because it undergoes non-isothermal tempering. Mukerjee presented a critical overview of which are the most diffused way in order to take into account the tempering process and its effect on tempered martensite. It has been proved that traditional isothermal kinetic functions can be generalized to obtain generalized kinetic functions, which can be used for the phenomenological description of non-isothermal process. It is clear that prediction of hardness of tempered martensite requires a generalized kinetic function. In order to do it, two different approaches could be exploited. In particular, up to now, the most diffused approach is purely experimental: samples must be quenched after austenitization and then subjected to isothermal tempering experiments under various combinations of temperature and time. The hardness vs time data generated at different temperatures are used to obtain the isothermal kinetic function. It has been proved that the decrease of hardness due to

tempering treatment can be described by the following isothermal kinetic function:

$$H_v = H_{v_0} - B\left[exp\left(-\frac{Q}{RT}\right)t\right]^n \qquad (4.47)$$

B,Q,n are evaluated using best fit values exploiting the hardness measurements performed. The generalized kinetic equation is given by:

$$H_v = H_{v_0} - B\int_0^t exp\left(-\frac{Q}{RT}\right)dt \qquad (4.48)$$

This last equation described the kinetic of the non-isothermal tempering process quite well, its use is restricted by the empirical constants of the equation which are composition dependent. This implies that, for any change of chemistry can no longer be used unless suitable experiments are carried out to determine the empirical constants. Conducting isothermal tempering experiments for every change in chemical composition is not practically feasible. Therefore, in order to generate an isothermal kinetic function which includes the effect of chemical composition, a multivariable regression analysis has been carried out using isothermal tempering data collected from literature. Exploiting all the data based on different kind of alloys recollected in literature, the following model has been developed:

$$ln(H_v) = A_0 + \sum_{i=1}^n A_i\, ln(C_i) + A_t \ln(t) + A_T T \qquad (4.49)$$

Values for the constants are available for each element introduced in chemical composition. It is quite evident that this model takes into account both the chemistry and even the time-temperature parameters involved in the tempering process.

| C2 | | |
|---|---|---|
| Input variable | Regression coefficient | |
| Intercept | $A_0$ | 8.4592 |
| ln(C, wt%) | $A_1$ | 0.2417 |
| ln(Si, wt%) | $A_2$ | 0.0092 |
| ln(Mn, wt%) | $A_3$ | −0.0094 |
| ln(Cr, wt%) | $A_4$ | 0.0063 |
| ln(Mo, wt%) | $A_5$ | 0.0113 |
| ln(V, wt%) | $A_6$ | −0.0049 |
| ln(W, wt%) | $A_7$ | 0.0184 |
| ln(N, wt%) | $A_8$ | −0.0076 |
| ln(Ni, wt%) | $A_9$ | 0.0006 |
| ln(P, wt%) | $A_{10}$ | −0.0027 |
| ln(S, wt%) | $A_{11}$ | −0.0020 |
| ln(Ti, wt%) | $A_{12}$ | −0.0350 |
| ln(Cu, wt%) | $A_{13}$ | 0.0087 |
| ln(Nb, wt%) | $A_{14}$ | 0.0666 |
| ln(t, s) | $A_t$ | −0.0438 |
| Temperature, K | $A_T$ | −0.0018 |

*Figure 4.19 Coefficients exploited in the model*

It is a well-known fact that the same material property (here hardness) may be attained by heat treatments with different time–temperature combinations. Therefore, using the generalized kinetic functions, it should be possible to derive equivalent isothermal tempering parameters which will produce the same hardness as the non-isothermal processes. These equivalent isothermal tempering parameters will not only enable comparison of different non-isothermal processes using numerical criteria, but also make a concise characterization of the processes at changing temperature, possible. The equivalent isothermal tempering time ($t_e$) corresponding to an isothermal tempering temperature equal to the maximum temperature that the specimen attains during non-isothermal tempering ($T_{max}$), is calculated. Also, the equivalent temperature ($T_e$) corresponding to the total duration of the non-isothermal tempering cycle ($t_{tot}$) is calculated. The equivalent time can be obtained as:

$$t_e = exp\left(-\frac{A_T T_{max}}{A_t}\right)\left[\int_0^t exp\left(\frac{A_T T}{A_t}\right)\right] \qquad (4.50)$$

For the equivalent temperature instead:

$$T_e = \frac{A_t}{A_T} ln\left(\frac{t_e}{t_{tot}}\right) + T_{max} \qquad (4.51)$$

## 4.3  Combining metallurgical-mechanical thermal model

This concluding section of literature's review wants to provide some examples about the way in which the models described up to now must be combined (or at least coupled) in order to simulate industrial heat treatments and offer a tool in order to foresee the results obtained varying the parameters of the process considered. With this final section, the present state of the art regarding the trial to model thermal process coupling thermal-metallurgical-mechanical models is described.

Yang et al. simulated heating, holding and cooling stages in rail-head's quenching process through FEM software ANSYS. The time-varying temperature fields at heating, holding stages and the structure after water-cooled were obtained and the numerical simulation method to predict the quenching results was provided. Adopting Creusot-Loire approach previously described, the impact of temperature fields on phases formed has been evaluated. Comparing results with the critical cooling speed evaluated on TTT curves, the fraction of each fase developed during the process has been evaluated.
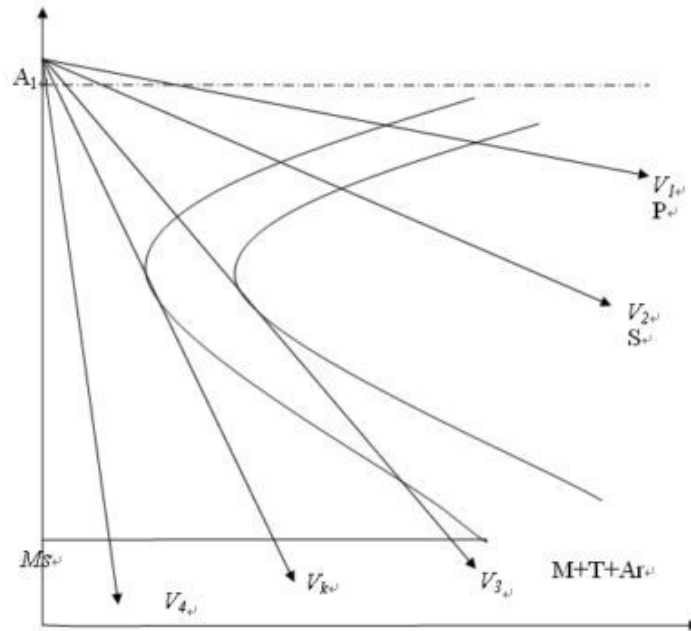
*Figure 4.20 Evaluation of critical cooling speed on TTT diagram*

Gongfa et al. simulated the evolution of temperature field in the cooling process of heavy rail. Then, the phase changing temperature of steel U71Mn was got based on CCT curves.
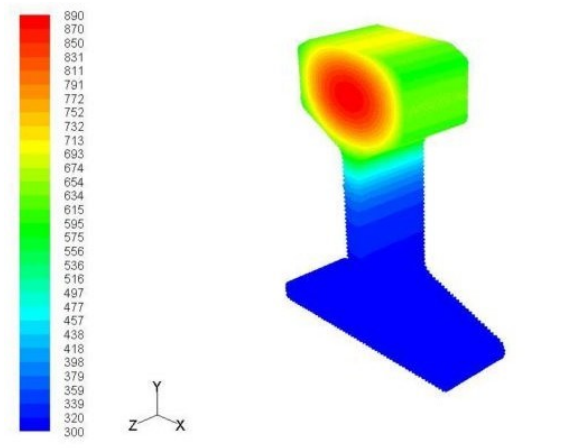


*Figure 4.21 Temperature figure for heavy rail on air-cooled at t=50s*

Using the Fluent software built the model of heavy rail in air-cooled quenching process, to simulate the inner and external flow field of air-jet, obtained the rule of flow field of external of air-jet, and then through setting the surface heat transfer coefficient of air-cooled, obtained the temperature

field distribution of heavy rail in air-cooled quenching of 50s. Finally, according to Creusot-Loire method previously described , to gather statistics of the cooling rate of key nodes in hardened layer, the cooling curves were fitted with MATLAB software, and then the cooling rate at 700°C was obtained by derivation and compared with critical speed of the quenching structure, then forecasted the final quenching structure. The whole simulation results were accurate. Through this method it is possible to study the dimension of parameters about air-jet and predict the quenching structure, which it was Cetinel et al., through the use a finite element method, solved the heat transfer equations and computed the amount of phases after transformation. A Fortran 77 computer program has been developed for the study. A quenching simulation has been made utilizing the finite element method for different quenching duration; the changes in the internal structures and self-tempering temperatures have been determined for each node. The numerical results obtained via the finite element method have been compared with the experimental results. It has been seen that the agreement is reasonably good. In the finite element method, heat transfer equations, which have been added to equations determining the transition from isothermal time temperature transformation (TTT) to continuous cooling transformation (CCT), have been solved by a Fortran 77 program. With this program the temperature, internal structure, and time have been determined for each node.

Regarding the metallurgical model adopted instead, using the additivity rule, the amount of the phases transformed during the continuous cooling can be determined from TTT curves. For this purpose, the cooling curve  is converted to a step curve consisting of many isothermal steps. The partial amounts of the volume transformed at these isothermal steps gives the total amount of phases that occur in steel because of continuous cooling as depicted in fig.4.22.

Comparing simulated and experimental results:

- Internal structures obtained by the simulations of quenching, cooling in air and holding in cooling bed match the experimental results well.
- The volume percentages of phases and self-tempering temperatures obtained from the experimental study fall into a narrow band due to small changes in the initial parameters. The numerical simulation fall within this bands. This shows that the volume fraction of phases and the values of self-tempering temperatures which have been determined by the finite element method for different quenching duration and bar diameters, are within acceptable tolerance.

### 4.3.1 **Thermomechanical process**

Thermo-mechanical treatments have the purpose of conferring metals at the end of a deformation cycle that begins with high temperatures,

particular grain and precipitate morphologies aimed at increasing the mechanical and chemical properties of the finished product.

Since the 1950s, ferritic grain refinement in structural steels has been the goal of the technology of thermo-mechanical processes. The use of controlled rolling and accelerated cooling has refined the rolled microstructures to a smaller size than those obtainable by standardization. In micro-alloy steels, the magnitude of the ferritic grain is about 5 μm in comparison to the 15 μm of low-rolled C-steels without control of process conditions. Controlled rolling has played an important role in the development of HSLA steels. In the 1960s, the development of controlled rolling mills was supported by the research carried out at Sheffield, which in the 1970s was accompanied by industrial development based on research carried out at steel mills in Japan.

Controlled rolling is a technique that allows to produce resistant and tough steels by refining ferritic grains. In the process, the recrystallization that takes place during the hot rolling is guided by both process variables: temperature T and deformation velocity, as well as alloy elements such as Nb, Ti, V. These elements despite their very low content order of 0.02-0.04% by weight) during controlled cooling between the pastes of the finisher precipitate as very fine Nb (CN), TiC and VN which block the mobility of both the edges of the grain, preventing the recrystallization and of the dislocations within the grains and thus increasing the steel resistance increase the non-recrystallization range by shifting the T to higher values. The thermo-mechanical process is therefore a technique designed to provide steel by controlling the hot deformation process, used to obtain finished products, the higher mechanical properties that conventional rolling is obtained by additional thermal treatments. Controlled rolling, controlled cooling and direct hardening make the thermo-mechanical process.

Figure 4.22 shows the evolution of grains during a controlled rolling process.
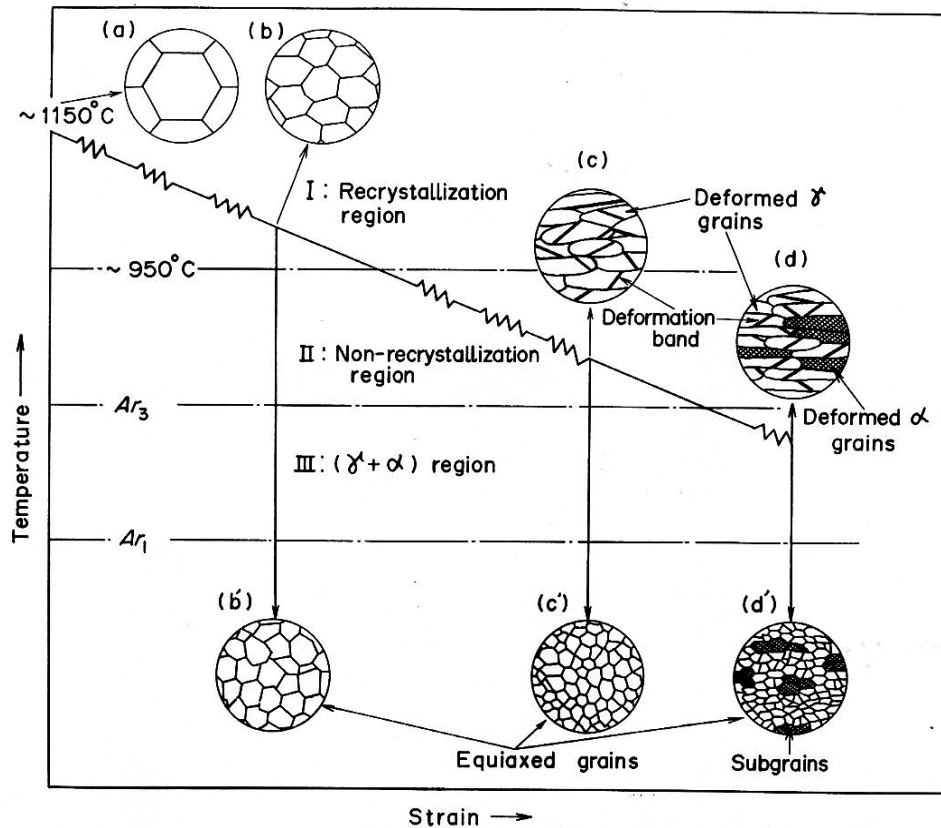
*Figure 4.22 Scheme of controlled rolling seen through the microstructures obtained at different temperature and deformation ranges. (a) recrystallization of coarse grains of austenite; (b) recrystallized austenite, the smaller grains than the previous ones are due to the lower deformation temperature. Below are the ferrite structures obtained by cooling; (c) deformation in the non-recrystallization region: pancakes offer numerous nucleation centers for α grains which are very small and equilibrated; (d) deformation in the region near the biphasic region: there are some coarse grains α, which remain cooled, and elongated γ grains that will cool to a very fine α.*

## 4.3.2 Evolution of Thermomechanical process

Thermo-mechanical processes were introduced around the 1950s in the rolling of C-Mn steels used in marine constructions and the manufacture of welded pipes for gas transportation from Alaska. In the course of the war, many Liberty-class ships, built with welded plates, were concerned with the fragile fracture triggered around the welded hull joints. The study of the dramatic drawbacks revealed that tenacity is a property independent of ductility. Crochet tenacity became a requirement for steels used in marine constructions. In the same period, the 1950s, changes were made in the formulation and manufacture of steels at Mn-C by increasing the Mn/C ratio and deoxidizing with Al. The rolling took place according to the conventional scheme (Fig. 4.23 a): homogenization at 1250° C,

followed first by the blanking and then by the finishing which ended at 1000° C. Throughout the entire rolling cycle, the steel is recrystallized either during contact with the rollers or between the pastures in the reversible mill, ~ 10s. In the first case, the recrystallization is called "dynamic" (DRX), while the other is "static" (SRX). At the end of the process, the permanence of steel at high temperatures allows the austenitic recrystallized grains to widen. Under these conditions at Ar3 temperature, ferritic grains are rather coarse. To increase the shear strength and lower the fragile-duct transition, the rolling was subjected to the normalization treatment that refined ferritic grain.

Instead of following this route, some steel mills in Europe proceeded to refine ferritic grain by pushing the finisher to roll at low temperatures (Fig. 4.23 b). The finisher was interrupted about 1000° C when the rolled reached the thickness of 1.65 of the finished product and was resumed at 900° C to terminate at Ar3, i.e. at about 800° C, lower than that of the conventional finishing . At lower rolling temperatures than in the previous case, both dynamic and static recrystallization produce fairly austenitic grains but of different sizes, then at T ≤ Ar3 they are also transformed into α-ferrite grains also mixed in size.

The operating conditions used for low T in the case of Mn steel (Fig.4.23b) appear similar to those used for micro-alloyed steel with Nb (Fig. 4.23c) but the effect is different as their metallurgical bases are quite different. In fact, the steel finishing temperature at C-Mn, while being low (T <900° C), is included in the recrystallization interval; the steel then recrystallizes by affixing the grains γ. In micro-alloy steels with Nb during cooling, carbon bands, Nb (CN), at 950° C are formed, having average dimensions around 10 nm capable of blocking the movement of both dislocations within the grains, reinforcing steel, both of the grain boundaries, inhibiting recrystallization. Then at the end of the finishing while the C-Mn steels have recrystallized γ granules those at Nb show non-recrystallized elongated grains.

With the low-temperature controlled rolling process, the delicate fragile duct transition temperature is reduced by 10-15° C. In non-recrystallized austenite grains, elongated in the direction of rolling, deformation and gemstones are also formed. These bands within the grains and the grain boundaries represent a considerable surface on which ferritic grains are nucleated. The smaller the surface is the ferritic grains. Numerous non-metallic inclusions, predominantly of MnS, lie along the rolling direction causing a lowering of the toughness in the transverse direction. This tendency that is fatal, especially in the tubes, can be reduced by cross-rolling. The extension of rolling with the finisher within the region γ + α increases the ferritic grain refinement and the resistance

### 4.3.3 Controlled rolling advantages

The role of controlled rolling is to introduce a high density of nucleation sites for α grains within the matrix γ during transformation by controlling the hot deformation and hence to sharpen the steel structure after transformation. The α nucleation sites to be considered are: i) the austenitic grain boundaries, ii) the germinate interface formed during deformation, and iii) the deformation bands. The main factor to control the structure of γ during the rolling is the temperature.
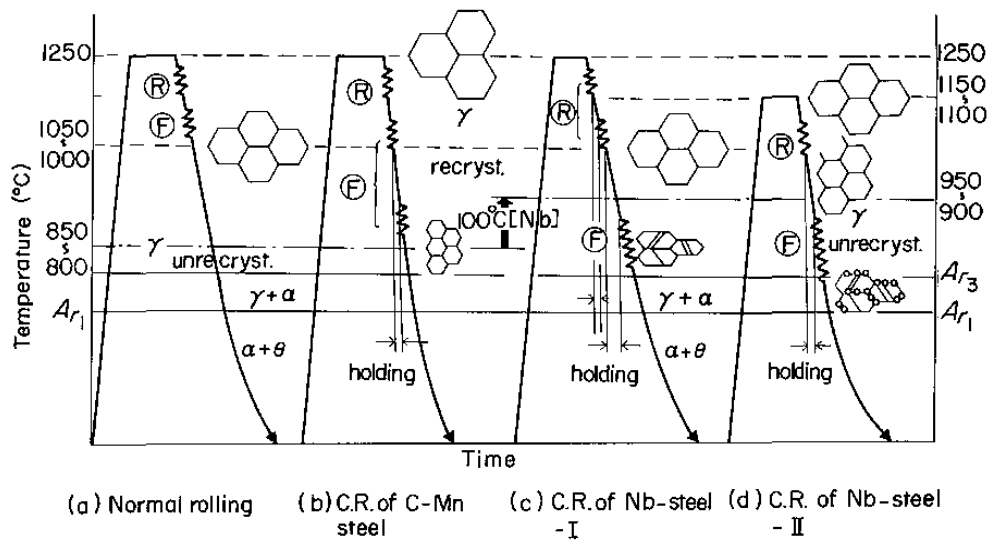


*Figure 4.23 Evolution of controlled rolling. R: Roughing mill; F: Finishing rolling.*

The conventional rolling (Fig. 4.23a), carried out without condition control, ends at 1050-900° C, according to the thickness of the plate. In the controlled rolling of Si-Mn steel, the recrystallized γ grains are refined in the final finals of the low T finisher: 950-800° C, where recrystallization can still take place. The refining of grains α is obtained in the transformation of fine grains γ (Fig. 4.23b). Further refinement of the transformed structure would still be possible by rolling within the non-recrystallization range, but proximity to Ar3 does not produce any significant effects. The presence of Nb, in solution and in NbCN precipitates, delays both static and dynamic reconditioning and thus extends the non-recrystallization T range of about 100 ° C (Fig. 4.23c). Non-recrystallization T is commonly called "pancake" as the grains, not recrystallizing, form an elongated structure microstructure (Fig. 4.22). The α-ferritic grain nucleation sites are therefore the boundaries of (i) the austenitic γ grains elongated during the reduction in the non-recrystallization range (Fig. 4.23), ii) the geminates iii) of the slides. The

"density" of these interfaces and their activity as nucleation sites of the phase α increase with rolling in the non-recrystallization range (Fig.4.23c and Fig.4.23d), in the latter one notices on the boundaries mentioned numerous nuclei of α grains.
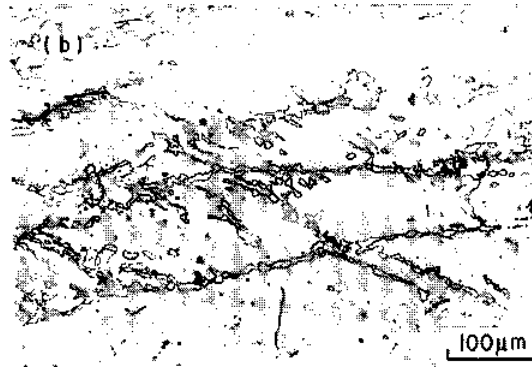


*Figure 4.24 Grain α formation on slides and on the edge of the grain stretched.*

Elongated, non-recrystallized elongated grains with no sliding or twisted bands produce uneven homogeneous grains. Preliminary refinement of high T-recrystallized γ for controlled rolling or increasing total reduction in the non-recrystallization area is necessary to obtain a fine and uniform texture that gives good tensile strength. An improvement in the ductility of the crown is obtained with the last passes of the grout between 1000-950 ° C. The finisher extension in α-γ range for steels with and without Nb increases resistance, delicate-duct transition temperature but lowers thickness-dependent properties such as Charpy's energy, especially in the transverse direction to the direction of rolling. The remarkable advantages obtained with controlled thermo-rolling are therefore the result of a synthesis between the composition of steels and the clever handling of process variables. However, it should be emphasized that: (i) the advantages described are rarely combined with the general increase in steel properties, plant productivity and costs; ii) process selection is often limited by the low flexibility of the plants; iii) transferability of the process from one plant to another is rarely possible for the diversity of control systems.

## 4.3.4 Hot plastic strains

When T elevates a metal, deforms it plastically, it slides due to increased density of displacements. Depending on the value of temperature and deformation velocity, the roughness is balanced by fading processes leading to annihilation and the organization of sublocal wall dislocations. In some metals, the screed completely balances the hardening, giving rise

to a steady state that can extend even for major deformations up to the fracture (Fig. 4.25).
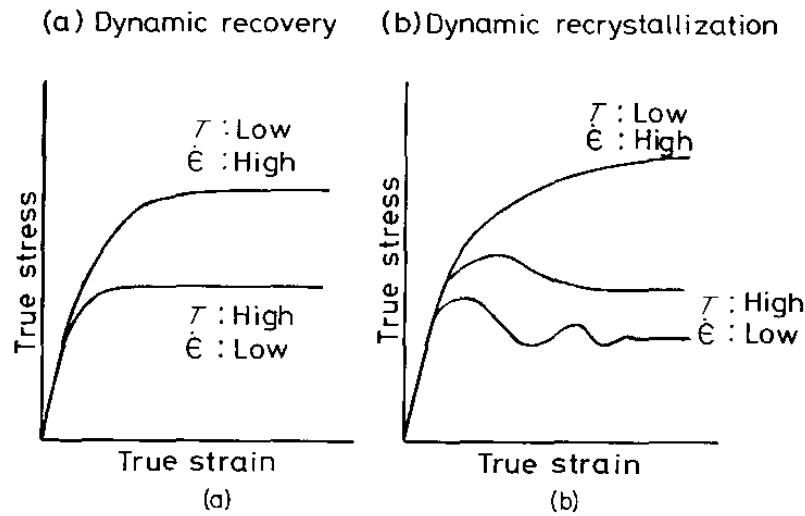


*Figure 4.25 Strain behavior in function on temperature and strain rate*

In others the detection is less rapid and under certain conditions of temperature and deformation leads to the formation of high density dislocation areas that form the nuclei of the recrystallized grains. The phenomena occurring in the short contact time of the metal with the rolling rollers are called "dynamic", they will then have dynamic detection (DRV) and dynamic recrystallization (DRX), Fig. 4.25b. If, on the other hand, phenomena take place in the past, they are called "static"; they will then have static (SRV) and static recrystallization (SRX). The same figure shows the deformation trends in different temperature, T, and deformation velocities. As the T increases, the stress decreases as it increases with the deformation velocity. The evolution of the grain structure during hot deformation is shown in Figure 4.26. An austenitic stainless steel was chosen to verify the austenite behavior at room temperature.
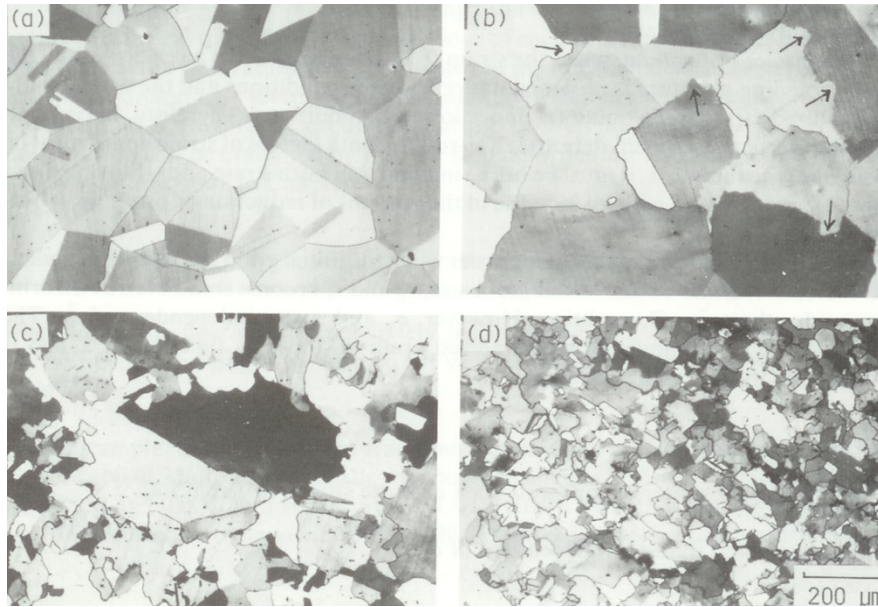
*Figure 4.26 Fe-32Ni-3C austenitic optical micrographs showing microstructure change with plastic strain at 1000° C, strain rate = 1.7x10-2s-1. a) as received: grains with linear boundaries and with gemstones inside b) ε = 0,08, before the peak of recrystallization, buzzing appear at the grain boundaries indicated by arrow; c) ε = 0,24 deformation just after the peak of recrystallization: small, recrystallized grains are noticed; d) ε = 0.40 steel is completed by recrystallization with an equilibrated grain structure (non-orientated).*

The deformation variables are correlated with each other in the following equation, known as Zener-Hollomon:

$$Z = \dot{\varepsilon}\, exp(Q/RT) \qquad\qquad (4.52)$$

where $\dot{\varepsilon}$ (s-1) is the deformation velocity, Q (joule per mole) the activation energy of the deformation process, which coincides with that of diffusion of Fe, R (joule per mole) is the universal constant of gas, and finally T (°K) the temperature of the deformation process.

The behavior of DRX or DRV depends on the SFE (stacking fault energy) of the various metals. In those high-value SFE, e.g. ferritic steels, aluminum (180 erg/cm2), during hot deformation, whatever the speed is, the DRV occurs, fig. (4.25a). The material during deformation hinges up to a maximum of the tension and results in a steady stress value that is the function of T and $\dot{\varepsilon}$. In low SFE metals, such as Cu (60 erg/cm2), austenite, the deformation curve has an upward and up to a maximum beyond which the metal softens by the effect of recrystallization, reaching a constant stress value which is a function of T and $\dot{\varepsilon}$, Fig. 4.25b) e Fig.4.27.
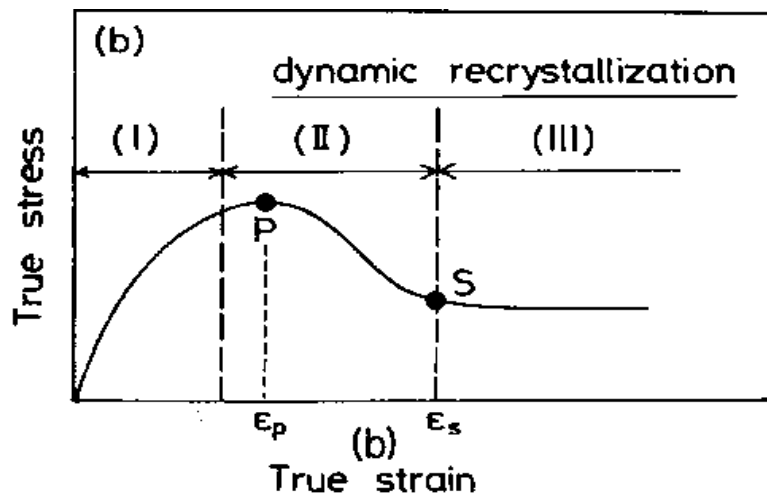
*Figure 4.27 Typical performance of a hot deformed metal that dynamically recrystallizes. The progressive increase of the dislocations (area of development), zone (I), leads to the beginning (~ 0.5-0.8 $\varepsilon p$) of dynamic recrystallization propagating (zone II) throughout the piece until completion; $\varepsilon s$, marks the beginning of stationary state (zone III).*

It is important to note that regeneration generally results in a decrease in the rate of reduction due to the reduction of the dislocation but does not alter the size and nature of the grain boundary. Over two types of recrystallization, the dynamic (which occurs during deformation) and the static (which occurs after deformation, e.g. in time between the passes) that are active during the hot deformation, also refers to "recrystallization metadynamic", MDRX, also known as post dynamic. It occurs when dynamically-generated nuclei fail to grow in the restricted time of dynamic recrystallization, they grow statically during time between the past. It is important to note that unlike SRX, MDRX does not require nucleation (which is a slow kinetic process); it essentially raises the nuclei produced by DRX, grain. During the hot deformation the stress reaches a maximum, decreases to $\varepsilon s$ and then stays constant (Fig. 4.27). The softening is due to dynamic recrystallization which is nucleated to a deformation of about 0.8 $\varepsilon P$ and propagates to the part of the rolling in contact with the rolling roll. Recrystallization cores, such as dislocated aggregates arranged in a "high angle boundary" and therefore moving, form within the unwracked areas and move in adjacent areas where the elastic tension is high, eliminating the displacements and then lowering the resistance.

In industrial practice rolling is performed for passing at different temperature and deformation rates. It is important to determine the effect of time between the passes on recrystallization, carbonitride precipitation, and the interaction between the two processes because the final microstructure and, consequently, the mechanical properties of the rolled

depend on it. Recrystallization and precipitation have quite different kinetics. Indeed, the start time of the recrystallization decreases almost linearly with the increase in T, while that of carbonitrile precipitation (case of Nb steels) has a minimum (10s) of about 930 ° C. This means that at high temperatures recrystallization is much faster than precipitation. The temperature and time intervals between the rolling passes vary according to the type of rolling mill and the product. Three types of systems are presented below, which change the conditions of rolling speeds and the times between passes.

1.  Reversible mill for thick flat products: $\dot\varepsilon$ varies from 1 to 30 s-1, time between the past: 8 to 10 s. The deformation velocities are relatively low and at 1000 ° C the dynamic and static recrystallization (in time between the pastures) precedes the precipitation, producing an equilateral grain structure whose magnitude tends to decrease by decreasing the T. Below 930 ° C begins precipitation that blocks recrystallization; the rolling leads to an elongation of the austenitic grains.

2.  Strip Mill: $\dot\varepsilon$ varies from 10 to 200 s-1, time between the pasts: from 0.4 to 4 s. The addition of Nb delayed the SRX leading to a deformation buildup. The times between the passes are not short enough to completely disregard both the precipitation of carbonitrile and SRX, nor are they long enough to allow complete precipitation and complete stopping of the SRX. In these cases, the composition of the steel is the determining factor for the definition of the mechanisms. Deformation accumulation in the early stages of rolling triggers the DRX that when it cannot complete itself as MDRX. The results of many researches have revealed that SRX kinetics is highly dependent on deformation but independent of $\dot\varepsilon$; while the meta dynamic recrystallization, MDRX, is dependent on debris independent of debris. Moreover, the MDRX kinetics is faster (about one order of magnitude) than the SRX kinetics. This implies that over time the main softening mechanism is MDRX.

3.  Rolling mill for long products: $\dot\varepsilon$ varies from 10 to 10,000 s-1, time between the past varies from 0.05 to 1 s. The first stages of rolling with the blender have virtually the times between the passes equal to those of the previous case. In the finisher the speeds increase considerably. At temperatures around 900 ° C the precipitation, which requires at least 10 s, and the slow kinetic SRX does not occur, then only a buildup of deformation occurs. As a result, when the accumulated deformation reaches the critical threshold $\varepsilon c$ (Fig. 4.27), DRX starts quickly followed by MDRX.

## 4.3.5 **Rolling model**

Several studies have been carried out to predict the evolution of the austenitic grain size of carbon steels during hot rolling.

Austenitic grain change in a rolling passage is determined by dynamic or static recrystallization and grain growth behavior during and after hot rolling and is formulated according to temperature, deformation velocity and initial size of grain wheat. Most studies refer to flat rolling with little research on other types of rolling such as rods.

Recently, some scholars have presented three-dimensional analysis of the finite elements of microstructure evolution in hot rolling, coupled with experiments on a laboratory scale and on the basis of a microstructural evolutionary model.

Considering the calculation time of this approach, which includes a large number of steps, complex mechanics, contour thermal conditions, a mathematical model that calculates passage by passing plastic deformation and temperature evolution in the material during rolling in a very short time ( less than a second) remains a tool that is still very useful and valid for the industry world.

There is still a strong demand to develop a mathematical model in a simple, reliable way and a non-iterative calculation framework to obtain the thermo-mechanical parameters (strain, strain rate and temperature) associated with the rolling process.

The reason is that these parameters are the key elements to predict the size of the austenitic grain during the rolling process.

T.M. Maccagno, a famous metallurgist scholar, in his study on the size of austenitic grain at each rolling pass, passing from a round oval section (and vice versa), calculated deformations by simply multiplying a constant factor for the deformed area obtained by taking the natural logarithm of the fractional reduction ratio in the cross-section through the rolling passage, assuming empirically that deformation is a steady-state factor of 1.7 the deformation due to the section reduction for roughing and 2.5 times per the finish. Simply these factors represent the relationship between the nominal deformations and those that he defined redundant due to the simple change of profile.

I. P. Kemp, another scholar, suggested that deformation for each rolling pass could be 1.5 to 2 times the deformed area in roughing and 2-3 times in later stages.

Both the Maccagno and Kemp studies do not have a mathematical logic for the use of multiplicative factors and the modeling approach for other thermomechanical parameters (strain and temperature rates) that are critical to determining the behavior of recrystallization, is absent.

Scientists Lenhert and Cuong proposed a model that calculated strain and

strain rate based on the hypothesis of a plane deformation state. The three-dimensional deformation zone has been divided into longitudinal strips of the same width in the direction of rolling and each strip is analyzed separately. However, the model has not been validated experimentally, but can only be applied if the shape of the cross-section at the output has been correctly calculated or predicted.

Finally, an analytical model was designed to calculate strain and strain velocity for each passage of the rolling process. The validity of this model was verified by experimental observations of hot rolling of rods with 4 consecutive passes.

The evolution of the austenitic grain calculated from the analytical model during the passage between the rolls was compared to that obtained by the hot torsion test under similar conditions (strain, strain rate, temperature, time).

## 4.3.5.1 Analytical model for strain and strain rate

Deformation in a rolling pass is defined as the actual effective plastic strain at a given time. The strain rate will be defined later. The following two paragraphs will give you the prerequisites for calculating strain $\varepsilon$ and strain rates $\dot{\varepsilon}$.

To determine the strain and strain rate values at each passing, it is necessary first to provide the contour of the material leaving the mill, especially the area that has not been directly contacted with the rollers. An analytical, effective and non-iterative model has been developed for this to predict the cross-sectional exit of rollers for oval-round sections and vice versa. The advantage of this model is that it requires only geometric considerations. Figure 4.28 shows the expected section and that measured after 4 rolling pass. A 28 mm diameter bar was used to produce a 19 mm diameter. Small differences are noticed between the expected form and the measured one but it is still satisfactory.
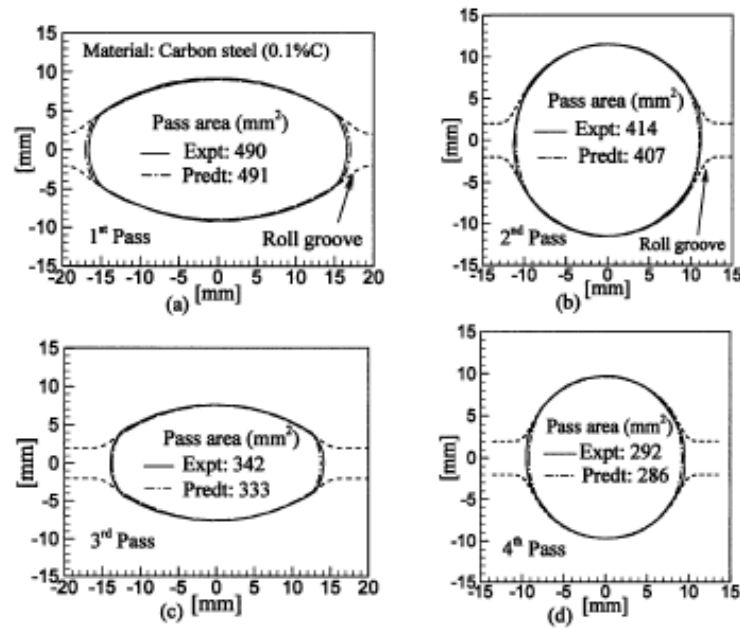
*Figure 4.28 – Sections comparison*

Since the shape of the cross section of the deformed part is not straight, there is difficulty in calculating deformation within a plane in Cartesian coordinates. To overcome this problem, an equivalent rectangular approximation method was developed that transforms the non-rectangular section into rectangular. There are several ways to achieve this goal at the same cross-sectional area. The constant value of cross section area is a necessary but not sufficient requirement. Figure 4.29 describes the equivalent rectangular sections in 3 different ways: the maximum height method, the maximum width method, and the width / height ratio method. The differences between these 3 methods are already apparent from the names.
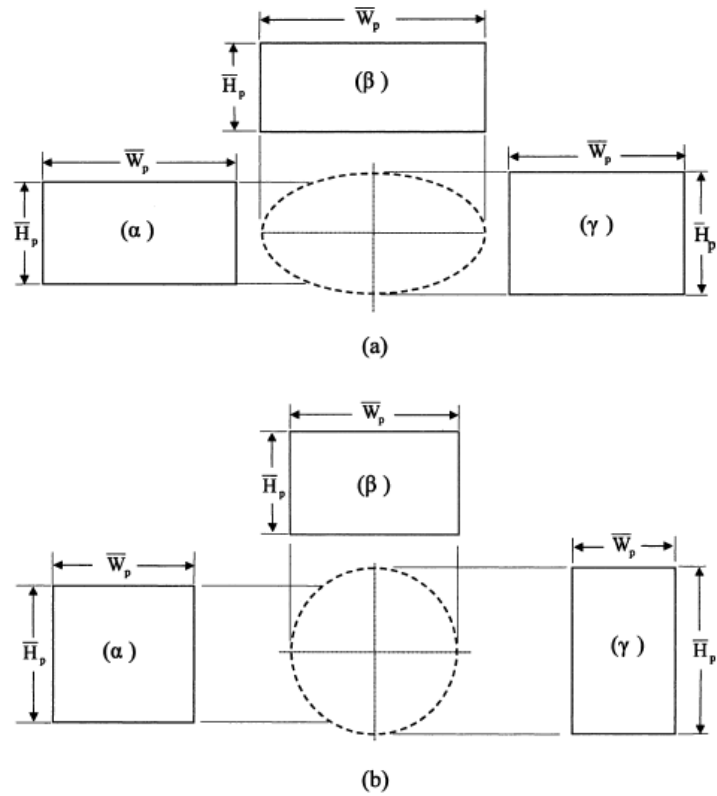
Figure 4.29 Methods of rectangular areas equivalent to the oval passage a) and the round b) where (α) the width/height ratio method, (β) the maximum width method and (γ) the method of the maximum height.
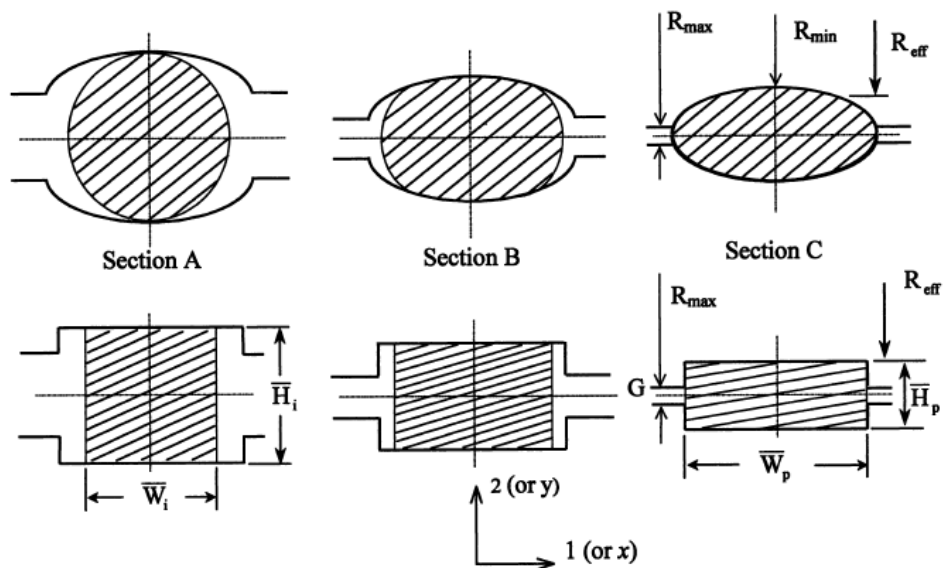


Figure 4.30 Round Descriptive Diagram-Oval (Front View), R_eff. It is the actual rolling radius.

In the case of the width/height method, the definition of width and height is arbitrary. So this method is to be discarded. The maximum height method is not acceptable from the point of view of the change in the shape of the workpiece during rolling and the method of calculating the passing speeds.

When cross sections are approximated in rectangles, the maximum height method indirectly reflects the increment (or decrement) of the output piece due to the change in the size of the incoming part. Finally, the maximum width method can directly reflect this. In addition, the actual rolling radius required for the calculation of the passage velocity is calculated by the maximum width method. Consequently, the cross sections are approximate to rectangles using the maximum width method. Figure 4.30 shows an example of the maximum width method applied to the round-oval passage in which there is an oval-shaped round and oval section bar. Sections A, B, C are the sections that represent the three rolling steps. The equivalent rectangular approximation is described in Figure 4.30 and can be applied to other types of rolling such as oval-round, oval-box and box-flat.

## 4.3.5.2 Strain

The deformation defined as the actual effective plastic strain at a given time and can be calculated by its transformed rectilinear shape. However, the calculation should include nonlinear variations of shape and elongation of deformed material. The hypotheses introduced to overcome this problem is the hypothesis of the deformation parallelepiped. According to this hypothesis a cube of material subjected to a load will become a rectangular prism and the angle of the sides remain orthogonal to those before the deformation. It should be noted that the calculation focuses on the total deformation of the workpiece. Elastic deformation components and neglected cutting edges, the incremental plastic deformation along each major axis can be assumed proportional:

$$d\varepsilon_1 : d\varepsilon_2 : d\varepsilon_3 = \varepsilon_1 : \varepsilon_2 : \varepsilon_3 \qquad (1) \qquad (4.53)$$

From constant condition:

$$\varepsilon_3 = -\varepsilon_1 - \varepsilon_2 \qquad (2) \qquad (4.54)$$

$$\bar{\varepsilon}_p = \left[ \frac{2}{3}\left( \varepsilon_1^2 + \varepsilon_2^2 + \varepsilon_3^2 \right) \right]^{\frac{1}{2}} = \frac{2}{\sqrt{3}} \varepsilon_2 \left[ 1 + \left( \frac{\varepsilon_1}{\varepsilon_2} \right)^2 + \left( \frac{\varepsilon_1}{\varepsilon_2} \right) \right]^{\frac{1}{2}} \qquad (3)\,(4.55)$$

where

$$\varepsilon_1 = \ln\left(\bar{W}_i / \bar{W}_p\right) \quad \text{e} \quad \varepsilon_2 = \ln\left(\bar{H}_i / \bar{H}_p\right) \qquad (4) \, (4.56)$$

## 4.3.5.3 Strain rate

Equation 4.55 is a closed-loop solution for deformation based on the assumption of a uniform parallelepiped strain of the material.

Equation 4.56 is valid under the assumption that the main deformations in the 3 axes are independent of each other. The positive sign is defined when the piece is in contraction. So the sign of $\varepsilon_2$ is always positive because of the contraction along the y axis, while the sign of $\varepsilon_1$ is negative due to the extension along the axis of the ascites. Equation 4.55 shows that if the ratio is negligible then the deformation in the workpiece may be approximated to a flat strain condition generally used in flat rolling.

$$\dot{\bar{\varepsilon}}_p = \bar{\varepsilon}_p / t_p \qquad (5) \qquad (4.57)$$

where $t_p$ represents the time interval for section A to go through section C (Figure 4.30). Below, the average deformation velocity is called deformation velocity. The time interval can be expressed as

$$t_p = \frac{60L}{2\pi N R_{eff}} \, [\text{s}] \qquad (6) \qquad (4.58)$$

where, $R_{eff}$ , L and N are respectively the actual rolling radius, the actual contact length projected on the groove rolled by the workpiece and the number of revolutions at each pass. Actual radius is calculated by the maximum width method. The actual contact length is expressed by

$$L = \sqrt{\left\{\left[R_{max} - \left(\frac{\bar{H}_p - G}{2}\right)\right]\left(\bar{H}_i - \bar{H}_p\right)\right\}} \qquad (7) \, (4.59)$$

## 4.3.6 Conclusions

The study of controlled rolling on Mn and Micro alloyed steels has led to a number of worldwide researches that have resulted in high-grade steels. The heart of the research has led to the identification of a series of austenite preparations with the optimized structure to provide the γ-α transition with a high density of nucleation centers to obtain very fine and homogeneous ferritic granules.
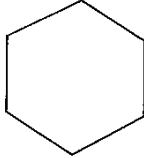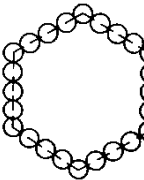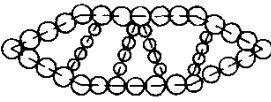
| | Conventional hot–rolling | Controlled rolling | Normalizing | Quenching |
|---|---|---|---|---|
| γ grain structure | | Deformation band | | |
| Nucleation of α grain | | | | Lath |
| α grain structure | | | | Cementite (Tempering) |

*Figure 4.31 Synthesis of the purposes of thermo-rolling controlled*

# Chapter 5

# 5. Process simulation & control system

## 5.1 Introduction

As already anticipated, the simulation is going to be split in three modules:

- thermal module: a heat transfer finite element model is going to be developed to achieve the temperature field history followed when a specimen undergoes a thermal treatment. In order to have a proper calibration of the thermal model, experimental results will be exploited;
- metallurgical module: once the thermal field is known, the main focus is going to be shifted towards the necessity to predict the metallurgical phases achieved during the process;
- mechanical module: knowing the phases developed along the section of the reference specimen and the thermal history which lead to their formation, the main requirement will be prediction of mechanical properties achieved locally.

The figure 5.1 depicts a general structure which the model must follow: thermal module must be the first step of the simulation in order to guarantee the temperature field history inside the treated part. Then the output of this first model will be the input for the metallurgical one which will be able to predict the phase developed. Finally a relationship between the microstructural evolution and the mechanical properties obtained will be provided by the mechanical module.
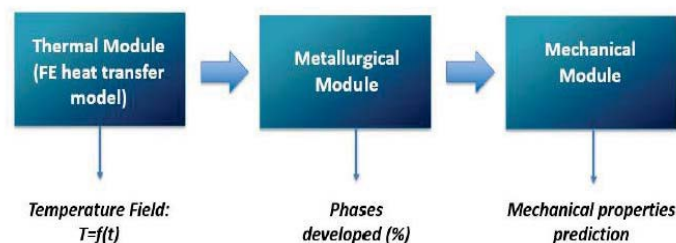


*Figure 5.1 Typical set-up among 3 modules which compose the model*

## 5.2   Thermal model

Assuming the processing material as isotropic and considering that there are no mass transport phenomena, the conservation of the thermal energy, according to the first law of thermodynamics and the Fourier model, writes as follows:

$$\rho c \frac{\partial T}{\partial t} = \nabla \cdot (K \nabla T) + u_{\text{gen}}$$

(5.1)

where T is the temperature, t is the time, and c are, respectively, the temperature dependent material density and specific heat capacity, K is the thermal conductivity, and $u_{\text{gen}}$ is the internal heat generation rate.
Rearranging Eq. (4), indicating as $q_n$ the thermal flow acting over the surface S characterized by the unit outward normal vector n, and taking into account the divergence theorem, one finally has:

$$\int_V \rho c \frac{\partial T}{\partial t} \delta T \, dV + \int_V \nabla \delta T \cdot (K \nabla T) \, dV = \int_S \delta T q_n \, dS + \int_V u_{\text{gen}} \delta T \, dV$$

(5.2)

the latent heat due to solid phase transformations has been taken into account and included into the energy balance equation, using the following heat generation rate form:

$$u_{\text{gen}} = \sum_i \Delta H_{i,j} \frac{\Delta F_{i,j}}{\Delta t_j}$$

(5.3)

where $\Delta H_{i,j}$ is the heat of transformation of the phase i formed during the time step j, at the temperature $T_j$; $\Delta F_{i,j}$ is the volume fraction of the transformed i phase, relatively to the same time step, and $\Delta t_{i,j}$ is duration of the time step j.

### 5.2.1   FEM Model

To create an independent tool from commercial software develop and in the aim to have a flexible system of control, it has been developed a dedicate FEM algorithm to calculate the thermal exchange in the process as follows.
Given a four-sided element, the node coordinates, and the value of the corresponding temperature can be indicated with a column array

$$x_i = \begin{Bmatrix} x_1 \\ x_2 \\ x_3 \\ x_4 \end{Bmatrix} \qquad y_i = \begin{Bmatrix} y_1 \\ y_2 \\ y_3 \\ y_4 \end{Bmatrix} \qquad T_i = \begin{Bmatrix} T_1 \\ T_2 \\ T_3 \\ T_4 \end{Bmatrix}$$

(5.4)

Within the element, the values of the coordinates and temperature of any internal point may be related to the value of the coordinates nodes through a forming function like:

$$N(r, s) = \left[ \tfrac{1}{4}(r+1)(s+1) \quad \tfrac{1}{4}(1-r)(s+1) \quad \tfrac{1}{4}(1-r)(1-s) \quad \tfrac{1}{4}(r+1)(1-s) \right]$$

(5.5)

where r and s are parameters between -1 and 1, varying which can be crossed all the element's internal space. A mapping was then established of the surface points of a square of 2 x 2 sides (with center of gravity on the origin of axes and natural coordinates) and an irregular quadrilateral with vertices of note coordinates (the node in global coordinates).
The item's coordinates are then expressed as

$$x(r, s) = N(r, s) \cdot x_i \qquad y(r, s) = N(r, s) \cdot y_i \qquad T(r, s) = N(r, s) \cdot T_i$$

(5.6)

Deriving the function 5.5,

$$\partial N(r, s) = \begin{bmatrix} \tfrac{1}{4}(s+1) & -\tfrac{1}{4}(s+1) & -\tfrac{1}{4}(1-s) & \tfrac{1}{4}(1-s) \\ \tfrac{1}{4}(r+1) & \tfrac{1}{4}(1-r) & -\tfrac{1}{4}(1-r) & -\tfrac{1}{4}(r+1) \end{bmatrix}$$

(5.7)

which allows to calculate the temperature gradient within the element

$$\partial T(r, s) = \partial N(r, s) \cdot T_i$$

(5.8)

By calculating the derivatives of the global coordinate than the natural ones can get the Jacobian of the transformation between the coordinates

$$J(r, s) = \begin{bmatrix} \frac{(1-s)\,x4}{4} - \frac{(1-s)\,x3}{4} - \frac{(s+1)\,x2}{4} + \frac{(s+1)\,x1}{4} & \frac{(1-s)\,y4}{4} - \frac{(1-s)\,y3}{4} - \frac{(s+1)\,y2}{4} + \frac{(s+1)\,y1}{4} \\ -\frac{(r+1)\,x4}{4} - \frac{(1-r)\,x3}{4} + \frac{(1-r)\,x2}{4} + \frac{(r+1)\,x1}{4} & -\frac{(r+1)\,y4}{4} - \frac{(1-r)\,y3}{4} + \frac{(1-r)\,y2}{4} + \frac{(r+1)\,y1}{4} \end{bmatrix}$$

(5.9)

Resolved as,

$$det J(r,s) = \frac{1}{8}\left[ -s\,(x_3\,y_4 - x_2\,y_4 - x_4\,y_3 + x_1\,y_3 + x_4\,y_2 - x_1\,y_2 - x_3\,y_1 + x_2\,y_1) \right.$$
$$+ r\,(x_2\,y_4 - x_1\,y_4 - x_2\,y_3 + x_1\,y_3 - x_4\,y_2 + x_3\,y_2 + x_4\,y_1 - x_3\,y_1)$$
$$\left. + x_3\,y_4 - x_1\,y_4 - x_4\,y_3 + x_2\,y_3 - x_3\,y_2 + x_1\,y_2 + x_4\,y_1 - x_2\,y_1) \right]$$

$$(5.10)$$

and allows conversion from finite areas into global coordinates to those in natural coordinates. Also useful is the evaluation of the invasion of the Jacobian, to shift from the derivatives in natural coordinates to those in global coordinates.

$$J^{-1}(r,s) = \begin{bmatrix} \frac{-r\,(y_4 - y_3 + y_2 - y_1) - y_4 - y_3 + y_2 + y_1}{4\,det J} & \frac{s\,(y_4 - y_3 + y_2 - y_1) - y_4 + y_3 + y_2 - y_1}{4\,det J} \\ \frac{r\,(x_4 - x_3 + x_2 - x_1) + x_4 + x_3 - x_2 - x_1}{4\,det J} & \frac{-s\,(x_4 - x_3 + x_2 - x_1) + x_4 - x_3 - x_2 + x_1}{4\,det J} \end{bmatrix}$$

$$(5.11)$$

The derivative of form functions 5.5 & 5.6 with respect to global coordinates is expressible through the following matrix, useful for evaluating the usages within the element

$$B(r,s) = invJ \cdot \partial N = \begin{pmatrix} b_{11} & b_{12} & b_{13} & b_{14} \\ b_{21} & b_{22} & b_{23} & b_{24} \end{pmatrix}$$

$$(5.12)$$

Where,

$$b_{11} = \frac{1}{8\,det J}\left( -r*(y_4 - y_3) - y_4 - s*(y_3 - y_2) + y_2 \right)$$

$$b_{12} = \frac{1}{8\,det J}\left( r*(y_4 - y_3) + s*(y_4 - y_1) + y_3 - y_1 \right)$$

$$b_{13} = \frac{1}{8\,det J}\left( -s*(y_4 - y_1) + y_4 + r*(y_2 - y_1) - y_2 \right)$$

$$b_{14} = \frac{1}{8\,det J}\left( s*(y_3 - y_2) - y_3 - r*(y_2 - y_1) + y_1 \right)$$

$$b_{21} = \frac{1}{8\,det J}\left( r*(x_4 - x_3) + x_4 + s*(x_3 - x_2) - x_2 \right)$$

$$b_{22} = \frac{1}{8\,det J}\left( -r*(x_4 - x_3) - s*(x_4 - x_1) - x_3 + x_1 \right)$$

$$b_{23} = \frac{1}{8\,det J}\left( s*(x_4 - x_1) - x_4 - r*(x_2 - x_1) + x_2 \right)$$

$$b_{24} = \frac{1}{8\,det J}\left( -s*(x_3 - x_2) + x_3 + r*(x_2 - x_1) - x_1 \right)$$

#### 5.2.1.1 Definition of the weak solution matrices

The calculation of the conductive stiffness matrix of the heat problem in form weak provides the following result

$$K_K = \int_V B^T \cdot K \cdot B \, dV = \sum_{n=1}^{N} \int_{r=-1}^{r=1} \int_{s=-1}^{s=1} B^T \cdot K \cdot B \cdot detJ \, dr \, ds$$

(5.13)

having had the conductivity in the two dimensions as well $K = \begin{bmatrix} k & 0 \\ 0 & k \end{bmatrix}$

Other volume integrals derived are the mass matrix

$$C = \int_V \rho \, c_p \, N^T \cdot N \, dV = \sum_{n=1}^{N} \int_{r=-1}^{r=1} \int_{s=-1}^{s=1} \rho \, c_p \, N^T \cdot N \cdot detJ \, dr \, ds$$

(5.14)

and the array of inside heat generation

$$Q_B = \int_V N^T q_B \, dV = \sum_{n=1}^{N} \int_{r=-1}^{r=1} \int_{s=-1}^{s=1} N^T q_B \cdot detJ(r,s) \, dr \, ds$$

(5.15)

Integrations to the edges of the item follow the following convention:

- Top edge, $S_1$ → s=1
- Left edge, $S_2$ → r=-1
- Bottom edge, $S_3$ → s=-1
- Right edge, $S_4$ → r=1

where $S_i$ are the four edge of the quadrilateral with their respective values of one of the natural coordinates, which in the case of the edges is constant. The Jacobian edge has been calculated as follows

$$J_{S1} = \left( -\frac{x2-x1}{2} \quad -\frac{y2-y1}{2} \right)$$

$$J_{S2} = \left( -\frac{x3-x2}{2} \quad -\frac{y3-y2}{2} \right)$$

$$J_{S3} = \left( \frac{x4-x3}{2} \quad \frac{y4-y3}{2} \right)$$

$$J_{S4} = \left( -\frac{x4-x1}{2} \quad -\frac{y4-y1}{2} \right)$$

(5.16)

Resolved by,

$$det J_{S1} = \sqrt{\frac{(y2 - y1)^2}{4} + \frac{(x2 - x1)^2}{4}}$$

$$det J_{S2} = \sqrt{\frac{(y3 - y2)^2}{4} + \frac{(x3 - x2)^2}{4}}$$

$$det J_{S2} = \sqrt{\frac{(y4 - y3)^2}{4} + \frac{(x4 - x3)^2}{4}}$$

$$det J_{S4} = \sqrt{\frac{(y4 - y1)^2}{4} + \frac{(x4 - x1)^2}{4}}$$

(5.17)

In addition, the form functions have been specialized on the four edges

$$N_{S1} = \left(\frac{r+1}{2} \quad -\frac{r-1}{2} \quad 0 \quad 0\right)$$

$$N_{S2} = \left(0 \quad \frac{s+1}{2} \quad -\frac{s-1}{2} \quad 0\right)$$

$$N_{S3} = \left(0 \quad 0 \quad -\frac{r-1}{2} \quad \frac{r+1}{2}\right)$$

$$N_{S4} = \left(\frac{s+1}{2} \quad 0 \quad 0 \quad -\frac{s-1}{2}\right)$$

(5.18)

allowing a simpler calculation of the surface integral of the solution weak. The convective rigidity matrix is now computable as

$$K_C = \int_S N_{Si}^T \cdot N_{Si} \cdot h_{Si} \, dS = \int_{S_i} N_{Si}^T \cdot N_{Si} \cdot h_{Si} \cdot det J_{Si} \, dS_i$$

(5.19)

Convective array as

$$Q_C = \int_S N_{Si} \cdot h_{Si} \cdot T_{amb} \, dS = \int_{S_i} N_{Si} \cdot q_{Si} \cdot det J_{Si} \, dS_i$$

(5.20)

Heat flux array on the surfaces as

$$Q_S = \int_S N_{Si} \cdot q_{Si} \, dS = \int_{S_i} N_{Si} \cdot q_{Si} \cdot det J_{Si} \, dS_i$$

(5.21)

All matrices together form the thermal problem with thread elements, expressible with the following matrix equation

$$C \cdot \frac{dT}{dt} + [K_K + K_C]T = Q_B + Q_S + Q_C$$

(5.22)

to be solved by applying a typical numerical method such as the 'Method' Theta 'already known for its application to the finite differences, in its explicit variants, implicit or mixed.

For the idRHa+ control software, an explicit method has been implemented, not unconditionally stable but useful in modeling conditions at the edge suddenly change over time, as it is not necessary reverse the stiffness matrices at each time step. It was therefore necessary reduce this dt step according to the size of the mesh, in quotient smaller elements require smaller time increments to avoid temperature fluctuations tend to swing in and out overflow of memory.

### 5.2.1.2   Numerical Integrations

Calculation of the resolving system matrices requires integration inside of the volume of the finite element and on the element surface. To do so, was chosen the Gauss 4-point integration method on the element two-dimensional, with the advantage of having weights $w_{ij}$ all unitary and calculating exactly grade 3 polynomials.

$$\int_V f(x)\,dx \simeq \sum_{i=1}^{2}\sum_{j=1}^{2} f(x_i, y_i)w_{ij} \overset{(w_{ij}=1)}{=} \sum_{i=1}^{2}\sum_{j=1}^{2} f(x_i, y_i)$$

(5.23)

This is to evaluate the function on 4 points ($x_i$; $y_i$) of the domain. Having a mapping compared to the square of side 2 previously mentioned, integration becomes

$$\int_{-1}^{1}\int_{-1}^{1} g(r,s)\,dr\,ds \simeq \sum_{i=1}^{2}\sum_{j=1}^{2} g(r_i, s_i)w_{ij} \overset{(w_{ij}=1)}{=} \sum_{i=1}^{2}\sum_{j=1}^{2} g(r_i, s_i)$$

(5.24)

taking care to evaluate the function g(r,s) in the four points given by $r_i = \pm\frac{\sqrt{3}}{3}$ e $s_i = \pm\frac{\sqrt{3}}{3}$.

### 5.2.2   Thermal exchange coefficient

To complete the activity of thermal exchange evaluation, it's needed to do the experimentation of heat exchange coefficients, carried out on flat

plate, for spray nozzles which are installed in the IdRHa system (Annex 2). Cooling tests have been performed on real rail specimens and on an austenitic plate, equipped with several thermocouples. The samples have been heated up to 900 °C and then have been cooled down to ambient temperature using different nozzles pressures. All trials have been modeled by a commercial finite element software and related HTCs have been obtained by inverse modeling techniques.
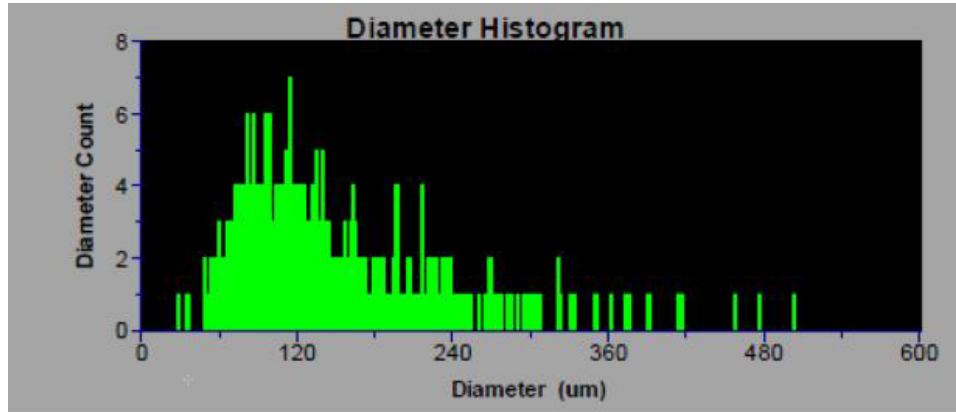


*Figure 5.2 Water diameter*

Air mist jet properties like water specific flows, droplet velocities and Souter mean diameter have been measured and a comprehensive HTC correlation as function of air and water pressures has been found in accordance to the following literature equation:

$$HTC = kT_{wall}^{a}W^{b}v_{impact}^{c}f(D_{32})$$

(5.25)

The result of the job is a series of HTC curves in function of surface temperature of the plate, for different operating pressures a 3, 4 and 5 bar air and various water pressure points within the regime of mixed operation of the atomizer nozzle. These all curves have a shape sigmoidal type that can be accurately approximated by a relationship

$$HTC(T) = y_0 + \frac{a}{1 + \left(\frac{T}{T_0}\right)^b}$$

(5.26)

The sigmoid parameters a, b, $t_0$ and $y_0$ were evaluated for each pair of air-water pressures by means of non-linear regression techniques. The parameter $y_0$ equals the exchange rate at high operating temperatures; $T_0$ indicates the temperature at which the zone of increase of the power of the spray; $b$ is a slope gradient index for temperatures around $T_0$; $t_0$ is the coefficient of heat exchange at 0°C. Parameter values of the sigmoid were

compared for each group of air pressures by trying to bind them to the properties of the spray; with a unclear proportionality report established, it has been linked these parameters at the single water flow by means of polynomials of grade 3. Therefore direct linkages with $P_w$ water pressure, diameter of drop $D_{32}$ and drop speed $v$. It's recognized that $D_{32}$ and $v$ are in effect on thermal exchange properties, but it was not possible to get one report that using such quantities would allow them to get the coefficients of experimental exchange with acceptable approximation.

| Parametro | Coefficienti del polinomio interpolante | | | |
|---|---|---|---|---|
| $y_0$ | $c_0$ | $c_1$ | $c_2$ | $c_3$ |
| $P_a = 3bar$ | -285.5973431 | 744.7016957 | -146.8913532 | 8.943182517 |
| $P_a = 4bar$ | -351.6777039 | 911.4818648 | -166.7062385 | 9.447072993 |
| $P_a = 5bar$ | -543.2014422 | 1248.936326 | -243.2141432 | 14.37151155 |
| $T_0$ | $c_0$ | $c_1$ | $c_2$ | $c_3$ |
| $P_a = 3bar$ | 3144.1399721 | 151.953893 | -35.16881892 | 2.229265434 |
| $P_a = 4bar$ | 133.1356606 | 162.2112137 | -33.13791673 | 1.926002544 |
| $P_a = 5bar$ | 79.39172459 | 280.4453181 | -64.16777476 | 4.099278747 |
| $a$ | $c_0$ | $c_1$ | $c_2$ | $c_3$ |
| $P_a = 3bar$ | 6915.816714 | 8979.530043 | -1165.055998 | 52.4133783 |
| $P_a = 4bar$ | -55.95201426 | 14321.91179 | -2804.451293 | 177.5875474 |
| $P_a = 5bar$ | 19153.57112 | -1902.481594 | 1045.985973 | -90.25168888 |
| $b$ | $c_0$ | $c_1$ | $c_2$ | $c_3$ |
| $P_a = 3bar$ | 3.541645203 | 2.023794369 | -0.4515945 | 0.02665584 |
| $P_a = 4bar$ | 2.926024198 | 2.441710022 | -0.483246489 | 0.027457965 |
| $P_a = 5bar$ | 3.578830783 | 2.192675623 | -0.488134819 | 0.031686225 |

*Table 5.1 Polynomial regression of HTC sigmoid*

## 5.3   Metallurgical model

The cooling curves are the graphical representation of the cooling law, that is, the temperature variations in time, of the steel considered, from the beginning of the cooling to the end of the operation.
For this purpose there are TTT (temperature, time, transformation) and TRC (continuous cooling transformation), also called CCTs (Continuous Cooling Transformation), depending from the process type both of which are essential for predicting the structural transformations occurring during the heat treatment of the steel. Of course, any type of steel, with respect to its chemical composition and the magnitude of its austenitic grain, has specific experimental transformation curves that allow to determine which temperature, type and speed of cooling should be chosen to obtain certain structures final and therefore certain mechanical characteristics.

The TTT curves are obtained practically in the following way: the subtle samples, after austenitization, are immersed in saline or leaded baths carried and fixed at a certain temperature. After being in such conditions for a certain time, varying from a few seconds to many hours, the samples are cooled in water; after the isothermal maintenance, with fast cooling, the austenite can be transformed into martensite (easily distinguishable from the structure produced at the temperature of the baths). It is thus possible to know by means of metallographic examinations and X-ray diffraction methods the percentage of structure that has been transformed for a certain permanence at a certain temperature and the nature of this structure. It should be noted that the start and end ferrite transformation curves tend to be asymptotically to the horizontal corresponding to the temperature A3, while those of the pearlitic transformation tend to temperature A1, these two temperatures coincide with eutectic steels. The position and shape of all the lines are deeply modified as well as carbon content, even by the presence of special elements. The influence of these elements is generally manifested with a more or less accentuated shift of the curves to the right (with the exception of cobalt only), as well as with a modification of the shape of them, very variable from case to case. The curves of isothermal transformations but also those of anisoterms do not depend solely on the chemical composition of steel; the temperature and the austenitization time, which affect the size of the austenitic grain, change the positions of the beginning and end curves; an increase in austenitic grain. Instead, if steel is subjected to deformation leading to austenitic grain refinement, the curves move to the left as it increases the density of grain edges that represent preferred sites for nucleation of ferrite.

In a non-constant cooling process in terms of:

- Interrupt cooling process with HTC (heat transfer coefficient) changing during cooling phase depending from pressure utilized
- process conditions with zone of material reheating

the Anisoterm curves of Austenite or CCT curves doesn't adapt with correct accuracy to these behavior; so in this case the TTT curves, typically used for steel maintained at constant temperature, are adopted with the modification of Scheil laws that permit to adapt these curves to the continuous and changing cooling process in terms of speed, time and efficiency.

Figure 5.3 shows the symbolic diagram which shows:

- on the abscissa axis, the values of the logarithmic decimal scale for convenience of representation;
- on the axis of the ordered the temperature values in °C
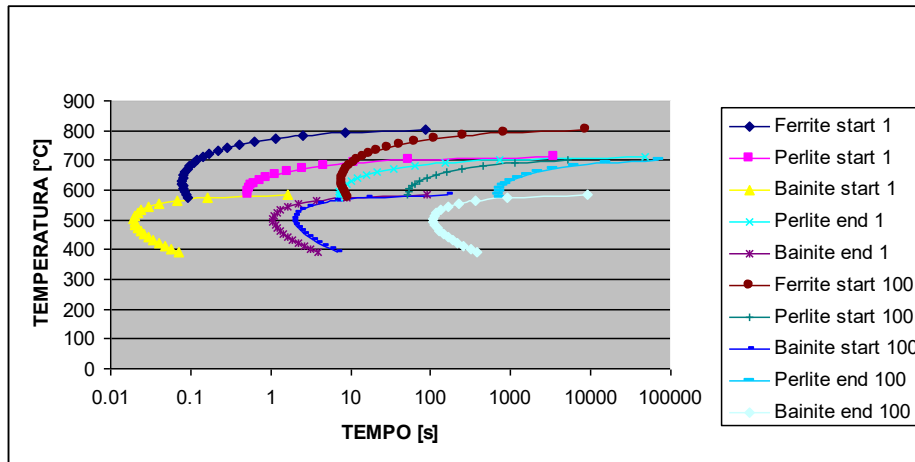
*Figure 5.3 – TTT diagram*

This diagram permit to design a set of thermal cooling curves in the semi logarithmic coordinate system logarithmic: decimals of time/temperature diagram, which defines, for each continuous cooling temperature, the temperatures at which it begins and end of the austenite transformations.
it can be stated that:

- the austenitized steel is cooled rapidly to room temperature, so that the cooling curve does not intersect either the bainitic or pearlitic transformation zone, the austenite remains stable until the temperature $M_s$ begins progressively to transform into martensite; at the $M_f$ temperature the transformation is practically completed (with any traces of residual austenite, that is, untransformed austenite, which is at room temperature);

- If austenitized steel at the temperature is moderately cooled so that the cooling curve crosses the transformation fields, the austenite transforms into the typical aggregates of the crossed region: bainite, ferrite, ferrite + cementite;

The role of controlled rolling is to introduce a high density of nucleation sites for grains $\alpha$ within the matrix $\gamma$ during transformation. The $\alpha$ nucleation sites to be considered are mainly the austenitic grain boundaries; therefore nucleation sites increase as the grain edges increase and the transformation takes place at lower times, resulting in a shift in the left-hand side of the cooling curves of the same chemical composition of the steel. One of the dilemmas that you face: but how and how do these curves move according to the average diameter of austenitic grain?
Through the JMatPro software (see appendix 3), it was possible to calculate the position and shape of the curves from the chemical composition of the steel, the austenitization temperature and the time to stay at that temperature. The last two, in particular, as mentioned above,

are necessary for the software to be able to calculate the diameter of the austenitic grain ($d\gamma$) starting parameter, which influences the movement of the curves: an increase in the size of the austenitic grain causes the displacement of the austenitic wheat curves to the right or higher times as it slows the conversion of austenite to other phases such as ferrite that require nucleation and growth times. To calculate the curve displacement law according to the austenitic grain diameter, we went to simulate the starting and ending curves of the same steel with different austenitic diameters as shown in Figure 5.4 an example of TTT curves with two different diameters. At this point we went to calculate the time needed to reach the ferrite start curves, perlite start (which coincides with ferrite end), perlite end, start bainite and end bainite. An example of the values obtained for nose times in the TTT curves of the U71Mn steel at different diameters is given in Table

| d austenitic (mm) | Ferrite start | Perlite start | Bainite start | Perlite end |
|---|---|---|---|---|
| 10 | 0.8 | 5.2 | 0.2 | 70.6 |
| 20 | 1.6 | 10.4 | 0.4 | 141.1 |
| 40 | 3.2 | 20.7 | 0.8 | 282.2 |
| 60 | 4.7 | 31.1 | 1.2 | 423.3 |
| 80 | 6.3 | 41.5 | 1.6 | 564.4 |
| 100 | 7.9 | 51.8 | 2.0 | 705.5 |
| 120 | 9.5 | 62.2 | 2.4 | 864.6 |
| 140 | 11.0 | 72.6 | 2.7 | 987.7 |
| 160 | 12.6 | 82.9 | 3.1 | 1128.8 |
| 180 | 14.2 | 93.3 | 3.5 | 1269.9 |
| 200 | 15.8 | 103.7 | 3.9 | 1411.0 |

*Table 5.2. Transformation time*

By normalizing the times of the noses with respect to a value, for example in this case compared to the time obtained at 10 mm, as shown in Table 5.3, the normalized data are identical except for a minimal negligible deviation of the bainite start (due to difficulty in detecting the position and time of bainitic nose).

| d austenitic ($\mu$m) | $d_x/d_{10}$ | Ferrite start | Perlite start | Bainite start | Perlite end |
|---|---|---|---|---|---|
| 10 | 1 | 1.0 | 1.0 | 1.0 | 1.0 |
| 20 | 2 | 2.0 | 2.0 | 2.0 | 2.0 |
| 40 | 4 | 4.0 | 4.0 | 3.9 | 4.0 |
| 60 | 6 | 6.0 | 6.0 | 5.9 | 6.0 |

| | | | | | |
|---|---|---|---|---|---|
| **80** | 8 | 8.0 | 8.0 | 7.8 | 8.0 |
| **100** | 10 | 10.0 | 10.0 | 9.8 | 10.0 |
| **120** | 12 | 12.0 | 12.0 | 11.8 | 12.3 |
| **140** | 14 | 14.0 | 14.0 | 13.7 | 14.0 |
| **160** | 16 | 16.0 | 16.0 | 15.7 | 16.0 |
| **180** | 18 | 18.0 | 18.0 | 17.6 | 18.0 |
| **200** | 20 | 20.0 | 20.0 | 19.6 | 20.0 |

*Table 5.3. Transformation time normalized on 10 micron*

For TTT curves it has been noted that their displacement is a linear function of the average grain size. Considering a TTT curve associated with a particular value of dγ, it is possible from it to get all the others by multiplying the values in abscissa, the times, for a factor of the type $\frac{d_x}{d_{known}}$ where $d_x$ is the new average diameter of the austenitic grain and so is the reference diameter to which the curves (master curves) have been calculated. The variation of the average diameter of austenitic grain in TTT therefore does not cause displacements along the vertical (along the temperature axis) as can be seen from the graph of Figure 2 obtained by simulating two hypothetical austenitic grain diameters with the JMatPro software.

This has led to a more general linear formula (see Figure 5.4) that allows to determine the time shift of the TTT and CCT curves relative to the average diameter of the austenitic:

$$t_x = \left(\frac{d_x}{d_{known}}\right) \cdot t_{known} \qquad (5.27)$$

dove $t_x$ where is the time we want to calculate a generic curve referring to an average diameter of the grain $d_x$, whereas $t_{known}$ is the time of a known curve referring to the average diameter of the austenitic grain $d_{known}$ (master curve).
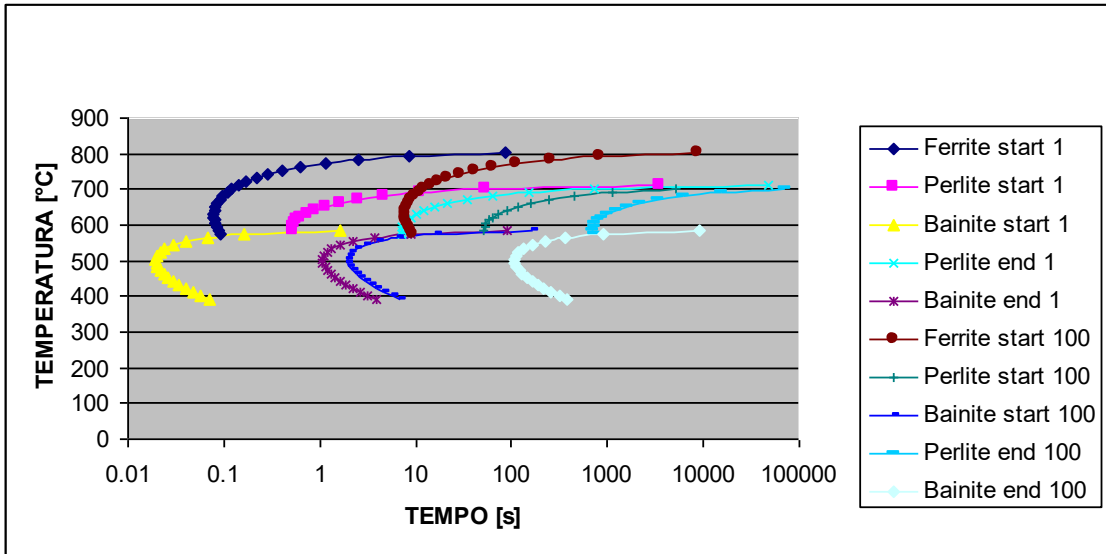
*Figure 5.4 – Moving curves from 1 to 100 micron*

The same procedure has been verified on several steels ranging from hypoeutectoid to hypereutectoid, giving the same result.

This relationship thus proved to be valid in the same way for TTT curves: having a known cooling curve referring to a certain diameter of the austenitic grain of any steel (also taken from the Handbooks), it is able to trace all the curves of that material for any other magnitude of the austenitic starting grain.



$$\frac{t}{t_{master}} = \frac{1 d_\gamma}{d_{known}} \qquad R^2 = 1$$
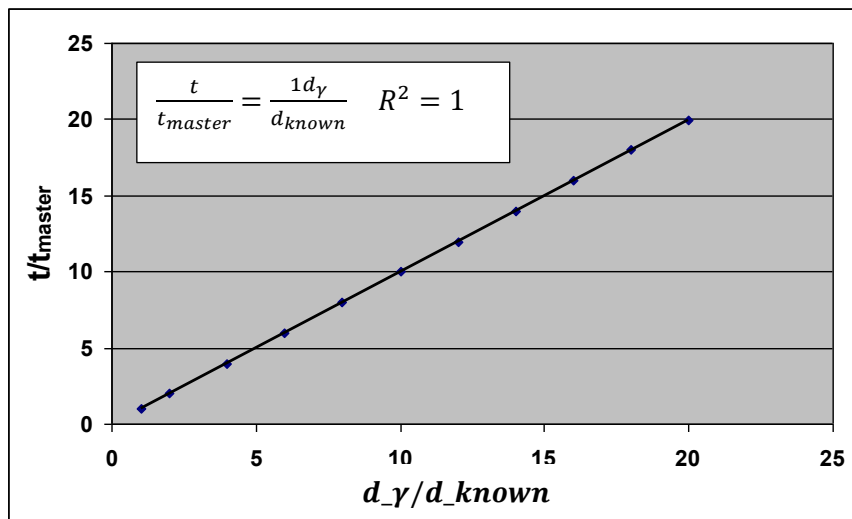
*Figure 5.5 – Diagram of normalized values trend linear.*
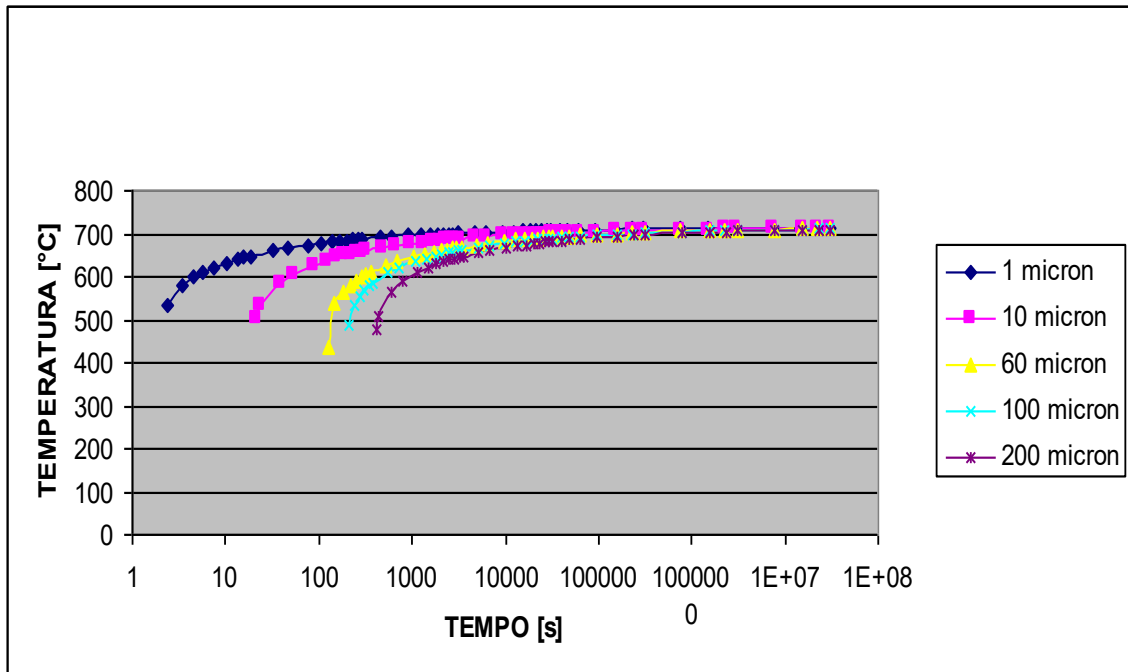
*Figura 5.6 – Spostamento della perlite start in funzione del diametro del grano austenitico dell'acciaio AISI 1020.*

## 5.3.1 Calculation of critical temperature

The equilibrium structures of the iron-carbon alloys are represented in the relevant state diagram. In particular, pure iron is polymorphic, i.e. may be present in various forms of the crystalline lattice. From the carbon iron diagram it is possible to distinguish:

- iron $\alpha$ with cubic network centered body, stable up to 912° C and magnetic up to 770° C (Curie point);
- iron $\gamma$ with cubic network centered faces, stable between 912° C and 1394° C;
- iron $\delta$ with cubic network centered body, stable between 1394° C and iron fusion temperature (1538° C).

The critical temperatures of the iron-carbon diagram are defined as the temperatures at which such polymorphic transformations take place. In addition, when dealing with problems related to the solidification and cooling of iron-carbon alloys, it can be discussed in terms of phases or in terms of structural constituents. Therefore, the main critical points are defined as follows:

- $A_1$, austenite equilibrium temperature-perlite; austenite forms to

heat up or breaks down to cool, forming ferritic + cementite eutectoids;

- Ac₁, the temperature at which the austenite begins to form in the heating conditions;
- Ac₃, temperature at which ferrite - austenite transformation is complete in heating conditions;
- Ac$_m$, austenite - cementitious equilibrium temperature in the case of hypereutectic steels, above which the austenite is stable and below which cementitious progressively appears

A typical TTT diagram contains the following elements: the temperature *Ae*3 below which the formation of ferrite becomes thermodynamically possible, the *Bs* temperature or the start bainitic transformation, *Ms* temperature or martensitic transformation start, a set of nose curves describing the trend of diffuse transformations (ferrite, perlite), a set of nose curves describing the trend of the transformation no diffusive (bainite). Most of the transformations are the result of simultaneous nucleation processes and growth.
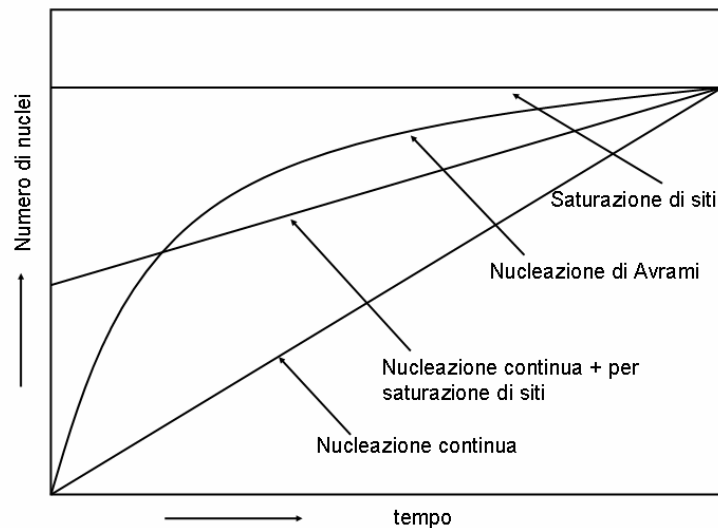


*Figure 5.7 Nucleation models*

Finally, the temperature Ms (martensitic processing start temperature) is characteristic for each steel and varies with its chemical composition. It generally decreases with the increase in carbon content, but also varies depending on the concentration of some alloy elements.

Numerous models are available in literature that allow you to calculate critical temperatures for a steel. Most of these models, however, consider only the chemical composition of the material, but reasonable reasoning.

Below are some of these models for calculating critical temperatures, especially for A1 and A3 in addition to Ms and M95.

|     |       | Ac1   |       |          |         |         |       | Ar3   |       |       |
|-----|-------|-------|-------|----------|---------|---------|-------|-------|-------|-------|
| Ac1 | 741.5 | 731.4 | 738.8 |          | 737.2   |         |       |       |       |       |
|     | [1]   | [2]   | [4]   |          | average |         |       |       |       |       |
|     |       | Ac3   |       |          | Ac3     |         |       | Ar3   |       |       |
| Ac3 | 826.5 | 843.9 | 835.9 | 827.3    | 815.7   | 833.4   | 811.6 | 813.9 | 809.5 | 829.8 |
|     | [2]   | [3]   | [4]   | [6]      | [16]    | average | [10]* | [16]  | [17]  |       |
| Ms  | 444.9 | 436.8 | 412.2 | 407.4 | 431.2 | 413.5 | 445.3 | 434.9 | 409.3 | 421.6 | 425.5 |
|     | [7]   | [8]   | [9]   | [11]  | [12]  | [13]  | [14]  | [15]  | [15]  | [1]   | [15]+[1] |
| Mf  | 244.9 | 236.8 | 212.2 | 207.4 | 231.2 | 213.5 | 245.3 | 234.9 | 209.3 | 221.6 |
| Bs  | 706.0 |       | Bf    | 682.0 |       | Tnr   | 930.0 |

$$A_1[°C]= 723-10.7\%Mn- 6.9\%Ni+29.1\%Si+16.9\%Cr+6.38\%W +290\%As$$

$$A_{c3}[°C]= 910-203(\%C)^{1/2}-15.2\%Ni+ 44.7\%Si+ 104\%V+ 31.5\%Mo+ 13.1\%W-30\%Mn-11\%Cr- 20\%Cu+700\%P+120\%As$$

$$A_{r3}[°C]= 910-273\%C-74\%Mn-57\%Si-16\%Cr-9\%Mo-5\%Cu$$

$$Ms[°C]= 529.5-371.5\%C-50.2\%Mn-18.85\%Ni-8\%Si- 21.05\%Cr-3.75\%Mo-2.5\%Cu$$

$$M_{95}[°C]= 349.5-371.5\%C-50.2\%Mn-18.85\%Ni-8\%Si- 21.05\%Cr-3.75\%Mo-2.5\%Cu$$

$$T_{nr}[°C]= 887+464\%C+6445\%Nb-644\%Nb^{1/2} +732\%V - 230V^{1/2} + 890\%Ti+363\%Al-357\%Si$$

## 5.3.2  Grain growth during "Preheat" phase

The average grain size is one of the main factors contributing to determining the mechanical properties of a material. It may vary over time and depends in turn on many other factors such as strains and stresses, process temperature, and permanence time.

In the rolling process, which is the subject of our study, the average diameter of grain **d** varies throughout the process.

The theoretical-experimental rolling model adopted and subsequently validated describes the diameter of each step by means of mathematical equations but the missing one is the starting diameter or its value at the

end of the pre-heating phase and the beginning of the past of roughness.

In fact, the first stage of experimental testing requires a grain growth model or a correlation between the average grain size and the temperature and dwell time values to which the steel is subject. It is necessary to find a mathematical law experimentally describing the trend of the average dimension according to its two parameters.

For this purpose, each of the steels under consideration is experimentally subjected to different thermal tests by means of samples, each of which is characterized in turn by a given temperature and by a given time of permanence. The generic thermal test consists of preheating the oven at a pre-set temperature which, once reached, opens and inserts into it samples of a given type of steel. These same samples, at predetermined time intervals, are then extracted and cooled abruptly in water (hardened) in order to instantly freeze their structure and prevent any change in average diameter of austenitic grain.

Testing involves the initial selection of temperature values in this case of 900, 1000, 1100 and 1200° C and the selected dwell time as 16 min, 1h and 2h. By combining the time and temperature parameters chosen for each type of steel, it is necessary to perform twelve thermal treatments and use, accordingly, twelve specific samples.

The steels utilized in the study and in the construction model are:

- U75V
- U71Mn
- Φ76

### 5.3.3 Experimental results

After heat treatment, the specimens were embedded, mirror polished and subsequently chemically attached with acid solution; 2 chemical attacks were used nital 4 (4% nitric acid solution in ethyl alcohol) and picral 4 (ethyl alcohol solution with 4g picric acid). After the chemical attack he went to observation at the optical microscope (Figures 5.8, 5.9 and 5.10).
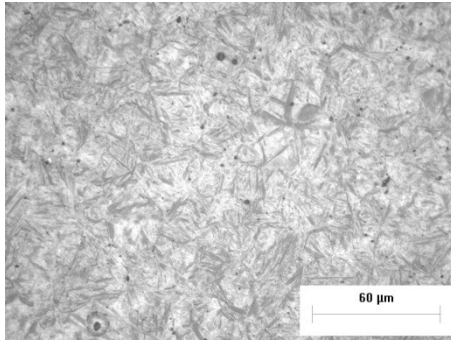
a) 900°C, 16 min
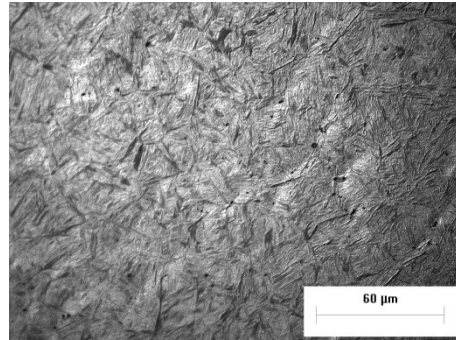
b) 900°C, 1 h
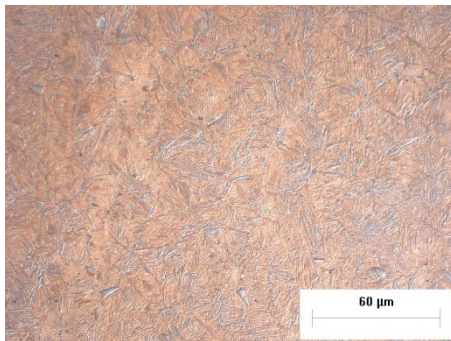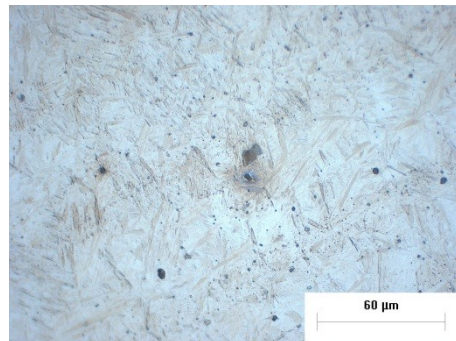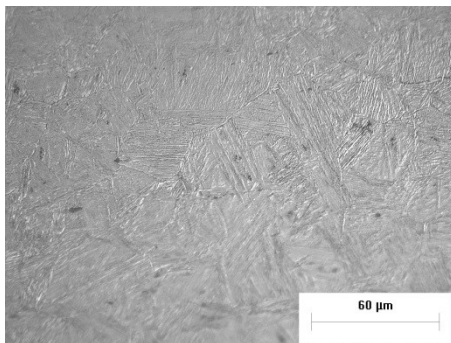
c) 900°C, 2 h
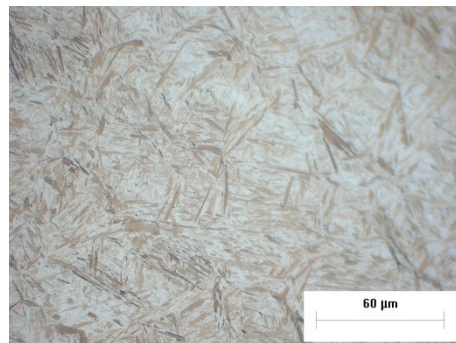
d) 1000°C, 16 min
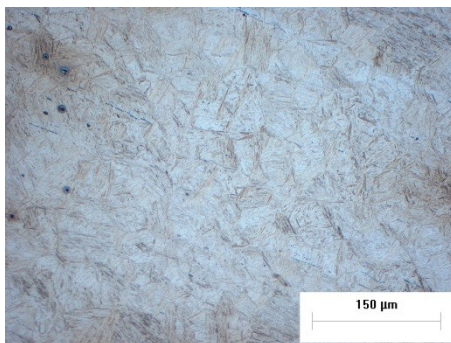
e) 1000°C, 1h
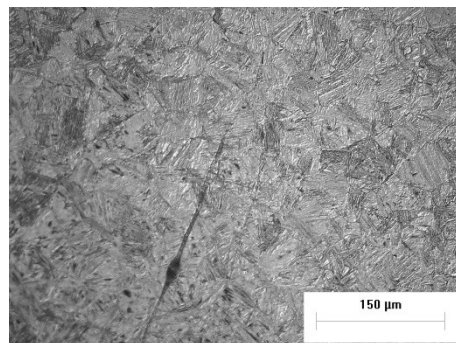
f) 1000°C, 2h
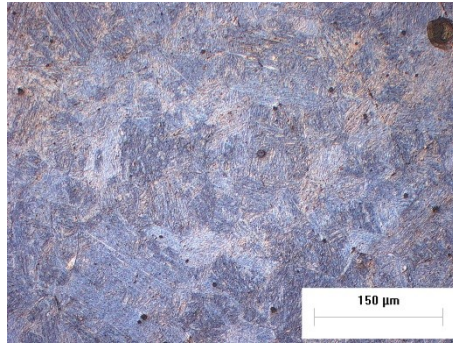
g) 1100°C, 16 min

h) 1100°C, 1h

*Figure 5.8 – micrographs U75V after heat treatment*

**i) 1100°C, 2h**



**a) 900°C, 16 min**



**b) 900°C, 1 h**



**c) 900°C, 2 h**



**d) 1000°C, 16 min**



**e) 1000°C, 1h**



**f) 1000°C, 2h**

**g) 1100°C, 16 min**



**h) 1100°C, 1h**
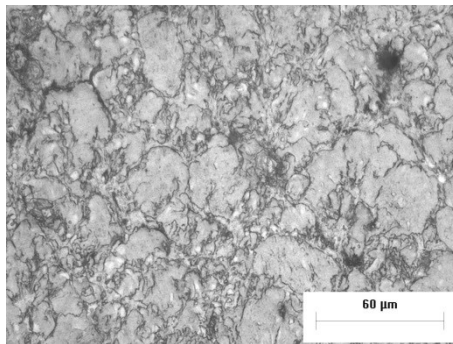


**i) 1100°C, 2h**

*Figure 5.9 – micrographs U71Mn after heat treatment*



**a) 900°C, 16 min**



**b) 900°C, 1 h**



**c) 900°C, 2 h**



**d) 1000°C, 16 min**

**e) 1000°C, 1h**



**f) 1000°C, 2h**



**g) 1100°C, 16 min**



**h) 1100°C, 1h**



**i) 1100°C, 2h**
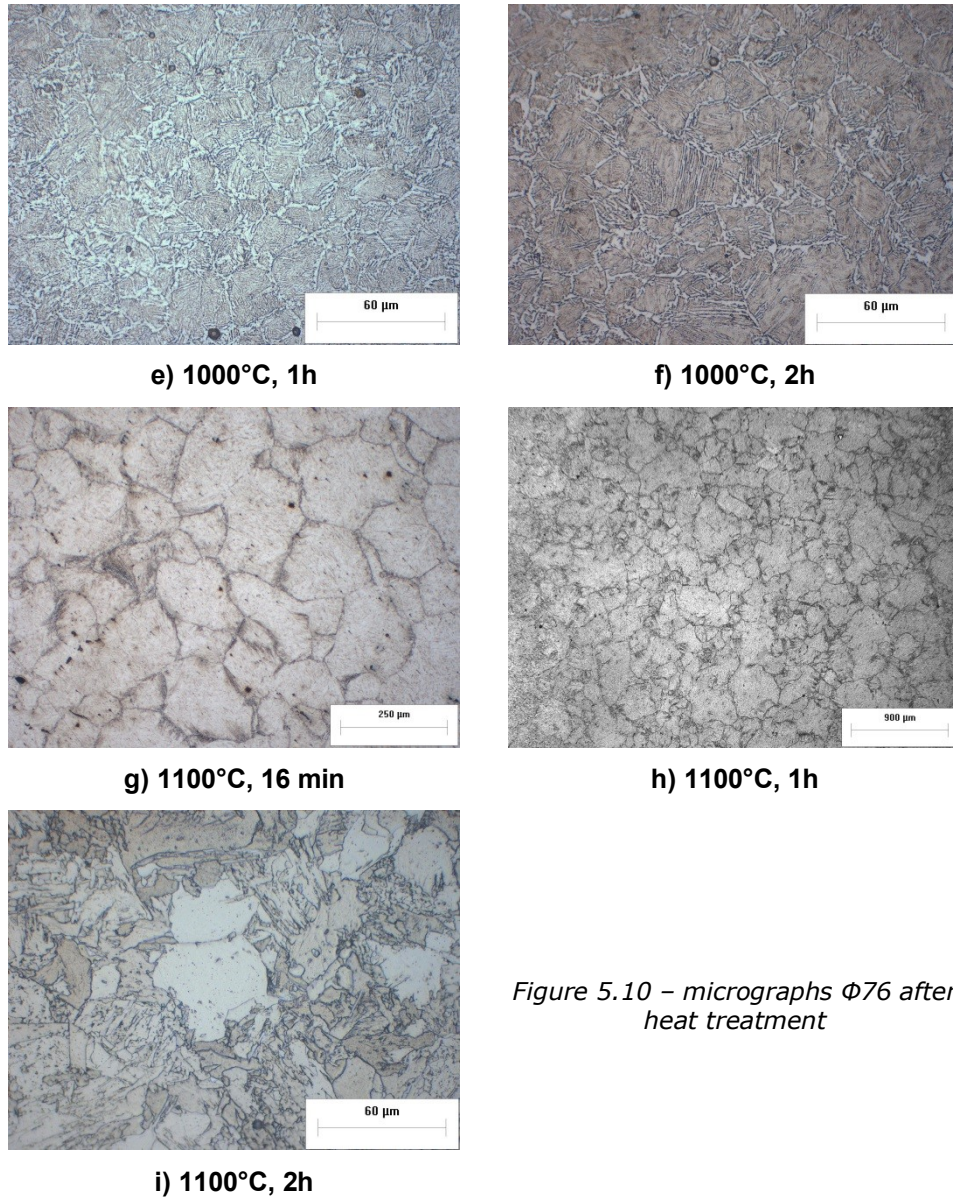
*Figure 5.10 – micrographs Φ76 after heat treatment*

The average diameter of the initial austenitic grain, also known as PAG (Primary Austenite Grain), was calculated by combining the results obtained through the intercept method and those obtained by digital image analysis using the Image-Pro Plus software suitable for that use.

|  | U75V | U71Mn | Φ76 |
|---|---|---|---|
| 900_16min | 22.8 | 13.0 | 15.2 |
| 900_1h | 32.5 | 13.6 | 17.8 |
| 900_2h | 33.3 | 17.3 | 22.1 |
| 1000_16min | 27.7 | 14.5 | 25.8 |
| 1000_1h | 47.9 | 15.5 | 35.7 |

| | | | |
|---|---|---|---|
| 1000_2h | 70.0 | 23.4 | 55.5 |
| 1100_16min | 67.6 | 135.1 | 85.1 |
| 1100_1h | 117.4 | 180.7 | 124.5 |
| 1100_2h | 170.0 | 183.0 | 165.3 |
| 1200_16min | 177.5 | 220.0 | 203.5 |
| 1200_1h | 260.0 | 300.0 | 274.9 |
| 1200_2h | 295.9 | 330.0 | 338.1 |

*Table 5.4. Experimental average austenitic grain size expressed  in µm*

The histogram shown in Figure 5.11 depicts the trend of the average diameter of the grain ($\mu_m$) according to the type of steel tested and the temperature and dwell time associated with it.
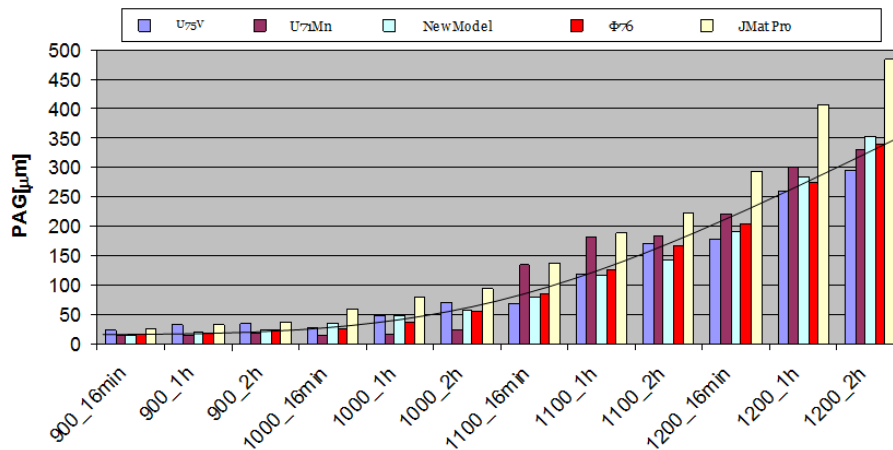


*Figure 5.11 Comparison graph between calculation grain size method*

Also in the histogram is the trend of the average diameter extracted from the J.MatPro software conceived as a database to predict the cooling properties and curves of steels in function of their chemical composition.
How easy is to note the J.MatPro software overestimates the values actually obtained from experimental tests using the following mathematical model that has been able to extrapolate:

$$d_\gamma = A*EXP(B*C)$$ (5.28)

where:

- A = 0.001444
- B = 0.000363
- C= *T(K) x {D+ log[t(s)]}*
- D=20

From the comparison of the mathematical model extracted from the program with the actual data obtained, a new mathematical model was deduced more precisely and closer to the average representation made by the curve superimposed on the histogram:

$$d_\gamma = A'* EXP(B'* C')$$  (5.29)

where:

- A'= 0.00055641
- B'= 0.00048097
- C'= $T(K) \times \{D'+ log[t(s)]\}$
- D' = 15

It should be noted that up to 1000 ° C the Ancona model slightly overestimates the austenitic diameter of AISI 1020 steel, this probably due to the presence of vanadium in the chemical composition of carbon-N forming up to about 1000° C as can be seen in Figure 5.12.

.
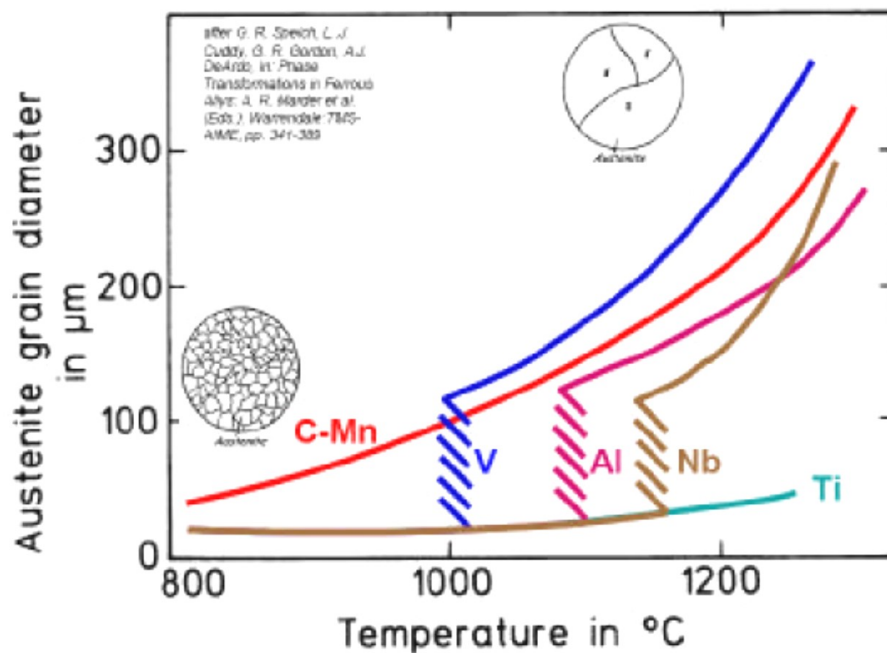


*Figure 5.12 Effect of micro alloyed on grain size during heating*

### 5.3.1   JMAK model review

The metallurgical model adopted in the tool is based on kinetics nucleation and growth as formulated by Johnson-Mehl-Avrami-Kolmogorov, also called JMAK, according to which the fraction of Austenite transformed in the product according to time and under isothermal conditions it is expressed by the following formula:

$$F = 1 - e^{-kt^n} \tag{5.30}$$

where parameter n expresses the rate of growth, i.e. the rate of advance of transformation, while parameter k indicates the nucleation rate and thus the speed of commencement of transformation. These sizes are generally temperature functions T, although often in literature n is considered constant for the date type of phase formed, whether it is Ferrite, Perlite or Bainite (provided that the kinetics is nucleation and growth). In modeling we have adopted a structured k

$$k = P_1 e^{-\left|\frac{T-P_2}{P_3}\right|^{P_4}} \tag{5.31}$$

where $P_1$ is the maximum value of k; $P_2$ is the nose temperature of the transformation; $P_3$ is the width of the function k and $P_4$ is a representative parameter of the activity of k function. The n function adopted, for those materials where it was necessary to introduce dependence on temperature by TTT curves, is as follows: structured:

$$n = \sum_{i=0}^{p} n_i (T - P_2)^i \tag{5.32}$$

$$p = polynomial\ regression$$

| Sigla acciaio | Fase finale | Coefficienti di $k$ | | | | Coefficienti di $n$ | | |
|---|---|---|---|---|---|---|---|---|
| | | P1 | P2 | P3 | P4 | n0 | n1 | n2 |
| U75V | Pearlite | $1.753\,E^{-3}$ | 525 | 31.22 | 1.5 | 2.635 | $-1.958\,E^{-3}$ | $-7.417\,E^{-5}$ |
| | Bainite | $5.452\,E^{-4}$ | 425 | 34.74 | 1.5 | 1.925 | $-5.751\,E^{-4}$ | - |
| U71Mn | Pearlite | 0.0115688 | 506 | 28.59 | 1.38 | 2.038 | $-2.543\,E^{-3}$ | $-2.026\,E^{-5}$ |
| | Bainite | $7.950\,E^{-4}$ | 450 | 69.82 | 2.53 | 2.212 | $7.418\,E^{-3}$ | $4.571\,E^{-5}$ |
| Φ76 | Pearlite | $4.725\,E^{-3}$ | 575 | 71.34 | 4.57 | 3.785 | - | - |
| | Bainite | $5.292\,E^{-3}$ | 575 | 73.37 | 1.97 | 3.513 | - | - |

*Table 5.5 Coefficient table of k e n in the JMAK model*

Through the two parameters previously mentioned, it is possible to calculate the TTT curves of the material in question, by means of the following reverse formula:

$$\tau_F = \left[-\frac{ln(1-F)}{k}\right]^{\frac{1}{n}} \tag{5.33}$$

through which, on the chosen temperature, it is sufficient to insert the initial and final fraction transformed F = 0.01 and F = 0.99 to obtain respectively start time and transformation time 1% and 99%. Obviously, for fractions intermediate transforms, such as 25%, 50%, 75%, etc. . . you can calculate the corresponding transformation times.

Through optimization techniques it was possible to evaluate the parameters of k and n that allowed to approximate at best the TTT curves of the individual rail materials (U75V, U71Mn, 76).

The transition from the isotope transformation model JMAK to a formulation Anisoterm has been implemented through the principle of additivity. In particular, for each small time increase dt the parameters were calculated n (T) and k (T) and on the basis of the residual austenite fraction Does the preceding instant t *the corresponding equivalent feed time* was calculated transformations at the relative temperature and for the time instant *t+dt*.

$$\tau_{eq} = \ \tau_{F_a} + dt \qquad\qquad (5.34)$$

Subsequently, the fraction of Austenite transformed into time t + dt has been calculated applying $\tau_{F_a}$ to the JMAK formula and the corresponding heat of transformation released was estimated multiplying the fraction of Austenite transformed for the total latent transformation heat of the single phase formed. Martensite's formation, although being avoided, has been molded converting residual Austenite in proportion to the temperature value reached below Martensite Start MS and terminating transformations to achieving Martensite Finish MF.

Through calorimetric tests performed these are the results for enthalpy values:

- U75V: 74 kJ/kg for Pearlite-Bainite; 81.2 kJ/kg for Martensite

- U71Mn:77.2 kJ/kg for Pearlite-Bainite; 83.35 kJ/kg for Martensite

- Φ76: as for U75V

### 5.3.2   Phase change model

Nucleation and growth processes of diffusive, as well as displaced transformations have been modeled according to the Scheil's Additivity Rule, using a fictitious time procedure. The Yu parabolic model has been adopted to handle the diffusionless austenite-martensite decomposition. The forced cooling leads to austenite decomposition into martensite, pearlite, bainite, ferrite, and iron carbide, whose formation is strongly influenced by the chemical composition of the steel and the local cooling rate.

Solid phase changes are characterized by nucleation and growth processes, the former defined by the time needed to obtain a detectable volume fraction of the product phase, the latter characterized by the progressive decomposition of the parent phase into the product phase. It is generally accepted that some phase transformations, such as the austenite decomposition into ferrite, pearlite, or bainite, and vice versa, are diffusion controlled, temperature and time dependent and are strongly influenced by the nucleation and growth mechanisms. The austenite decomposition into martensite, and vice versa, are characterized by negligible nucleation time and diffusionless growth mechanisms, resulting in being very fast and, with optimal approximation, only temperature dependent. The Isothermal Transformation (IT) diagrams, should be correctly interpreted as being composed of at least two separate and partially overlapped C curves, describing, respectively, diffusional transformations (austenite-equiaxed ferrite and austenite-pearlite on cooling) and displaced transformations (austenite_Widmanstätten ferrite and austenite_bainite on cooling), characterized, therefore, by specific nucleation and growth processes. In isothermal conditions, the amount of the product phase, formed according the diffusional or displaced phase changes, can be evaluated according to the JMAK model, as follows:

$$F_i(T) = 1.0 - \exp\left[-a(T) \cdot t\,(T)^{n(T)}\right]$$

$$(5.35)$$

where $F_i$ is the volume fraction of the product phase i, t is the time elapsed since the transformation beginning, i.e. after the nucleation process, a and n are material parameters, dependent on the isothermal temperature and the forming phase. The diffusional coefficient a and the transformation exponent n can be evaluated by the IT diagram of the considered material, taking into account the time $\tau_s$ and $\tau_f$, needed for the conversion, in isothermal conditions, of detectable start and finish volume fractions, indicated, respectively, as Fs and Ff , of the forming phase, as follows:

$$a(T) = -\ln(F_s)\tau_s(T)^{-n(T)}, \qquad n(T) = \frac{\ln(\ln(F_f) - \ln(F_s))}{\ln(\tau_s(T)) - \ln(\tau_f(T))}$$

$$(5.36)$$

where the subscripts s and f refer to the starting and finishing conditions of the phase change. In the present investigation

$F_s$ and $F_f$ have been assumed, respectively, as 0.01 and 0.99.

The temperature-time curves have been discretized into a series of isothermal steps; on each step of the microstructural model the volume fraction of product phase is calculated using isothermal kinetics and the Additivity Rule.

According to the modified JMAK model, for each time step j, corresponding to the temperature Tj, the cumulative volume fraction of

the specific i phase, indicated as Fi;j-1, transformed up to the last time step j-1; results in a fictitious time $t_{j,fict}$, which represent the time needed, at the temperature $T_j$, to obtain the same amount of cumulative transformed phase. Some manipulations of Eq. (7), allow one to evaluate the fictitious time $t_{j,fict}$, as follows:

$$t_{j,\text{fict}}\left(T_j\right) = \left[\frac{-\ln(1 - F_{i,j-1})}{a\left(T_j\right)}\right]^{\frac{1}{n(T_j)}}$$

(5.37)

As a consequence, the total permanence time $t_j$ at the temperature Tj can be written as the sum of the fictitious time $t_{j,fict}$ and the duration $t_j$ of the time step j, as follows:

$$t_j = \Delta t_j + t_{j,\text{fict}} = \Delta t_j + \left[\frac{-\ln(1 - F_{i,j-1})}{a\left(T_j\right)}\right]^{\frac{1}{n(T_j)}}$$

(5.38)

while the amount of the product phase at the end of the considered time step j, assuming the aforesaid meaning for the subscripts i and j, writes:

$$F_{i,j} = 1 - \exp\left(-a\left(T_j\right) t_j^{n(T_j)}\right)$$

(5.39)

It should also be considered, moreover, that the JMAK model, in the form described by eq. 5.39 is valid only to analyze the decomposition of the parent phase into a single product phase, which is not the general case of continuous cooling relative to the conventional quenching process. Indeed, as the local temperature decreases, different phases can nucleate and grow at specific locations of the parent phase grains, but only the new product phase formed into the untransformed parent phase should be considered. To handle this aspect, the following procedure has been applied: for each time step j of the microstructure model, the existing volume fraction $F_{i,j-1}$ of the potential forming phase i has been divided by the sum of the volume fraction $F_{p,j-1}$ of the parent phase p and the existing volume fraction $F_{i,j-1}$ is as follows:

$$F_i = \frac{F_{i,j-1}}{\left(F_{i,j-1} + F_{p,j-1}\right)}$$

(5.40)

The volume fraction $F_i$ has been adjourned according to eq. 5.39, and finally the volume fraction of the i phase $F_{i,j}$, transformed at the end of time step j is provided by:

$$F_{i,j-1} = F_i\left(F_{i,j-1} + F_{p,j-1}\right)$$

(5.41)

Scheil's Additivity Rule has also been adopted to take into account the nucleation stage. It is assumed that, for each time step j, the time _tj, spent at temperature $t_j$, divided by the incubation time at that temperature, $\tau_s(T_j)$, is a fraction of the total nucleation time required. As a

consequence, the transformation begins when the following condition is satisfied:

$$\sum_{j=1}^{n} \frac{\Delta t_j}{\tau_s\left(T_j\right)} \geq 1$$

(5.42)

$n$ being the present time step. The above procedure has been applied to consider nucleation and growth processes of diffusional and displaced transformations, in each node of the finite element model, between the temperature Ar3, which represents the starting temperature for the incubation of the austenite_pearlite transformation on cooling and the temperature martensite start, up to a complete conversion.

Austenite conversion into martensite, during the cooling stage, is a diffusionless transformation, characterized by a negligible nucleation time. As a consequence, it can be assumed that the amount of the formed martensite is not time or temperature history dependent but only temperature dependent. Several approaches have been proposed in the literature to model the diffusionless transformation, using opportune techniques to model the irreversibility of the martensite transformation, in particular, the empirical Koistinen-Marburger model has been widely used. However, it has been evidenced that the simple form of the Koistinen-Marburger model, is not capable of handling the complete austenite-martensite decomposition in the temperature range defined between the start and finish transformation temperatures.

In this paper the Yu model has been implemented to consider diffusionless transformations: the austenite-martensite phase change is described, on cooling, by a parabolic law defined between the temperatures Ms and Mf , where subscripts s and f refer to the transformation start and finish; as a consequence the total decomposition of austenite into martensite can be achieved if the final temperature is less than Mf . To model the irreversibility of the martensite transformation, it is assumed that, at the end of each microstructural time step, the total martensite fraction is equal to the maximum volume fraction evaluated at the present and the previous time steps. In this way the reduction of the transformed martensite fraction due to an eventual temperature increase, related to the phase change latent heat, has been avoided. The implemented algorithm finally writes:

$$F_{m,i} = \begin{cases} F_a \cdot \left[ 1 - \left( \dfrac{T - M_f}{M_s - M_f} \right)^2 \right] & \text{if } F_{m,i} \geq F_{m,i-1} \\ F_{m,i-1} & \text{if } F_{m,i} < F_{m,i-1} \end{cases} \qquad M_f < T < M_s$$

(5.43)

To optimize the solution routine, reducing computational time, the thermal and phase change models have been decoupled, and a different time step, for each model, has been adopted. To improve accuracy, a

relatively finer time step has been used for the microstructure model. Each thermal step is divided into several microstructure steps, assuming a linear temperature variation inside the thermal step, and for each microstructure step the mean temperature has been evaluated and used to evaluate the transformed volume fractions and phase change enthalpies, according to the above procedure. The volume fractions and phase change enthalpies, at the end of each thermal step are obtained as the sum of the contributions due to all microstructure steps. The cumulative heat generation rate due to the evaluated phase transitions is then used as additional internal heat source in the successive thermal steps.

### 5.3.3   Properties of materials

There are few methods to measure phase transformations, among them the most popular is the dilatometry, the measurement of the variation of the length of the specimens as a function of time and temperature. Steels exhibit a significant volume variation during cooling or cooling heating due to thermal expansion and phase transformations. The dilatometry is used to determine the start and end temperatures of the transformations in the steels.

The following practice is applicable to the determination of steel phase transformation behavior under isothermal conditions. This practice covers the determination of hypoeutectoid steel phase transformation behavior by using high-speed dilatometry techniques for measuring linear dimensional change as a function of time and temperature, and reporting the results as linear strain in either a numerical or graphical format. This is applicable to high-speed dilatometry equipment capable of programmable thermal profiles and with digital data storage and output capability.

This practice is used to provide steel phase transformation data required for use in numerical models for the prediction of microstructure evolutions during heat treatment.

At each instant the variation of sample length is defined as $\varepsilon = (L - L_0)/L_0$ with $L_0$ and $L$ that are the sample length at the reference temperature and temperature T. It consists of three parts: the dimensional variation of the phases due to the temperature:

$$\Delta\varepsilon_i^{\,T} = f_i(t)k_i^{\,T}(t)\Delta T$$

(5.44)

with $f_i(t)$ representing the volumetric fraction of phase i at time t and $\Delta T$ the change of temperature in a time interval, $k_i$ is the thermal expansion

coefficient of phase i; the variation dimensional due to the variation in the carbon content of the phases:

$$\Delta\varepsilon_i{}^C = f_i(t)k_i{}^C\Delta C_i$$

(5.45)

with $k_i{}^C$ which indicates the solute expansion coefficient and $\Delta C_i$ changes the content of carbon phase i in a time interval; and the dimensional variation due to the transformation phase:

$$\Delta\varepsilon_{\gamma\to i(+j)}(t) = -k^{Trans}{}_{\gamma\to i(+j)}(t)\Delta f_\gamma(t)$$

(5.46)

with $k^{Trans}$ Transformation phase coefficient of phase $\gamma \to i(+j)$

We include the interpolating formulas used in the software to evaluate the thermo-mechanical properties of steel for railways, expressed wherever necessary depending on the metallurgical phase formed.

These formulas are attached in Annex 1, the temperatures T quoted in the formulas are from Kelvin degrees. For each considered integration point of the FEM model it is possible to evaluate P the properties of the material through a *rule of mix type* $Xmix(T) = \sum_i Xi(T) \cdot Fi$, $Fi$ as phase volumetric fraction $i$ and $Xi(T)$ properties of phase I at temperature T.

### 5.3.3.1 Time Temperature Transformation (TTT) Diagram Generation

All thermal cycles employed shall be carried out under a vacuum of $1.33 \times 10^{-3}$ Pa maximum. Test specimens are to be machined from steel product stock to the dimensions and tolerances shown in following figures. Test specimens must be properly prepared and thermocouples must be properly attached to the specimens to ensure reliable and repeatable results. Care must also be taken to properly install specimens in the dilatometer apparatus.

**Solid Test Specimens**



L = 8 mm, 9 mm, or 10 mm
Tolerance = +/- 0.13 mm
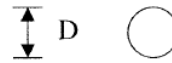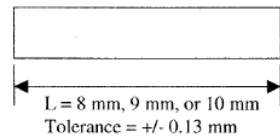
D = 3 mm, 4 mm, or 5 mm
Tolerance = +/- 0.025 mm

**Hollow Test Specimens**



L = 8 mm, 9 mm, or 10 mm
Tolerance = +/- 0.13 mm
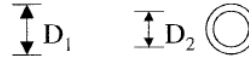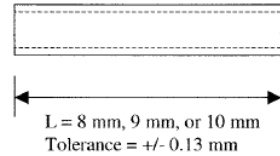
$D_1$ = 4 mm, $D_2$ = 3 mm
or
$D_1$ = 5 mm, $D_2$ = 4 mm
or
$D_1$ = 6 mm, $D_2$ = 5 mm
Tolerance = +/- 0.025 mm

NOTE—All machining surface finishes being 0.8 μm RMS

*Figure 5.13 Test specimens for induction heating apparatus*

Each isothermal transformation thermal cycle shall consist of heating a test specimen to an austeniting temperature (greater than Ac3), at a nominal rate of 10°C/s. The test specimen shall be held at the austeniting temperature for sufficient time to obtain the target Austenitic Grain Size and then quenched to the isothermal hold temperature. A cooling rate of at least 175°C/s shall be employed.

During the quench, the temperature of the test specimen must not undershoot the isothermal hold temperature by more than 20°C, and must be stabilized at the isothermal hold temperature within 2s. The temperature of the specimen must be maintained within ±5°C of the isothermal hold temperature during dimension measurement. The test specimen is to be held at the isothermal hold temperature, and dimension continuously measured until transformation is 100% complete.

The specimen must then be quenched to room temperature. Complete transformation is defined as the time at which maximum dimensional change has occurred. A separate test specimen shall be employed for each thermal cycle.

At least twelve specimens must be evaluated over a temperature range between Ac1 and room temperature to completely characterize each steel composition.

The purpose of quenching from the austeniting temperature is to avoid transformation of austenite prior to the isothermal hold temperature, and to permit measurement of the start, progress, and finish of transformation at constant temperature. It should be recognized that some steel grades might exhibit very rapid transformation kinetics at certain temperatures, and partial transformation of austenite may occur during the quench. Under these circumstances uncertainty in determining the start of

transformation may be encountered.

Thermal strain occurs during the quench from the austeniting temperature to the isothermal hold temperature. Thermal strain is determined from the change in test specimen length or diameter, which occurs between the austeniting temperature and the isothermal hold temperature. At the isothermal hold temperature, the transformation strain is determined from the change in test specimen length or diameter between the time at which transformation begins and the time at which transformation ends.

The progress of austenite transformation under isothermal conditions can be estimated from plots of strain versus time and temperature versus time. Each isothermal test results in discrete corresponding values of time, temperature, and strain. Both strain and temperature are plotted versus time for each isothermal cycle using the strain, temperature, and time data. An example of such a graph is shown in figure 5.14.
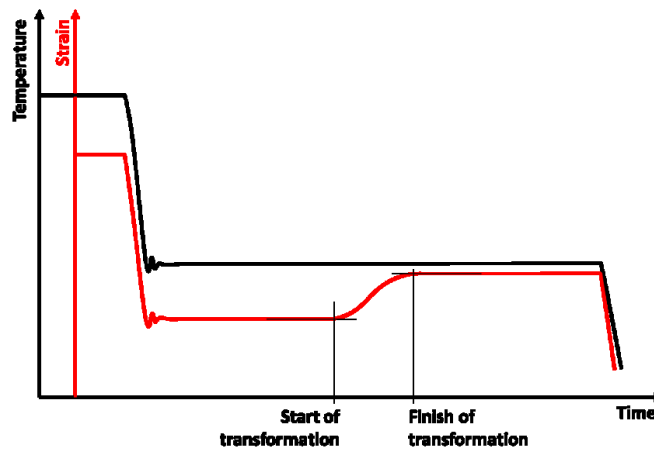


*Figure 5.14 Cycle Strain-Temperature*

A stable value of strain and temperature is exhibited during austeniting. Both temperature and strain rapidly decrease during the quench to the isothermal hold temperature. Both temperature and strain are stabilized at the isothermal hold temperature, and strain then increases while temperature remains constant as transformation proceeds. The start and finish of transformation can be estimated by drawing horizontal lines tangent to the point of minimum and maximum strain respectively.

    The microstructure of test specimens shall be documented. The ASTM Test Methods E3 "Guide for Preparation of Metallographic Specimens" and ASTM Test Methods E407 "Practice for Micro-etching Metals and Alloys" should be followed.

In addition to documenting all of the products of transformation of austenite and the amount of retained austenite in the microstructure, it may be desirable to determine the prior austenite grain size of one or

more specimens. Procedures for this determination are described in ASTM Test Methods E112 "Test Methods for Determining Average Grain Size". It may also be desirable to check the specimens for decarburization. If decarburization is detected in a specimen, a new specimen should be tested. It may be desirable to document the initial microstructure prior to performing transformation measurement procedures using a separate specimen that has not been subjected to transformation measurement procedures.

## 5.3.3.2 Prior Austenitic Grain Size (Pags) Determination

In order to maximize the useful of the TTT diagram, this should be generated considering the actual PAGS of rail before the heat treatment. In order to measure the as rolled rail PAGS the following procedure is suggested:

1. Removing rail head (at least 500 mm length)
2. Cutting a sample of 200 mm length
3. Quenching the sample in a water tank
4. Cutting a sample of 10 mm length from sample at point 2
5. Measuring of PAGS according to ASTM Test Methods E112
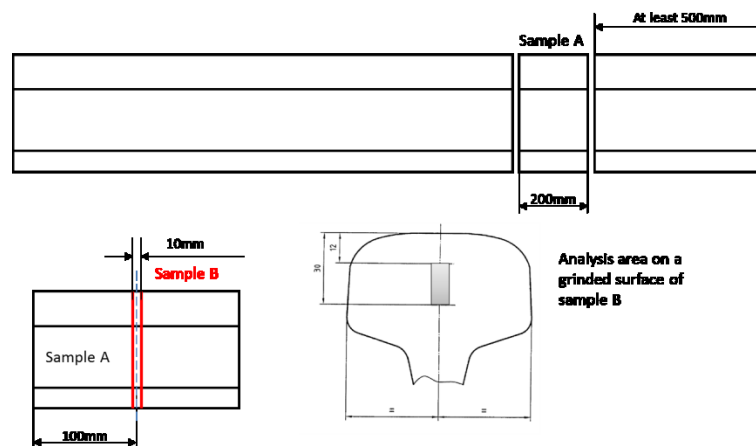


*Figure 5.15 Test method procedure*

The cutting procedure shall be carried out without generating strain or overheating in the cutting zone. Wet cutting or wire cutting have less impact on sample surface.

After the cutting the sample surface shall be grinded using wet grinding wheel. The material of grinding wheel should be selected considering the material hardness: usually aluminum oxide grinding wheel is suitable for iron-based material, silicon carbide grinding wheel is recommended for non-ferrous metal, diamond blade is necessary for hard metal or ceramic. The grinded thickness shall be at least 0.7 mm.

After grinding the sample shall be washed and dried. After the sample

surface shall to be hand gridded from coarse to fine grinding. Sandpaper used for polishing should be tiled in diamond, alumina or magnesium oxide, from coarse to fine grit sizes. Sandpaper should be changed once every sample. The sample shall be turned 90° respect the old grinding direction (perpendicular direction to direction to the old mill grinding marks). The polishing method can be mechanical polishing, electrolytic polishing, chemical polishing, polishing vibration, micro grinding. The operator, before o polishing procedure should also wash his hands to eliminate grits coming from sandpaper.

After sample polishing or during microscope grinding pits and other defects are highlighted the sample should be re-polished. The sample shall be subjected to etching following the Standard GB/T 226 "Steel macrostructure and defect etching test method" or equivalent ISO 4969.

If microstructure is not fully martensitic the sampling should be repeated considering a new sample B taken near the external surface of sample A. If the problem persists, the quenching process has to be improved reducing the dimension of sample A or improving the cooling rate.

The mean AGS measured in the rail head should be reproduced with dilatometer to identify the more adapt austenitization temperature and time.

In order to define identify this two parameter several test of austenitization at different temperature and holding time should be carried out by means of dilatometer. Each test shall consist of heating a specimen to an austeniting temperature (greater than Ac3), for instance 50°C greater then Ac3, at a nominal rate of 10°C/s. The test specimen shall be held at the austeniting temperature for different time and then quenched to room temperature. A cooling rate of at least 175°C/s shall be employed.

## 5.4 Mechanical model

Once the amount of each phase is predicted, next step is devoted to the prediction of mechanical properties achieved locally. In order to be coherent with the models most spread in industrial application and trying to develop a quite flexible tool, the idea has been to start from the models already described in literature.

Mechanical prediction clearly will have to be split in two stages:

- Stage 1: quenching phase;
- Stage 2: tempering phase;

In order to be on the state of the art, for helpful on engineering and commissioning phases has been developed a tool able to follow the evolution of mechanical properties of the treated parts through in-line thermal process along the whole procedure. It means that the possibility

to predict the mechanical properties must be guarantee in each moment of the process during the treatment.

Such an approach was not still available in literature and because of this reason, it has been necessary to exploit models available but improved through numerical approach.

The effort implies an higher computational cost but it allows to be more adherent with the real temperature's field developed during the process.

So, innovative aspects regard the relationship existing between the metallurgical model and the mechanical one. It means that if up to now, as amply described in literature, the output results obtained by metallurgical model represent the input parameters for the mechanical module, following present approach developed metallurgical and mechanical module works in parallel.

Main advantages regards the possibility to be as more precise as possible in defining the mechanical properties of each phase developed during the thermal process. It means that there won't be any approximation in description and consideration of the thermal process developed, but the real temperature field history fronted during the process is considered by both metallurgical and mechanical module.

Each stage requires the monitoring of mechanical characteristics in different ways. Hardness will be the mechanical properties followed in this section because:

- it is the mechanical property most discussed in literature analysis;
- it is the less expensive property both in terms of time and cost to be experimentally checked;
- it governs all the other mechanical properties achieved and through simply conversion it is possible to determine the other mechanical properties.

During quenching phase, the hardness has been predicted referring to the model Creusot-Loire. Recalling formulas, Vickers hardnesses (HV) versus composition and cooling rate developed by Creusot-Loire for martensite (M), bainite (B), and ferrite pearlite (FP) are:

$$HV_M = 127 + 949C + 27Si + 11Mn + 8Ni + 16Cr + 21\log_{10}\frac{dT}{dt}$$

$$HV_B = -323 + 185C + 330Si + 153Mn + 65Ni + 144Cr + 191Mo+$$
$$+ (89 + 53C - 55Si - 22Mn - 10Ni - 20Cr - 33Mo)\log_{10}\frac{dT}{dt}$$

$$HV_{FP} = 42 + 223C + 53Si + 30Mn + 13Ni + 7Cr + 19Mo+$$
$$+ (10 - 19Si + 4Ni + 8Cr + 130V)\log_{10}\frac{dT}{dt}$$
(5.47)

It is interesting to focus on the fact that these models depend just on

chemical composition of the material treated and on the cooling rate fronted during the process.

These models have been developed in order to be applied in case of constant cooling rate but in order to satisfy the requirements of present thesis, it has been necessary to improve the approach and to split the real temperature field and apply these models step by step.

In this way, through numerical approximation, the code developed is able to take into account any oscillations in cooling rate verified during the process. So, the model is not going to consider approximated thermal treatment in which cooling rate is considered as constant during the whole process but it is going to take into account the real temperature's history.

The model won't be able to define simply three values of hardness for martensite, bainite and ferrite- pearlite as Creusot-Loire did, but it will gives in output a different value for each phase developed at each time step: it means that in this approach, defining a martensite's hardness value" will be no sensed due to the fact that each fractions of martensite developed in case on no constant cooling rate will be different from the others.

Such approach has been expressly required in order to allow local prediction and not to foresee averaged values on the whole part. Once the hardness related to each microstructural constituent is achieved, combining with the fractions obtained by metallurgical module, exploiting the "Rule of mixtures", hardness value is computed as:

$$HV_{mix} = \sum_1^i HV_i \cdot X_i$$

(5.48)

where the total hardness is evaluated weighting on the fractions and hardnesses of each phase.

During tempering phase instead, in order to be adherent with the real thermal cycle the evaluation of equivalent time and temperature of tempering is achieved. Recalling the formulas, the equivalent time can be obtained as:

$$t_e = exp(-\frac{A_T T_{max}}{A_t})(\int_0^t exp(\frac{A_T T}{A_t}))$$

(5.49)

For the equivalent temperature instead:

$$T_e = \frac{A_t}{A_T} ln(\frac{t_e}{t_{tot}}) + T_{max}$$

(5.50)

### 5.4.1 Calculation of Inflection:

Given two thermal rail maps evaluated in two stages of redundancy successive and not excessively distant (hereinafter referred to as numbers 1 and 2), after calculating the volumetric fraction of *Fi* formed phases and having applied the rule of mixture to calculate, RP$_{02}$ and E, it's developed a calculation of tension equilibrium as described below.

There have been defined the global magnitudes of deformation of the rail, indicating the longitudinal dilation/contraction and rotation of the section (considered flat during the essence) consisting of the elongation ratio $\frac{L_2}{L_1}$ in curves $x_1$ and $x_2$ and in curvature angles $\alpha_1$ and $\alpha_2$; the latter indicate the anti-clockwise rotation of the axis of rotation with respect to the horizontal axis passing through the center of gravity $(x_G; y_G)$.

There were then defined points of magnitude for each point of integration, consisting of true plastic deformation $\delta_{P_1}$ and elastic tension $\sigma$. The initial state of these variables, $\delta_{P_1}$ and $\sigma_1$, is known at the beginning of the calculation and it is assumed that at the exit of the finishing stand of mill train (where the temperature has been considered uniform throughout the section) elastic tension and plastic deformation they are both nil or negligible.

Indeed, it starts by imposing the equality of global variables and ratio $\frac{L_2}{L_1} = 1$. For each points of integration (x, y):

- It's calculated the *total real strain* by

$$\delta = \ln\left[\frac{L_2}{L_1}\frac{|1 - \chi_2[(y_2 - y_G)\cos(\alpha_2) - (x_2 - x_G)\sin(\alpha_2)]|}{|1 - \chi_1[(y_1 - y_G)\cos(\alpha_1) - (x_1 - x_G)\sin(\alpha_1)]|}\right]$$

- It's evaluated the *thermal expansion* $\delta_T = \ln\left[\left(\frac{\rho_1}{\rho_2}\right)^{1/3}\right]$

- And for difference the *effective elasto-plastic strain* $\delta_{ep} = \delta - \delta_T$

- So the *potential increasing plastic strain* is

$$\delta_{P_{inc}} = \delta_{ep} + \ln\left(1 + \frac{\sigma_1}{E_1}\right) - sign(\delta_{ep})\ln\left(1 + \frac{RP_{02,2}}{E_2}\right)$$

- That permit to evaluate the *real total plastic strain* as

$$\delta_{P2} = \begin{cases} \delta_{P1} + \delta_{P_{inc}} & \text{se } \delta_{ep} \cdot \delta_{P_{inc}} > 0 \\ \delta_{P1} & \text{altrimenti} \end{cases}$$

- And the *total elastic stress* as

$$\sigma_2| = \begin{cases} RP_{02,2} & \text{se } \delta_{ep} > 0 \text{ e } \delta_{P_{inc}} > 0 \\ -RP_{02,2} & \text{se } \delta_{ep} < 0 \text{ e } \delta_{P_{inc}} < 0 \\ E_2\left(\frac{\sigma_1}{E_1} + \delta_{ep}\right) & \text{altrimenti} \end{cases}$$

At this point it is possible to integrate numerically on the entire section of the rail the elastic tension $\sigma_2$ and its results for the distance from the axis of rotation, obtaining:

- Total load on section F

- Total bending moment *Mxx* around rotation axis inclined $\alpha$

- Total bending moment *Myy* perpendicular rotation axis

Using a suitable iterative method, you can then get the value of global deformation variables that satisfy the equilibrium of forces and moments on the section. In particular:

- F = 0, *Mxx* = 0 e *Myy* = 0 for the equilibrium point on the head rail
- F = 0, *Mxx* ≠ 0 e *Myy* ≠ 0 for the equilibrium point on whatsoever rail, applicando per esempio un momento pari a quello dovuto al peso proprio di uno spezzone.

### 5.4.2 Mathematical calculation of grain size evolution

When calculating the active thermo-mechanical parameters during rolling, the problem remains to calculate the average size of austenitic grain and its evolution throughout the process.
A careful analysis was also carried out in this field by following step by step the evolution of the size of austenitic grain during the rolling of a normal carbon steel. This was achieved by developing equations related to grain size and hot working parameters in an electronic spreadsheet. Considering the substantial effort developed during rolling, the analyzes reveal that meta dynamic recrystallization (MRX) is the dominant microstructure process, and this is also confirmed by the grain size.
The spreadsheet was also used to examine the effects of the practical modifications to rolling to sharpen the austenitic grain. Small benefits are obtained by increasing the deformation, increasing the cooling rate by forced air or lowering the temperature during rolling, i.e. high Z parameter values (Zener-Hollomon). Various strategies for this are still being discussed.
During the first rolling phases the deformations per pass are usually very

high, and easy to carry dynamic recrystallization. In the case of the finishing past, even if the nominal deformations are below the critical value to initiate dynamic recrystallization (DRX), the times are too short to start static recrystallization (SRX). As a result, deformations accumulate past after passing until they reach a critical value to initiate dynamic recrystallization. At the end of the past that involves dynamic recrystallization, recrystallization is no longer dynamic but meta-dynamic. Earlier studies indicate that meta dynamic recrystallization can result in fine austenitic grains with high Z values, high strain rate, and low temperature values. In a sense, the real importance of dynamic recrystallization is that it throws the foundation for that dynamic goal.

When past times are too short for significant amounts of static recrystallization, the rolling practice that exploits this potential grain refining takes the term of meta dynamic control of rolling. When interlaced times are short also for dynamic meta-recrystallization, rolling practice can be defined as dynamic recrystallization (this is the case for flat rolling).

The meta dynamic recrystallization in the rolling process can be introduced considering very short passage times due to the absence of carbonitrile.

In the past, the physical simulation of the material with torsion tests in the laboratory proved to be very useful in the design of the rolling mills, however high velocities of actual strain cannot easily be achieved by experimental lab tests. As a result, it is difficult to carry out physical simulations and provide information on the granulometry of the finishing fins where the speeds also exceed 100 1/s. To some extent, this can be overcome by making computer simulations of the material using the grain size equations for hot rolling. In the present case, an approach based on which evolution of the austenitic granulometry is outlined during the rolling phase is modeled by incorporating the related equations into a commonly used electronic spreadsheet. The model is then used to examine the effects of the various possible recurrent modifications during the rolling phase. The general purpose of these calculations is to explore the potential of refining the austenitic grain size by means of controlled meta dynamic.

### 5.4.3  Equation for austenitic grain size variations

Over the years several research groups have developed equations related to the evolution of austenitic granulometry to hot rolling parameters. A recent review is provided by Hodgson and Gibbs. Their equations have been inserted into an electronic spreadsheet (e.g. Microsoft Excel).

In the first step of the procedure, the critical deformation leading to the initiation of dynamic recrystallization is calculated as the softening mechanism of the material after each passage, which is conventional or

meta dynamic static recrystallization, depends on whether the deformation of the past is greater or less than this value; it is calculated from the initial grain size, the deformation rate and the absolute temperature T.

$$\varepsilon_c = 5,6*10^{-4} d_0^{0,3} Z^{0,17} \qquad (8) \qquad (5.51)$$

Where $Z = \dot{\varepsilon} \exp(\frac{300000}{8.13T})$ is the parameter of Zener Hollomon. This clear demarcation between static and meta dynamic resurfacing at the value of $\varepsilon_c$ is probably an excessive simplification as it implies that a small fraction dynamically recrystallized during deformation is sufficient to recrystallize the entire structure in a meta dynamic manner. However, this seems to be supported by several studies showing that the recrystallization kinetics is practically independent when passed $\varepsilon_c$ and perhaps even slightly higher deformations. The recrystallized fraction after one pass can be calculated through the Avrami law:

$$X = 1 - \exp\left[ -0,693 \left( \frac{t}{t_{0,5}} \right)^q \right] \qquad (9) \qquad (5.52)$$

where the exponent q and the time $t_{0.5}$ depend on the dampening due to static or meta dynamic recrystallization:

if $\varepsilon < \varepsilon_c$ (when there is static recrystallization) then:

$$t_{0,5} = 2.3 \times 10^{-15} \varepsilon^{-2.5} d_0^{2} \exp\left( \frac{230000}{8.13T} \right) \qquad (10)\ (5.53)$$

if $\varepsilon > \varepsilon_c$ (when there is meta dynamic recrystallization) then:

$$t_{0.5} = 1.1 Z^{-0.8} \exp\left( \frac{230000}{8.13T} \right) \qquad (11)\ (5.54)$$

where q = 1 for static recrystallization and q = 1.5 for meta dynamic recrystallization.
These equations were developed using the data of the sweetened fraction. However, it follows that it is assumed to be an exact value for describing the recrystallization kinetics. This only leads to small mistakes for the analysis, especially as the main objective of full recrystallization that coincides with complete softening.
If the softening is given by static recrystallization and there is enough time for complete recrystallization, the grain size is given by

$$d_{SRX} = 343\varepsilon^{-0.5}d_0^{0.4}\exp\left(\frac{-45000}{8.31T}\right) \qquad (12) \qquad (5.55)$$

Likewise, the grain size after full meta dynamic recrystallization is given by:

$$d_{MRX} = 2.6\times10^4 \cdot Z^{-0.23} \qquad (13) \qquad (5.56)$$

It is worth noting that equations for $t_{0.5}$ and d have been developed to originally describe behavior under isothermal conditions while the temperature during hot rolling is constantly changing. This can be taken into account using the compensation temperature. However, in this discussion the inter-pass times can be judged sufficiently brief for values of $t_{0.5}$ and d to be calculated at a single temperature, corresponding to the average of previous and subsequent passes.

   For rolling of bars and rods in steel, the inter-pass time is usually much higher than that required for complete meta dynamic recrystallization and therefore the wheat increase follows the recrystallization. Wheat ingrowth also occurs when there is complete static recrystallization. Basically, wheat grain is differentiated if the inter-pass time is greater than one second then the equations in which the grain size term is elevated to seventh power.

- SRX:

$$d^7 = d_{SRX}{}^7 + 1.5\times10^{27}\left(t_{ip} - 4.32t_{0.5}\right)\exp\left(\frac{-400000}{8.31T}\right) \qquad (14)\,(5.57)$$

- MRX

$$d^7 = d_{MRX}^7 + 8.2\times10^{25}\left(t_{ip} - 2.65t_{0.5}\right)\exp\left(\frac{-400000}{8.31T}\right) \qquad (15)\ (5.58)$$

but this formulation leads to an unrealistically rapid increase in short time. To work around this problem second-order equations are used for less than a second

- SRX:

$$d^2 = d_{SRX}^2 + 4.0\times10^7\left(t_{ip} - 4.32t_{0.5}\right)\exp\left(\frac{-113000}{8.31T}\right) \qquad (16)\,(5.59)$$

- MRX:

$$d^2 = d_{MRX}^2 + 1.2\times10^7\left(t_{ip} - 2.65t_{0.5}\right)\exp\left(\frac{-113000}{8.31T}\right) \qquad (17)\,(5.60)$$

where the constants are selected in such a way that the curves of the

second and seventh order intersect at the value of 1s (see Figure 5.16). The grain size after recrystallization is $d_0$ then entering the next stage. A further consideration is to be taken, if interlaced time is less than the total recrystallization time (the factors in parentheses round the equations 5.59-5.60) then no longer apply equations 5.59 and 5.60, and the diameter after time is considered equal to that of recrystallized without growth phenomena.
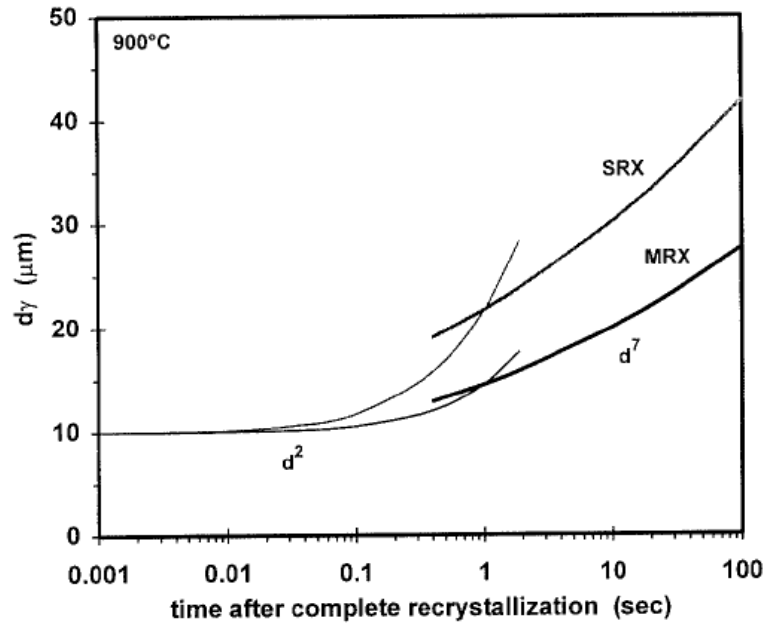


*Figure 5.16 Coalescence austenitic grain size*

If there is only partial recrystallization during the rolling past, the average grain size at the input of the next step can be calculated by a proportionality law that takes into account the proportion of sweetened grains rather than the previous steps:

$$d_{0i+1} = X_i^{4/3} \cdot d_{RX_i} + \left(1 - X_i\right)^2 \cdot d_{0i} \qquad (18) \qquad (5.61)$$

Here $d_{RX}$ is determined by both equations 5.46 and 5.47. Note that if the value of X is small, there are few negligible changes in the average grain size before the next stage. Partial recrystallization also means that part of the deformation is maintained at the next stage, then it is referred to accumulated deformation $\varepsilon_{ai}$ and is calculated according to the relation:

$$\varepsilon_{ai+1} = \varepsilon_{i+1} + \left(1 - x_i\right)\varepsilon_i \qquad (19) \qquad (5.62)$$

This is the strain value that is compared to that in equation 5.42 to determine whether dynamic recrystallization (followed by dynamic meta) has started during that step.

### 5.4.4   Application on rail rolling

Based on the equations already outlined and the spreadsheet on the next page, the 20 pass rolling mill for the rolling of a 360x300 mm bloom in a P65 rail bar was Excel file in order to calculate the average grain size for each rolling pass and especially at the exit of the finishing stand.

For each rolling pass, the relative strain values, strain rates, temperatures and processed by the spreadsheet were obtained, incorporating all equations related to the austenitic grain evolution. The various steps in the spreadsheet are shown in Table 5.5.

| Step | T def. [°C] | v def. [s-1] | t iterg. [s] | ε | dγ | εa | εc | εa > εc | td | X |
|------|-------------|--------------|--------------|-------|-------|-------|-------|---------|-------|------|
| 0 | | | | | 101.4 | | | | | |
| 1 | 1175 | 0.62 | 13.30 | 0.364 | 61.9 | 0.364 | 0.196 | Y | 0.587 | 1.00 |
| 2 | 1156 | 0.7021 | 10.80 | 0.344 | 55.2 | 0.344 | 0.184 | Y | 0.49 | 1.00 |
| 3 | 1142 | 1.6584 | 7.30 | 0.612 | 43.4 | 0.612 | 0.216 | Y | 0.369 | 1.00 |
| 4 | 1139 | 2.376 | 5.10 | 0.695 | 39.7 | 0.695 | 0.216 | Y | 0.293 | 1.00 |
| 5 | 1133 | 4.7621 | 3.50 | 0.742 | 34.4 | 0.742 | 0.242 | Y | 0.156 | 1.00 |
| 6 | 1115 | 5.6422 | 8.80 | 0.69 | 36.4 | 0.69 | 0.237 | Y | 0.122 | 1.00 |
| 7 | 1102 | 10.986 | 2.00 | 0.791 | 29.1 | 0.791 | 0.283 | Y | 0.072 | 1.00 |
| 8 | 1091 | 12.858 | 1.50 | 0.742 | 28.8 | 0.742 | 0.263 | Y | 0.058 | 1.00 |
| 9 | 1084 | 27.381 | 1.00 | 0.803 | 27.2 | 0.803 | 0.295 | Y | 0.029 | 1.00 |
| 10 | 1047 | 31.508 | 1.30 | 0.76 | 29.1 | 0.76 | 0.283 | Y | 0.024 | 1.00 |
| 11 | 1040 | 55.174 | 1.00 | 0.773 | 28.7 | 0.773 | 0.315 | Y | 0.014 | 1.00 |
| 12 | 998 | 179.62 | 0.30 | 0.69 | 20.8 | 0.69 | 0.312 | Y | 0.004 | 1.00 |
| 13 | 985 | 217.22 | 0.30 | 0.584 | 20.8 | 0.584 | 0.319 | Y | 0.003 | 1.00 |
| 14 | 970 | 225.96 | 2.60 | 0.592 | 25.7 | 0.592 | 0.316 | Y | 0.003 | 1.00 |
| 15 | 950 | 396.78 | 0.05 | 0.582 | 15.3 | 0.582 | 0.767 | N | 0.001 | 0.34 |
| 16 | 930 | 456.62 | 2.20 | 0.574 | 19.7 | 0.96 | 0.616 | Y | 0.001 | 1.00 |
| 17 | 910 | 512.34 | 0.05 | 0.479 | 18.2 | 0.479 | 1.206 | N | 9E-04 | 0.04 |
| 18 | 870 | 582.34 | 0.05 | 0.519 | 15.5 | 0.977 | 1.117 | N | 9E-04 | 0.09 |
| 19 | 840 | 598.88 | 0.05 | 0.319 | 14.5 | 0.794 | 1.006 | N | 5E-04 | 0.04 |
| 20 | 820 | 590.04 | 0.05 | 0.288 | 13.6 | 0.595 | 1.013 | N | 5E-04 | 0.03 |

*Table 5.5 Rolling process parameters*

From the model file, we calculated the CCT curves for the final diameter 13.6 μm diameters. The results of the simulation with the model are shown in Figure 5.18, in both cases there is no intersection between the cooling curves and the transformation curves, so we can state that even on the surface the steel has an austenitic structure at the exit stand.
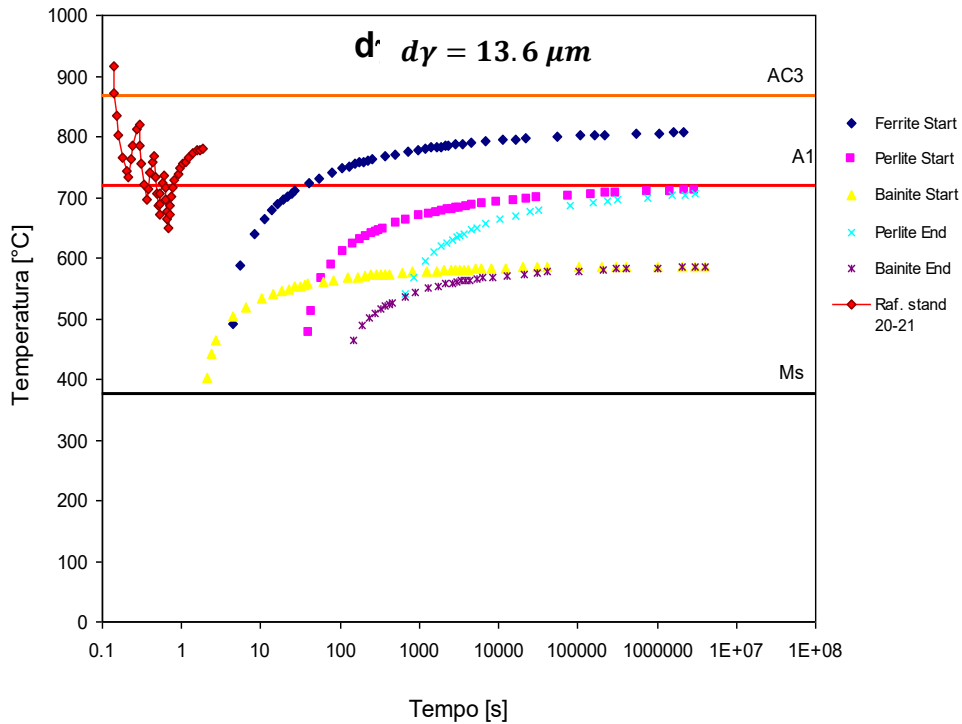
*Figure 5.17 Thermal diagram in CCT for rolled grain size*

However, wanting to estimate the average magnitude of the grains at the heart and the surface and their effect on the final diameter of the stages considered, the results of the model are summarized in tables 5.6, 5.7 and 5.8 on the variation in average grain (mean temperature) and surface respectively:

*Table 5.6, Average grain size diameter on medium temperature is 13.6 μm*

| Step | T def. [°C] | v def. [s-1] | t iterg. [s] | ε | dγ | εa | εc | εa > εc | td | X |
|------|------|------|------|------|------|------|------|------|------|------|
| 18 | 1090 | 225.96 | 2.60 | 0.592 | **25.65** | 0.592 | 0.316 | Y | 0.003 | 1.00 |
| 19 | 900 | 396.78 | 0.05 | 0.582 | **15.28** | 0.582 | 0.767 | N | 0.001 | 0.34 |
| 20 | 920 | 456.62 | 2.20 | 0.574 | **19.73** | 0.96 | 0.616 | Y | 0.001 | 1.00 |
| 21 | 800 | 512.34 | 0.05 | 0.479 | **18.19** | 0.479 | 1.206 | N | 9E-04 | 0.04 |
| 22 | 814 | 582.34 | 0.05 | 0.519 | **15.51** | 0.977 | 1.117 | N | 9E-04 | 0.09 |
| 23 | 826 | 598.88 | 0.05 | 0.319 | **14.46** | 0.794 | 1.006 | N | 5E-04 | 0.04 |
| 24 | 820 | 590.04 | 0.05 | 0.288 | **13.64** | 0.595 | 1.013 | N | 5E-04 | 0.03 |

Table 5.7, Average grain size diameter on core temperature is 15.5 μm.

| Step | T def. [°C] | v def. [s-1] | t iterg. [s] | ε | dγ | εa | εc | εa > εc | td | X |
|------|------|------|------|------|------|------|------|------|------|------|
| 18 | 1090 | 225.96 | 2.60 | 0.592 | **27.81** | 0.592 | 0.316 | Y | 0.003 | 1.00 |
| 19 | 940 | 396.78 | 0.05 | 0.582 | **15.56** | 0.582 | 0.661 | N | 0.001 | 0.40 |
| 20 | 920 | 456.62 | 2.20 | 0.574 | **21.92** | 0.922 | 0.619 | Y | 0.001 | 1.00 |
| 21 | 840 | 512.34 | 0.05 | 0.479 | **19.77** | 0.479 | 1.014 | N | 9E-04 | 0.06 |
| 22 | 814 | 582.34 | 0.05 | 0.519 | **17.24** | 0.971 | 1.146 | N | 9E-04 | 0.07 |
| 23 | 826 | 598.88 | 0.05 | 0.319 | **16.27** | 0.801 | 1.039 | N | 5E-04 | 0.03 |
| 24 | 820 | 590.04 | 0.05 | 0.288 | **15.53** | 0.598 | 1.05 | N | 5E-04 | 0.03 |

Table 5.8, Average grain size diameter on surface temperature is 12.6 μm

| Step | T def. [°C] | v def. [s-1] | t iterg. [s] | ε | dγ | εa | εc | εa > εc | td | X |
|------|------|------|------|------|------|------|------|------|------|------|
| 18 | 1090 | 225.96 | 2.60 | 0.592 | **24.64** | 0.592 | 0.316 | Y | 0.003 | 1.00 |
| 19 | 880 | 396.78 | 0.05 | 0.582 | **15.20** | 0.582 | 0.83 | N | 0.001 | 0.30 |
| 20 | 920 | 456.62 | 2.20 | 0.574 | **18.70** | 0.978 | 0.615 | Y | 0.001 | 1.00 |
| 21 | 780 | 512.34 | 0.05 | 0.479 | **17.40** | 0.479 | 1.323 | N | 9E-04 | 0.04 |
| 22 | 814 | 582.34 | 0.05 | 0.519 | **14.64** | 0.979 | 1.103 | N | 9E-04 | 0.09 |
| 23 | 826 | 598.88 | 0.05 | 0.319 | **13.54** | 0.79 | 0.989 | N | 5E-04 | 0.04 |
| 24 | 820 | 590.04 | 0.05 | 0.288 | **12.68** | 0.594 | 0.994 | N | 5E-04 | 0.04 |

An interesting point to note is that meta dynamic recrystallization depends only on deformation velocity and temperature (Equation 5.47), the grain size at the end of the past is independent of the grain size at the beginning. The spreadsheet suggests that past deformation is not sufficient to initiate dynamic recrystallization, presumably because a 190°C lower temperature and higher deformation velocities make it more difficult to reach critical deformation required. The calculation model gave a final average austenitic diameter of 13.6 μm at the exit of the mill.

## 5.4.5   Final considerations on the model

Figure 5.18 shows schematically the path followed to obtain the final quantities of the laminated product. In summary, the illustrated rolling

model predicts the punctual diameter of austenitic grain at the end of the preheating stage, allowing it to study all its evolution during the process of its recrystallized fraction, the type of recrystallization and to find its final value.
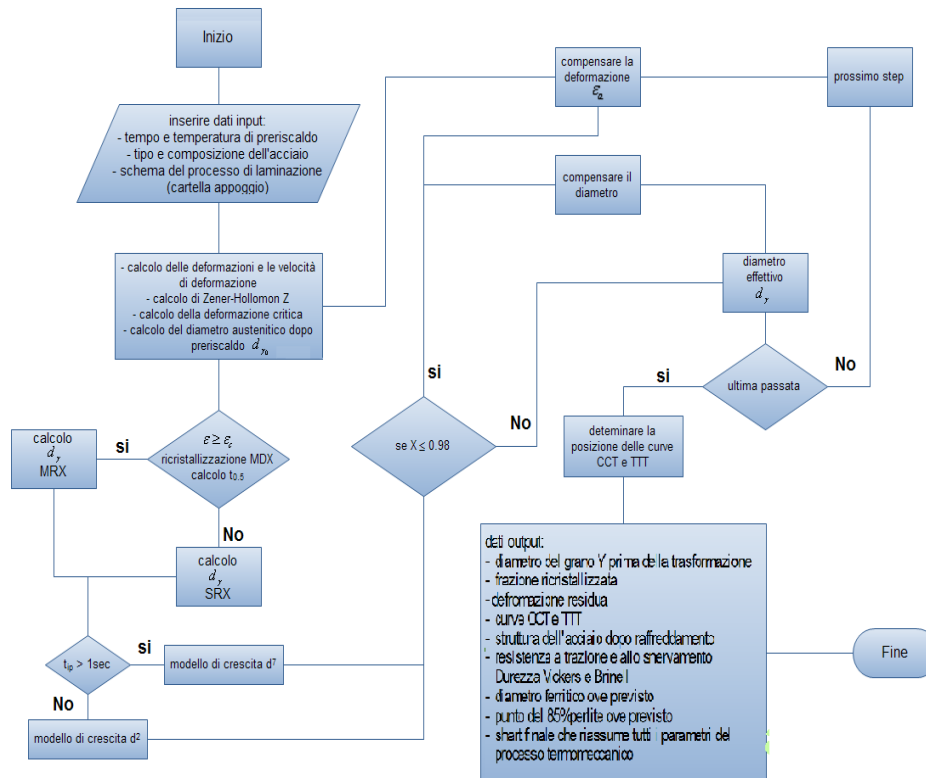


*Figure 5.18 Model algorithm scheme*

All of this model is also been tested by a series of FEM simulation in order to optimize the calculation efficiency through the following steps:

- Thermal analysis during rolling
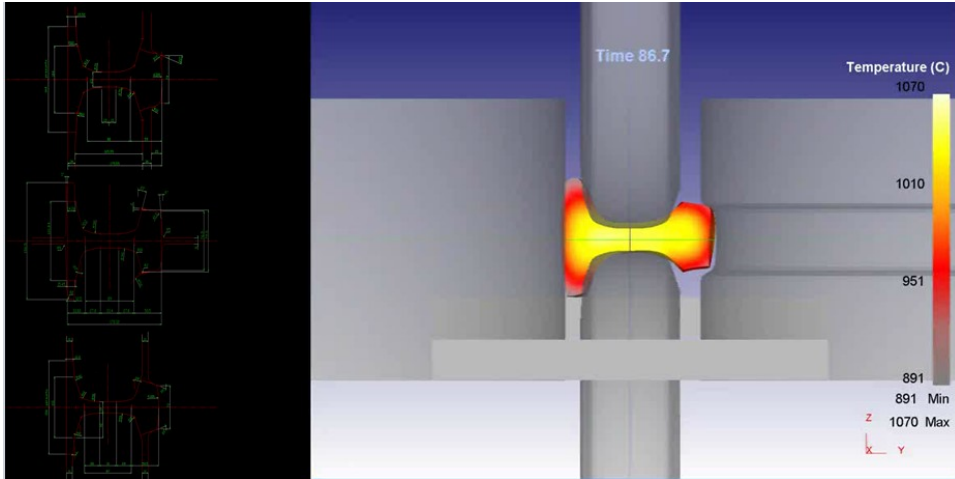
*Figure 5.19 Thermal FEM simulation*

- Stress analysis during rolling
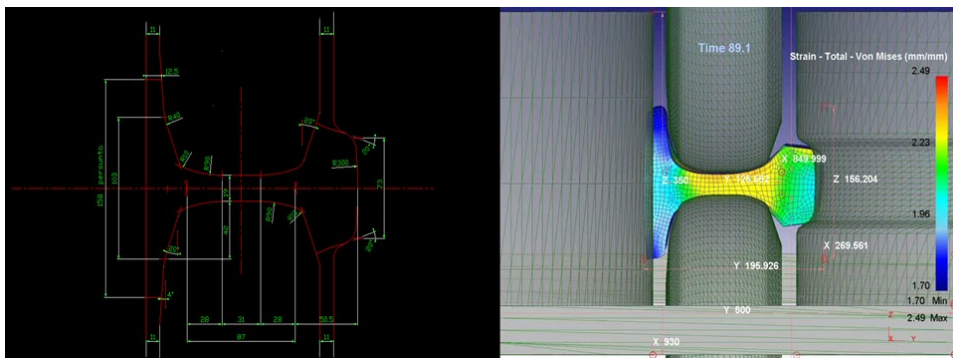


*Figure 5.20 Stress FEM simulation*

- Strain analysis during rolling
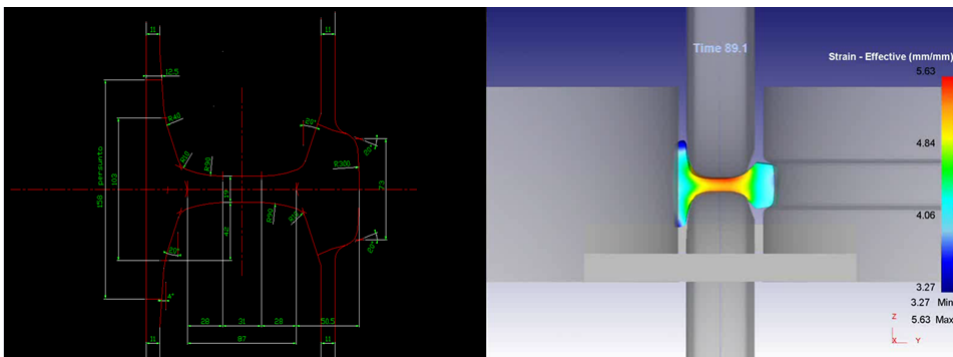


*Figure 5.21 Strain FEM simulation*

- Strain rate analysis during rolling
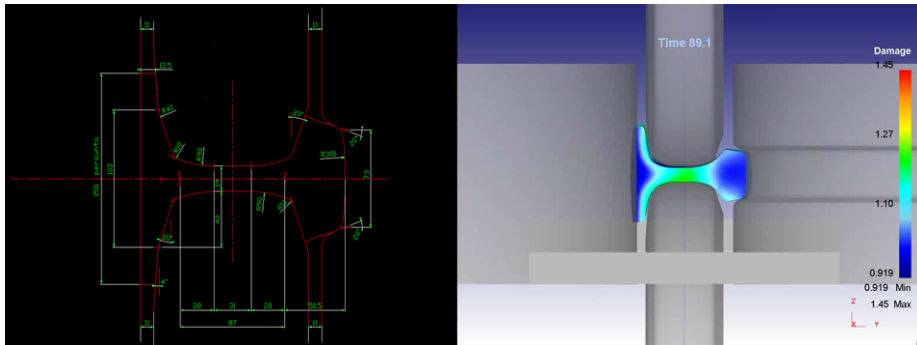


*Figure 5.22 Strain rate FEM simulation*

- Metallurgical analysis during rolling
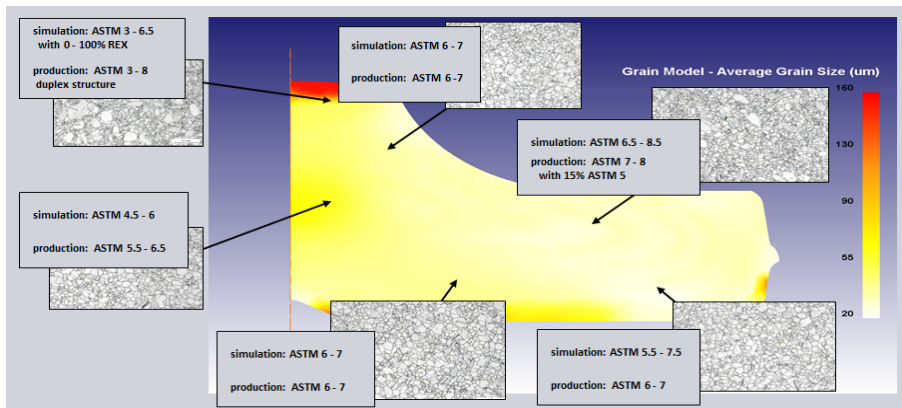


*Figure 5.23 Metallurgical FEM simulation*

- Microstructure analysis during rolling
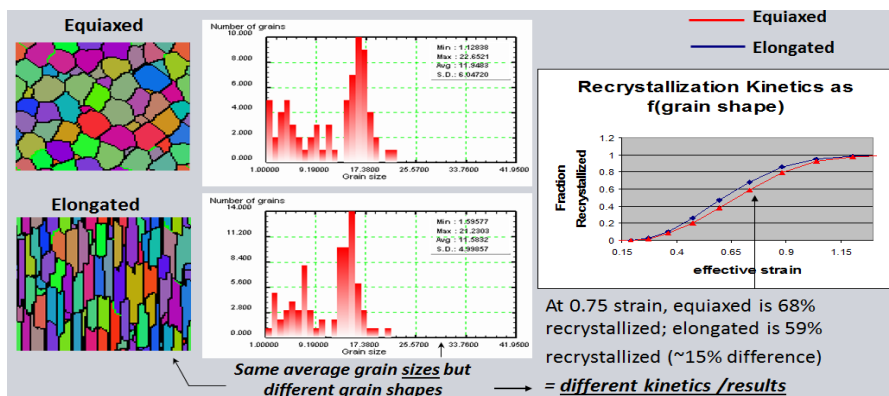


*Figure 5.24 Microstructure FEM simulation*

- Cooling simulation on cooling bed:
  - After 100s is possible to analyze:
    - Greater decrease in temperature on the foot than the head → bigger contraction of the foot in comparison with the head → positive camber
    - Greater decrease in temperature on the foot tip than the foot core → generation of tensile stress on the foot tip and compressive stress on the foot core
    - No transformation occurred
    - Positive camber
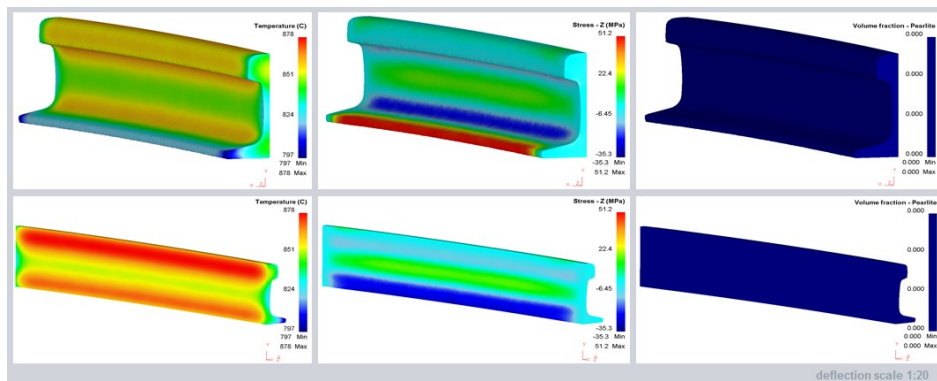


*Figure 5.25 Mechanical and metallurgical FEM simulation after rolling (100s)*

  - After 450s is possible to analyze:
    - Pearlitic transformation on the foot tip → expansion of the foot tip due to the transformation → change in deformation direction
    - Expansion of the foot tip in comparison to the foot core → generation of compression stress on the foot tip and tensile stress on the foot core
    - Positive camber
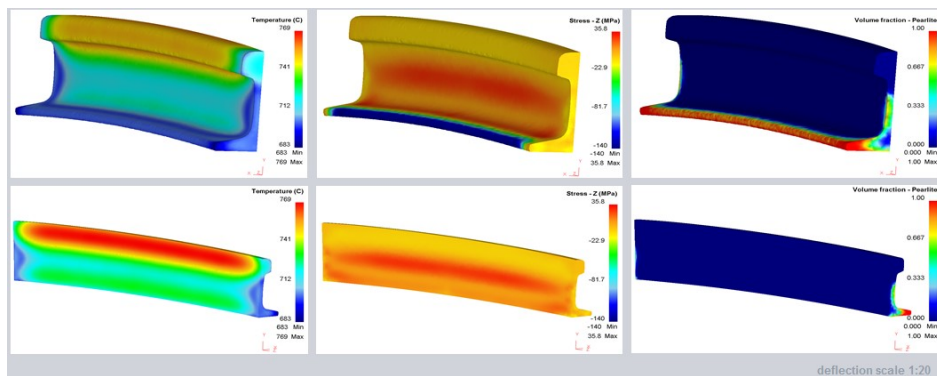


*Figure 5.26 Mechanical and metallurgical FEM simulation after rolling (450s)*

o After 600s is possible to analyze:
- Increase of the pearlitic transformation in the foot → expansion of the foot due to the transformation
- Expansion of the foot → change of the camber
- Negative camber
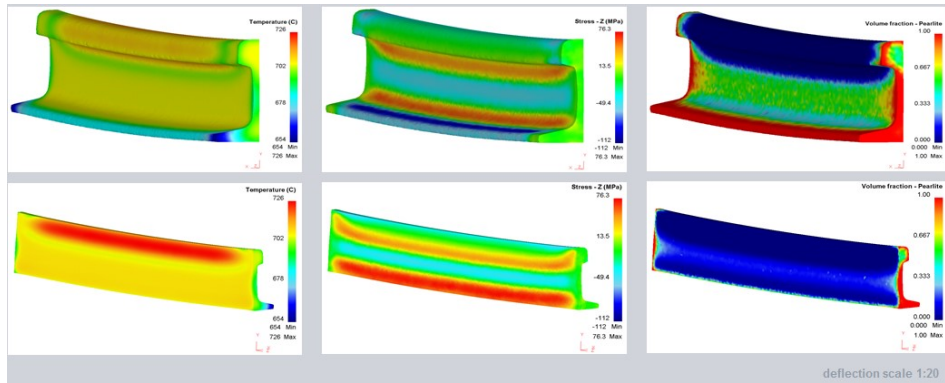


*Figure 5.27 Mechanical and metallurgical FEM simulation after rolling (600s)*

o After 1000s is possible to analyze:
- Start of the pearlitic transformation in the head → expansion of the head due to the transformation
- Expansion of the head → change of the camber
- Positive camber
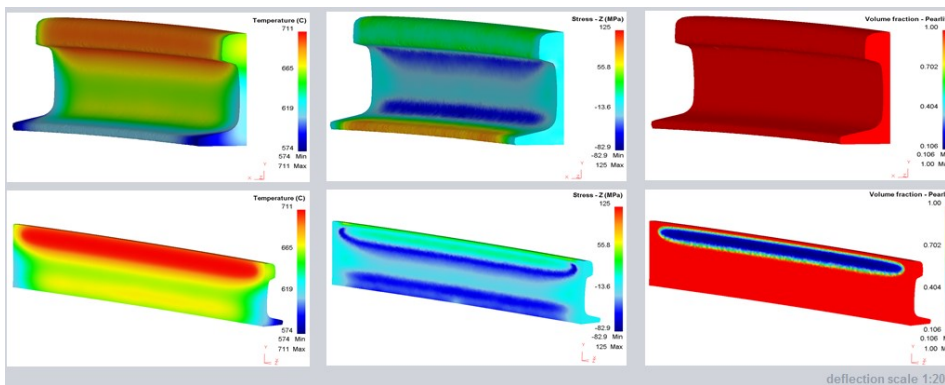


*Figure 5.28 Mechanical and metallurgical FEM simulation after rolling (1000s)*

o After 2000s is possible to analyze:
- Increase of the pearlitic transformation in the head → expansion of the head due to the transformation
- Expansion of the head → increase of the positive camber
- Transformation concluded
- Positive camber
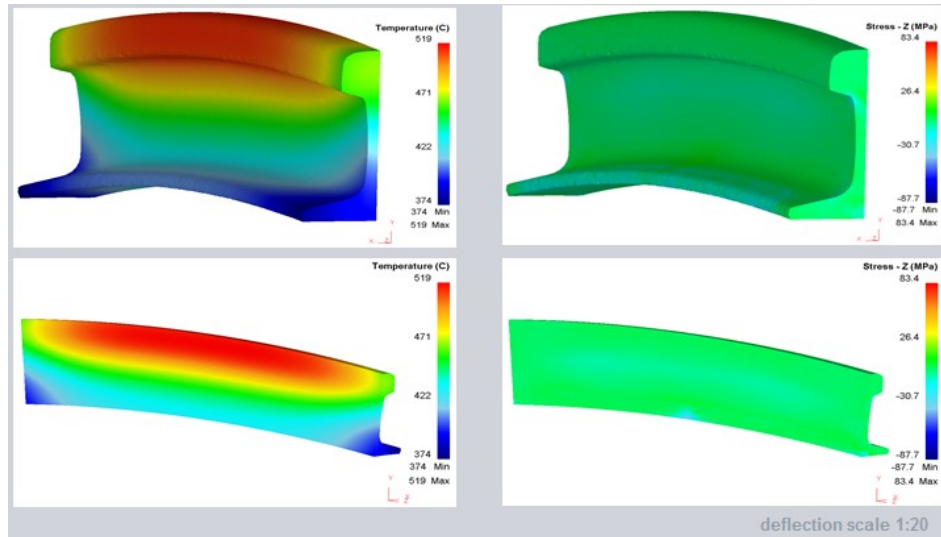
*Figure 5.29 Mechanical and metallurgical FEM simulation after rolling (2000s)*

- o After 7000s, at the exit of cooling bed, is possible to analyze:
  - Increase of the pearlitic transformation in the head → expansion of the head due to the transformation
  - Expansion of the head → increase of the positive camber
  - Transformation concluded
  - Positive camber
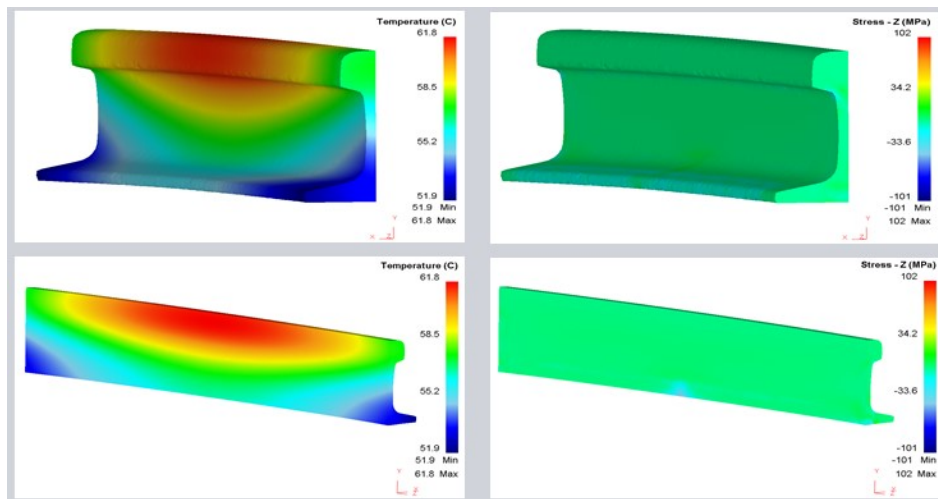


*Figure 5.28 Mechanical and metallurgical FEM simulation after rolling (7000s)*

## 5.5    ProMod Software control

ProMod is the Siemens software dedicated to the rail hardening treatment. It has been thought and developed for air mist and air blades cooling systems. Due to its modular concept, it is flexible enough to be suited to any kind of plant configurations.

Any number of sectors, modules per sector, module types and nozzles collectors can be selected: this can be useful in case of plant configuration changes (e.g. substitution of mist modules with air one or vice versa).

The main scope of the software is the calculation of the optimal air and water pressure settings required in order to achieve a very fine pearlite microstructure on the head of the rail and at the same time to control the rail bending deformation. This calculation will be done online as function of rail geometry, steel grade, process speed and inlet rail temperature.

The system will compare continuously the temperature at the pyrometers with the calculated one and in case of out of tolerance will correct pressures accordingly. These temperature differences can be due to changes in the nozzles behavior consequent to wear or clogging.

The core of the system is a finite element simulator able to give accurate temperatures evaluations and fast enough to be used as an on-line calculation system.

### 5.4.6    Input data

In this section it is explained the main input data required by software in order to calculate pressure settings.

### 5.4.6.1 Rail mesh and control points

An optimized mash will be associated to each rail geometry. Starting from these sparse points (blue in figure) the software will generate the corresponding quadrilateral elements and will calculate the reciprocal connectivity. Section properties such as total area and moments of inertia will be calculated and stored.

Some control points will be positioned on the surface and inside volume of the rail (red rhombus in figure 5.29). These points will be used in order to follow the rail cooling history subject to a certain pressure setting and pressure corrections will be evaluated accordingly.
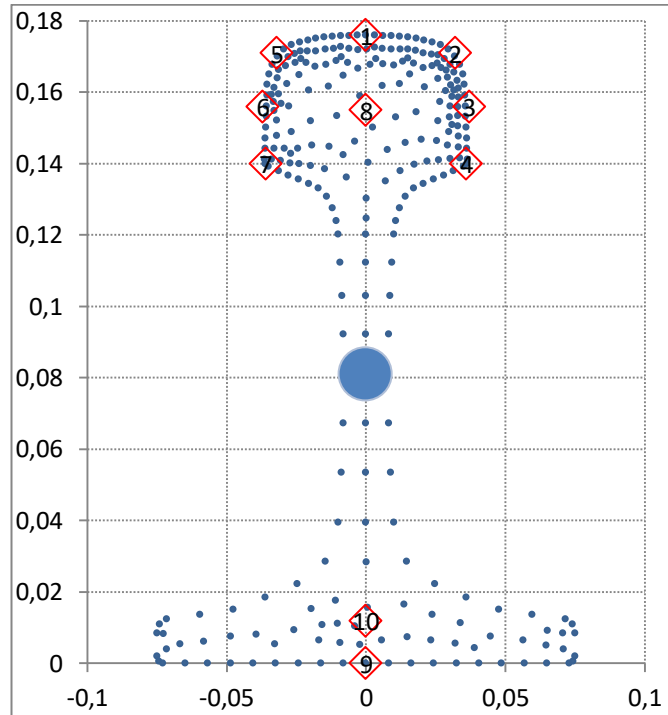
*Figure 5.29 Mesh structure*

## 5.4.6.2 Material properties

The software requires very few rail steel thermal properties:
- Density (kg/m3)
- Conductivity (W/m/K)
- Specific heat (J/kg/K)
- Thermal expansion coefficient (1/K)

Moreover, in order to achieve a good pearlitic structure, ProMod will consider the metallurgy. For this purpose the TTT diagram of the material processed must be filled in the input data.
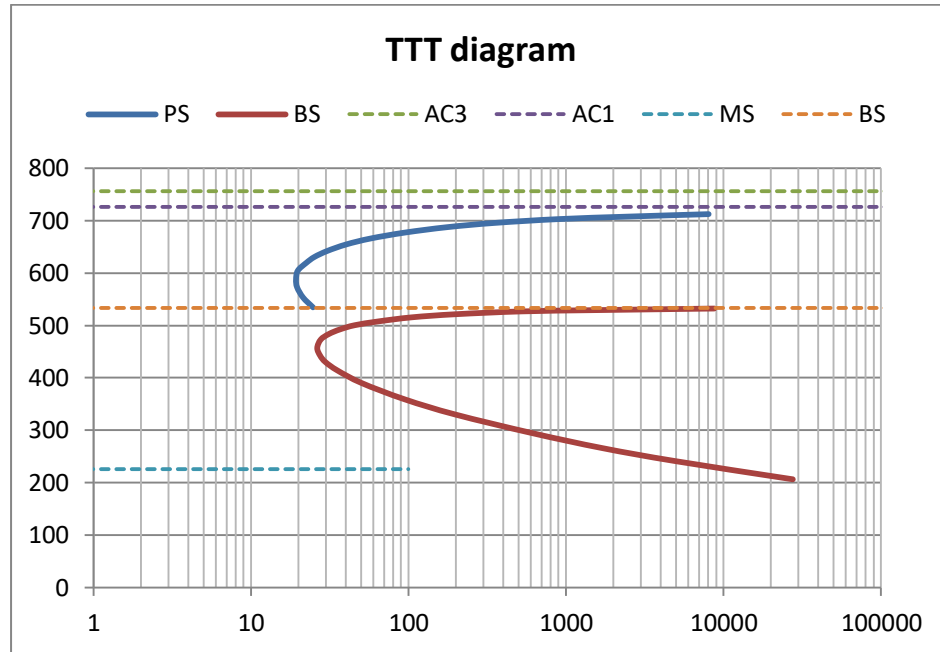
*Figure 5.30 TTT Diagram*

### 5.4.6.3 Cooling system configuration

As previously introduced, ProMod is flexible and modular. For this the following features has to be filled:

- Cooling sectors
- Control groups (CG), meaning two modules that share the same air and water pressures
- Cooling modules, both air mist one and air blade one Cooling sections

### 5.4.7   Output results

#### 5.4.7.1 Mist jet coverage

As previously mentioned, upper and lateral cooling section position determines the rail head impingement surface. In order to have a good spray coverage, ProMod furnishes a view of the surfaces directly impacted by the jet (so excluding the surfaces wetted by indirect flowing water, as on the web or on the top of the foot).
This view can be useful in order to decide a priori the upper cooling section height and then to optimize the jet impingement according to the simulated thermal paths.
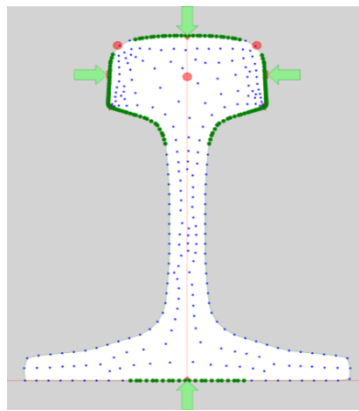


*Figure 5.31 Affected mesh on cooling surface*

#### 5.4.7.2 Inlet thermal map

According to the temperatures read by the pyrometers at the inlet of the cooling system, ProMod is able to calculate the inlet thermal map (see figure at right side). This temperature field represents the starting heat content of the rail and on the base if its intensity very different pressure settings can be required in order to satisfy final metallurgical target.
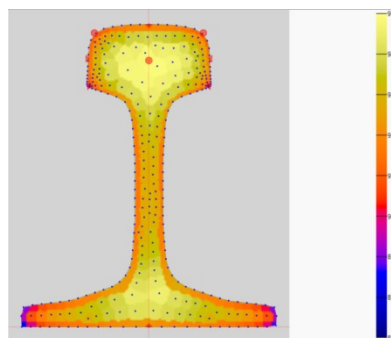


*Figure 5.32 Thermal FEM map*

### 5.4.7.3 Optimized thermal path

Once the inlet thermal map has been established, ProMod is able to try different pressure settings for each control group, then simulate the corresponding thermal path and finally, after some iterations, find out the optimized one.

Optimization is based on the following sequence

- Very fast temperature drop at the early stages of the heat treatment. This choice will permit both to control metallurgical transformations as long as possible inside the idRHa+ system and furthermore to obtain harder structures.
- Surface tempering temperature over the pearlite limit (PL) so as to avoid bainite start.
- Maintaining the surface temperatures very close to a predefined target temperature until micro-structural transformations have finished.
- Pressure adjustment so as to keep the rail straight.

The following picture 5.23 shows the cooling path optimization. The red line represents the target temperature above which it's necessary to stay in order to guarantee a pearlitic micro-structure. Almost all of the previous criteria can be easily ascertained looking at this figure.
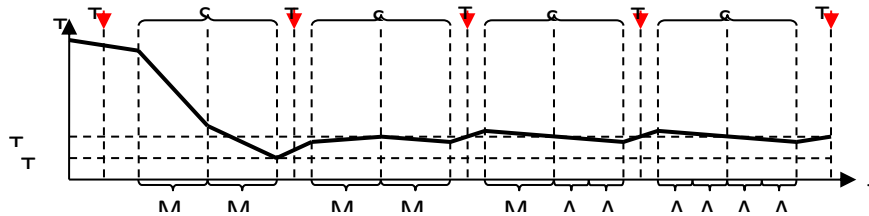


*Figure 5.33 Cooling path optimization*

Transformation start time will be calculated by ProMod for each rail control points and pressure setting will be elaborated in order to avoid bainite transformations and keep temperature as close as possible to the target (that means very fine pearlite structure). The figure 5.31 below shows the transformation start (red circle) for a certain control point and the subsequent temperature bouncing on the remaining cooling line.
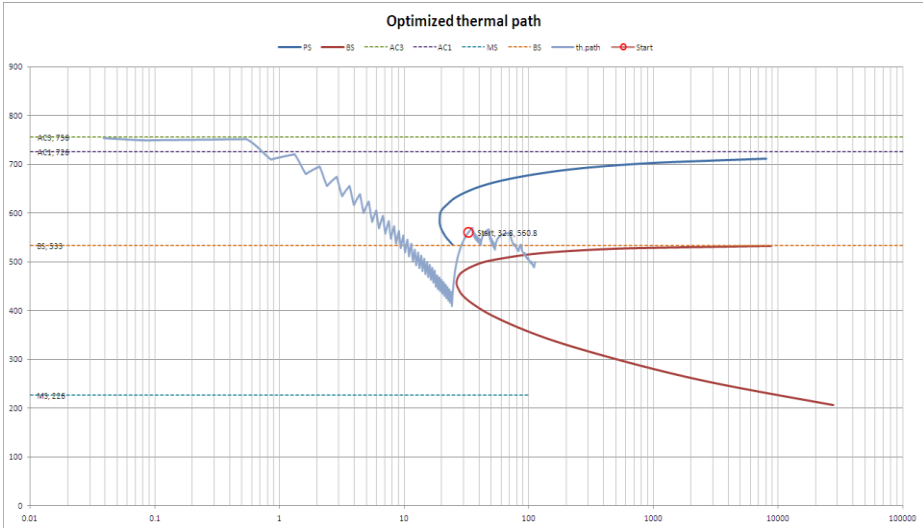
*Figure 5.34 Control starting phase transformation*

# Chapter 6

# 6. Experimental tests

## 6.1   Introduction

In line hardening of long rail requires an extensive process optimization to minimize final properties deviation from the standard requirements and to identify unique recipe for a specific rail profile. The rail product is worldwide used independently of climatic situation and generally can be subjected to a temperature range of 80°C (-4' + 40). The rail product for use in cold regions of the world beside the requirement of high hardness (e.g. head hardened pearlitic rail steel with hardness of 350÷370 HB for freight railways) requires a good toughness at very low temperature.

In order to drive the design of the operative rail plant that Siemens will erect in Kazakhstan in the direction of Russian rail market, the main rail product requirements have been analyzed. GOST standard and the suggestion of Russian Railways for the highest rail grade (HH) require a specific "past the post" full scale drop test. A most significant test is also proposed from GOST standard and Russian Railways: the KIC toughness measurement (fig. 6.2). This toughness measurement, according to EU standard (even if at -20°C), is a best way to establish the toughness of material in particular on eutectoid pearlitic steel. Pearlitic rail steels for operating temperature are in brittle condition and the full-profile rails work, and in general the toughness impact tests, could not representative of behavior of rails at low temperature.

Moreover a past the posttest have three limits:

a. The measured fracture work is an average of microstructure in the whole rail section (important aspect especially in the head hardened pearlitic rails).

b. The measured fracture work is influenced by rail section shape. c. Do not allow to do a ranking of rail steel product as a function of process production parameters and steel grades. On the other hand the KIC allow to define a ranking also in the case of brittle materials and it is possible to define the influence of microstructure parameters on toughness. Where possible, a correlation can be defined between results of KIC tests and most influencing microstructure parameters

and to give first guideline on production process to improve toughness property. In this way it is possible to maximize the ratio toughness/strength.

## 6.2  Test equipment

The pilot plant (see fig. 6.1) is composed of a natural gas fired furnace to reheat properly the rail, a rail support system to execute the extraction cycle, the cooling rig that reproduce the industrial configuration of the idRHa+®. The gas furnace is controlled by thermocouples and can guarantee a precise temperature control with a reheating temperature up to 1200°C with a precision of ± 10°C. The rail clamping unit is moved by a pneumatic cylinder and can introduce and/or extract the rail from the furnace in 5 s.



Pressure gauge

Proportional valve

On-Off valve

a) heating configuration          b) cooling configuration
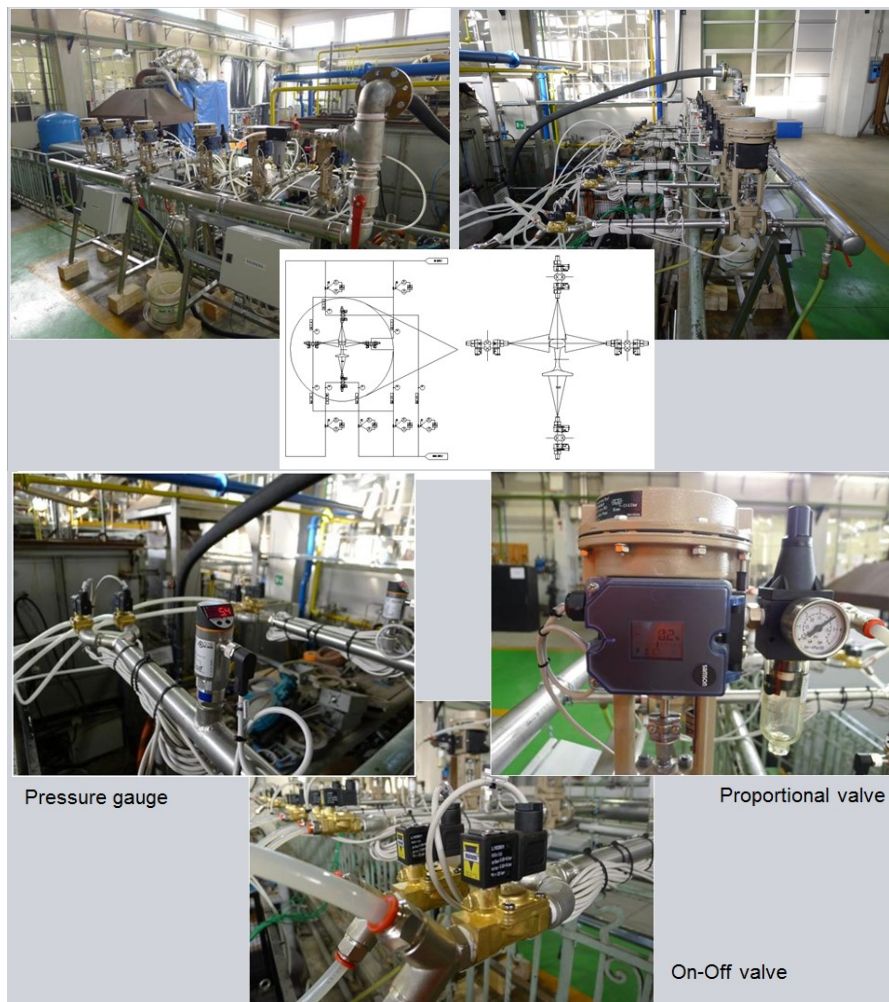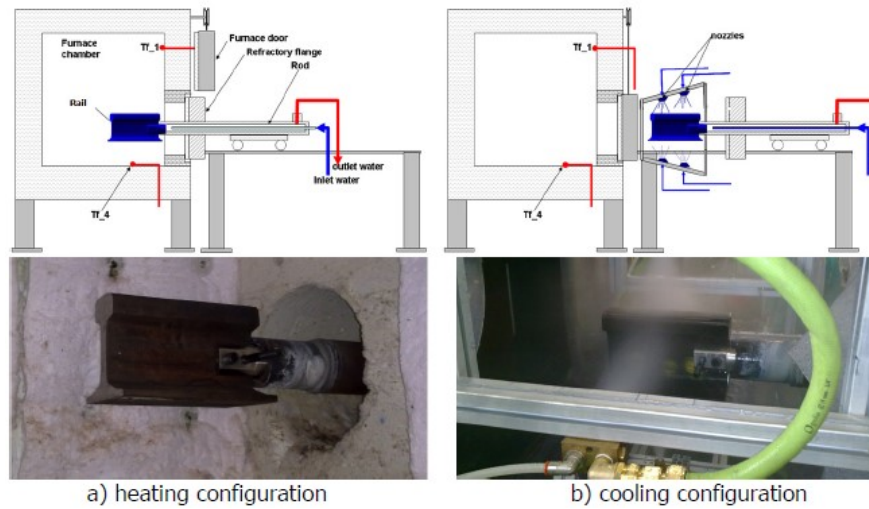
*Figure 6.1 Overview of the pilot plant installation*

The main water circuit is composed by a manifold that supply water to six independently regulated proportional valves. Each valve controls a single spray dedicated to cool the rail head top, the rail head side or the rail foot (see fig. 6.3). In parallel to the water circuit a similar distribution has been adopted for the air supply. With this system it is possible to reproduce a wide range of working condition with required heat exchange factor. In fact, it is possible to work with only water, only air or air mist with a pressure working range for both water and air of 1 to 5 bars
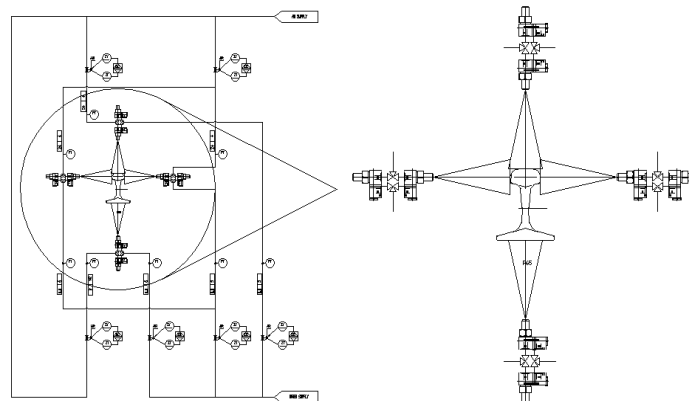


*Figure 6.2. Schema of the cooling ramp*

All the process parameters are monitored and controlled by a dedicated PLC that execute the cooling cycle in accordance with the calculated recipe. The difference stages of the cooling are monitored with a thermocamera the ensure the required data for post processing calculation. The cooling path can be clearly monitored and thus the nozzle geometry as well as the nozzle distance from the rail surface optimized.
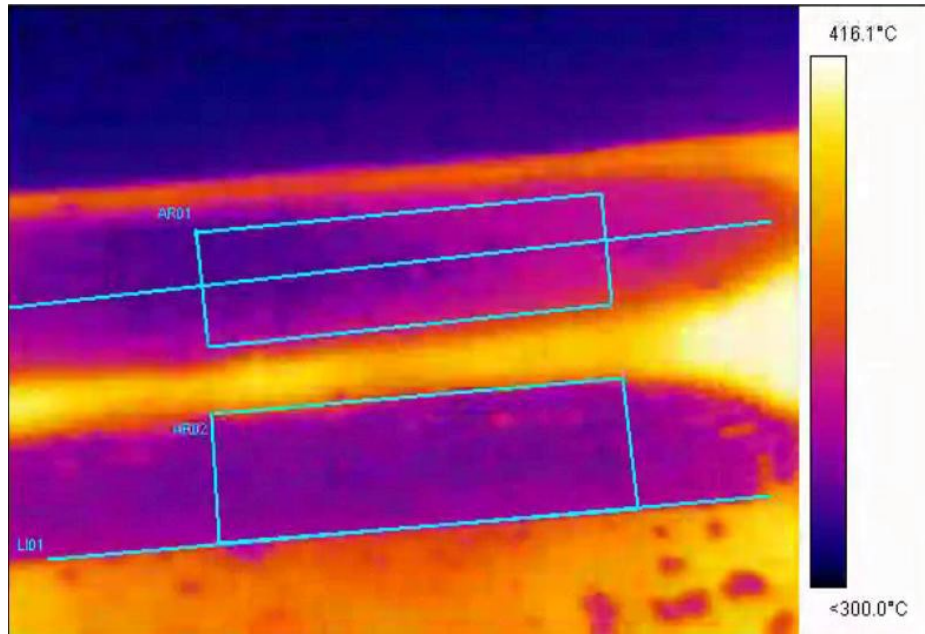
*Figure 6.3. Thermocamera acquisition of the cooling path on the rail head*

## 6.3 Trials

Several trials on P65 K76F rail steel samples were carried out by using the pilot plant built in order to reproduce a section of idRHa+ cooling plant (four nozzles: top, left, right and foot).

The chemical composition of rail steel grade and the rail categories reachable are collected in Table 6.1.

| Rail Category | Steel grade | Element Mass Fraction, % | | | | | | | |
|---|---|---|---|---|---|---|---|---|---|
| | | Carbon | Manganese | Silicon | Vanadium | Chromium | Phosphorus | Sulphur | Aluminium |
| | | | | | | | no more | | |
| OT350CC OT350 HT260 | 76Φ | 0.71-0.82 | 0.75-1.25 | 0.25-0.60 | 0.03-0.15 | Max. 0.20 | 0.020 | 0.020 | 0.004 |

*Table 6.1 Chemical composition and rail categories for K76F steel grades.*

The samples with length of 270mm were instrumented by eight thermocouples in order to measure the thermal evolution during the whole thermal treatment (Figure 6.1). Two different austenitization conditions were used in order to obtain two different Prior Austenitic Grain Size: small (10mm) and large (110mm).

After the austenitization phase the cooling strategies simulating the in-line industrial process applicable by idRHa+ were applied in order to reproduce the microstructure and mechanical properties of head hardened pearlitic rail steel.
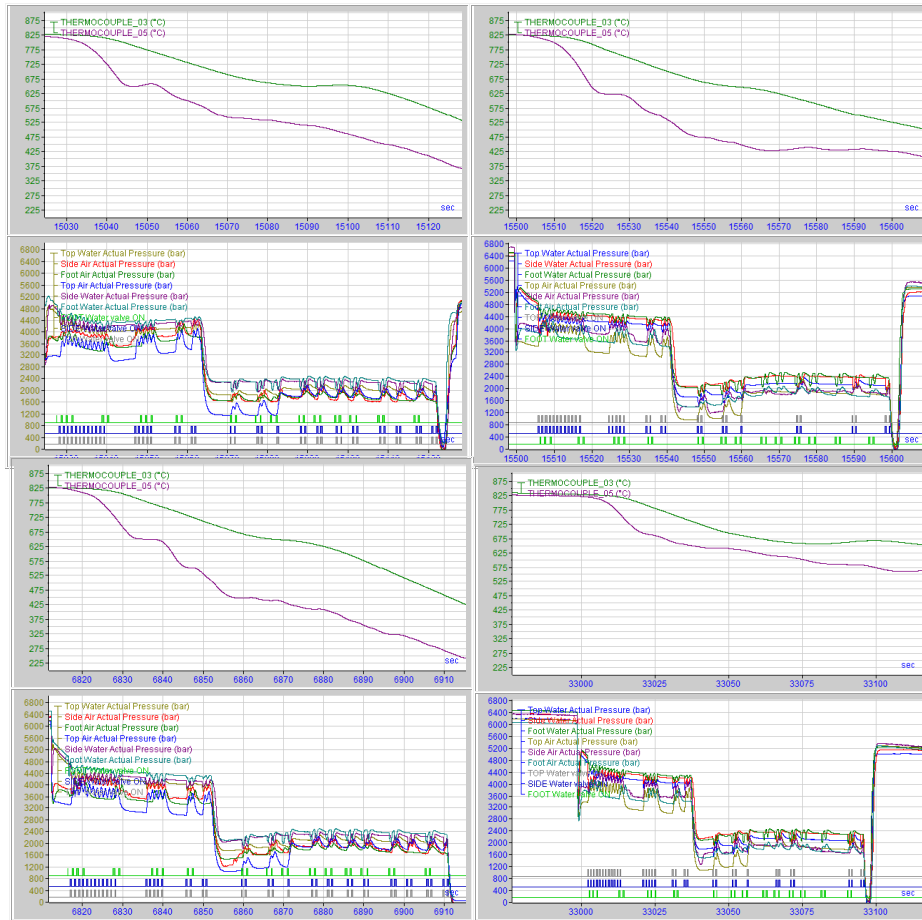
*Figure 6.4 Thermocouple recorded data during the thermal treatment (KP01÷04)*

Several trials are dedicated to identify the working window for idRHa+ in terms of upper and lower cooling curves to reach respectively both the minimum requirement and the maximum performances for head hardened rails considering the industrial productivity. The cooling rate measured by thermocouple at 10 mm on 45° straight line from the rail corner (in correspondence of 3 and 4 rail hardness measurement points, see rail standards) is in the range of 5÷14 °C/s. Some cooling strategies were forced until formation of mixed microstructure (some island of degenerate pearlite and/or bainite) near the outer surface in order to define the process limits.
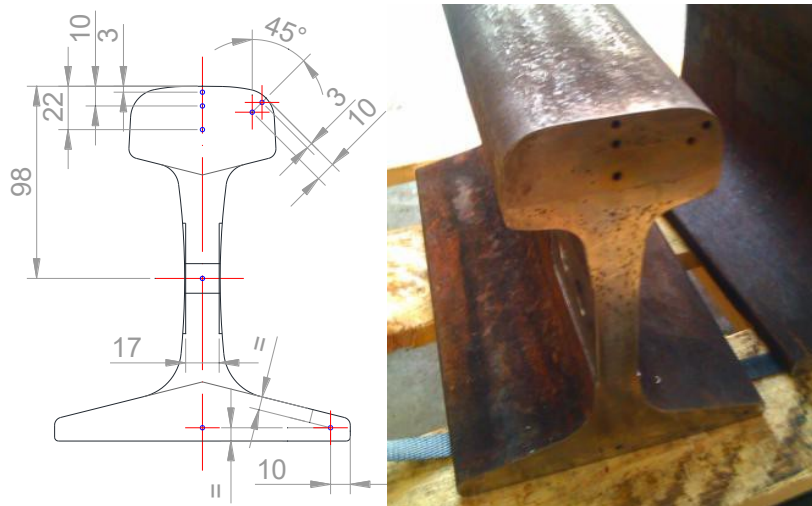
*Figure 6.5 P65 K76F rail sample with thermocouple holes for instrumented trials*

After the thermal treatments mechanical and microstructural characterizations on tested samples were performed in order to determine the correlation between the performance of rail, the cooling strategies and the microstructure characteristic. Particular attention was given at hardness and toughness measurements. In addition a characterization of rails in as-received condition was performed in order have some data for comparison. The as-received rails are thermal treated by an off-line industrial process.

## 6.4   Operational control testing

Product samples can be used to define dimensional properties so that finishing mill settings can be adjusted to improve finished rail tolerance. Mechanical properties, such as hardness, tensile strength and elongation, can be obtained from a Sample & Test Station. This record of sample physical properties can give immediate feedback information for correcting idRHa+ cooling settings. These tests are valuable for the present production run, and can also give some useful information for future runs of different sizes and grades. Moreover, mechanical property information can point out problems, such as scratches and other surface defects. These information are needed for maintenance of the mill equipment, as well as of the testing equipment itself. Micro-samples can be taken from the same test sample areas to verify microstructure characteristics. The appearance of unresolved bainite/martensite may require cooling process changes and/or billet quality investigation. Photo-micro-graphs can be taken from test samples and kept on record or given to customers as certification of products and production run quality.

### 6.4.1 Microstructure Analysis

The microstructure shall be verified in accordance of GOST Standard GOST 51685-2011: "whole section of the rail should be pearlite microstructure, allowing a small amount of ferrite, there should be no martensite, bainite and grain boundary infiltration". Microstructure should be observed on rail head location shown in Figure 6.6. Microstructure shall be determined at a magnification of x500.
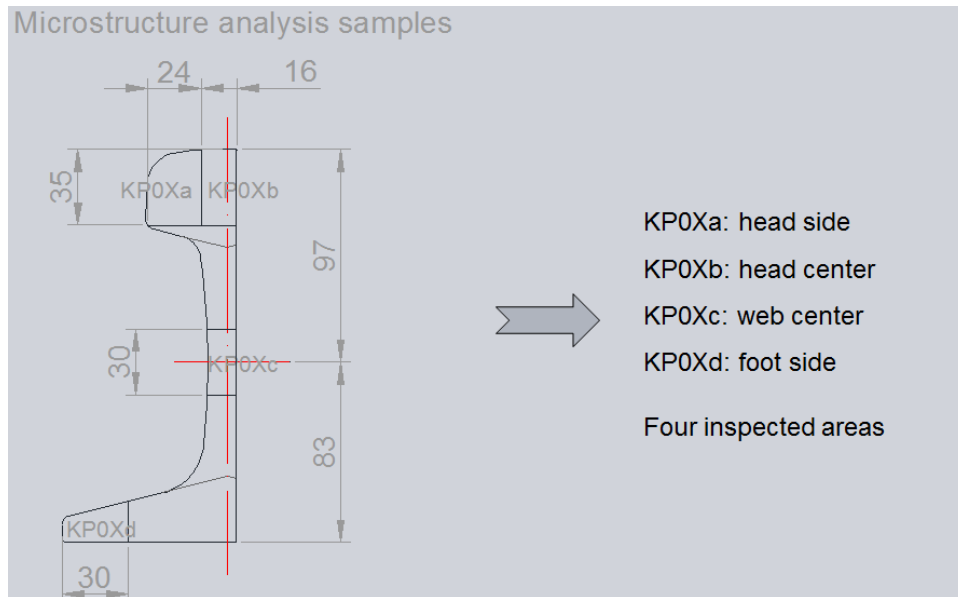


*Figure 6.6 Microstructure points positions*

In order to study the influence of Prior Austenite Grain Size (PAGS) on rail performances the PAGS evolution relationship have been determined. The PAGS relationship have been obtained using both application of metallurgical models and FEM rolling simulation on rail steel grade and experimental trials. Four temperatures and three soaking times have been selected to compile the data matrix and have resulted into satisfactory correspondence with the calculated data.
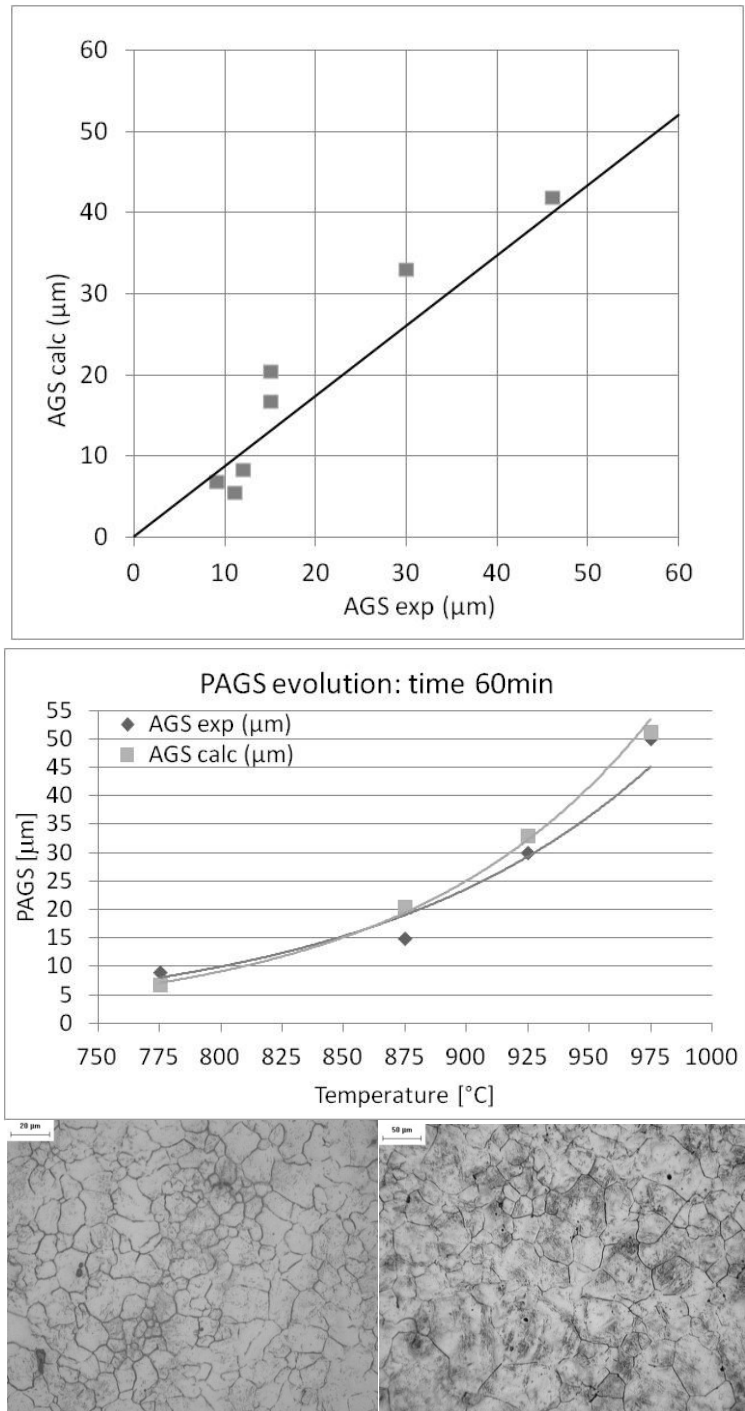
*Figure 6.7 Correspondence PAGS evolution between measured and calculated PAGS (i.e.775°C and 925°C after 60 min)*

PAGS have been calculated on the base of grain grow evolution relationship:

| Trial [ID] | Austenitisation Temperature [°C] | Holding time [min] | PAGS [µm] | $C_{R800-700}$ [°C/s] |
|---|---|---|---|---|
| 01 | 825 | 30 | 10 | 11.4 |
| 02 | 825 | 30 | 10 | 10.6 |
| 03 | 825 | 30 | 10 | 12.8 |
| 04 | 975 | 60 | 50 | 9.6 |
| 05 | 975 | 60 | 50 | 9.1 |
| 06 | 975 | 60 | 50 | 9.4 |
| 07 | 1075 | 60 | 110 | 5.5 |
| 08 | 1075 | 60 | 110 | 5.2 |
| 09 | 1075 | 60 | 110 | 7.1 |
| 10 | 825 | 30 | 10 | 8.6 |
| 11 | 825 | 30 | 10 | 9.5 |
| 12 | 825 | 30 | 10 | 9.3 |
| Trial [ID] | Austenitisation Temperature [°C] | Holding time [min] | PAGS [µm] | $C_{R800-700}$ [°C/s] |
| KP01 | 825 | 30 | 10 | 13.9 |
| KP02 | 1075 | 60 | 110 | 12.4 |
| KP03 | 825 | 30 | 10 | 13.7 |
| KP04 | 1075 | 60 | 110 | 9.2 |

*Table 6.2 Grain grow evolution relationship*

### 6.4.1.1 Sample preparation

The cutting procedure shall be carried out without generating deformation or overheating in the cutting zone. Wet cutting or wire cutting have less impact on sample surface.

After cutting the sample surface shall be grinded using wet grinding wheel. The material of grinding wheel should be selected considering the material hardness: usually aluminum oxide grinding wheel is suitable for iron-based material, silicon carbide grinding wheel is recommended for non-ferrous metal, diamond blade is necessary for hard metal or ceramic.

The grinded thickness shall be at least 0.7 mm.

After grinding the sample shall be washed and dried. After the sample surface shall be hand gridded from coarse to fine grinding. Sandpaper used for polishing should be tiled in diamond, alumina or magnesium oxide, from coarse to fine grit sizes.

Sandpaper should be changed once every sample. The sample shall be turned 90° respect the old grinding direction (perpendicular direction to direction of the old mill grinding marks).

The polishing method can be mechanical polishing, electrolytic polishing, chemical polishing, polishing vibration, micro grinding. The operator, before o polishing procedure should also wash his hands to eliminate grits coming from sandpaper.

After sample polishing or during microscope analysis, if grinding pits and other defects are highlighted, the sample should be re-polished.

The sample shall be subjected to etching following the Standard GOST 51685 "Steel macrostructure and defect etching test method" or equivalent ISO 4969.

## 6.4.2   Hardness analysis

The hardness distribution in the rail shall be verified in accordance of Russian Standard 51685-2011.

| Code | Steel Grade | Tensile Strength Rm MPa | Elongation After broken A | Head hardness along centre line HBW （HBW10/3000） |
|------|-------------|------------------------|---------------------------|---------------------------------------------------|
| H320 | U71Mn | ≥1080 | ≥10 | 320～380 |
| H340 | U75V | ≥1180 | ≥10 | 340～400 |
| H370 | U77MnCr | ≥1230 | ≥10 | 360～420 |
|  | U78CrV | ≥1280 | ≥10 | 370～420 |
|  | U76CrRE | ≥1280 | ≥10 | 370～420 |

*Table 6.3 Tensile, elongation and head harness after heat treatment*

## 6.4.2.1 Rail running surface hardness

Hardness value on rail head center line should be the same as reported in Table 6.2. In the same rail, hardness variation should not exceed 30HB.

Test points should be at least five. The sample length should not be less than 100 mm and should be taken randomly on the rail. A depth of 0.5 mm shall be ground from the rail running surface before a hardening impression is made.

The test method shall be Brinell hardness test, and shall be follow the Standard 51685 "Metallic materials Brinell hardness test-Part 1: Test method" or equivalent ISO6506-1.

### 6.4.2.2 Cross-sectional hardness

For online heat treatment rail should be inspected its section hardness as showed in chart 6.7 b. Section hardness should comply with figure 6.7a value. The sample cross section should be randomly selected.

The hardness shall be measured by means Rockwell test following the Standard GB/T 230.1 "Metallic Rockwell hardness test-Part 1:Test method (scales A,B,C,D,E,F,G,H,K,N, T)" or equivalent ISO6508.

| Code | Grade | Rail Type kg/m | Section Hardness in different level HRC | |
| --- | --- | --- | --- | --- |
| | | | A1，B1，C1，D1，E1 | A4，B5，C5，D3，E3 |
| H320 | U71Mn | 43，50，60 | 34.0~40.0 | ≥32.0 |
| H340 | U75V | 43，50，60,75 | 36.0~42.0 | ≥34.0 |
| H370 | U77MnCr | 60,75 | 37.0~44.0 | ≥35.0 |
| | U78CrV | 60,75 | 37.0~44.0 | ≥36.0 |
| | U76CrRE | 60,75 | 37.0~44.0 | ≥36.0 |
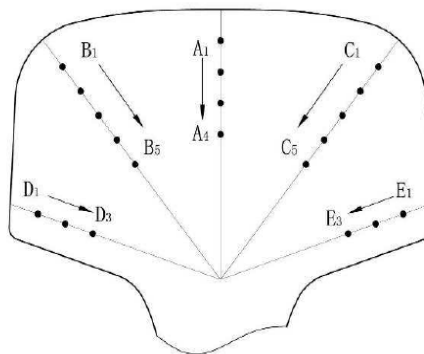


1ˢᵗ Point is 5mm to surface，distance between points is 5mm；D、E line to bottom jaw is 5mm

*Figure 6.8 Hardness inspection values(a) and points(b)*

### 6.4.2.3 Sample preparation

The cutting procedure shall be carried out without generating deformation or overheating in the cutting zone. Wet cutting or wire cutting have less impact on sample surface. After cutting the sample surface shall be grinded using wet grinding wheel. The material of grinding wheel should be selected considering the material hardness: usually aluminum oxide grinding wheel is suitable for iron-based material, silicon carbide grinding wheel is recommended for non-ferrous metal, diamond blade is necessary for hard metal or ceramic. The grinded thickness shall be at least 0.7 mm.

### 6.4.3 Tensile strength and elongation

The tensile strength and elongation shall be verified in accordance to Russian Standard 51685-2011. These shall comply with the value given in Table 6.2.

Test samples from the rail shall be taken as given in Figure 6.8. The manufacturer shall determine the tensile properties in accordance with Standard GB/T 228-1 "Metallic materials –Tensile testing at ambient temperature" or equivalent ISO 6892-1, using a proportional circular test piece of 10mm diameter (d0) and initial length between the reference point (L0) equal to 50 mm.

| Steel Grade | Tensile Strength Rm MPa | Elongation After broken A | Head hardness along centre line   HBW |
|---|---|---|---|
| U71Mn | ≥880 | ≥10 | 260～300 |
| U75V | ≥980 | ≥10 | 280～320 |
| U77MnCr | ≥980 | ≥9 | 290～330 |
| U78CrV | ≥1080 | ≥9 | 310～360 |
| U76CrRE | ≥1080 | ≥9 | 310～360 |

| Code | Steel Grade | Tensile Strength Rm MPa | Elongation After broken A | Head hardness along centre line HBW （HBW10/3000） |
|---|---|---|---|---|
| H320 | U71Mn | ≥1080 | ≥10 | 320～380 |
| H340 | U75V | ≥1180 | ≥10 | 340～400 |
| H370 | U77MnCr | ≥1230 | ≥10 | 360～420 |
| | U78CrV | ≥1280 | ≥10 | 370～420 |
| | U76CrRE | ≥1280 | ≥10 | 370～420 |

*Figure 6.9 Tensile Strength and Elongation*

## 6.5 Results

Four samples from each treated rail was taken in order to investigate the microstructure by Light Microscope (LM). Two sample from the rail head (side and center), one sample from the web (middle portion) and one sample from the foot (foot end) were considered: fine pearlite microstructure was observed for all samples. Just in the case of most drastic cooling strategies some trace of mixed pearlite-bainite microstructure near the outer surface were observed. Further investigations by Scanning Electron Microscope (SEM) were performed in order to confirm the observed microstructure and to measure the Interlamellar Spacing (IS): the best value IS is 0.07±0.02 mm.

From Figure 6.10 to Figure 6.13 the micrographs of observed microstructure and the scheme of hardness points are collected. In Figure 6.11 the hardness profiles measured along the straight line from the rail corner at 45° for treated rails are shown.
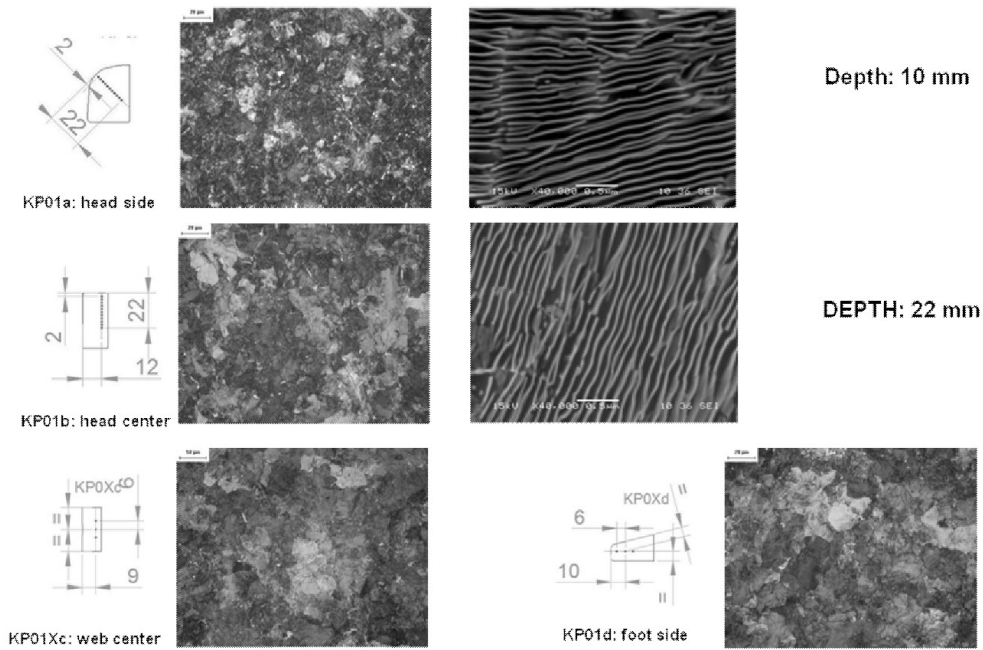
*Figure 6.10 – Microstructure investigation by Light Microscope (LM) and Scanning Electron Microscope (SEM): KP01 sample*
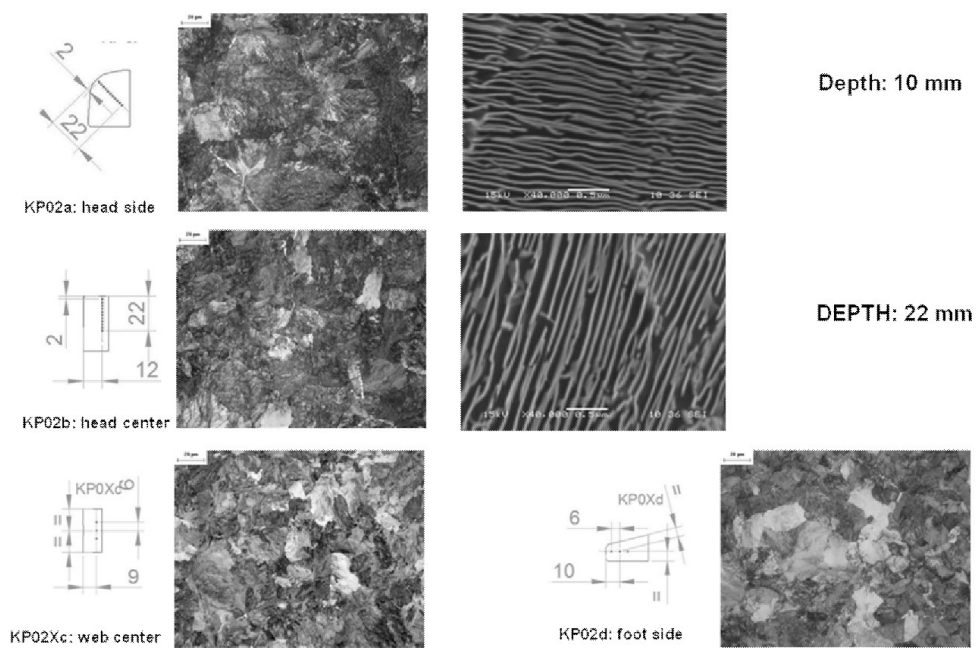


*Figure 6.11 Microstructure investigation by Light Microscope (LM) and Scanning Electron Microscope (SEM): KP02 sample*
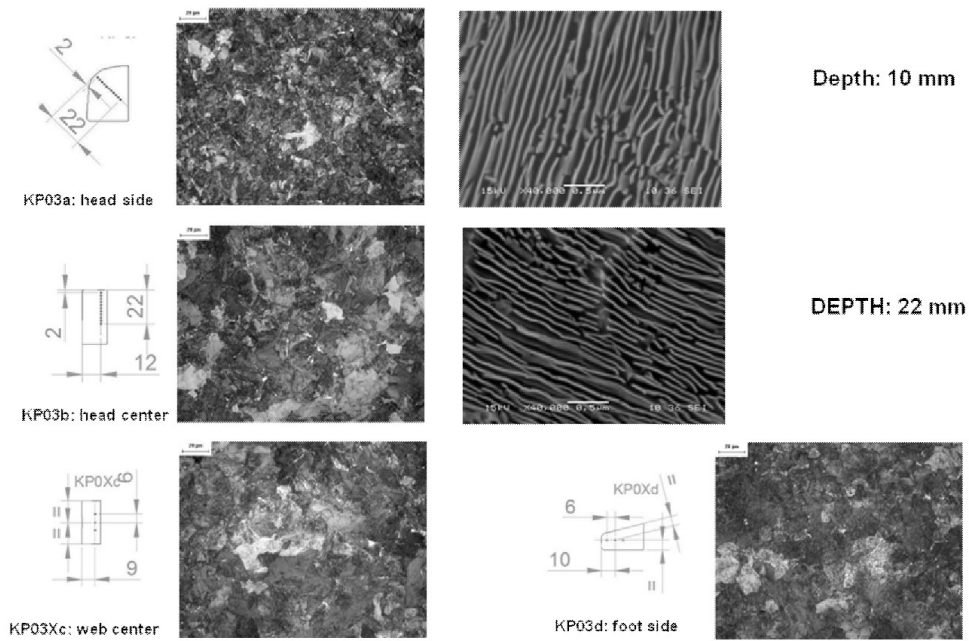
*Figure 6.12 Microstructure investigation by Light Microscope (LM) and Scanning Electron Microscope (SEM): KP03 sample.*
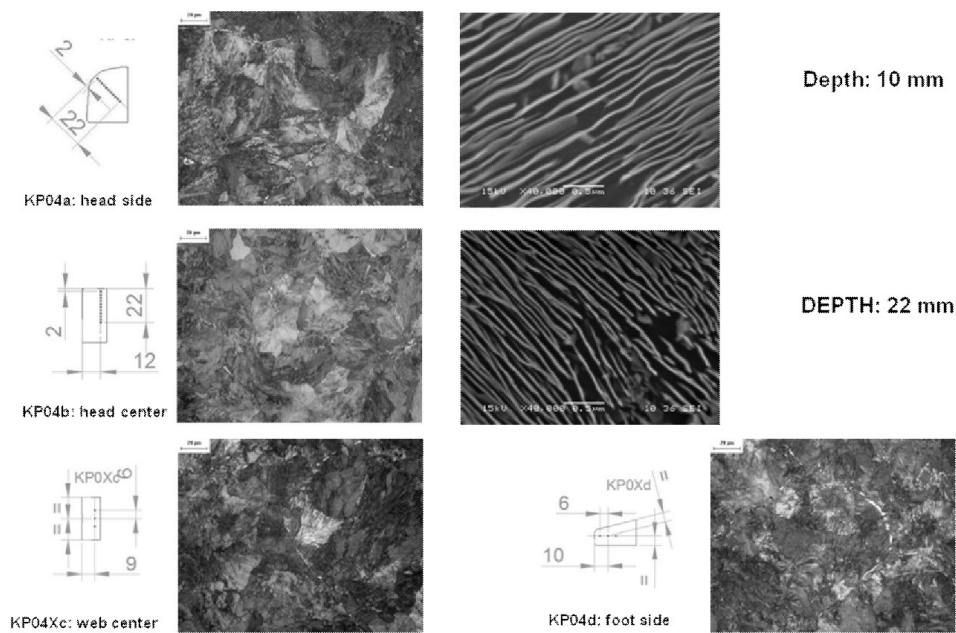


*Figure 6.13 Microstructure investigation by Light Microscope (LM) and Scanning Electron Microscope (SEM): KP04 sample*
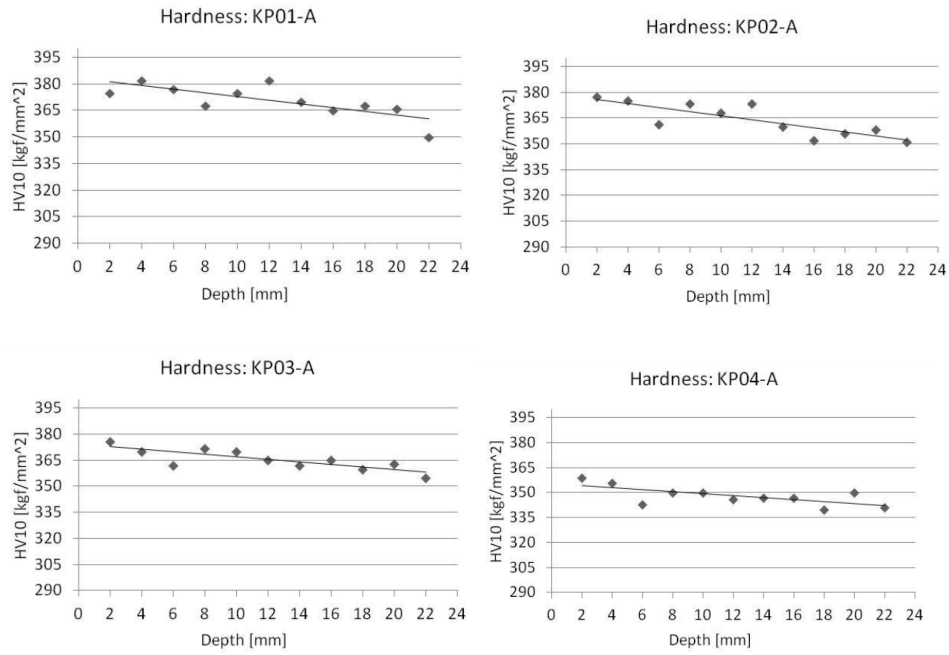
*Figure 6.14  Hardness HV10 profile on head side*

In figure 6.15 is also made an evaluation of decarburized layer depth on the ferrite network: the maximum thickness is less than 200μm. So there is no evidence of degenerated pearlite (it was present in the off-line threated rail).
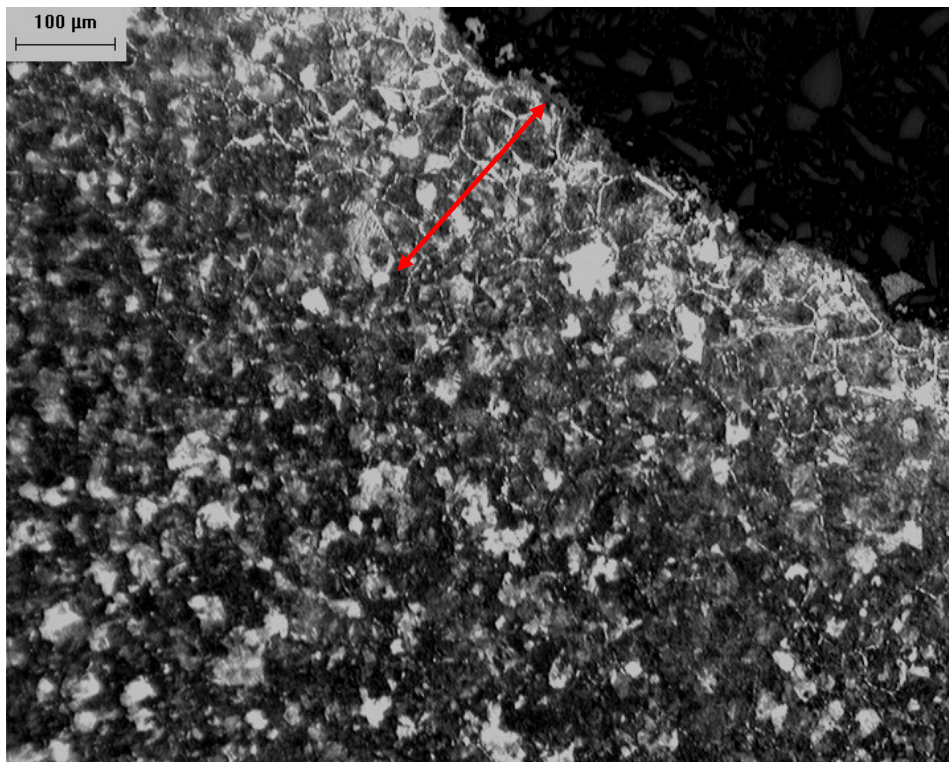


*Figure 6.15  Decarburized layer depth on ferrite network*

Toughness measurements in terms of KIC following the ASTM E399 were performed. In Figure 6.16 an example of experimental curves and fracture surface after toughness bend test were collected. A toughness comparison between as-received rails (off-line heat treated) and heat treated rail by pilot plant (in-line thermal treatment simulation) is shown in Figure 6.17. The fracture toughness measured on samples treated with cooling profile simulating the idRHa+ industrial plant are always higher than those measured on as-received rails. The maximum improvement in toughness have been observed for smallest PAGS (10mm). The average value measured on as-received condition and treated samples are respectively $37\pm3$ Mpa+m^1/2 and $47\pm2$ Mpa+m^1/2.

| Velocità traversa (mm/sec) | | *crosshead speed* | 0.05 | 0.05 |
|---|---|---|---|---|
| T (°C) | temperatura di prova | *test temperature* | -60 | -60 |
| di (mm) | Diametro Iniziale | *Original Diameter* | 4.93 | 4.93 |
| ti (mm) | Spessore Iniziale | *Original Thickness* | / | / |
| wi (mm) | Larghezza Iniziale | *Original Width* | / | / |
| S0 (mm2) | Sezione Iniziale | *Original Cross Area* | 19.09 | 19.09 |
| L0(mm) | Tratto Utile | *Gage Length* | 35 | 35 |
| Le(mm) | Base Estensimetro | *Estensom. Gage Length* | 25 | 25 |
| Fp 0,2 % (N) | Carico Scost. Prop. | *Load Yield Strength* | 16936 | 16298 |
| FeH (N) | Carico Snerv. Sup. | *Load Yield Point HIGH* | / | / |
| FeL (N) | Carico Snerv. Inf. | *Load Yield Point LOW* | / | / |
| Fmax (N) | Carico Massimo | *Load Maximum* | 26688 | 27036 |
| Lu (mm) | Lunghezza Ultima | *Total Elongation* | 38.54 | 38.90 |
| du (mm) | Diametro Ultimo | *Smallest Diameter* | 4.15 | 4.09 |
| tu(mm) | Spessore Ultimo | *Smallest Thickness* | / | / |
| wu (mm) | Larghezza Ultima | *Smallest Width* | / | / |
| Su (mm2) | Sezione Ultima | *Smallest Cross Section* | 13.53 | 13.14 |
| Rp 0,2 % | C. Unit. Sc. Prop. | *Yield Strength* | 887 | 854 |
| ReH (MPa) | C. Unit. Snerv. Sup. | *Yield Point HIGH* | / | / |
| ReL (MPa) | C. Unit. Snerv. Inf. | *Yield Point LOW* | / | / |
| Rm (MPa) | C. Unit. A Rottura | *Tensile Strength* | 1398 | 1416 |
| A (%) | Allungamento Perc. | *Elongation* | 10 | 11 |
| Z (%) | Strizione Perc. | *Reduction Of Area* | 29 | 31 |

*Table 6.4 Data for KCU test*

| Sample ID | Impact Energy [J/cm$^2$] | Temperature test [°C] |
|-----------|--------------------------|------------------------|
| A | 12 | -20 |
| B | 15 | -20 |
| C | 16 | -20 |
| D | 11 | -60 |
| E | 10 | -60 |
| F | 8 | -60 |
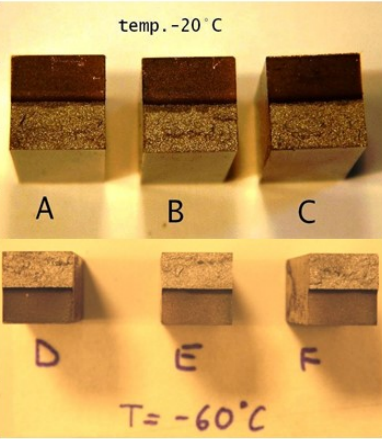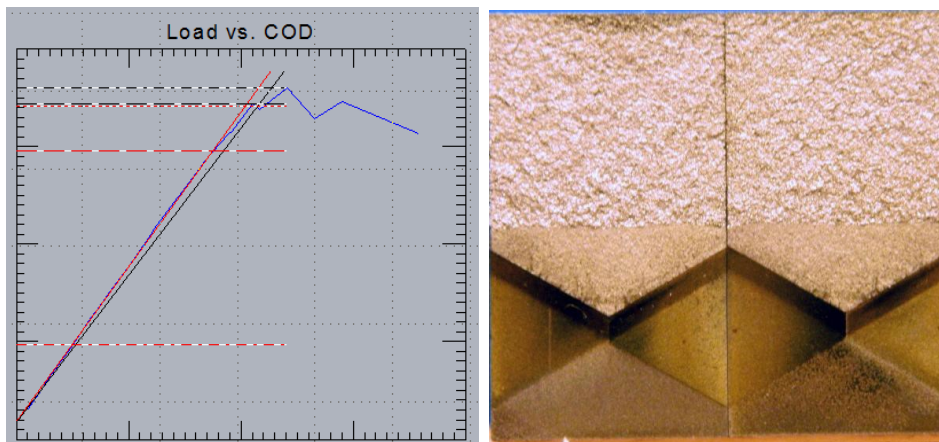




*Figure 6.16 Example of KIC toughness trial: on the left experimental curve; on the right crack surface.*
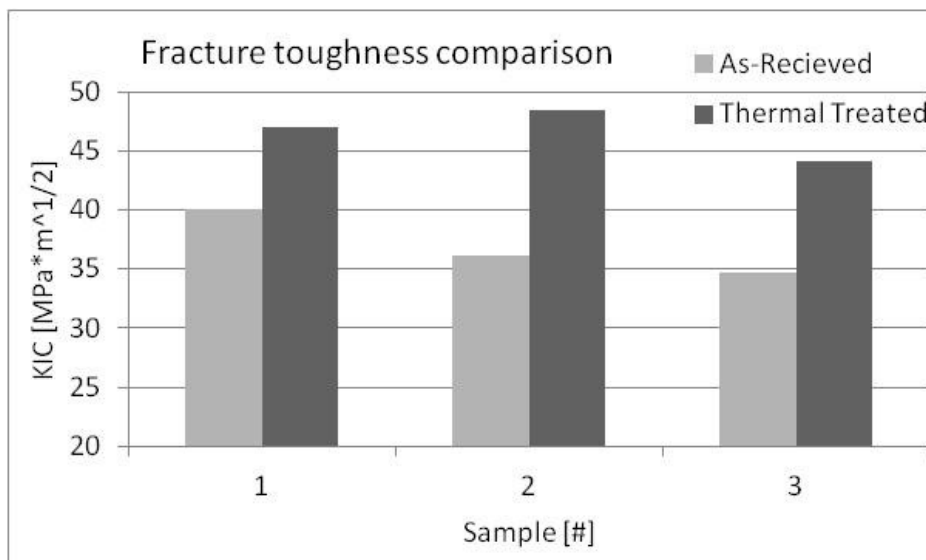


*Figure 6.17 Fracture toughness comparison between as-received rails and thermal treated rails*

Hardness HB measurements in whole rail transversal rail section were performed on tested rails. The requirement of rail standards are completely satisfied for first two trials for both PAGS, small and large. Just some lower value are measured for the less drastic cooling strategies.



| | Hardness HB | | | | | |
|---|---|---|---|---|---|---|
| | Position | | | | | |
| Trial | 1 | 2 | 3,4 | 5 | 6 | 7,8 |
| KP01 | 363 | 357 | 355 | 350 | 264 | 284 |
| KP02 | 365 | 342 | 372 | 337 | 300 | 301 |
| KP03 | 359 | 345 | **334** | 327 | 268 | 283 |
| KP04 | 361 | **334** | **332** | **316** | 296 | 340 |
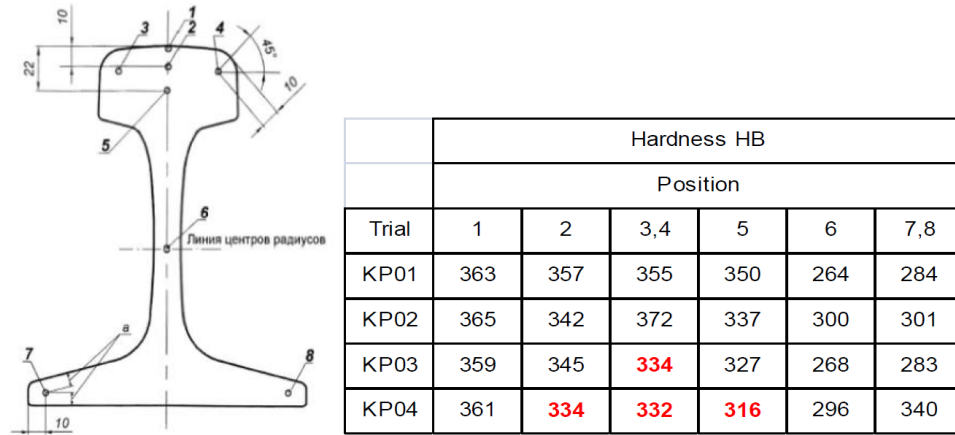
*Figure 6.18 Hardness HB measurement on rail section*

## 6.6   Advantageous Air-water mist system vs Air system

In this paragraph finally are presented also the test conducted with the only air cooling effect system and are compared with the water-air mist system to underline which are the differences and so the advantageous in terms of performances results.

The goal was to reach to develop a system that with the introduction of water to the air increase the cooling exchange and so the hardening of the steel, but in the same time maintained the same homogeneity of the metallurgical structure inside the rail, typical advantage of the low aggressive cooling treatment.
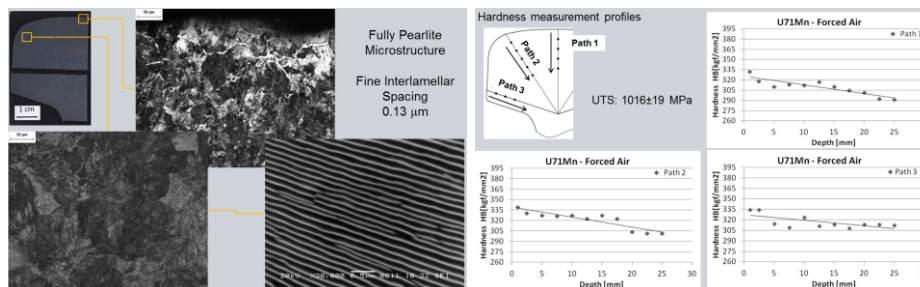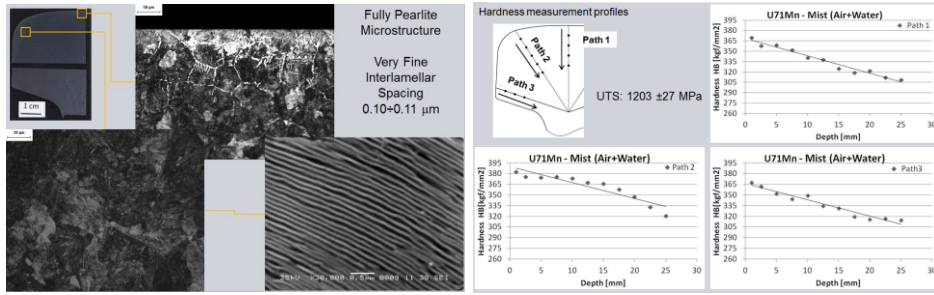
*Figure 6.19 U71Mn Forced air vs Air-water mist*
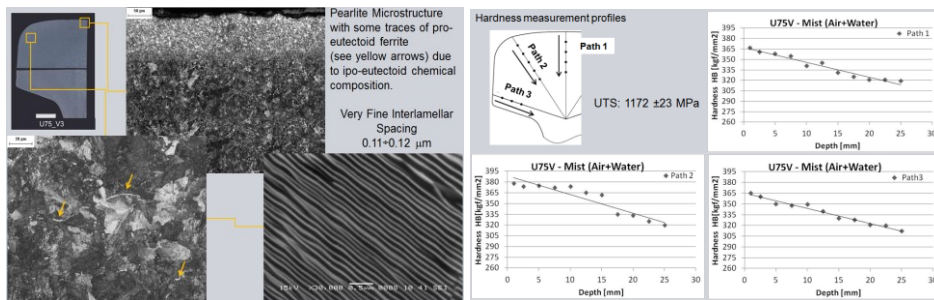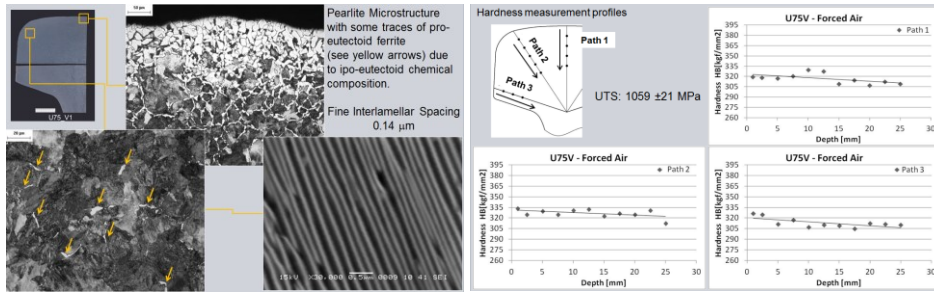


*Figure 6.20 U75Mn Forced air vs Air-water mist*
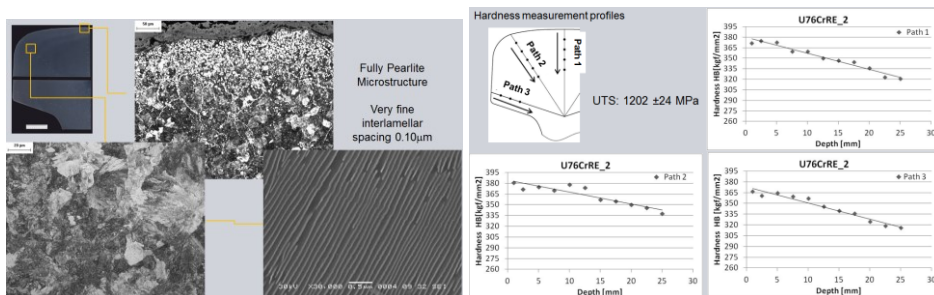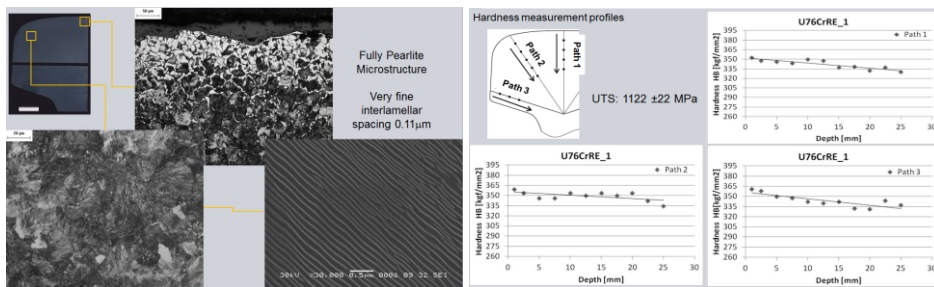


*Figure 6.21 U76CrRE Forced air vs Air-water mist*

So it's possible to see that, for 3 different type of eutectoidic and hypereutectoidic steel U71Mn, U75V and U76CrRE, with the introduction of air-water mist is being possible increase the mechanical properties about 15-20% and maintained the delta hardness inside section with a maximum increasing difference of 5%.

All of this, beyond the cooling strategy, was reached with a deep characterization analysis of the spray nozzles in terms of correct speed impact, dimension flux water, distance between piece and spray nozzles.

## 6.7 Conclusions

The performances obtained on rail samples after pilot plant tests simulating the idRHa+ inline industrial process are comparable or higher than those measured on rail off-line treated.

With the steel grade 76Ф and applying the in-line continuous cooling process by idRHa+ it is demonstrated to reach the Д Т350 rail category. The hardness profile measured for the rail sample with small PAGS (10 mm) is comparable with that measured in rail in as-received condition (Figure 6.16 graph on the left). The hardness profile measured for the rail sample with large PAGS (110mm) is slight higher than that measured in rail in as-received condition (Figure 6.18 graph b). Good hardening depth were observed for all tested rails.
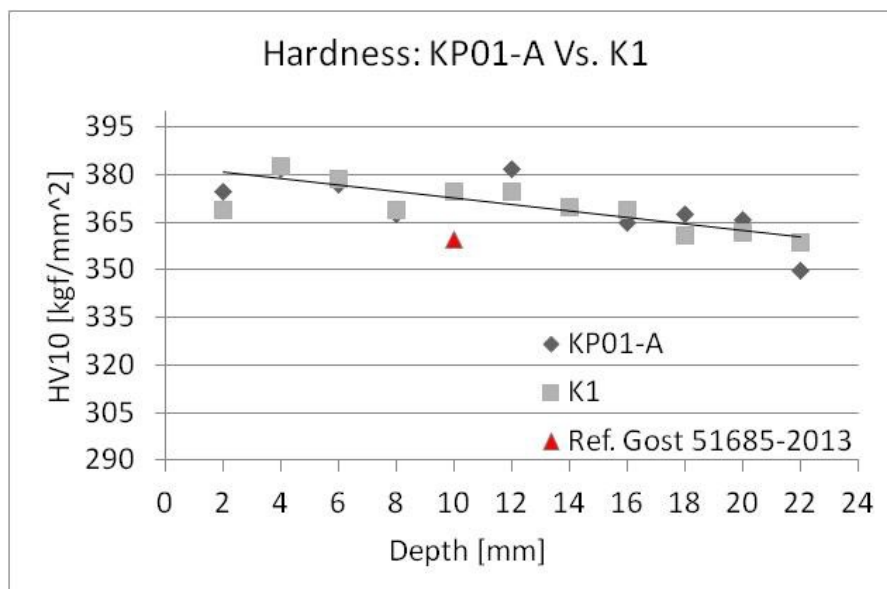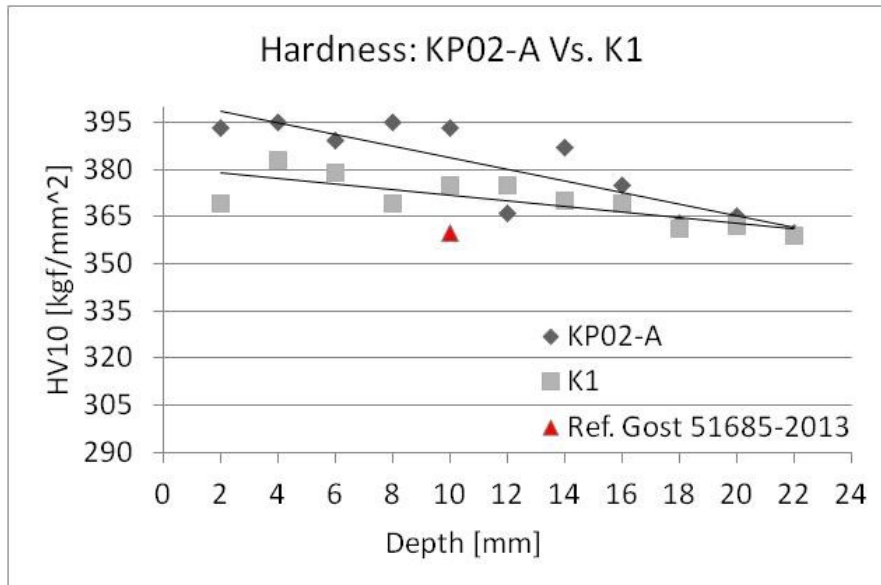
*Figure 6.19 Hardness comparison between as-received condition and thermal treated rails*

Fracture toughness KIC measured values on treated rail samples are always greater than those measured on rail in as-received conditions. In the case of highest hardness profile and smallest PAGS (10mm) the increase in terms of KIC value is more than 25%.

Finally all these results are simulated and calculated by the simulation software, as shown in the figure 6.22 where the thermal profile is in accordance to the experimental test and so the relative mechanical properties respect the values obtained.

In fact in the in line scanner pyrometers diagram is possible to see the behavior of skin temperature for top and side rail respectively for the 5 sector of cooling in which the rail pass through and in the left diagram the foreseen temperature for each sector follows the same trend with the exactly final exit temperature of the product about 550°C.

Temperature trend model

In line scanner pyrometers

Austenite trend model
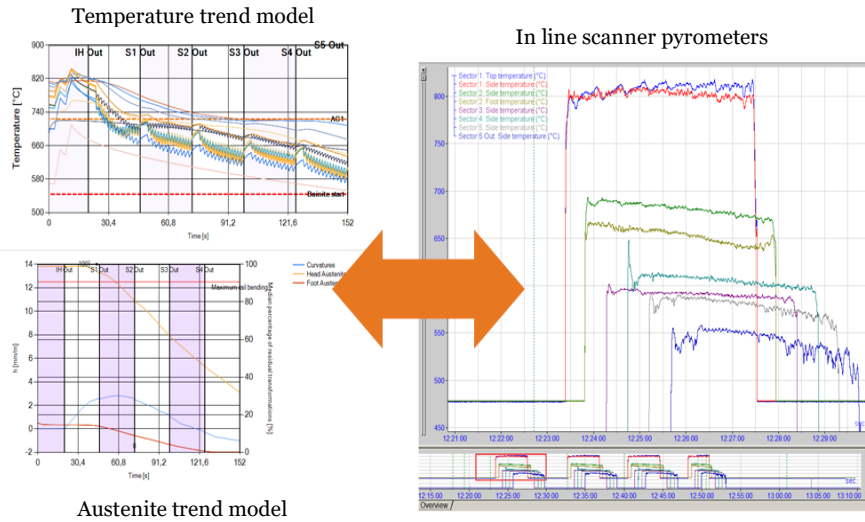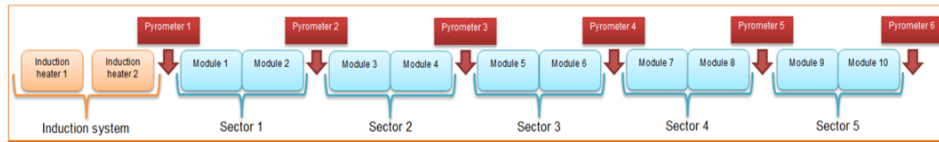
*Figure 6.22 Comparison between real and simulated profile temperature (a) and metallurgical final phase, bending and final hardness(b)*

# Chapter 7

# 7. Conclusions

## 7.1 Final considerations

According to the temperatures read by the in-line pyrometers positioned at the inlet of the cooling system, the algorithm developed is able to estimate the rail incoming thermal profile; once the thermal map has been established, the process control system performs calculations at different pressure settings for each control group, then simulates the corresponding thermal path and finally, after a few iterations, finds out the optimized one.

Cooling path optimization is based on the following criteria:

- Very fast temperature drop at the early stages of the heat treatment. This choice guarantees to both control metallurgical transformations as long as possible inside the idRHa+ system and to obtain hard structures deep inside the rail surface.
- Increasing the surface temperature over the pearlite limit (PL) so as to avoid bainite start.
- Keeping the surface temperatures very close to a predefined target temperature until micro-structural transformations have finished.
- Adjusting the pressures so as to keep the rail straight.

All the thermal profiles, cooling paths and calculation results are clearly displayed and can be easily queried by a mouse click. User interface is very intuitive and straightforward to use, getting the customer confident and autonomous just after a few minutes.
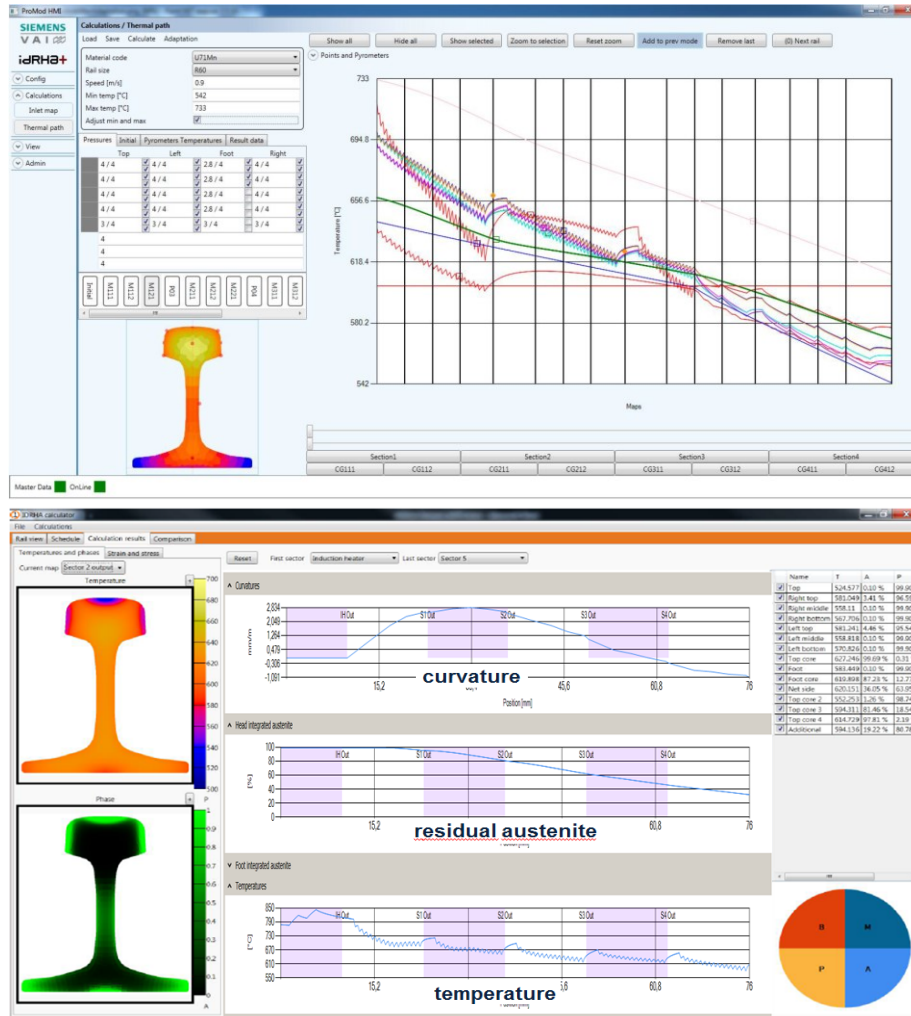
*Figure 8.1 Software simulation output*

Currently, ProMod rail hardening control software is used by "Baogang Iron and Steel" in Baotou (China) and ARBZ steel in Aktobe (Kazakhstan). This thermo-metallurgical software has been employed for the first time during the idRHa+ hot commissioning in April 2016, giving valuable information about the possible cooling strategies and suggesting the applicable pressure settings for different rail shapes, materials, temperatures and process velocities.

The idRHa+ rail hardening technology developed, comprises several innovative design peculiarities that make it the most flexible and efficient apparatus nowadays available on the market. IdRHa+ is powered by an embedded know-how made of complex numerical models and of experimental data derived from extensive trials on an industrial pilot unit.

The application of idRHa+ in the rail plants, new or existing, can be easily studied and adapted due to its modular design; specific design choices grant a unique flexibility of use and consistency of performance at

sustainable cost.

All these aspects together makes Siemens idRHa+ the optimal "tool" to keep the pace with the continuous progression of the technological features of the steel rails: whereas the driving factors for the rail end-Users are "faster, heavier, longer, durable", the answer from the Producers can only be "consistent, reliable, performing, flexible", can only be idRHa+.

## Attachments:

*Annex 1*

Densità $(kg/m^3)$

$$\rho_{Ferrite} = -0.00006\,T^2 - 0.264040000000104\,T + 7929.65466000001$$

$$\rho_{Pearlite} = -0.00008000619195\,T^2 - 0.227411665634982\,T + 7902.94789994437$$

$$\rho_{Bainite} = -0.00008000619195\,T^2 - 0.227411665634982\,T + 7902.94789994437$$

$$\rho_{Martensite} = -0.000055216450216\,T^2 - 0.26120857142899\,T + 7785.13322742433$$

$$\rho_{Austenite} = -0.501\,T + 8126.673$$

Conducibilità termica $(W/m/K)$

$$k_{Ferrite} = 0.000010004422822\,T^2 - 0.058266395400265\,T + 80.6893018045111$$

$$k_{Pearlite} = -0.000004996904025\,T^2 - 0.024574167182664\,T + 57.5802950278643$$

$$k_{Bainite} = -0.000004996904025\,T^2 - 0.024574167182664\,T + 57.5802950278643$$

$$k_{Martensite} = -0.000004996904025\,T^2 - 0.024574167182664\,T + 57.5802950278643$$

$$k_{Austenite} = 0.0091\,T + 15.5081$$

Calore specifico $(J/kg/K)$

$$cp_{Ferrite} = 0.0009 * T^2 - 0.526200000000007 * T + 568.1665$$

$$cp_{Pearlite} = 0.0002 * T^2 + 0.192501176470581 * T + 403.273437647062$$

$$cp_{Bainite} = 0.0002 * T^2 + 0.192501176470581 * T + 403.273437647062$$

$$cp_{Martensite} = 0.0002 * T^2 + 0.192501176470581 * T + 403.273437647062$$

$$cp_{Austenite} = 0.1569 * T + 433.2087$$

Young modulus $(MPa)$

$$E = -0.000178586008569\,T^3 + 0.278321708347223\,T^2$$
$$-227.172508001371\,T + 257358.306541531$$

*Austenite Yield stress (MPa)*

*Temperatura* $> 923K$

$$RP02_{Austenite} = -0.000060561765549\,T^2 + 0.022771223846374\,T + 100.453813499571$$

*Temperatura* $> 623K$

$$RP02_{Austenite} = -0.85\,T + 854.55$$

*Temperatura* $< 623K$

$$RP02_{Austenite} = -0.000204086416557\,T^2 - 0.069751753816442\,T + 447.532938941853$$

*Pearlite Yield stress (MPa)*

*Temperatura* $> 873K$

$$RP02_{Pearlite} = 0.000000694089545\,T^3 - 0.001990205170105\,T^2$$
$$+ 1.53752387199369\,T - 136.893838546324$$

*Temperatura* $> 673K$

$$RP02_{Pearlite} = 0.0025\,T^2 - 5.51500000000009\,T + 3059.27250000003$$

*Temperatura* $< 673K$

$$RP02_{Pearlite} = 0.000000040843955\,T^4 - 0.000082506330065\,T^3$$
$$+ 0.060649123020722\,T^2 - 19.6732190471141\,T + 3021.75805652772$$

*Bainite Yield stress (MPa)*

*Temperatura* $> 1173K$

$$RP02_{Bainite} = 0.00015\,T^2 - 0.5169\,T + 444.93435$$

*Temperatura* $> 873K$

$$RP02_{Bainite} = -0.000013399122807\,T^3 + 0.043993148496237\,T^2$$
$$- 49.166291036964\,T + 18811.9846123391$$

*Temperatura* $< 873K$

$$RP02_{Bainite} = -0.000000014130016\,T^4 + 0.000028656404763\,T^3$$
$$- 0.021196054729901\,T^2 + 6.52557343146362\,T + 98.8725873324658$$

*Martensite Yield stress (MPa)*

*Temperatura* $> 673K$

$$RP02_{Martensite} = 93331.96518855\,e^{-0.006294466326877\,T}$$

*Temperatura* $< 673K$

$$RP02_{Martensite} = -0.002104100761906\,T^2 + 0.723225396398747\,T + 1833.19513764476$$

*Annex 2*

Portata aria $Q_A$

$y_{0w} = -0.985608151835037 + 0.835839369642001\, p_a$

$a_w = 12.8386230684441 - 0.796839050061844\, p_a + 0.851920610450695\, p_a^2$

$b_w = -2.25499518253688 + 5.53127630095935\, p_a - 0.759033949366547\, pa^2$

$x_{0w} = -2.31383557622115\, 10^{-2} + 0.936216586520645\, pa$

$Q_a = y_{0w} + a_w/(1 + (p_w/x_{0w})^{b_w})$

Portata acqua $Q_W$

$Q_{MAX} = \dfrac{60.3961186521591}{(1+(\frac{p_w}{141.952205957054})^{-0.470832963895867})}$

$y_{0w} = 1.13442063464564\, 10^{-2} - 7.42436751639657\, 10^{-3}\, p_a$

$a_w = 0.683155868613509 + 0.626376851425763\, p_a - 0.448717191058613\, p_a^2 + 0.116968965228778\, p_a^3 - 1.01132542573571\, 10^{-2}\, p_a^4$

$b_w = 3.4456617824092 - 11.2081621058932\, p_a + 5.14544380422953\, p_a^2 - 0.977842360833016\, p_a^3 + 6.42710563809678\, 10^{-2}\, p_a^4$

$x_{0w} = 0.885947445983446 + 0.553457558413885\, pa + 7.90287385497811\, 10^{-2}\, pa^2$

$Q_W = (y_{0w} + a_w/(1 + (p_w/x_{0w})^{b_w})) * Q_{MAX}$

Diametro di goccia $D_{32}$

$D_{32} = -196.782788446022 + 375.278917152818\, p_a + 65.1212275130692\, Q_w - 14.817282209228\, p_a\, Q_w - 120.063845543312\, p_a^2 - 2.04290349941177\, Q_w^2 - 0.714704973822232\, p_a^2\, Q_w + 2.00765378912389\, p_a\, Q_w^2 + 12.2676737381146\, p_a^3 - 0.355799118400798\, Q_w^3$

Velocità di goccia $v_i mp$

$v_i mp = 27.2784799409101 - 10.3262358592614\, p_a - 19.3667806189177\, Q_w + 7.36240193752055\, p_a\, Q_w + 0.249825244451951\, p_a^2 + 5.96060074692236\, Q_w^2 - 0.366308757619466\, p_a^2\, Q_w - 1.33251322556388\, p_a\, Q_w^2 + 0.85617099228923\, p_a^3 - 0.803267233974912\, Q_w^3 + 0.100731147830093\, p_a^2\, Q_w^2 - 4.29922275242747\, 10^{-2}\, p_a^3\, Q_w + 2.60359623450487E-02\, p_a\, Q_w^3 - 0.108735396015939\, p_a^4 + 4.83274612589268\, 10^{-2}\, Q_w^4$

## Annex 3

### Condizioni al contorno (Ugelli misti)

#### *1 Ugello laterale*

##### 1.1 nodi bagnati

Superficie e punti interni del cono per ugello laterale

```
(%i1) intCono: -(x-x0)^2/c^2+(y-y0)^2/b^2+(z-z0)^2/a^2<=0;
```
$$(\%o1)\quad \frac{(z-z0)^2}{a^2}+\frac{(y-y0)^2}{b^2}-\frac{(x-x0)^2}{c^2}<=0$$

Tagliamo con piano z=zt

```
(%i2) intParabola: subst(zt,z,intCono);
```
$$(\%o2)\quad \frac{(zt-z0)^2}{a^2}+\frac{(y-y0)^2}{b^2}-\frac{(x-x0)^2}{c^2}<=0$$

Sostituendo le coordinate (xn, yn) del un nodo di bordo n-esimo possiamo sapere se è bagnato dallo spray

```
(%i3) subst([x=xn, y=yn], intParabola);
```
$$(\%o3)\quad \frac{(zt-z0)^2}{a^2}+\frac{(yn-y0)^2}{b^2}-\frac{(xn-x0)^2}{c^2}<=0$$

##### 1.2 lati bagnati

Tutti i lati con entrambi i nodi bagnati

##### 1.3 lati parzialmente bagnati

Per i lati con un solo nodo bagnato cerchiamo l'intersezione della parabola con il lato di bordo

Equazione retta passante per il lato di bordo

```
(%i4) eqRetta: y-y1 = (y2-y1)/(x2-x1)*(x-x1);
```
$$(\%o4)\quad y-y1=\frac{(x-x1)(y2-y1)}{x2-x1}$$

```
(%i5) bordoParabola: lhs(intParabola)=0;
```
$$(\%o5)\quad \frac{(zt-z0)^2}{a^2}+\frac{(y-y0)^2}{b^2}-\frac{(x-x0)^2}{c^2}=0$$

sostituisco retta nella parabola

```
(%i6) eqRetta + y1$
       facsum(ratsubst(rhs(%),y,bordoParabola),x,[a,b,c])$
       intersezione: part(lhs(%),1)=0;
```
$$(\%o8)\quad b^2\,c^2\,(x2-x1)^2\,(z0-zt)^2+a^2\,c^2\,(x2\,y0-x1\,y0+x1\,y2-x2\,y1)^2+x\,(2\,a^2\,b^2\,(x2-x1)^2\,x0-2\,a^2\,c^2\,(y2-y1)\,(x2\,y0-x1\,y0+x1\,y2-x2\,y1))-a^2\,b^2\,(x2-x1)^2\,x0^2+x^2\,(a^2\,c^2\,(y2-y1)^2-a^2\,b^2\,(x2-x1)^2)=0$$

isolo per ottenere a*x^2 + b*x +c = 0

```
(%i9) ax2: part(lhs(intersezione),5)$
       a: part(%,2)$ print("a = ", a)$
       bx: part(lhs(intersezione),3)$
       b: part(%,2)$ print("b = ", b)$
       c: part(lhs(intersezione),1)+part(lhs(intersezione),2)+part(lhs(intersezione),4)$ print("c = ", c)$
```
$$a = a^2\,c^2\,(y2-y1)^2-a^2\,b^2\,(x2-x1)^2$$
$$b = 2\,a^2\,b^2\,(x2-x1)^2\,x0-2\,a^2\,c^2\,(y2-y1)\,(x2\,y0-x1\,y0+x1\,y2-x2\,y1)$$
$$c = b^2\,c^2\,(x2-x1)^2\,(z0-zt)^2+a^2\,c^2\,(x2\,y0-x1\,y0+x1\,y2-x2\,y1)^2-a^2\,b^2\,(x2-x1)^2\,x0^2$$

Risolvo con x = (-b+-radq(b^2-4ac))/(2a)
delle due soluzioni accetto quella per cui abs(x-x1)+abs(x-x2)=abs(x1-x2)
oppure per evitare errori di troncamento sostituisco l'uguaglianza con "< epsilon" con epsilon tendente a zero
Sostituisco in eqRetta per ottenere la y

#### *2 Ugelli sulla testa e sul piede*

##### 2.1 nodi bagnati

Superficie e punti interni del cono per ugelli sulla testa e sul piede

```
(%i17) kill(a,b,c)$
        intCono: +(x-xV)^2/c^2-(y-yV)^2/b^2+(z-zV)^2/a^2<=0;
```
$$(\%o18)\quad \frac{(z-zV)^2}{a^2}-\frac{(y-yV)^2}{b^2}+\frac{(x-xV)^2}{c^2}<=0$$

Tagliamo con piano z=zt

```
(%i19) intParabola: subst(zt,z,intCono);
```
$$(\%o19)\quad \frac{(zt-zV)^2}{a^2}-\frac{(y-yV)^2}{b^2}+\frac{(x-xV)^2}{c^2}<=0$$

Sostituendo le coordinate (xn, yn) del un nodo di bordo n-esimo possiamo sapere se è bagnato dallo spray

(%i20) subst([x=xn, y=yn], intParabola);

$$(\%o20)\ \frac{(zt-zV)^2}{a^2}-\frac{(yn-yV)^2}{b^2}+\frac{(xn-xV)^2}{c^2}<=0$$

## 2.2 lati bagnati

Tutti i lati con entrambi i nodi bagnati

## 2.3 lati parzialmente bagnati

Per i lati con un solo nodo bagnato cerchiamo l'intersezione della parabola con il lato di bordo

Equazione retta passante per il lato di bordo

(%i21) eqRetta: y-y1 = (y2-y1)/(x2-x1)*(x-x1);

$$(\%o21)\ y-y1=\frac{(x-x1)(y2-y1)}{x2-x1}$$

(%i22) bordoParabola: lhs(intParabola)=0;

$$(\%o22)\ \frac{(zt-zV)^2}{a^2}-\frac{(y-yV)^2}{b^2}+\frac{(x-xV)^2}{c^2}=0$$

sostituisco retta nella parabola

(%i23) eqRetta + y1$
    facsum(ratsubst(rhs(%),y,bordoParabola),x,[a,b,c])$
    intersezione: part(lhs(%),1)=0;

$(\%o25)\ b^2\,c^2(x2-x1)^2(zV-zt)^2-a^2\,c^2(x2\,yV-x1\,yV+x1\,y2-x2\,y1)^2-x(2\,a^2\,b^2(x2-x1)^2\,xV-2\,a^2\,c^2(y2-y1)(x2\,yV-x1\,yV+x1\,y2-x2\,y1))+a^2\,b^2(x2-x1)^2\,xV^2-x^2$
$(a^2\,c^2(y2-y1)^2-a^2\,b^2(x2-x1)^2)=0$

isolo per ottenere a*x^2 + b*x +c = 0

(%i26) ax2: part(lhs(intersezione),5)$
    a: part(%,0)*part(%,1,2)$ print("a = ", a)$
    bx: part(lhs(intersezione),3)$
    b: part(%,0)*part(%,1,2)$ print("b = ", b)$
    c: part(lhs(intersezione),1)+part(lhs(intersezione),2)+part(lhs(intersezione),4)$ print("c = ", c)$

$a\ =\ -(a^2\,c^2(y2-y1)^2-a^2\,b^2(x2-x1)^2)$
$b\ =\ -(2\,a^2\,b^2(x2-x1)^2\,xV-2\,a^2\,c^2(y2-y1)(x2\,yV-x1\,yV+x1\,y2-x2\,y1))$
$c\ =\ b^2\,c^2(x2-x1)^2(zV-zt)^2-a^2\,c^2(x2\,yV-x1\,yV+x1\,y2-x2\,y1)^2+a^2\,b^2(x2-x1)^2\,xV^2$

Risolvo con x = (-b+-radq(b^2-4ac))/(2a)
delle due soluzioni accetto quella per cui abs(x-x1)+abs(x-x2)=abs(x1-x2)
oppure per evitare errori di troncamento sostituisco l'uguaglianza con "< epsilon" con epsilon tendente a zero
Sostituisco in eqRetta per ottenere la y

## 3 Frazione di superficie bagnata

Se entrambi i nodi sono bagnati la superficie bagnata è pari a

(%i34) SL = sqrt((x2-x1)^2+(y2-y1)^2);

$$(\%o34)\ SL=\sqrt{(y2-y1)^2+(x2-x1)^2}$$

altrimenti, dato l'unico nodo bagnato (xn,yn) ed il punto di intersezione precedentemente calcolato (x,y)

(%i35) S=sqrt((x-xn)^2+(y-yn)^2);

$$(\%o35)\ S=\sqrt{(y-yn)^2+(x-xn)^2}$$

Dal rapporto delle due sopra è possibile ottenere la frazione di superficie bagnata
ed utilizzarla come fattore di riduzione del flusso di calore sulla superficie dell'elemento

(%i36) ratio=S/SL;

$$(\%o36)\ ratio=\frac{S}{SL}$$

## 4 Un caso limite, da noi non utilizzato

Se entrambi i punti di intersezione con la parabola soddisfano l'uguaglianza, l'elemento è gigante o lo spray è attaccato alla superficie.
Chiamiamo il primo punto (xA, yA) ed il secondo (xB, yB). In questo caso posso calcolare la superficie bagnata come

(%i37) S = sqrt((xA-xB)^2+(yA-yB)^2);

$$(\%o37)\ S=\sqrt{(yA-yB)^2+(xA-xB)^2}$$

e calcolo la frazione di superficie bagnata come in precedenza

# Calcolo matrici di rigidezza, di massa e vettori dei termini noti

## *1 Discretizzazione a elementi quadrilateri*

Vettori, coordinate nodali e temperature nodali

```
(%i134) x_i: matrix([x1],[x2],[x3],[x4])$
        y_i: matrix([y1],[y2],[y3],[y4])$
        T_i: matrix([T1],[T2],[T3],[T4])$
        print("x_i=", x_i,"y_i=", y_i,"T_i=", T_i)$
```

$$x\_i = \begin{bmatrix} x1 \\ x2 \\ x3 \\ x4 \end{bmatrix} \quad y\_i = \begin{bmatrix} y1 \\ y2 \\ y3 \\ y4 \end{bmatrix} \quad T\_i = \begin{bmatrix} T1 \\ T2 \\ T3 \\ T4 \end{bmatrix}$$

Funzione di forma, quadrato con $-1 \leq (\xi, \eta) \leq 1$, numerazione dei nodi antioraria con primo nodo nel primo quadrante (in alto a destra)

```
(%i138) N: matrix([(1+r)*(1+s), (1-r)*(1+s), (1-r)*(1-s),(1+r)*(1-s)])/4$
        print("N(r,s) = ",N)$
        n11: N[1,1]$ n12: N[1,2]$ n13: N[1,3]$ n14: N[1,4]$
        Nii:matrix(['n11,'n12,'n13,'n14])$
        print("N(r,s) = ",Nii)$
```

$$N(r,s) = \begin{bmatrix} \frac{(r+1)(s+1)}{4} & \frac{(1-r)(s+1)}{4} & \frac{(1-r)(1-s)}{4} & \frac{(r+1)(1-s)}{4} \end{bmatrix}$$

$$N(r,s) = \begin{bmatrix} n11 & n12 & n13 & n14 \end{bmatrix}$$

derivate funzione di forma

```
(%i146) DN: addrow(diff(N,r),diff(N,s))$
        print("DN(r,s) = ",DN)$
```

$$DN(r,s) = \begin{bmatrix} \frac{s+1}{4} & \frac{s+1}{4} & \frac{1-s}{4} & \frac{1-s}{4} \\ \frac{r+1}{4} & \frac{1-r}{4} & \frac{1-r}{4} & \frac{r+1}{4} \end{bmatrix}$$

Campi, mappati dalla funzione di forma, sono i valori delle coordinate o della temperatura all'interno dell'elemento

```
(%i148) x: N.x_i$ y: N.y_i$ T: N.T_i$
        print("x(r,s) = ", x)$
        print("y(r,s) = ", y)$
        print("T(r,s) = ", T)$
```

$$x(r,s) = \frac{(r+1)(1-s)x4}{4} + \frac{(1-r)(1-s)x3}{4} + \frac{(1-r)(s+1)x2}{4} + \frac{(r+1)(s+1)x1}{4}$$

$$y(r,s) = \frac{(r+1)(1-s)y4}{4} + \frac{(1-r)(1-s)y3}{4} + \frac{(1-r)(s+1)y2}{4} + \frac{(r+1)(s+1)y1}{4}$$

$$T(r,s) = \frac{(r+1)(1-s)T4}{4} + \frac{(1-r)(1-s)T3}{4} + \frac{(1-r)(s+1)T2}{4} + \frac{(r+1)(s+1)T1}{4}$$

Jacobiano

```
(%i154) J:addcol(DN.x_i,DN.y_i)$
        print("J(r,s) = ", J)$
```

$$J(r,s) = \begin{bmatrix} \frac{(1-s)x4}{4} + \frac{(1-s)x3}{4} + \frac{(s+1)x2}{4} + \frac{(s+1)x1}{4} & \frac{(1-s)y4}{4} + \frac{(1-s)y3}{4} + \frac{(s+1)y2}{4} + \frac{(s+1)y1}{4} \\ \frac{(r+1)x4}{4} + \frac{(1-r)x3}{4} + \frac{(1-r)x2}{4} + \frac{(r+1)x1}{4} & \frac{(r+1)y4}{4} + \frac{(1-r)y3}{4} + \frac{(1-r)y2}{4} + \frac{(r+1)y1}{4} \end{bmatrix}$$

determinante Jacobiano

```
(%i156) detJ:facsum(determinant(J),r,s)$
        print("detJ(r,s) = ", detJ)$
```

$$detJ(r,s) = \frac{-s(x3\,y4-x2\,y4-x4\,y3+x1\,y3+x4\,y2-x1\,y2-x3\,y1+x2\,y1)+r(x2\,y4-x1\,y4-x2\,y3-x4\,y2+x3\,y2+x4\,y1-x3\,y1)+x3\,y4-x1\,y4-x4\,y3+x2\,y3-x3\,y2+x1\,y2+x4\,y1-x2\,y1}{8}$$

Inverso dello Jacobiano

```
(%i158) invJ:facsum(invert(J),r, s)$
        facsum(%*detJ*4,r,s)*'detJ^-1*4^-1$
        print("invJ(r,s) = ", %)$
```

$$invJ(r,s) = \begin{bmatrix} \frac{-s(y4-y3+y2-y1)+y4-y3+y2-y1}{4\,detJ} & \frac{s(y4-y3+y2-y1)-y4+y3+y2-y1}{4\,detJ} \\ \frac{r(x4-x3+x2-x1)+x4+x3-x2-x1}{4\,detJ} & \frac{-r(x4-x3+x2-x1)+x4-x3-x2+x1}{4\,detJ} \end{bmatrix}$$

Derivate temperatura rispetto alle coordinate naturali

```
(%i61) DN.T_i$
       ratsimp(%*4)$
       DT:%*'4^-1$
       print("DT(r,s) = ", DT)$
```

$$DT(r,s) = \begin{bmatrix} \dfrac{(1-s)\ T4+(s-1)\ T3+(-s-1)\ T2+(s+1)\ T1}{4} \\ \dfrac{(-r-1)\ T4+(r+1)\ T3+(1-r)\ T2+(r-1)\ T1}{4} \end{bmatrix}$$

Derivate funzioni di forma rispetto alle coordinate globali
B matrice 2x4

```
(%i65) B: facsum(invJ.DN,r,s)$
       %*detJ*8$ %.'detJ^-1*'8^-1$
       print("B(r,s) = ", %)$
       b11: B[1,1]$ b12: B[1,2]$ b13: B[1,3]$ b14: B[1,4]$
       b21: B[2,1]$ b22: B[2,2]$ b23: B[2,3]$ b24: B[2,4]$
       Bii: matrix(['b11,'b12,'b13,'b14],['b21,'b22,'b23,'b24])$
       print("B(r,s) = ", Bii)$
```

$$B(r,s) = \begin{bmatrix} -r(y4-y3)-y4-s(y3-y2)+y2 & r(y4-y3)+s(y4-y1)+y3-y1 & -s(y4-y1)+y4+r(y2-y1)-y2 & s(y3-y2)-y3-r(y2-y1)+y1 \\ r(x4-x3)+x4+s(x3-x2)-x2 & -r(x4-x3)-s(x4-x1)-x3+x1 & s(x4-x1)-x4-r(x2-x1)+x2 & -s(x3-x2)+x3+r(x2-x1)-x1 \end{bmatrix} \cdot \frac{1}{detJ}$$

$$B(r,s) = \begin{bmatrix} b11 & b12 & b13 & b14 \\ b21 & b22 & b23 & b24 \end{bmatrix}$$

Matrice di conducibilità termica 2D

```
(%i79) K: k*diagmatrix(2,1)$ print("K = ", K)$
```

$$K = \begin{bmatrix} k & 0 \\ 0 & k \end{bmatrix}$$

## 2 Calcolo argomenti degli integrali della forma debole
Gli argomenti possono essere integrati numericamente
sommando i valori ai 4 nodi di Gauss di coordinate
r=+-radq(3)/3, s=+-radq(3)/3

Argomento dell'integrale di volume della matrice di rigidezza conduttiva(uso detJ per integrare tra -1 e 1)
arg[Kk]: matrice 4x4

```
(%i81) transpose(Bii).K.Bii*'detJ$
       argKk: ratsimp(%/k/'detJ).k.'detJ$
       print("integrando della matrice [Kk] = ", argKk)$
```

$$\text{integrando della matrice } [Kk] = \begin{bmatrix} b21^2+b11^2 & b21\,b22+b11\,b12 & b21\,b23+b11\,b13 & b21\,b24+b11\,b14 \\ b21\,b22+b11\,b12 & b22^2+b12^2 & b22\,b23+b12\,b13 & b22\,b24+b12\,b14 \\ b21\,b23+b11\,b13 & b22\,b23+b12\,b13 & b23^2+b13^2 & b23\,b24+b13\,b14 \\ b21\,b24+b11\,b14 & b22\,b24+b12\,b14 & b23\,b24+b13\,b14 & b24^2+b14^2 \end{bmatrix} \cdot k \cdot detJ$$

Argomento dell'integrale di volume della matrice di massa
arg[C]: matrice 4x4

```
(%i84) rho*cp*transpose(Nii).Nii*'detJ$
       %/rho/cp/'detJ$
       argC: %.rho.cp.'detJ$
       print("integrando della matrice [C] = ", argC)$
```

$$\text{integrando della matrice } [C] = \begin{bmatrix} n11^2 & n11\,n12 & n11\,n13 & n11\,n14 \\ n11\,n12 & n12^2 & n12\,n13 & n12\,n14 \\ n11\,n13 & n12\,n13 & n13^2 & n13\,n14 \\ n11\,n14 & n12\,n14 & n13\,n14 & n14^2 \end{bmatrix} \cdot \rho \cdot cp \cdot detJ$$

Argomento dell'integrale di volume del vettore di generazione interna
arg[QB]: vettore 4x1

```
(%i88) argQB: transpose(N).qB.'detJ$
       print("integrando del vettore {QB} = ", argQB)$
```

$$\text{integrando del vettore } \{QB\} = \begin{bmatrix} \dfrac{(r+1)\,(s+1)}{4} \\ \dfrac{(1-r)\,(s+1)}{4} \\ \dfrac{(1-r)\,(1-s)}{4} \\ \dfrac{(r+1)\,(1-s)}{4} \end{bmatrix} \cdot qB \cdot detJ$$

Funzioni di forma di superficie, numerate per lato, seguendo la numerazione dei nodi

```
(%i90) N1S: ratsubst(1,s,N)$
       N2S: ratsubst(-1,r,N)$
       N3S: ratsubst(-1,s,N)$
       N4S: ratsubst(1,r,N)$
       print("N1S = ",N1S)$
       print("N2S = ",N2S)$
       print("N3S = ",N3S)$
       print("N4S = ",N4S)$
```

$N1S = \begin{bmatrix} \frac{r+1}{2} & \frac{r-1}{2} & 0 & 0 \end{bmatrix}$

$N2S = \begin{bmatrix} 0 & \frac{s+1}{2} & \frac{s-1}{2} & 0 \end{bmatrix}$

$N3S = \begin{bmatrix} 0 & 0 & \frac{r-1}{2} & \frac{r+1}{2} \end{bmatrix}$

$N4S = \begin{bmatrix} \frac{s+1}{2} & 0 & 0 & \frac{s-1}{2} \end{bmatrix}$

Jacobiani di superficie

```
(%i98) dxsudr: J[1,1]$
       dysudr: J[1,2]$
       dxsuds: J[2,1]$
       dysuds: J[2,2]$
       J1S: ratsubst(1,s,matrix([dxsudr, dysudr]))$
       J2S: ratsubst(-1,r,matrix([dxsuds, dysuds]))$
       J3S: ratsubst(-1,s,matrix([dxsudr, dysudr]))$
       J4S: ratsubst(1,r,matrix([dxsuds, dysuds]))$
       print("J1S = ", J1S)$
       print("J2S = ", J2S)$
       print("J3S = ", J3S)$
       print("J4S = ", J4S)$
```

$J1S = \begin{bmatrix} \frac{x2-x1}{2} & \frac{y2-y1}{2} \end{bmatrix}$

$J2S = \begin{bmatrix} \frac{x3-x2}{2} & \frac{y3-y2}{2} \end{bmatrix}$

$J3S = \begin{bmatrix} \frac{x4-x3}{2} & \frac{y4-y3}{2} \end{bmatrix}$

$J4S = \begin{bmatrix} \frac{x4-x1}{2} & \frac{y4-y1}{2} \end{bmatrix}$

determinanti di superficie
dS=t*dl con dl=detJS*dr

```
(%i110) detJ1S: sqrt(J1S[1,1]^2+J1S[1,2]^2)$
        detJ2S: sqrt(J2S[1,1]^2+J2S[1,2]^2)$
        detJ3S: sqrt(J3S[1,1]^2+J3S[1,2]^2)$
        detJ4S: sqrt(J4S[1,1]^2+J4S[1,2]^2)$
        print("detJ1S = ",detJ1S)$
        print("detJ2S = ",detJ2S)$
        print("detJ3S = ",detJ3S)$
        print("detJ4S = ",detJ4S)$
```

$detJ1S = \sqrt{\frac{(y2-y1)^2}{4}+\frac{(x2-x1)^2}{4}}$

$detJ2S = \sqrt{\frac{(y3-y2)^2}{4}+\frac{(x3-x2)^2}{4}}$

$detJ3S = \sqrt{\frac{(y4-y3)^2}{4}+\frac{(x4-x3)^2}{4}}$

$detJ4S = \sqrt{\frac{(y4-y1)^2}{4}+\frac{(x4-x1)^2}{4}}$

Argomenti degli integrali di superficie della matrice di rigidezza convettiva
arg[Kc]: matrice 4x4

```
(%i118) transpose(N1S).N1S*h1*'detJ1S$
        facsum(%/h1/'detJ1S)$
        argKc1:%.h1.'detJ1S$
        transpose(N2S).N2S*h2*'detJ2S$
        facsum(%/h2/'detJ2S)$
        argKc2:%.h2.'detJ2S$
        transpose(N3S).N3S*h3*'detJ3S$
        facsum(%/h3/'detJ3S)$
        argKc3:%.h3.'detJ3S$
        transpose(N4S).N4S*h4*'detJ4S$
        facsum(%/h4/'detJ4S)$
        argKc4:%.h4.'detJ4S$
        print("integrando della matrice [Kc] per il lato 1 = ",argKc1)$
        print("integrando della matrice [Kc] per il lato 2 = ",argKc2)$
        print("integrando della matrice [Kc] per il lato 3 = ",argKc3)$
        print("integrando della matrice [Kc] per il lato 4 = ",argKc4)$
```

$integrando\ della\ matrice\ [Kc]\ per\ il\ lato\ 1 = \begin{bmatrix} \frac{(r+1)^2}{4} & \frac{(r-1)(r+1)}{4} & 0 & 0 \\ \frac{(r-1)(r+1)}{4} & \frac{(r-1)^2}{4} & 0 & 0 \\ 0 & 0 & 0 & 0 \\ 0 & 0 & 0 & 0 \end{bmatrix} \cdot h1 \cdot detJ1S$

$integrando\ della\ matrice\ [Kc]\ per\ il\ lato\ 2 = \begin{bmatrix} 0 & 0 & 0 & 0 \\ 0 & \frac{(s+1)^2}{4} & \frac{(s-1)(s+1)}{4} & 0 \\ 0 & \frac{(s-1)(s+1)}{4} & \frac{(s-1)^2}{4} & 0 \\ 0 & 0 & 0 & 0 \end{bmatrix} \cdot h2 \cdot detJ2S$

$integrando\ della\ matrice\ [Kc]\ per\ il\ lato\ 3 = \begin{bmatrix} 0 & 0 & 0 & 0 \\ 0 & 0 & 0 & 0 \\ 0 & 0 & \frac{(r-1)^2}{4} & \frac{(r-1)(r+1)}{4} \\ 0 & 0 & \frac{(r-1)(r+1)}{4} & \frac{(r+1)^2}{4} \end{bmatrix} \cdot h3 \cdot detJ3S$

$integrando\ della\ matrice\ [Kc]\ per\ il\ lato\ 4 = \begin{bmatrix} \frac{(s+1)^2}{4} & 0 & 0 & \frac{(s-1)(s+1)}{4} \\ 0 & 0 & 0 & 0 \\ 0 & 0 & 0 & 0 \\ \frac{(s-1)(s+1)}{4} & 0 & 0 & \frac{(s-1)^2}{4} \end{bmatrix} \cdot h4 \cdot detJ4S$

Argomenti degli integrali di superficie del vettore di convezione
arg[Qc]: vettore 4x1

172

FEM.wxm                                                                                         8 / 10

```
(%i134) transpose(N1S)*h1*Ta1*'detJ1S$
        facsum(%/h1/Ta1/'detJ1S)$
        argQc1:%.h1.Ta1.'detJ1S$
        transpose(N2S)*h2*Ta2*'detJ2S$
        facsum(%/h2/Ta2/'detJ2S)$
        argQc2:%.h2.Ta2.'detJ2S$
        transpose(N3S)*h3*Ta3*'detJ3S$
        facsum(%/h3/Ta3/'detJ3S)$
        argQc3:%.h3.Ta3.'detJ3S$
        transpose(N4S)*h4*Ta4*'detJ4S$
        facsum(%/h4/Ta4/'detJ4S)$
        argQc4:%.h4.Ta4.'detJ4S$
        print("integrando del vettore {Qc} per il lato 1 = ",argQc1)$
        print("integrando del vettore {Qc} per il lato 2 = ",argQc2)$
        print("integrando del vettore {Qc} per il lato 3 = ",argQc3)$
        print("integrando del vettore {Qc} per il lato 4 = ",argQc4)$
```

$$\text{integrando del vettore \{Qc\} per il lato 1} = \begin{bmatrix} \frac{r+1}{2} \\ \frac{r-1}{2} \\ 0 \\ 0 \end{bmatrix} \; . \; h1 \; . \; Ta1 \; . \; detJ1S$$

$$\text{integrando del vettore \{Qc\} per il lato 2} = \begin{bmatrix} 0 \\ \frac{s+1}{2} \\ \frac{s-1}{2} \\ 0 \end{bmatrix} \; . \; h2 \; . \; Ta2 \; . \; detJ2S$$

$$\text{integrando del vettore \{Qc\} per il lato 3} = \begin{bmatrix} 0 \\ 0 \\ \frac{r-1}{2} \\ \frac{r+1}{2} \end{bmatrix} \; . \; h3 \; . \; Ta3 \; . \; detJ3S$$

$$\text{integrando del vettore \{Qc\} per il lato 4} = \begin{bmatrix} \frac{s+1}{2} \\ 0 \\ 0 \\ \frac{s-1}{2} \end{bmatrix} \; . \; h4 \; . \; Ta4 \; . \; detJ4S$$

Argomenti degli integrali di superficie del vettore flusso di calore
arg[QS]: vettore 4x1

FEM.wxm                                                                                         9 / 10

```
(%i150) transpose(N1S)*qS1*'detJ1S$
        facsum(%/qS1/'detJ1S)$
        argQS1:%.qS1.'detJ1S$
        transpose(N2S)*qS2*'detJ2S$
        facsum(%/qS2/'detJ2S)$
        argQS2:%.qS2.'detJ2S$
        transpose(N3S)*qS3*'detJ3S$
        facsum(%/qS3/'detJ3S)$
        argQS3:%.qS3.'detJ3S$
        transpose(N4S)*qS4*'detJ4S$
        facsum(%/qS4/'detJ4S)$
        argQS4:%.qS4.'detJ4S$
        print("integrando del vettore {QS} per il lato 1 = ",argQS1)$
        print("integrando del vettore {QS} per il lato 2 = ",argQS2)$
        print("integrando del vettore {QS} per il lato 3 = ",argQS3)$
        print("integrando del vettore {QS} per il lato 4 = ",argQS4)$
```

$$\text{integrando del vettore \{QS\} per il lato 1} = \begin{bmatrix} \frac{r+1}{2} \\ \frac{r-1}{2} \\ 0 \\ 0 \end{bmatrix} \; . \; qS1 \; . \; detJ1S$$

$$\text{integrando del vettore \{QS\} per il lato 2} = \begin{bmatrix} 0 \\ \frac{s+1}{2} \\ \frac{s-1}{2} \\ 0 \end{bmatrix} \; . \; qS2 \; . \; detJ2S$$

$$\text{integrando del vettore \{QS\} per il lato 3} = \begin{bmatrix} 0 \\ 0 \\ \frac{r-1}{2} \\ \frac{r+1}{2} \end{bmatrix} \; . \; qS3 \; . \; detJ3S$$

$$\text{integrando del vettore \{QS\} per il lato 4} = \begin{bmatrix} \frac{s+1}{2} \\ 0 \\ 0 \\ \frac{s-1}{2} \end{bmatrix} \; . \; qS4 \; . \; detJ4S$$

## Soluzione

FEM.wxm                                                                                        10 / 10

```
Soluzione
[C(T)]{T'} + ([Kk(T)]+[Kc(T,t)]){T} = {QB}+{QS}+{Qc}    con   {T'} = {Tn+1 - Tn} / dt
semplificabile a
[C]{T'} + [K]{T} = [Q]
Metodo theta
([C]+theta*dt*[K]){Tn+1} = ([C]-(1-theta)*dt*[K]) {Tn} + dt(theta{Qn+1}+(1-theta){Qn})
```

*Annex 4*

## Scope of work
Definition of one or more mathematical laws able to predict the heat transfer coefficient (HTC) behavior of nozzle atomizer based on the available data set within the temperature and pressures ranges:
$200 \leq T_{wall} \leq 1000$ °C,
$P_a \leq 4.0$ bar,
$P_w \leq 5.0$ bar.

## Activity performed
A data analysis of experimental data to define the "training" and "test" subsamples data has
been carried out. Several mathematical laws able to predict HTC behaviour of nozzle atomizer as function of fluid dynamic variable of spray have been investigated.
The "BEST" function has been defined considering:
- predicted value and so estimation error (following named RESIDUAL);
- function shape;
- function applicability in control system.

Additional six mathematical laws of spray fluid dynamic behaviour have been determined as a function of the pressure of air and water. In particular:
- Air flow rate: $Q_{air}$
- Water flow rate: $Q_{water}$
- Water specific flow rate: W
- Impact area $Area_{impact}$
- Impact velocity $v_{impact}$
- Sauter mean diameter (droplet diameter): $D_{32}$

## Statistical analysis: sample data
HTC experimental and fluidynamic data have been divided in different subsamples:
- for training: where the model/mathematical law is trained
- for test: where the model/mathematical law is tested.

In particular:

## Training1:
Data have been composed by the points of intersection for 2,3,4,5,6 bar of air pressure and 2,3,4,5,6 bar of water pressure. Data have been used to obtain the model/mathematical law relating to $Q_w$, $Q_a$, $Area_{impact}$, W.
In this way the **design of experiment for $Q_w$ and $Q_a$ is central composite design** (CCD) that is well balanced therefore the best to detect the mathematical functions that bind variables of influence with the variable that measure the phenomenon to be studied.
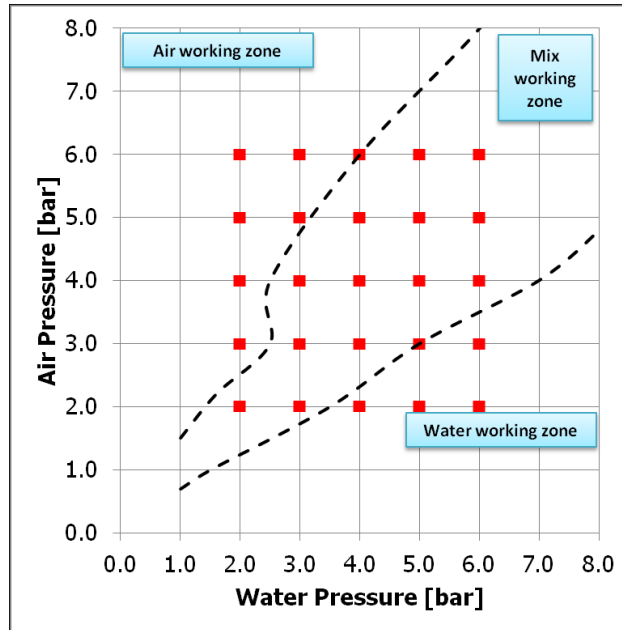
**Training2:**
Data have been selected from the starting sample at the points of intersection for 1,2,3,4,5,6 bar of air pressure and 1,2,3,4,5,6 bar of water pressure. Only the points within the mix working condition have been considered. Data have been used to get the model/mathematical law relative to $D_{32}$ and $v_{impact}$.
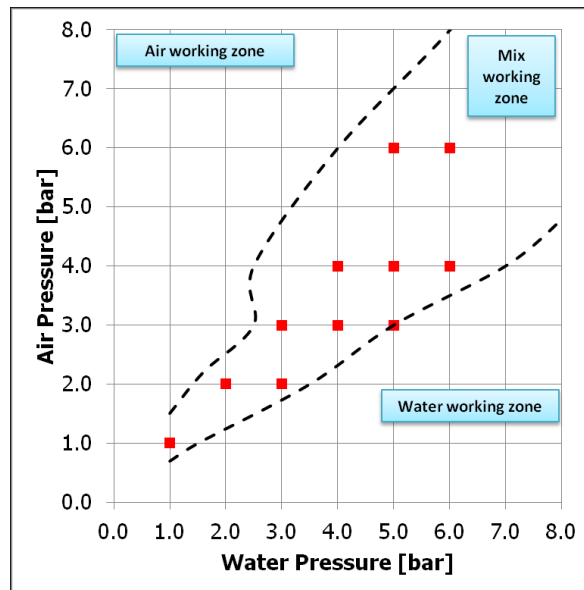


**Training3:**
Data have been selected from the starting sample at the points of intersection 1,2,3,4,5,6 bar of air pressure and 1,2,3,4,5,6 bar of water pressure. Only the mix working zone intersections have been considered.
Only the points where the value of the variable HTC is measured have been considered. Data have been used to get the model / mathematical law relative to HTC.
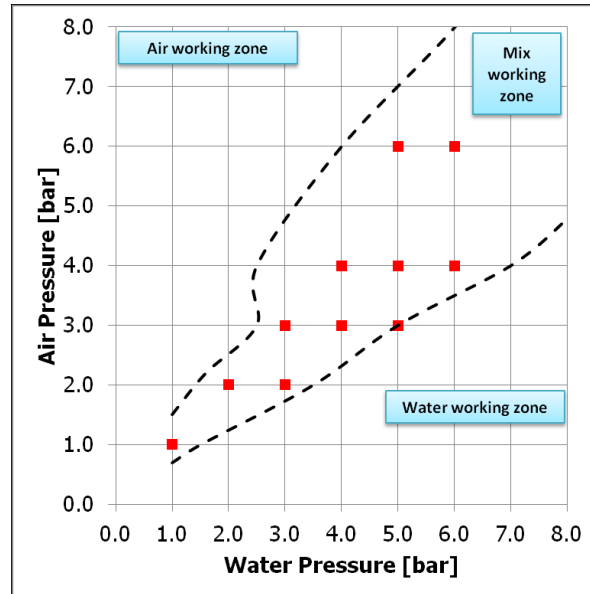
**Test1**:
Data have been used to test the model/mathematical law relating to $Q_w$, $Q_a$, Area$_{impact}$, W. Contains all the data in mix working zone not used in Training1. Data have been selected in the Training1 network.

**Test2**:
Data have been used to test the model/mathematical law relating to $Q_w$, $Q_a$, Area$_{impact}$, W. Contains all the points outside the network of Training1.

**Test3:**
Data have been used to test the model/mathematical law relating to $Q_w$, $Q_a$, Area$_{impact}$, W. Major points of interest contains all points with network:
$2 \leq Pw \leq 5$ bar
$2 \leq Pa \leq 4$ bar
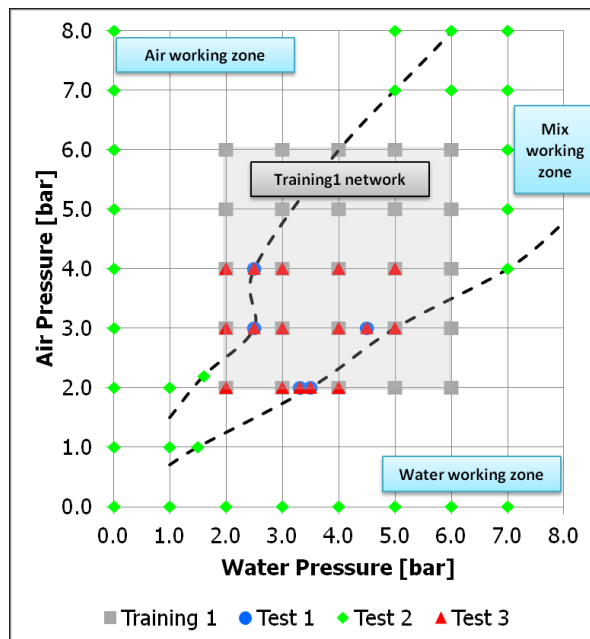
**Test4**:
Data have been used to test the model/mathematical law relative to $D_{32}$ and $V_{impact}$. Contains all the data in mix working zone not used in Training2.
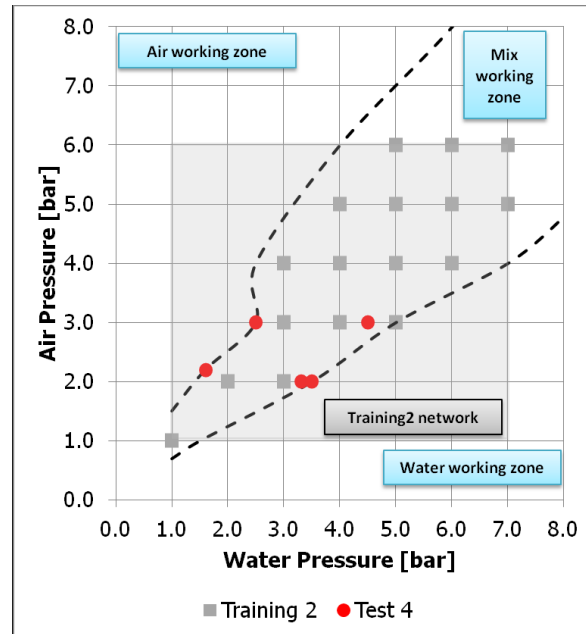


**Test5**:
Data have been used to test the model/mathematical law relative to HTC. Contains all the data in mix working zone not used in Training3.
Has been selected in the Training3 network.
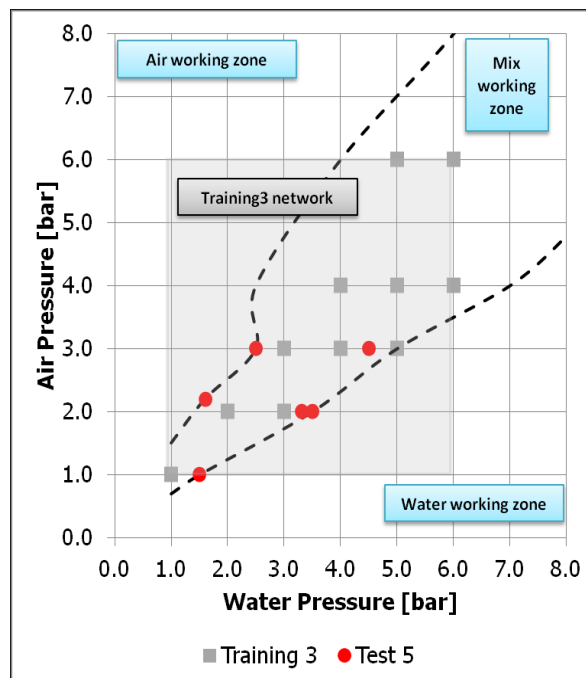
**Methodology used**

The identification of the model (multiple variables) was performed by linear regression using the procedures called "stepwise" and "backward" in a reasoned way to select the variables to be entered in the prediction model.

The procedure "stepwise" inserts the variables one at a time, as long as their contribution is significant, in particular cases, removes the variables whose contribution is no more significant due to the entry of other variables in the model.

The procedure "backward" removes the variables whose contribution is not significant one by one. Moreover, in addition to the calculation of the coefficients of the regression model and the calculation dell'R-sq, the analysis includes:

The test associated to the null hypothesis that all the coefficients of the regression are simultaneously equal to zero. It assesses the goodness of the global model: if this test is successful (reject null hypothesis), the contribution of the regression model to the explanation of the variability of the dependent variables against independent is significant at least at 95%. If this test is not successful null hypothesis (accept null hypothesis), the model is discarded.

The tests associated to the null hypothesis that each coefficient of the regression is equal to zero. If this test is successful (reject null hypothesis), the contribution to the explanation of the variability of the dependent variable against the independent variable is significant at least at 90%. If this test is not successful null hypothesis (accept null hypothesis), the model is discarded.

The variables are also some non-linear mathematical functions that tie together even more variables.

| livelli | Temperature | vimp | W | D32 | HTC vimp | HTC W | HTC D32 | HTC Temperature |
|---|---|---|---|---|---|---|---|---|
| 1 | | 7.09 | 67.86 | 84.33 | 1.21 | 1.21 | 0.78 | |
| 2 | | 11.34 | 78.17 | 174.40 | 1.46 | 0.78 | 1.71 | |
| 3 | 200 | 12.84 | 101.42 | 192.97 | 1.71 | 1.43 | 1.20 | 2.85 |
| 4 | 400 | 16.76 | 135.23 | 202.37 | 1.67 | 1.80 | 1.43 | 2.55 |
| 5 | 500 | 16.83 | 152.13 | 225.80 | 1.43 | 1.71 | 1.88 | 2.32 |
| 6 | 600 | 17.35 | 233.28 | 228.20 | 1.69 | 1.69 | 1.80 | 1.98 |
| 7 | 700 | 21.31 | 241.76 | 245.90 | 2.04 | 1.46 | 1.69 | 1.33 |
| 8 | 800 | 21.55 | 250.14 | 255.45 | 1.80 | 1.20 | 1.21 | 0.79 |
| 9 | 1000 | 23.58 | 309.89 | 267.32 | 1.88 | 1.88 | 2.04 | 0.33 |
| 10 | 1200 | 24.31 | 330.83 | 274.42 | 1.20 | 1.67 | 1.71 | 0.23 |
| 11 | | 27.60 | 414.29 | 276.18 | 0.78 | 2.04 | 1.46 | |
| 12 | | 29.10 | 433.85 | 335.73 | 1.71 | 1.71 | 1.67 | |

| Media Vimp | 19.14 |
|---|---|
| Media W | 229.07 |
| Media D32 | 230.26 |
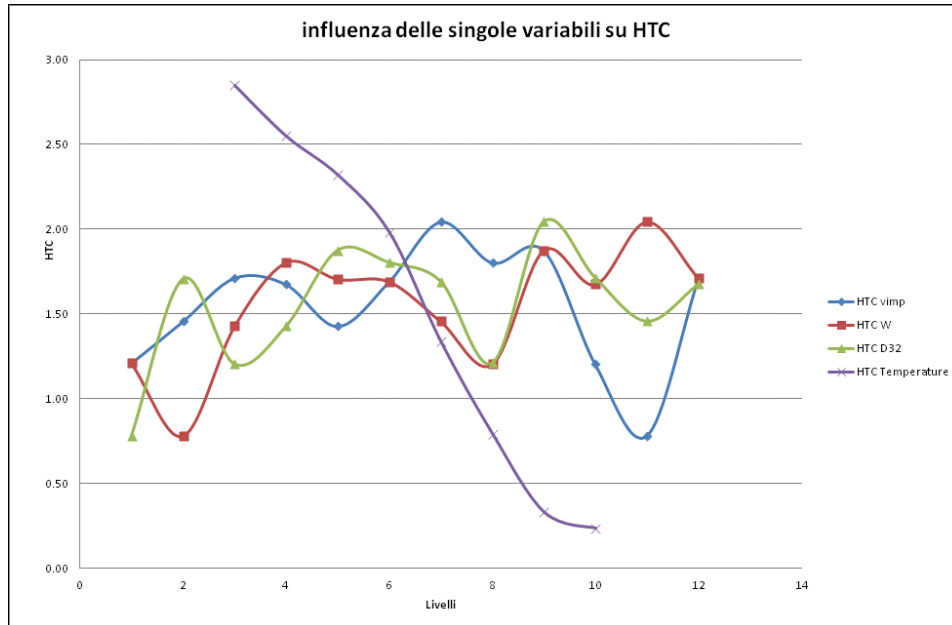
Literature like equation:
• Many authors break the correlation in three/four branches with changes in temperature. Usually, ranges are 0 - 200 ° C, 200 ° C - 400/500 ° C, 400/500 ° C - 700/800 ° C, T> 700/800 ° C.

$$HTC = kT_{wall}^a W^b v_{impact}^c f(D_{32})$$

We opt to utilize an evolution method for better confidence named Sigmoid equation:

$$HTC = HTC_0 + \frac{a}{1+\left(\frac{T_w}{T_0}\right)^b}$$

$$HTC = HTC_0 + \frac{a}{1+\left(\frac{T_w}{T_0}\right)^b}$$

$$HTC_0 = yo$$

$$T_0 = x_1 W^{x_2} D_{32}^{x_3} \left(\frac{Q_w}{Q_a}\right)^{x_4}$$

$$a = a_1 W^{a_2} D_{32}^{a_3} \left(\frac{Q_w}{Q_a}\right)^{a_4} v_{imp}^{a_5}$$

$$b = b_1 W^{b_2} D_{32}^{b_3} \left(\frac{Q_w}{Q_a}\right)^{b_4}$$

| | |
|---|---|
| yo | 0.00331 |
| x1 | 658.54 |
| x2 | 0.14 |
| x3 | -0.123 |
| x4 | -0.03568 |
| a1 | 0.0308 |
| a2 | 0.1434 |
| a3 | 0.6409 |
| a4 | -0.1271 |
| a5 | 0.0872 |
| b1 | 0.3328 |
| b2 | -0.0591 |
| b3 | 0.6015 |
| b4 | -0.0442 |

## Regressione
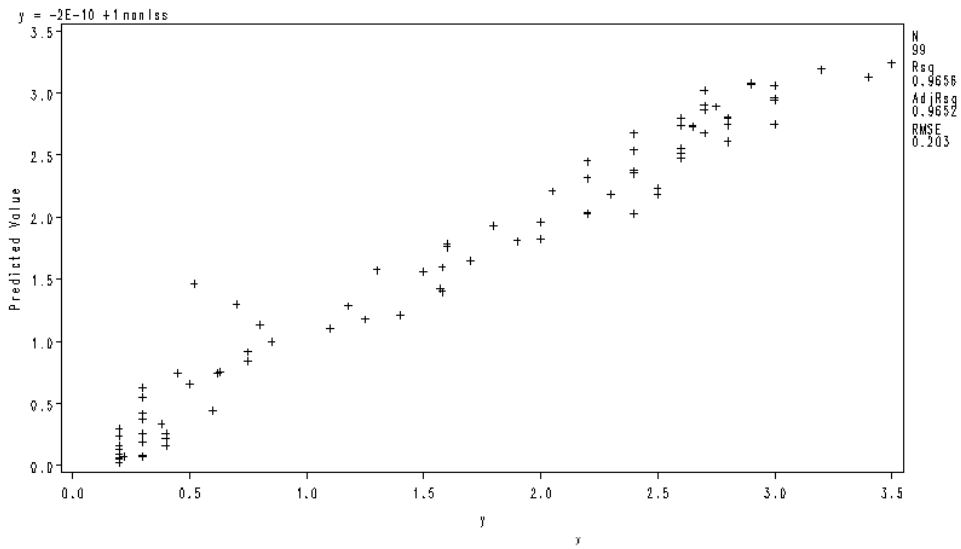


### Training

| Variable | N | Minimum | Maximum | Mean |
|---|---|---|---|---|
| y | 99 | 0.20 | 3.50 | 1.76 |
| sigmoide_new | 99 | 0.02 | 3.24 | 1.76 |
| residuo_sigmoide_new | 99 | -0.95 | 0.37 | 0.00 |

### Test

| Variable | N | Minimum | Maximum | Mean |
|---|---|---|---|---|
| y | 88 | 0.20 | 3.40 | 1.54 |
| sigmoide_new | 88 | 0.03 | 3.23 | 1.46 |
| residuo_sigmoide_new | 88 | -0.93 | 1.00 | 0.08 |

| Source | DF | Sum of Squares | Mean Square | F Value | Pr > F |
|---|---|---|---|---|---|
| Model | 1 | 112.12121 | 112.12121 | 2719.52 | <.0001 |
| Error | 97 | 3.99915 | 0.04123 | | |
| Corrected Total | 98 | 116.12036 | | | |

#### Sigmoide

| Variable | DF | Parameter Estimate | Standard Error | t Value | Pr > \|t\| | Standardized Estimate | Variance Inflation |
|---|---|---|---|---|---|---|---|
| Intercept | 1 | -2.04E-10 | 0.0395 | 0 | 1 | 0 | 0 |
| HTC | 1 | 1 | 0.01918 | 52.15 | <.0001 | 0.98263 | 1 |

| R-Square | 0.9656 |
|---|---|
| Adj R-Sq | 0.9652 |

## test 5
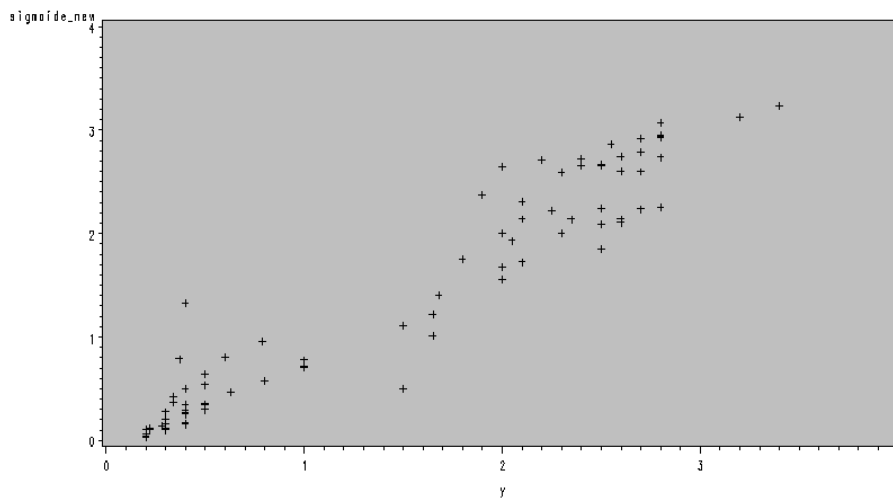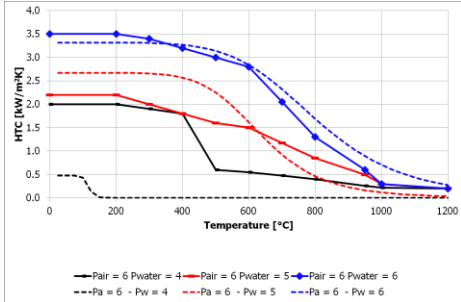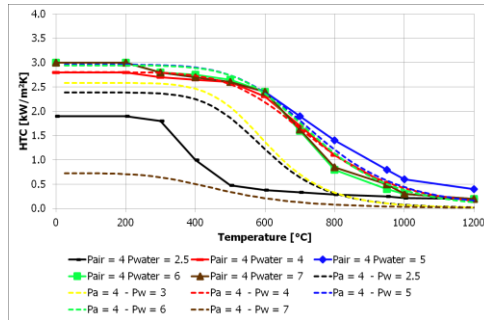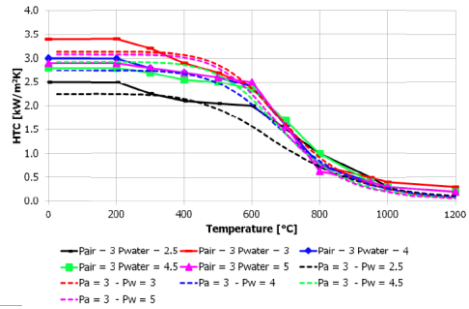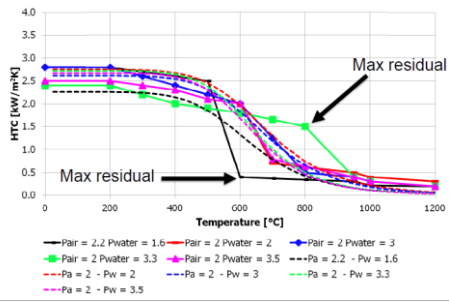
### Computational Methods for variables derived from the primary variables

For the system of equations represented by the nonlinear model

$$\mathbf{Y} = \mathbf{F}(\beta_0, \beta_1, \ldots, \beta_r, \mathbf{Z}_1, \mathbf{Z}_2, \ldots, \mathbf{Z}_n) + \epsilon = \mathbf{F}(\beta^*) + \epsilon$$

where **Z** is a matrix of the independent variables, $\beta^*$ is a vector of the parameters, $\epsilon$ is the error vector, and **F** is a function of the independent variables and the parameters, there are two approaches to solving for the minimum. The first method is to minimize

$$L(\beta) = 0.5(\mathbf{e}'\mathbf{e})$$

where $\mathbf{e} = \mathbf{Y} - \mathbf{F}(\beta)$ and $\beta$ is an estimate of $\beta^*$.

The second method is to solve the nonlinear "normal" equations

$$\mathbf{X}'\mathbf{F}(\beta) = \mathbf{X}'\mathbf{Y}$$

where

$$\mathbf{X} = \frac{\partial \mathbf{F}}{\partial \beta}$$

In the nonlinear situation, both **X** and $\mathbf{F}(\beta)$ are functions of $\beta$ and a closed-form solution generally does not exist. Thus, PROC NLIN uses an iterative process: a starting value for $\beta$ is chosen and continually improved until the error sum of squares $\epsilon'\epsilon$ is minimized.

The iterative techniques that PROC NLIN uses are similar to a series of linear regressions involving the matrix **X** evaluated for the current values of $\beta$ and $\mathbf{e} = \mathbf{Y} - \mathbf{F}(\beta)$, the residuals evaluated for the current values of $\beta$.

The iterative process begins at some point $\beta_0$. Then **X** and **Y** are used to compute a $\Delta$ such that

$$SSE(\beta_0 + k\Delta) < SSE(\beta_0)$$

The four methods differ in how $\Delta$ is computed to change the vector of parameters.

$$\text{Gauss-Newton: } \Delta = (\mathbf{X}'\mathbf{X})^-\mathbf{X}'\mathbf{e}$$

#### *Gauss-Newton*

The Gauss-Newton method uses the Taylor series

$$\mathbf{F}(\beta) = \mathbf{F}(\beta_0) + \mathbf{X}(\beta - \beta_0) + \cdots$$

where $\mathbf{X} = \partial\mathbf{F}/\partial\beta$ is evaluated at $\beta = \beta_0$.

Substituting the first two terms of this series into the normal equations

$$
\begin{aligned}
\mathbf{X}'\mathbf{F}(\beta) &= \mathbf{X}'\mathbf{Y} \\
\mathbf{X}'(\mathbf{F}(\beta_0) + \mathbf{X}(\beta - \beta_0)) &= \mathbf{X}'\mathbf{Y} \\
(\mathbf{X}'\mathbf{X})(\beta - \beta_0) &= \mathbf{X}'\mathbf{Y} - \mathbf{X}'\mathbf{F}(\beta_0) \\
(\mathbf{X}'\mathbf{X})\Delta &= \mathbf{X}'\mathbf{e}
\end{aligned}
$$

and therefore

$$\Delta = (\mathbf{X}'\mathbf{X})^-\mathbf{X}'\mathbf{e}$$

# Experimental vs Predicted Data
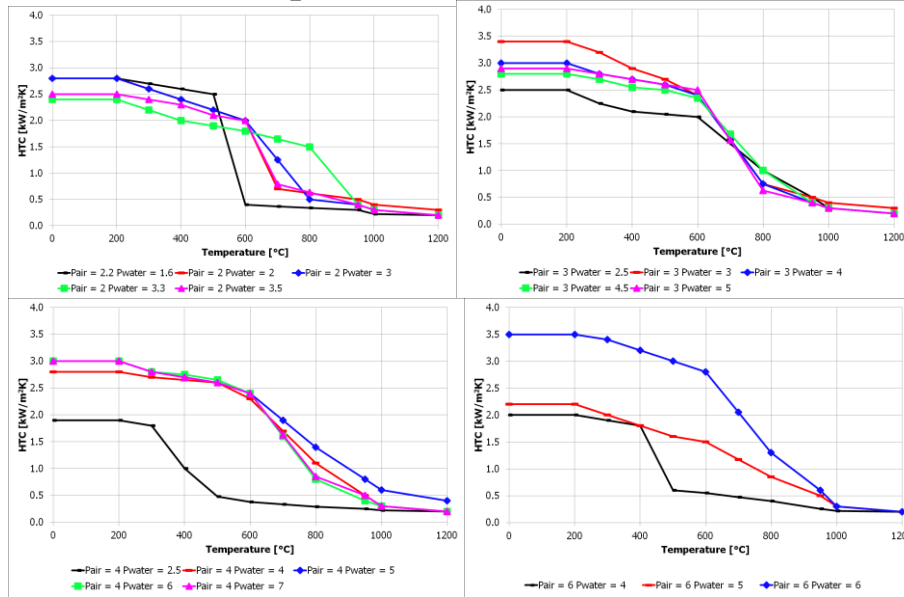


## HTC Literature Tw≤200°C
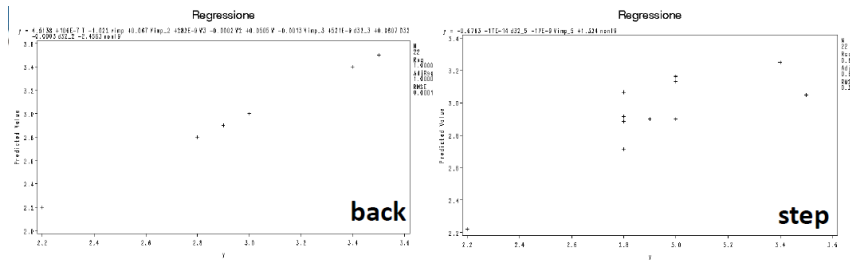


back

step

Training

| Variable | N | Minimum | Maximum | Mean |
|---|---|---|---|---|
| y | 22 | 2.20 | 3.50 | 2.93 |
| y_stim_step | 22 | 2.22 | 3.25 | 2.93 |
| y_stim_back | 22 | 4.64 | 41.82 | 22.03 |
| residuo_y_stim_step | 22 | -0.27 | 0.45 | 0.00 |
| residuo_y_stim_back | 22 | -38.92 | -2.44 | -19.10 |

Test

| Variable | N | Minimum | Maximum | Mean |
|---|---|---|---|---|
| y | 12 | 2.40 | 2.80 | 2.60 |
| y_stim_step | 12 | 2.56 | 2.95 | 2.69 |
| y_stim_back | 12 | 8.09 | 46.52 | 28.52 |
| residuo_y_stim_step | 12 | -0.24 | 0.13 | -0.09 |
| residuo_y_stim_back | 12 | -44.02 | -5.59 | -25.92 |

| back | | | | | |
|---|---|---|---|---|---|
| Variable | DF | Parameter Estimate | t Value | Pr > \|t\| | Standardized Estimate |
| Intercept | 1 | 4.51376 | 741.62 | <.0001 | 0 |
| T | 1 | 0.00001059 | 55.54 | <.0001 | 0.00285 |
| vimp | 1 | -1.02197 | -621.66 | <.0001 | -20.82717 |
| Vimp_2 | 1 | 0.06702 | 1463.8 | <.0001 | 51.43726 |
| W3 | 1 | 2.82E-07 | 6856.36 | <.0001 | 20.16536 |
| W2 | 1 | -0.00022029 | -5107.6 | <.0001 | -36.38477 |
| W | 1 | 0.05049 | 2543.71 | <.0001 | 17.28142 |
| Vimp_3 | 1 | -0.00127 | -2347.6 | <.0001 | -30.35955 |
| d32_3 | 1 | 5.21E-07 | 873.09 | <.0001 | 15.40308 |
| D32 | 1 | 0.08065 | 329.64 | <.0001 | 15.43383 |
| d32_2 | 1 | -0.00034534 | -596.62 | <.0001 | -28.23234 |
| nonl9 | 1 | -2.45629 | -135.08 | <.0001 | -1.64195 |

| R-Square | 1 |
|---|---|
| Adj R-Sq | 1 |

| step | | | | | |
|---|---|---|---|---|---|
| Variable | DF | Parameter Estimate | t Value | Pr > \|t\| | Standardized Estimate |
| Intercept | 1 | -0.67927 | -1.01 | 0.3259 | 0 |
| d32_5 | 1 | -1.70E-13 | -3.39 | 0.0033 | -0.59569 |
| Vimp_5 | 1 | -1.65E-08 | -2.17 | 0.0435 | -0.34091 |
| nonl9 | 1 | 1.32395 | 5.63 | <.0001 | 0.88502 |

| R-Square | 0.6727 |
|---|---|
| Adj R-Sq | 0.6182 |

$$nonl \;= e + T^{a} W^{b} v^{c}_{imp} D^{d}_{32}$$

| Parameter | Estimate |
|---|---|
| a | 0.000087 |
| b | -0.0204 |
| c | 0.122 |
| d | 0.2207 |
| e | -1.2593 |

## HTC Literature 200°C<Tw≤500°C



| Training | Variable | N | Minimum | Maximum | Mean |
|---|---|---|---|---|---|
| | y | 22 | 1.60 | 3.20 | 2.55 |
| | y_stim_step | 22 | 1.81 | 2.89 | 2.55 |
| | y_stim_back | 22 | 1.65 | 3.21 | 2.59 |
| | residuo_y_stim_step | 22 | -0.27 | 0.46 | 0.00 |
| | residuo_y_stim_back | 22 | -0.21 | 0.04 | -0.04 |

| Test | Variable | N | Minimum | Maximum | Mean |
|---|---|---|---|---|---|
| | y | 29 | 1.90 | 3.40 | 2.49 |
| | y_stim_step | 29 | 1.99 | 3.09 | 2.55 |
| | y_stim_back | 29 | 1.91 | 3.98 | 2.82 |
| | residuo_y_stim_step | 29 | -0.51 | 0.51 | -0.07 |
| | residuo_y_stim_back | 29 | -1.58 | 0.30 | -0.33 |

| back | | | | |
|---|---|---|---|---|
| Variable | DF | Parameter Estimate | t Value | Pr > \|t\| | Standardized Estimate |
| Intercept | 1 | 1.94287 | 3.56 | 0.0052 | 0 |
| vimp | 1 | -0.45317 | -5.45 | 0.0003 | -8.61975 |
| Vimp_2 | 1 | 0.0202 | 6.63 | <.0001 | 14.46573 |
| Vimp_4 | 1 | -0.00000878 | -6.62 | <.0001 | -5.80599 |
| d32_3 | 1 | 6.36E-07 | 5.27 | 0.0004 | 17.54429 |
| d32_4 | 1 | -4.17E-09 | -6.63 | <.0001 | -39.93224 |
| d32_5 | 1 | 7.02E-12 | 7.6 | <.0001 | 23.00925 |
| w5 | 1 | 9.57E-12 | 4.22 | 0.0018 | 118.98222 |
| W4 | 1 | -8.84E-09 | -3.85 | 0.0032 | -253.88123 |
| W3 | 1 | 0.00000266 | 3.4 | 0.0067 | 177.2064 |
| W2 | 1 | -0.0002717 | -2.9 | 0.0157 | -41.88382 |
| nonl | 1 | 1.27442 | 7.3 | <.0001 | 0.92234 |

| R-Square | 0.9925 |
|---|---|
| Adj R-Sq | 0.9843 |

| Step | | | | |
|---|---|---|---|---|
| Variable | DF | Parameter Estimate | t Value | Pr > \|t\| | Standardized Estimate |
| Intercept | 1 | -0.64683 | -1.15 | 0.2643 | 0 |
| d32_5 | 1 | -1.14E-13 | -2.23 | 0.0378 | -0.37278 |
| nonl | 1 | 1.30012 | 5.64 | <.0001 | 0.94094 |

| R-Square | 0.6341 |
|---|---|
| Adj R-Sq | 0.5956 |

$$nonl = e + T^{a}W^{b}v_{imp}^{c}D_{32}^{d}$$

| Parameter | Estimate |
|---|---|
| a | -0.1546 |
| b | -0.0165 |
| c | 0.1615 |
| d | 0.3184 |
| e | -0.6042 |

## HTC Literature 500°C<Tw≤800°C
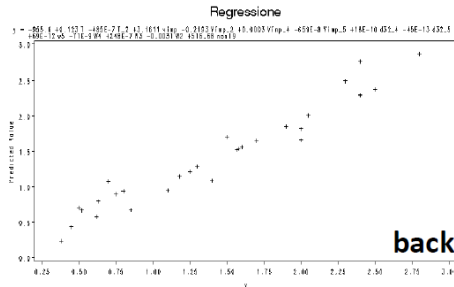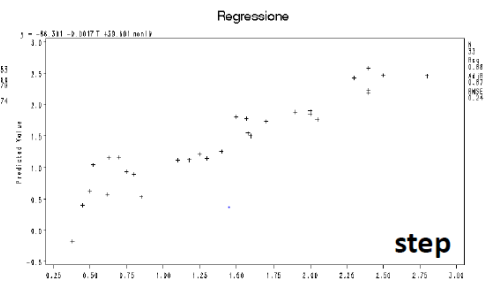


| | Variable | N | Minimum | Maximum | Mean |
|---|---|---|---|---|---|
| Training | y | 33 | 0.38 | 2.80 | 1.45 |
| | y_stim_step | 33 | -0.17 | 2.58 | 1.45 |
| | y_stim_back | 33 | 0.25 | 2.75 | 1.35 |
| | residuo_y_stim_step | 33 | -0.53 | 0.55 | 0.00 |
| | residuo_y_stim_back | 33 | -0.38 | 0.50 | 0.10 |

| | Variable | N | Minimum | Maximum | Mean |
|---|---|---|---|---|---|
| Test | y | 18 | 0.34 | 2.35 | 1.22 |
| | y_stim_step | 18 | -0.24 | 2.22 | 1.08 |
| | y_stim_back | 18 | -7.23 | 3.48 | 1.08 |
| | residuo_y_stim_step | 18 | -0.69 | 0.70 | 0.14 |
| | residuo_y_stim_back | 18 | -3.08 | 8.27 | 0.14 |

| back | | | | | |
|---|---|---|---|---|---|
| Variable | DF | Parameter Estimate | t Value | Pr > |t| | Standardized Estimate |
| Intercept | 1 | -955.5964 | -3.63 | 0.0018 | 0 |
| T | 1 | 0.12297 | 3.15 | 0.0053 | 14.23351 |
| T_2 | 1 | -0.00004849 | -2.9 | 0.0093 | -7.86476 |
| vimp | 1 | 3.16113 | 2.88 | 0.0097 | 29.68113 |
| Vimp_2 | 1 | -0.21931 | -3.03 | 0.0069 | -77.54266 |
| Vimp_4 | 1 | 0.00033238 | 3.11 | 0.0057 | 108.51926 |
| Vimp_5 | 1 | -0.00000659 | -3.13 | 0.0055 | -62.62139 |
| d32_4 | 1 | 1.76E-09 | 2.18 | 0.0421 | 8.30687 |
| d32_5 | 1 | -4.51E-12 | -2.14 | 0.0456 | -7.30333 |
| w5 | 1 | 6.89E-11 | 3.33 | 0.0035 | 423.11909 |
| W4 | 1 | -7.10E-08 | -3.32 | 0.0036 | -1007.11714 |
| W3 | 1 | 0.0000248 | 3.3 | 0.0038 | 816.32061 |
| W2 | 1 | -0.00313 | -3.28 | 0.0039 | -238.06739 |
| nonl9 | 1 | 516.68099 | 3.66 | 0.0016 | 10.36338 |

| R-Square | 0.9453 |
|---|---|
| Adj R-Sq | 0.9079 |

| Step | | | | | |
|---|---|---|---|---|---|
| Variable | DF | Parameter Estimate | t Value | Pr > |t| | Standardized Estimate |
| Intercept | 1 | -66.39128 | -8.61 | <.0001 | 0 |
| T | 1 | -0.00171 | -2.34 | 0.0259 | -0.19831 |
| nonl9 | 1 | 39.60065 | 9.39 | <.0001 | 0.79429 |

| R-Square | 0.8866 |
|---|---|
| Adj R-Sq | 0.8791 |

$$nonl9 = e + T^a W^b v_{imp}^c D_{32}^d$$

| | Estimate |
|---|---|
| a | -0.2222 |
| b | 0.0203 |
| c | 0.063 |
| d | 0.0333 |
| e | 1.3712 |

## HTC Literature 800°C<Tw≤1200°C
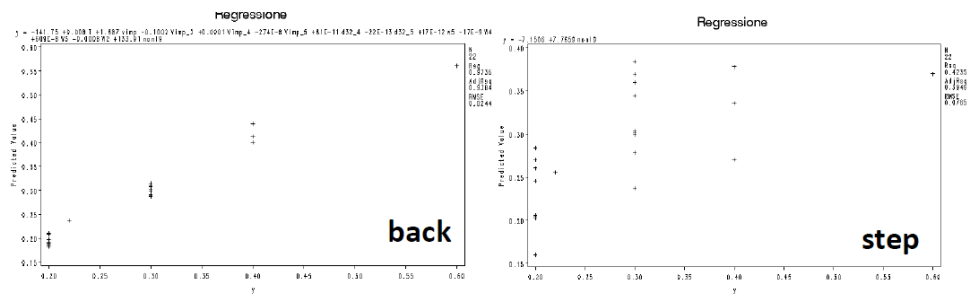


| Variable | N | Minimum | Maximum | Mean |
|---|---|---|---|---|
| y | 22 | 0.20 | 0.60 | 0.29 |
| y_stim_step | 22 | 0.16 | 0.38 | 0.29 |
| y_stim_back | 22 | 0.11 | 0.57 | 0.29 |
| residuo_y_stim_step | 22 | -0.09 | 0.23 | 0.00 |
| residuo_y_stim_back | 22 | -0.10 | 0.09 | -0.01 |

Training

| Variable | N | Minimum | Maximum | Mean |
|---|---|---|---|---|
| y | 29 | 0.20 | 0.80 | 0.36 |
| y_stim_step | 29 | 0.14 | 0.41 | 0.31 |
| y_stim_back | 29 | -2.51 | 2.18 | 0.38 |
| residuo_y_stim_step | 29 | -0.06 | 0.40 | 0.05 |
| residuo_y_stim_back | 29 | -1.88 | 2.71 | -0.02 |

Test

| back | | | | | |
|---|---|---|---|---|---|
| Variable | DF | Parameter Estimate | t Value | Pr > \|t\| | Standardized Estimate |
| Intercept | 1 | -141.75047 | -2.19 | 0.0566 | 0 |
| T | 1 | 0.00796 | 2.05 | 0.0709 | 8.28868 |
| vimp | 1 | 1.68702 | 2.52 | 0.0326 | 116.36462 |
| Vimp_2 | 1 | -0.10019 | -2.51 | 0.0336 | -260.23915 |
| Vimp_4 | 1 | 0.00014026 | 2.51 | 0.0335 | 336.40172 |
| Vimp_5 | 1 | -0.00000274 | -2.52 | 0.033 | -190.94098 |
| d32_4 | 1 | 8.10E-10 | 2.77 | 0.0218 | 28.12861 |
| d32_5 | 1 | -2.24E-12 | -2.92 | 0.017 | -26.625 |
| w5 | 1 | 1.66E-11 | 1.86 | 0.0951 | 748.35947 |
| W4 | 1 | -1.73E-08 | -1.91 | 0.0889 | -1804.5522 |
| W3 | 1 | 0.00000609 | 1.96 | 0.082 | 1472.33371 |
| W2 | 1 | -0.00075449 | -2.01 | 0.075 | -421.78323 |
| nonl9 | 1 | 133.90651 | 2.18 | 0.0573 | 11.22045 |

| R-Square | 0.9736 |
|---|---|
| Adj R-Sq | 0.9384 |

| step | | | | | |
|---|---|---|---|---|---|
| Variable | DF | Parameter Estimate | t Value | Pr > \|t\| | Standardized Estimate |
| Intercept | 1 | -7.1506 | -3.68 | 0.0015 | 0 |
| nonl9 | 1 | 7.76592 | 3.83 | 0.001 | 0.65073 |

| R-Square | 0.4235 |
|---|---|
| Adj R-Sq | 0.3946 |

$$nonl = e + T^a W^b v_{imp}^c D_{32}^d$$

| Parameter | Estimate |
|---|---|
| a | -0.1866 |
| b | -0.00792 |
| c | 0.0469 |
| d | 0.0415 |
| e | 0.5861 |

## Spray Behavior

Mathematical laws of spray fluid dynamic behavior have been determined as a function of the pressure of air and water. In particular:
- Air flow rate: Qair
- Water flow rate: Qwater
- Water specific flow rate: W
- Impact area Areaimpact, (spray angle α and transversal spray angle β)
- Sauter mean diameter (droplet diameter): D32
- Impact velocity vimpact

### 1. Air Flow rate



Water Capacity & Flow Rate vs Water Pressure
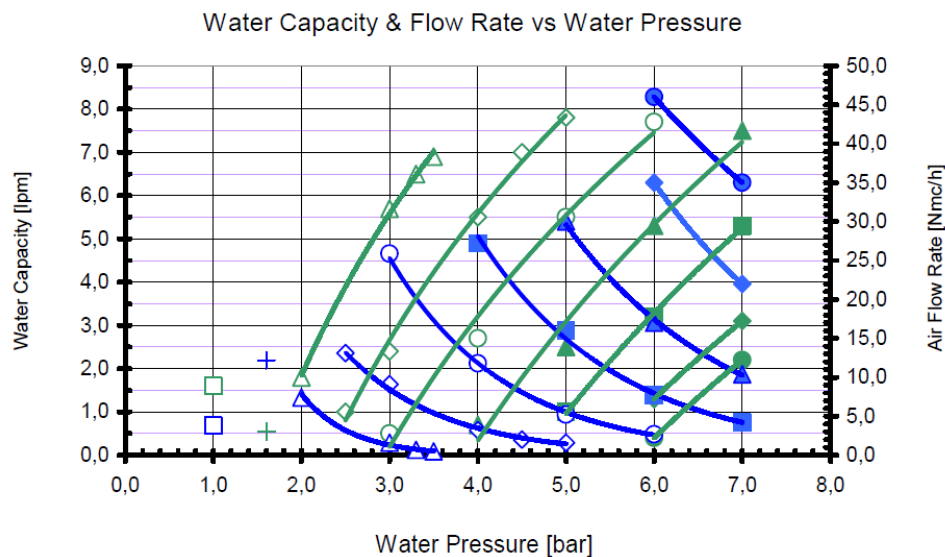
$$Q_a = \begin{cases} 0.8483 + \dfrac{107.544}{1+\left(\dfrac{P_a}{9.6438}\right)^{-1.1721}} & se & \begin{array}{l} P_w = 0 \\ P_a \geq -0.0544P_w^2 + 1.7295P_w + -0.3388 \end{array} \\ y_0 + \dfrac{a}{1+\left(\dfrac{P_a}{x_0}\right)^b} & & P_a < -0.0544P_w^2 + 1.7295P_w + -0.3388 \end{cases}$$

No water limit

$a = -0.6508P_w^2 + 11.942P_w + 13.866$

$b = 0.1341P_w^2 - 1.5739P_w - 1.8009$

$x_0 = 1.0172P_w + 0.7365$

$y_0 = -.0216P_w + 0.0446$



$$se \quad \begin{array}{l} P_w = 0 \\ P_a \geq -0.0544P_w^2 + 1.7295P_w + -0.3388 \end{array}$$

$$Q_a = -3.30932 + 1.09394 \left( 0.8483 + \dfrac{107.544}{1+\left(\dfrac{P_a}{9.6438}\right)^{-1.1721}} \right)$$

Regressione
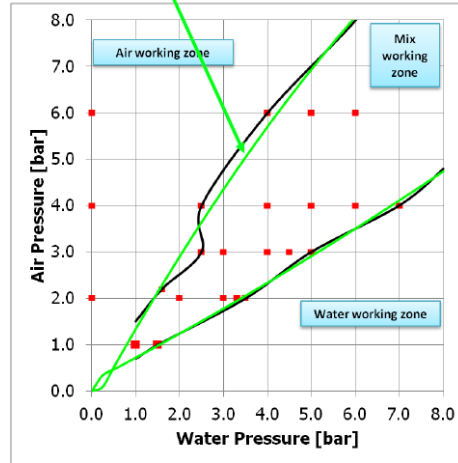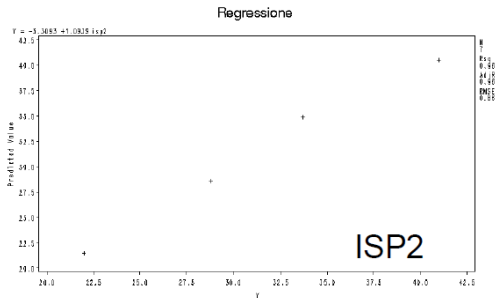


ISP2

Training

| Variable | N | Minimum | Maximum | Mean |
|---|---|---|---|---|
| Y | 7 | 22.00 | 41.00 | 34.46 |
| y_isp2 | 7 | 21.48 | 40.49 | 34.46 |
| residui_isp2 | 7 | -1.15 | 0.52 | 0.00 |

| isp2 | | | | | | | |
|---|---|---|---|---|---|---|---|
| Variable | DF | Parameter Estimate | Standard Error | t Value | Pr > \|t\| | Standardized Estimate | Variance Inflation |
| Intercept | 1 | -3.30932 | 1.88347 | -1.76 | 0.1393 | 0 | 0 |
| isp2 | 1 | 1.09394 | 0.05372 | 20.36 | <.0001 | 0.99403 | 1 |

| R-Square | 0.9881 |
|---|---|
| Adj R-Sq | 0.9857 |

**Test 1**

| Variable | N | Minimum | Maximum | Mean |
|---|---|---|---|---|
| Y | 1 | 28.80 | 28.80 | 28.80 |
| y_isp2 | 1 | 28.54 | 28.54 | 28.54 |
| residui_isp2 | 1 | 0.26 | 0.26 | 0.26 |

**Test 2**

| Variable | N | Minimum | Maximum | Mean |
|---|---|---|---|---|
| Y | 11 | 9.80 | 50.00 | 32.17 |
| y_isp2 | 11 | 5.34 | 50.03 | 31.74 |
| residui_isp2 | 11 | -1.52 | 4.46 | 0.43 |

**Test 3**

| Variable | N | Minimum | Maximum | Mean |
|---|---|---|---|---|
| Y | 3 | 22.00 | 28.80 | 26.53 |
| y_isp2 | 3 | 21.48 | 28.54 | 26.18 |
| residui_isp2 | 3 | 0.26 | 0.52 | 0.35 |

$$se \quad \begin{cases} P_w = 0 \\ P_a \geq -0.0544 P_w^2 + 1.7295 P_w + -0.3388 \end{cases}$$

$$Q_a = -3.30932 + 1.09394 \left( 0.8483 + \frac{107.544}{1 + \left( \dfrac{P_a}{9.6438} \right)^{-1.1721}} \right)$$
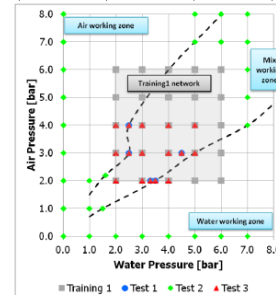


$$P_a < -0.0544 P_w^2 + 1.7295 P_w + -0.3388$$

$$Q_a = y_0 + \frac{a}{1 + \left( \dfrac{P_a}{x_0} \right)^b}$$

$$a = -0.6508 P_w^2 + 11.942 P_w + 13.866$$

$$b = 0.1341 P_w^2 - 1.5739 P_w - 1.8009$$

$$x_0 = 1.0172 P_w + 0.7365$$

$$y_0 = -.0216 P_w + 0.0446$$
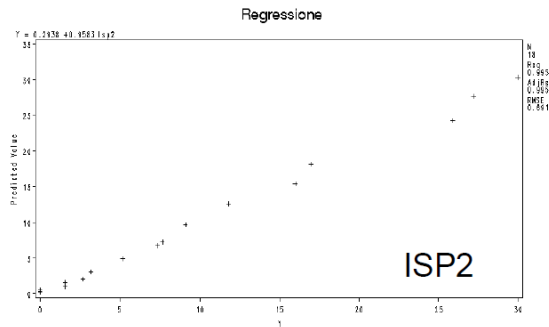


ISP2

**Training**

| Variable | N | Minimum | Maximum | Mean |
|---|---|---|---|---|
| Y | 18 | 0.00 | 30.00 | 9.24 |
| y_Isp2 | 18 | 0.23 | 30.29 | 9.24 |
| residui_isp2 | 18 | -1.15 | 1.61 | 0.00 |

| Isp2 | | | | | | | |
|---|---|---|---|---|---|---|---|
| Variable | DF | Parameter Estimate | Standard Error | t Value | Pr > \|t\| | Standardized Estimate | Variance Inflation |
| Intercept | 1 | 0.29376 | 0.22178 | 1.32 | 0.2039 | 0 | 0 |
| Isp2 | 1 | 0.95828 | 0.0161 | 59.53 | <.0001 | 0.99775 | 1 |

| R-Square | 0.9955 |
|---|---|
| Adj R-Sq | 0.9952 |

Test 1

| Variable | N | Minimum | Maximum | Mean |
|---|---|---|---|---|
| Y | 4 | 0.50 | 13.10 | 4.08 |
| y_isp2 | 4 | 0.86 | 15.20 | 4.72 |
| residui_isp2 | 4 | -2.10 | 0.27 | -0.65 |

Test 2

| Variable | N | Minimum | Maximum | Mean |
|---|---|---|---|---|
| Y | 10 | 0.00 | 46.00 | 16.91 |
| y_isp2 | 10 | 1.10 | 43.77 | 16.33 |
| residui_isp2 | 10 | -1.10 | 2.83 | 0.58 |

Test 3

| Variable | N | Minimum | Maximum | Mean |
|---|---|---|---|---|
| Y | 13 | 0.00 | 25.90 | 6.32 |
| y_isp2 | 13 | 0.52 | 24.29 | 6.42 |
| residui_isp2 | 13 | -2.10 | 1.61 | -0.10 |

Back_ordine3



Step_ordine3
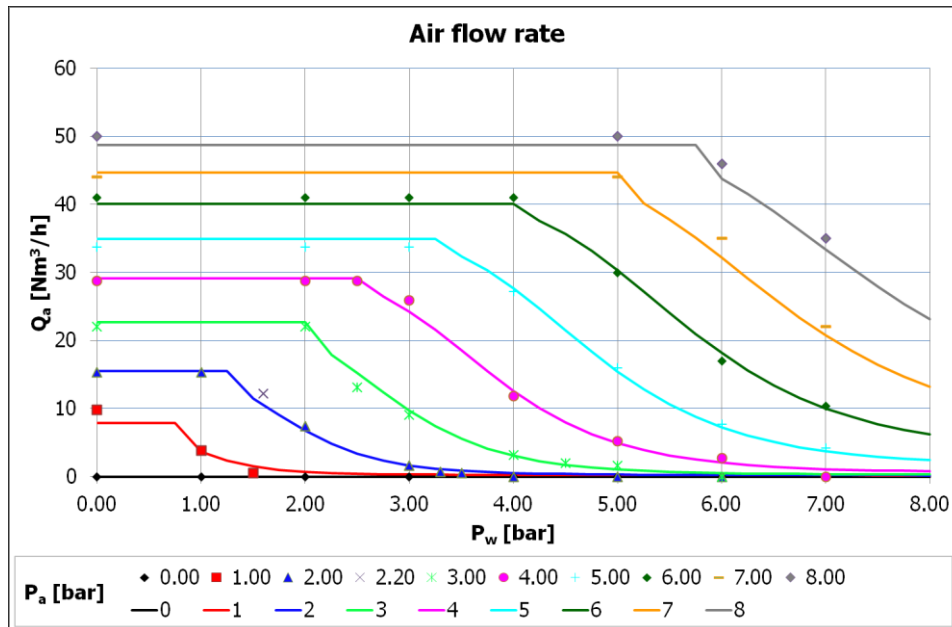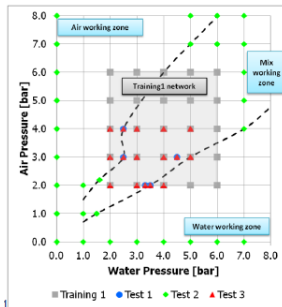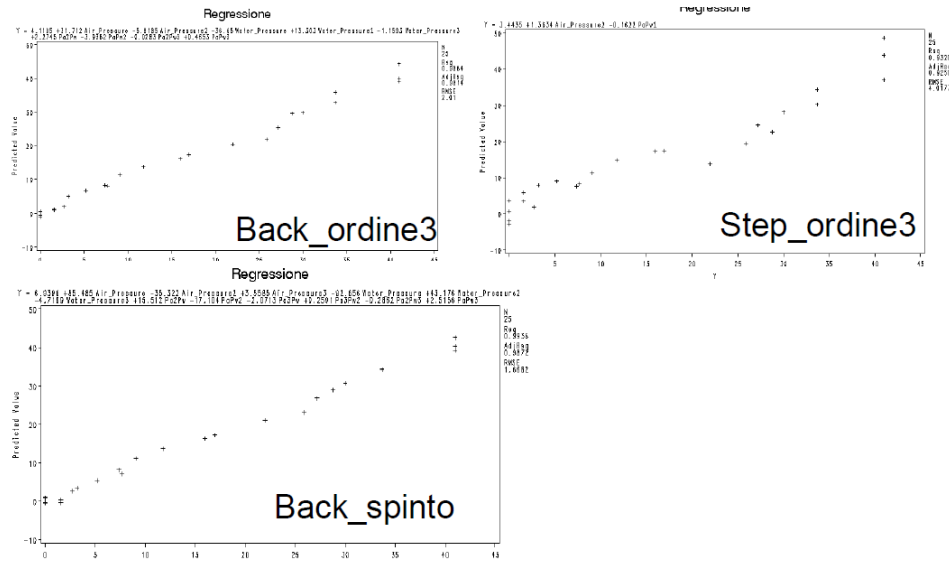


Back_spinto

### Training

| Variable | N | Minimum | Maximum | Mean |
|---|---|---|---|---|
| Y | 25 | 0 | 41 | 16.304 |
| Y_back_spinto | 25 | -0.5169361 | 42.5834965 | 16.304 |
| Y_back_doppi | 25 | -3.58214 | 42.92686 | 16.32052 |
| Y_cp_da_rag | 25 | -1.68398 | 42.12942 | 16.31024 |
| Y_back_ordine3 | 25 | -0.95249 | 44.30337 | 16.29779 |
| Y_step_ordine3 | 25 | -2.78294 | 48.63114 | 16.3041 |
| residui_step_ordine3 | 25 | -7.63114 | 8.23294 | -0.0001 |
| residui_back_ordine3 | 25 | -3.30337 | 4.08569 | 0.00621 |
| residui_back_spinto | 25 | -2.080096 | 2.8116895 | -1.33E-07 |
| residui_back_doppi | 25 | -3.4898 | 3.78546 | -0.01652 |
| residui_cp_da_rag | 25 | -2.74125 | 4.50612 | -0.00624 |

### Test 1
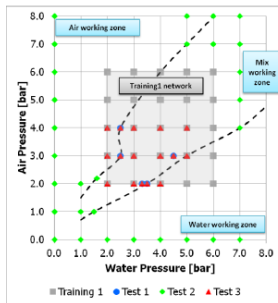


| Variable | N | Minimum | Maximum | Mean |
|---|---|---|---|---|
| Y | 5 | 0.5 | 28.8 | 9.02 |
| Y_back_spinto | 5 | -0.5145196 | 26.7231425 | 8.5700971 |
| Y_back_doppi | 5 | 0.8352775 | 25.45246 | 9.0619945 |
| Y_cp_da_rag | 5 | 0.205975 | 25.50049 | 8.9641211 |
| Y_back_ordine3 | 5 | -0.3144638 | 25.8336763 | 8.7649784 |
| Y_step_ordine3 | 5 | 4.92251 | 21.20172 | 10.003778 |
| residui_step_ordine3 | 5 | -4.6637484 | 7.59828 | -0.9837777 |
| residui_back_ordine3 | 5 | -2.3799225 | 2.9663237 | 0.2550216 |
| residui_back_spinto | 5 | -2.8432197 | 2.0768575 | 0.4499029 |
| residui_back_doppi | 5 | -2.2904975 | 3.34754 | -0.0419945 |
| residui_cp_da_rag | 5 | -2.6059925 | 3.29951 | 0.0558789 |

## Test 2

| Variable | N | Minimum | Maximum | Mean |
|---|---|---|---|---|
| Y | 29 | 0 | 50 | 18.034483 |
| Y_back_spinto | 29 | -144.921913 | 252.1296922 | 22.772549 |
| Y_back_doppi | 29 | -1.13954 | 58.99276 | 15.059226 |
| Y_cp_da_rag | 29 | -46.512 | 72.05728 | 8.5879712 |
| Y_back_ordine3 | 29 | -114.58069 | 68.95761 | 7.331718 |
| Y_step_ordine3 | 29 | -6.5379 | 90.6985 | 19.698703 |
| residui_step_ordine3 | 29 | -40.6985 | 7.89174 | -1.6642202 |
| residui_back_ordine3 | 29 | -28.95983 | 164.58069 | 10.702765 |
| residui_back_spinto | 29 | -202.129692 | 144.921913 | -4.7380658 |
| residui_back_doppi | 29 | -11.08036 | 38.91964 | 2.9752572 |
| residui_cp_da_rag | 29 | -26.05 | 82.65032 | 9.4465116 |

## Test 3



Training 1 ■  Test 1 ●  Test 2 ●  Test 3 ▲
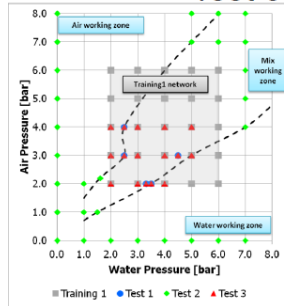
| Variable | N | Minimum | Maximum | Mean |
|---|---|---|---|---|
| Y | 16 | 0 | 28.8 | 10.10625 |
| Y_back_spinto | 16 | -0.5145196 | 28.893151 | 9.8538753 |
| Y_back_doppi | 16 | -1.539 | 27.15284 | 10.121187 |
| Y_cp_da_rag | 16 | -1.17226 | 29.7598 | 10.193029 |
| Y_back_ordine3 | 16 | -0.95249 | 29.56335 | 10.087048 |
| Y_step_ordine3 | 16 | 3.5472 | 22.6617 | 10.616584 |
| residui_step_ordine3 | 16 | -4.72714 | 8.23294 | -0.5103343 |
| residui_back_ordine3 | 16 | -2.3799225 | 4.08569 | 0.0192024 |
| residui_back_spinto | 16 | -2.8432197 | 2.8116895 | 0.2523747 |
| residui_back_doppi | 16 | -3.4898 | 3.78546 | -0.014937 |
| residui_cp_da_rag | 16 | -2.6059925 | 4.50612 | -0.0867791 |

### Back_ordine3

| Variable | DF | Parameter Estimate | Standard Error | t Value | Pr > \|t\| | Standardized Estimate | Variance Inflation |
|---|---|---|---|---|---|---|---|
| Intercept | 1 | 4.11051 | 14.22196 | 0.29 | 0.7765 | 0 | 0 |
| Air_Pressure | 1 | 31.71168 | 6.17261 | 5.14 | 0.0001 | 3.10251 | 471.52463 |
| Air_Pressure2 | 1 | -5.81851 | 1.32582 | -4.39 | 0.0005 | -4.60357 | 1422.69774 |
| Water_Pressure | 1 | -36.65048 | 14.34714 | -2.55 | 0.022 | -3.5857 | 2547.40261 |
| Water_Pressure2 | 1 | 13.30339 | 5.36087 | 2.48 | 0.0254 | 10.52555 | 23260 |
| Water_Pressure3 | 1 | -1.15929 | 0.56843 | -2.04 | 0.0594 | -6.04961 | 11376 |
| Pa2Pw | 1 | 2.27446 | 0.52835 | 4.3 | 0.0006 | 8.62166 | 5186.2161 |
| PaPw2 | 1 | -3.9362 | 1.1347 | -3.47 | 0.0034 | -14.92075 | 23920 |
| Pa2Pw3 | 1 | -0.02834 | 0.01006 | -2.82 | 0.013 | -3.7198 | 2256.1833 |
| PaPw3 | 1 | 0.46525 | 0.17264 | 2.69 | 0.0166 | 11.05197 | 21744 |

| | |
|---|---|
| R-Square | 0.9884 |
| Adj R-Sq | 0.9814 |

### Back_spinto

| Variable | DF | Parameter Estimate | Standard Error | t Value | Pr > \|t\| | Standardized Estimate | Variance Inflation |
|---|---|---|---|---|---|---|---|
| Intercept | 1 | 6.93958 | 15.3935 | 0.45 | 0.6602 | 0 | 0 |
| Air_Pressure | 1 | 85.48462 | 24.12166 | 3.54 | 0.004 | 8.36338 | 10480 |
| Air_Pressure2 | 1 | -35.32211 | 11.19956 | -3.15 | 0.0083 | -27.94662 | 147746 |
| Air_Pressure3 | 1 | 3.55845 | 1.26384 | 2.82 | 0.0156 | 18.56933 | 81847 |
| Water_Pressure | 1 | -92.65561 | 24.12166 | -3.84 | 0.0023 | -9.06495 | 10480 |
| Water_Pressure2 | 1 | 43.17646 | 11.19956 | 3.86 | 0.0023 | 34.16093 | 147746 |
| Water_Pressure3 | 1 | -4.71988 | 1.26384 | -3.73 | 0.0029 | -24.63008 | 81847 |
| Pa2Pw | 1 | 15.51234 | 4.43487 | 3.5 | 0.0044 | 58.80177 | 531784 |
| PaPw2 | 1 | -17.10433 | 4.43487 | -3.86 | 0.0023 | -64.83644 | 531784 |
| Pa3Pw | 1 | -2.07133 | 0.67558 | -3.07 | 0.0098 | -49.20384 | 484617 |
| Pa3Pw2 | 1 | 0.25908 | 0.0831 | 3.12 | 0.0089 | 34.01067 | 223917 |
| Pa2Pw3 | 1 | -0.28615 | 0.0831 | -3.44 | 0.0049 | -37.56413 | 223917 |
| PaPw3 | 1 | 2.51558 | 0.67558 | 3.72 | 0.0029 | 59.75694 | 484617 |

| | |
|---|---|
| R-Square | 0.9936 |
| Adj R-Sq | 0.9872 |

### Y_step_ordine3

| Variable | DF | Parameter Estimate | Standard Error | t Value | Pr > \|t\| | Standardized Estimate | Variance Inflation |
|---|---|---|---|---|---|---|---|
| Intercept | 1 | 3.44346 | 1.59083 | 2.16 | 0.0415 | 0 | 0 |
| Air_Pressure2 | 1 | 1.36336 | 0.07911 | 17.23 | <.0001 | 1.07869 | 1.26776 |
| PaPw2 | 1 | -0.16222 | 0.01651 | -9.82 | <.0001 | -0.61493 | 1.26776 |

| | |
|---|---|
| R-Square | 0.9667 |
| Adj R-Sq | 0.9639 |

### Y_back_doppi

| Variable | DF | Parameter Estimate | Standard Error | t Value | Pr > \|t\| | Standardized Estimate | Variance Inflation |
|---|---|---|---|---|---|---|---|
| Intercept | 1 | 11.08036 | 1.44579 | 7.66 | <.0001 | 0 | 0 |
| Pa2Pw | 1 | 2.54731 | 0.31682 | 8.04 | <.0001 | 9.65594 | 1335.34306 |
| PaPw2 | 1 | -2.73853 | 0.31682 | -8.64 | <.0001 | -10.3808 | 1335.34306 |
| Pa3Pw | 1 | -0.31908 | 0.05883 | -5.42 | <.0001 | -7.57974 | 1807.96505 |
| Pa3Pw2 | 1 | 0.05538 | 0.01149 | 4.82 | 0.0001 | 7.2693 | 2106.23504 |
| Pa2Pw3 | 1 | -0.06726 | 0.01149 | -5.85 | <.0001 | -8.82998 | 2106.23504 |
| PaPw3 | 1 | 0.42654 | 0.05883 | 7.25 | <.0001 | 10.13227 | 1807.96505 |

| | |
|---|---|
| R-Square | 0.9806 |
| Adj R-Sq | 0.9741 |

### Y_cp_da_rag

| Variable | DF | Parameter Estimate | Standard Error | t Value | Pr > \|t\| | Standardized Estimate | Variance Inflation |
|---|---|---|---|---|---|---|---|
| Intercept | 1 | -46.512 | 11.11253 | -4.19 | 0.0006 | 0 | 0 |
| Air_Pressure | 1 | 45.37991 | 6.52621 | 6.95 | <.0001 | 4.43974 | 490.45119 |
| Air_Pressure2 | 1 | -5.4559 | 0.89383 | -6.1 | <.0001 | -4.31667 | 601.67446 |
| Water_Pressure | 1 | 10.366 | 2.61925 | 3.96 | 0.001 | 1.01416 | 79 |
| Paw | 1 | -13.30424 | 1.78606 | -7.45 | <.0001 | -7.58968 | 1248.95169 |
| Pa2Pw | 1 | 2.10696 | 0.27747 | 7.59 | <.0001 | 7.98675 | 1330.91123 |
| Pa2Pw3 | 1 | -0.02484 | 0.00417 | -5.96 | <.0001 | -3.26129 | 360.77464 |
| PaPw3 | 1 | 0.10954 | 0.02097 | 5.22 | <.0001 | 2.60204 | 298.49497 |

| | |
|---|---|
| R-Square | 0.9859 |
| Adj R-Sq | 0.9801 |

## 2. Water Flow rate

Water Capacity & Flow Rate vs Water Pressure
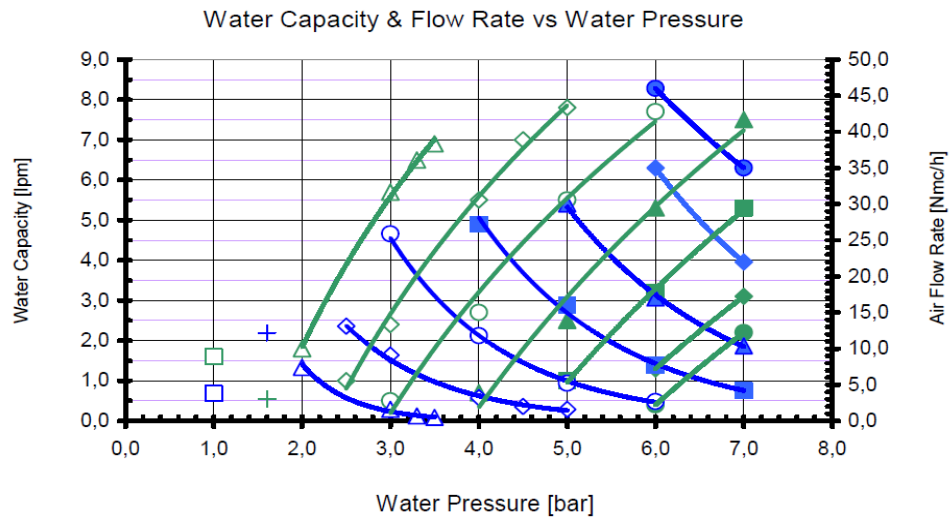


### *Water working zone*

$$Q_w = \begin{cases} 0.0995 + \dfrac{155.5435}{1+\left(\dfrac{P_w}{862.7358}\right)^{-0.5413}} & se \\[2em] y_0 + \dfrac{a}{1+\left(\dfrac{P_w}{x_0}\right)^b} \end{cases}$$

$$\begin{aligned} P_a = 0 \\ P_w \geq -0.048P_a^2 + 2.0015P_a + -0.4078 \end{aligned}$$

**No air limit**

$$P_w < -0.048P_a^2 + 2.0015P_a + -0.4078$$

$a = -0.2159P_a^2 + 3.1274P_a + 4.6313$

$b = -0.3768P_a - 3.1902$

$x_0 = -0.0337P_a^2 + 1.5462P_a + 0.1095$

$y_0 = 0$



$$se \quad \begin{aligned} P_a = 0 \\ P_w \geq -0.048P_a^2 + 2.0015P_a + -0.4078 \end{aligned}$$
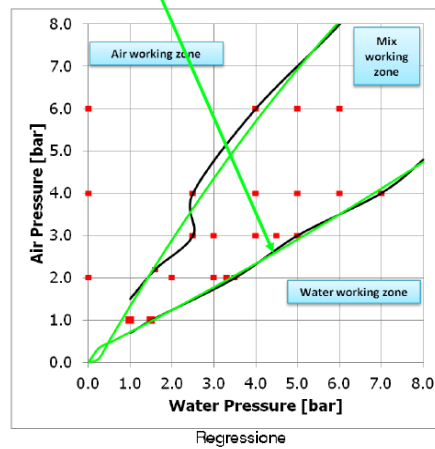
$$Q_w = 0.0995 + \dfrac{155.5435}{1+\left(\dfrac{P_w}{862.7358}\right)^{-0.5413}}$$

Regressione
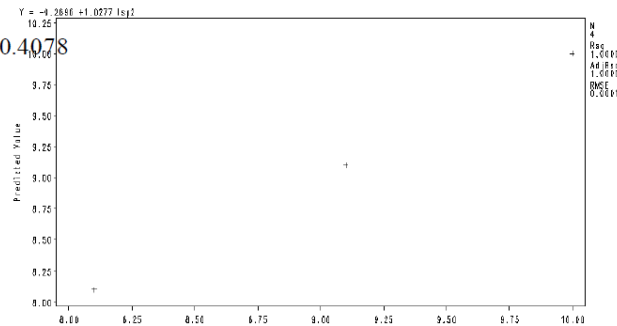


**Training**

| Variable | N | Minimum | Maximum | Mean |
|---|---|---|---|---|
| Y | 4 | 8.10 | 10.00 | 9.30 |
| y_lsp2 | 4 | 8.10 | 10.00 | 9.30 |
| residui_lsp2 | 4 | 0.00 | 0.00 | 0.00 |

| R-Square | 1 |
|---|---|
| Adj R-Sq | 1 |

| Isp2 | | | | | | | |
|---|---|---|---|---|---|---|---|
| **Variable** | **DF** | **Parameter Estimate** | **Standard Error** | **t Value** | **Pr > \|t\|** | **Standardized Estimate** | **Variance Inflation** |
| Intercept | 1 | -0.2696 | 0.00042353 | -636.54 | <.0001 | 0 | 0 |
| Isp2 | 1 | 1.02772 | 0.00004533 | 22670.3 | <.0001 | 1 | 1 |

**Test 1**

| **Variable** | **N** | **Minimum** | **Maximum** | **Mean** |
|---|---|---|---|---|
| Y | 1 | 6.90 | 6.90 | 6.90 |
| y_Isp2 | 1 | 7.55 | 7.55 | 7.55 |
| residui_Isp2 | 1 | -0.65 | -0.65 | -0.65 |

**Test 2**

| **Variable** | **N** | **Minimum** | **Maximum** | **Mean** |
|---|---|---|---|---|
| Y | 8 | 4.00 | 10.80 | 8.20 |
| y_Isp2 | 8 | 3.85 | 10.82 | 8.16 |
| residui_Isp2 | 8 | -0.02 | 0.15 | 0.04 |

**Test 3**

| **Variable** | **N** | **Minimum** | **Maximum** | **Mean** |
|---|---|---|---|---|
| Y | 2 | 6.90 | 8.10 | 7.50 |
| y_Isp2 | 2 | 7.55 | 8.10 | 7.83 |
| residui_Isp2 | 2 | -0.65 | 0.00 | -0.33 |
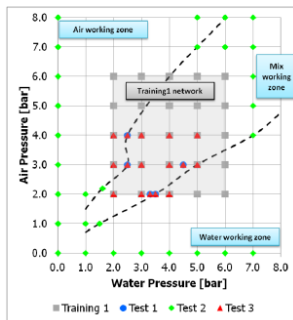


## Water-Air mixed working zone

$$P_w < -0.048 P_a^2 + 2.0015 P_a + -0.4078$$

$$Q_w = y_0 + \frac{a}{1 + \left(\dfrac{P_w}{x_0}\right)^b}$$

$$a = -0.2159 P_a^2 + 3.1274 P_a + 4.6313$$

$$b = -0.3768 P_a - 3.1902$$

$$x_0 = -0.0337 P_a^2 + 1.5462 P_a + 0.1095$$

$$y_0 = 0$$
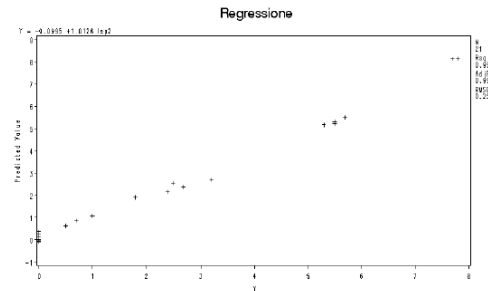


**Training**

| **Variable** | **N** | **Minimum** | **Maximum** | **Mean** | | |
|---|---|---|---|---|---|---|
| Y | 21 | 0.00 | 7.80 | 2.49 | **R-Square** | 0.9917 |
| y_Isp2 | 21 | -0.09 | 8.14 | 2.49 | **Adj R-Sq** | 0.9913 |
| residui_Isp2 | 21 | -0.42 | 0.50 | 0.00 | | |

| isp2 | | | | | | | |
|---|---|---|---|---|---|---|---|
| **Variable** | **DF** | **Parameter Estimate** | **Standard Error** | **t Value** | **Pr > \|t\|** | **Standardized Estimate** | **Variance Inflation** |
| Intercept | 1 | -0.09955 | 0.07718 | -1.29 | 0.2126 | 0 | 0 |
| Isp2 | 1 | 1.01257 | 0.02121 | 47.75 | <.0001 | 0.99586 | 1 |

**Test 1**

| Variable | N | Minimum | Maximum | Mean |
|---|---|---|---|---|
| Y | 4 | 0.00 | 7.00 | 3.63 |
| y_Isp2 | 4 | 0.22 | 6.84 | 3.63 |
| residui_Isp2 | 4 | -0.22 | 0.16 | 0.00 |

**Test 2**

| Variable | N | Minimum | Maximum | Mean |
|---|---|---|---|---|
| Y | 19 | 0.00 | 7.50 | 1.37 |
| y_Isp2 | 12 | 0.06 | 8.04 | 2.18 |
| residui_Isp2 | 12 | -0.54 | 0.81 | -0.01 |

**Test 3**

| Variable | N | Minimum | Maximum | Mean |
|---|---|---|---|---|
| Y | 14 | 0.00 | 7.80 | 3.31 |
| y_Isp2 | 14 | 0.02 | 8.14 | 3.29 |
| residui_Isp2 | 14 | -0.36 | 0.33 | 0.02 |

$$P_w < -0.048 P_a^2 + 2.0015 P_a + -0.4078$$

$$Q_w = y_0 + \frac{a}{1 + \left(\dfrac{P_w}{x_0}\right)^b}$$

$$a = -0.2159 P_a^2 + 3.1274 P_a + 4.6313$$

$$b = -0.3768 P_a - 3.1902$$

$$x_0 = -0.0337 P_a^2 + 1.5462 P_a + 0.1095$$

$$y_0 = 0$$





Water flow rate

$P_a$ [bar] — ♦ 0.00  ■ 1.00  ▲ 2.00  × 2.20  ✳ 3.00  ● 4.00  + 5.00  ◆ 6.00  — 7.00  ◆ 8.00
—0  —1  —2  —3  —4  —5  —6  —7  —8



Back_ordine3
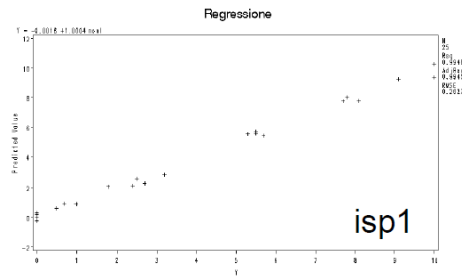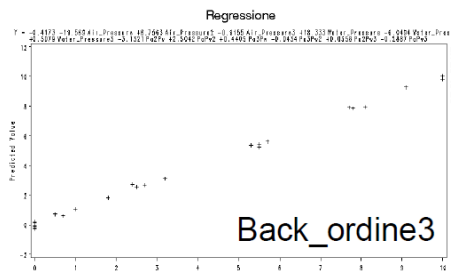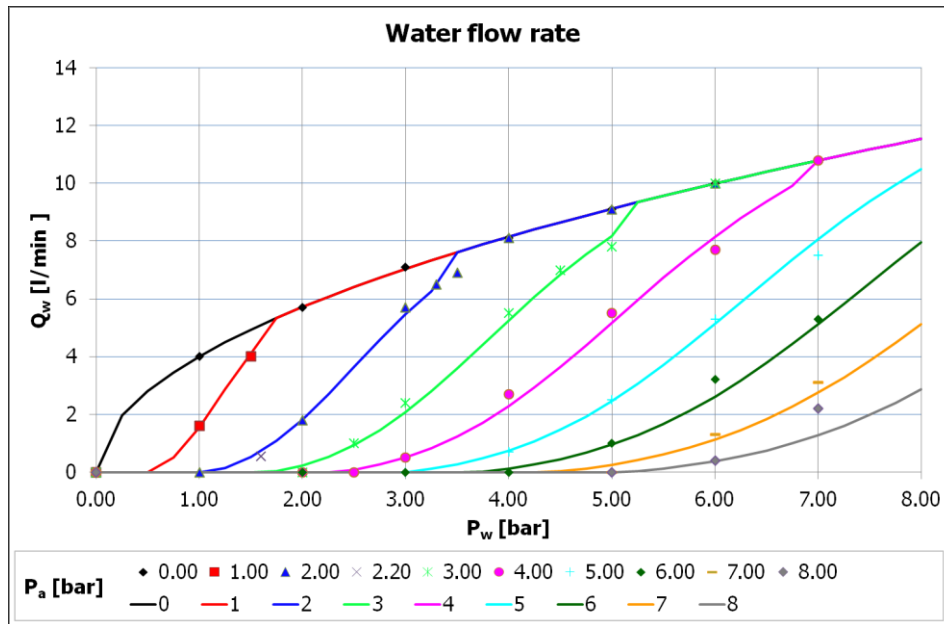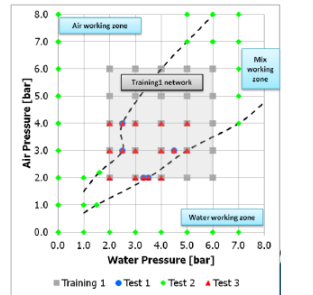


isp1

**Training**

| Variable | N | Minimum | Maximum | Mean |
|---|---|---|---|---|
| Y | 25 | 0 | 10 | 3.58 |
| y_r_back | 25 | -0.24133 | 10.01072 | 3.57716 |
| y_isp1 | 25 | -0.2316602 | 10.2845701 | 3.5788518 |
| residui_r_back | 25 | -0.31081 | 0.2702 | 0.00284 |
| residui_y_isp1 | 25 | -0.3085883 | 0.610578 | 0.0011482 |

Test 1

| Variable | N | Minimum | Maximum | Mean |
|---|---|---|---|---|
| Y | 5 | 0 | 7 | 4.28 |
| y_r_back | 5 | 0.1035 | 6.93962 | 4.3009376 |
| y_isp1 | 5 | 0.1456067 | 7.0127341 | 4.250762 |
| residui_r_back | 5 | -0.3065938 | 0.2971912 | -0.0209376 |
| residui_y_isp1 | 5 | -0.1456067 | 0.1964942 | 0.029238 |

Test 2

| Variable | N | Minimum | Maximum | Mean |
|---|---|---|---|---|
| Y | 29 | 0 | 10.8 | 3.1568966 |
| y_r_back | 29 | -65.2762 | 16.1144 | -0.0650774 |
| y_isp1 | 29 | -3.2957854 | 10.0142287 | 2.0363203 |
| residui_r_back | 29 | -10.4144 | 65.2762 | 3.2219739 |
| residui_y_isp1 | 29 | 0.0286192 | 5.4957854 | 1.1205763 |

Test 3

| Variable | N | Minimum | Maximum | Mean |
|---|---|---|---|---|
| Y | 16 | 0 | 8.1 | 3.8375 |
| y_r_back | 16 | -0.2056 | 7.95012 | 3.8299017 |
| y_isp1 | 16 | -0.2316602 | 8.0231198 | 3.8128513 |
| residui_r_back | 16 | -0.31081 | 0.2971912 | 0.0075983 |
| residui_y_isp1 | 16 | -0.2846845 | 0.3901568 | 0.0246487 |



| | | | ISP1 | | | | |
|---|---|---|---|---|---|---|---|
| Variable | DF | Parameter Estimate | Standard Error | t Value | Pr > \|t\| | Standardized Estimate | Variance Inflation |
| Intercept | 1 | -0.00184 | 0.07543 | -0.02 | 0.9808 | 0 | 0 |
| nonl | 1 | 1.00039 | 0.01512 | 66.18 | <.0001 | 0.99738 | 1 |

| R-Square | 0.9948 |
|---|---|
| Adj R-Sq | 0.9945 |

| | | | Back | | | | |
|---|---|---|---|---|---|---|---|
| Variable | DF | Parameter Estimate | Standard Error | t Value | Pr > \|t\| | Standardized Estimate | Variance Inflation |
| Intercept | 1 | -0.41732 | 2.05827 | -0.2 | 0.8427 | 0 | 0 |
| Air_Pressure | 1 | -19.56928 | 3.22532 | -6.07 | <.0001 | -7.93979 | 10480 |
| Air_Pressure2 | 1 | 8.75634 | 1.4975 | 5.85 | <.0001 | 28.73064 | 147746 |
| Air_Pressure3 | 1 | -0.91545 | 0.16899 | -5.42 | 0.0002 | -19.81115 | 81847 |
| Water_Pressure | 1 | 18.3331 | 3.22532 | 5.68 | 0.0001 | 7.43824 | 10480 |
| Water_Pressure2 | 1 | -6.04938 | 1.4975 | -4.04 | 0.0016 | -19.84877 | 147746 |
| Water_Pressure3 | 1 | 0.50788 | 0.16899 | 3.01 | 0.011 | 10.99105 | 81847 |
| Pa2Pw | 1 | -3.13211 | 0.59299 | -5.28 | 0.0002 | -49.23689 | 531784 |
| PaPw2 | 1 | 2.5042 | 0.59299 | 4.22 | 0.0012 | 39.36605 | 531784 |
| Pa3Pw | 1 | 0.44047 | 0.09033 | 4.88 | 0.0004 | 43.39145 | 484617 |
| Pa3Pw2 | 1 | -0.04341 | 0.01111 | -3.91 | 0.0021 | -23.63335 | 223917 |
| Pa2Pw3 | 1 | 0.03575 | 0.01111 | 3.22 | 0.0074 | 19.46458 | 223917 |
| PaPw3 | 1 | -0.2887 | 0.09033 | -3.2 | 0.0077 | -28.44047 | 484617 |

| R-Square | 0.998 |
|---|---|
| Adj R-Sq | 0.9961 |
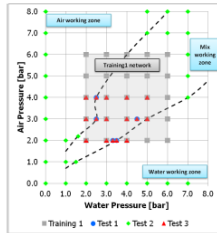
The Qw, water flow rate, is expressed by:

$$nonl = (a + bP_a)sinh^{-1}(P_w^{c+d*P_a} - (eP_a^2 + fP_a + g)) + hP_a^2 + iPa + l$$

| Parameter | Estimate |
|---|---|
| a | 4.4258 |
| b | -0.6033 |
| c | 0.8342 |
| d | 0.1094 |
| e | 0.2838 |
| f | 0.5004 |
| g | 0.3872 |
| h | -0.3352 |
| i | 2.3801 |
| l | 0.0642 |

## Water specific flow rate

Water specific flow rate is given by the ratio between the water flow rate and the impact area.
In this way the water specific flow rate are function of:
• Air pressure
• Water pressure
• Spray angles and transversal spray angles
• Distance between nozzle and surface.
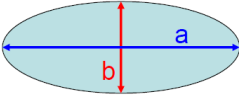
$$W = \frac{Q_w(p_a, p_w)}{A_{imp}(p_a, p_w, \alpha, \beta, d_{nozzle-plate})} = W(p_a, p_w, \alpha, \beta, d_{nozzle-plate})$$

### Impact area:

Impact area is given by the equation of ellipse area:

$$A_{imp} = \frac{\pi}{4} ab$$



Where:

• a is given by spray angles and distance between nozzle and impact surface

$$a = 2d_{nozzle-plate} \tan\left(\frac{\alpha}{2}\right)$$

• b is given by transversal spray angles and distance between nozzle and impact surface

$$b = 2d_{nozzle-plate} \tan\left(\frac{\beta}{2}\right)$$

**α e β are measured with 5° steps**

## *Spray angle α*



Training

| Variable | N | Minimum | Maximum | Mean |
|---|---|---|---|---|
| Y | 14 | 60.00 | 70.00 | 63.93 |
| nonl7_step | 14 | 59.45 | 70.59 | 63.92 |
| y_ratio | 14 | 59.48 | 70.62 | 63.93 |
| y_alfa_isp | 14 | 59.46 | 69.57 | 63.93 |
| residui_alfa_isp | 14 | -4.17 | 2.97 | 0.00 |
| residui_ratio | 14 | -2.80 | 2.99 | 0.00 |
| residui_nonl7_step | 14 | -0.89 | 1.36 | 0.01 |

Test 1

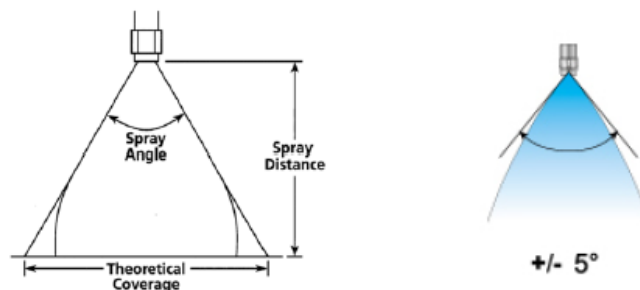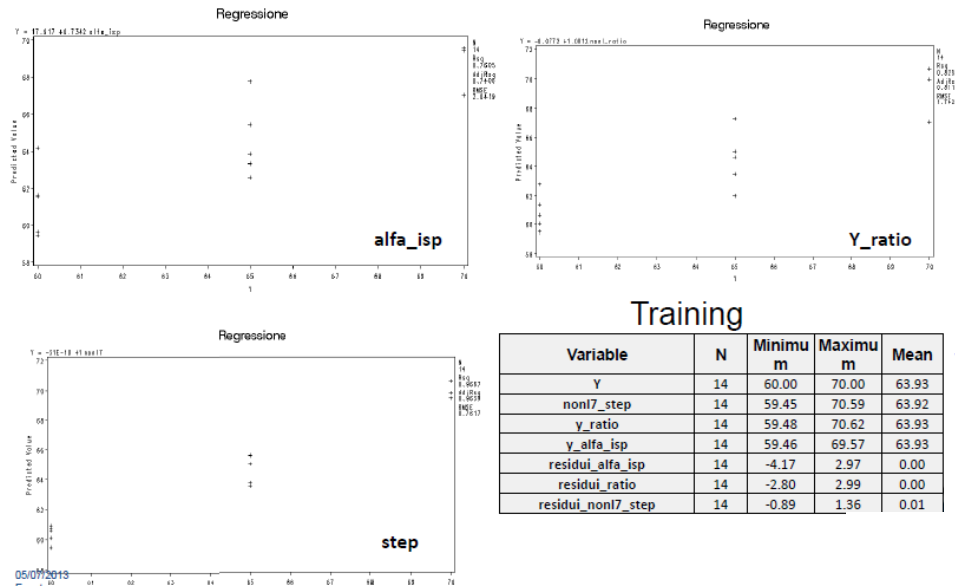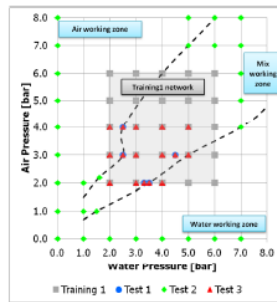| Variable | N | Minimum | Maximum | Mean |
|---|---|---|---|---|
| Y | 4 | 65.00 | 70.00 | 68.75 |
| nonl7_step | 4 | 62.78 | 70.94 | 68.62 |
| y_ratio | 4 | 63.35 | 76.73 | 71.00 |
| y_alfa_isp | 4 | 61.87 | 73.77 | 69.21 |
| residui_alfa_isp | 4 | -3.77 | 3.13 | -0.46 |
| residui_ratio | 4 | -6.73 | 1.65 | -2.25 |
| residui_nonl7_step | 4 | -0.94 | 2.22 | 0.13 |

Test 2

| Variable | N | Minimum | Maximum | Mean |
|---|---|---|---|---|
| Y | 8 | 55.00 | 70.00 | 60.00 |
| nonl7_step | 8 | 59.28 | 69.25 | 61.06 |
| y_ratio | 8 | 57.43 | 77.97 | 62.88 |
| y_alfa_isp | 8 | 57.95 | 73.50 | 62.75 |
| residui_alfa_isp | 8 | -6.26 | 8.14 | -2.75 |
| residui_ratio | 8 | -7.97 | 5.18 | -2.88 |
| residui_nonl7_step | 8 | -4.29 | 7.00 | -1.06 |



Test 3

| Variable | N | Minimum | Maximum | Mean |
|---|---|---|---|---|
| Y | 12 | 60.00 | 70.00 | 67.08 |
| nonl7_step | 12 | 60.76 | 70.94 | 67.08 |
| y_ratio | 12 | 61.38 | 76.73 | 67.35 |
| y_alfa_isp | 12 | 59.63 | 73.77 | 66.47 |
| residui_alfa_isp | 12 | -3.77 | 3.13 | 0.61 |
| residui_ratio | 12 | -6.73 | 2.99 | -0.27 |
| residui_nonl7_step | 12 | -0.94 | 2.22 | 0.00 |

| alfa_isp | | | | | | | | R-Square | 0.7605 |
|---|---|---|---|---|---|---|---|---|---|
| Variable | DF | Parameter Estimate | Standard Error | t Value | Pr > |t| | Standardized Estimate | Variance Inflation | Adj R-Sq | 0.7406 |
| Intercept | 1 | 17.91695 | 7.47336 | 2.4 | 0.0337 | 0 | 0 | | |
| alfa_isp | 1 | 0.73416 | 0.11893 | 6.17 | <.0001 | 0.87208 | 1 | | |

| y_ratio | | | | | | | | R-Square | 0.8257 |
|---|---|---|---|---|---|---|---|---|---|
| Variable | DF | Parameter Estimate | Standard Error | t Value | Pr > |t| | Standardized Estimate | Variance Inflation | Adj R-Sq | 0.8112 |
| Intercept | 1 | -0.07719 | 8.50238 | -0.01 | 0.9929 | 0 | 0 | | |
| nonl_ratio | 1 | 1.0012 | 0.1328 | 7.54 | <.0001 | 0.90867 | 1 | | |

| step | | | | | | | | R-Square | 0.9667 |
|---|---|---|---|---|---|---|---|---|---|
| Variable | DF | Parameter Estimate | Standard Error | t Value | Pr > |t| | Standardized Estimate | Variance Inflation | Adj R-Sq | 0.9639 |
| Intercept | 1 | -3.08E-09 | 3.43227 | 0 | 1 | 0 | 0 | | |
| nonl7 | 1 | 1 | 0.05359 | 18.66 | <.0001 | 0.9832 | 1 | | |

$$Alfa\_isp = 71.35 Q_a^{-0.059418} \left(\frac{Q_w}{Q_a}\right)^{0.008738}$$

$$Nonl\_ratio = a Q_a^{b} \left(\frac{Q_w}{Q_a}\right)^{c}$$

| Parameter | Estimate |
|-----------|----------|
| a | 77.0276 |
| b | -0.1054 |
| c | -0.0294 |

$$nonl_7 = a + \exp(e + cP_a^2 + dP_a + fP_aP_w^2 + gP_aP_w + hP_w)$$

| Parameter | Estimate |
|-----------|----------|
| a | 59.2849 |
| c | -0.3989 |
| d | -1.0797 |
| e | 3.5908 |
| f | -0.0884 |
| g | 1.1009 |
| h | -0.844 |
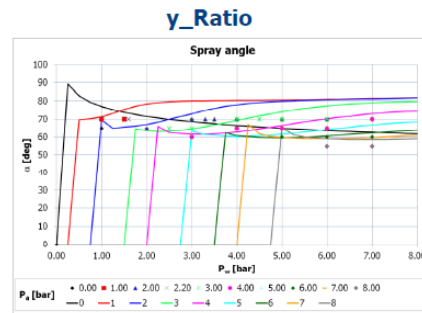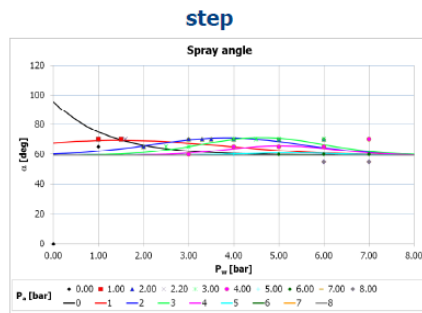
### step



### y_Ratio



## *Spray angle β*
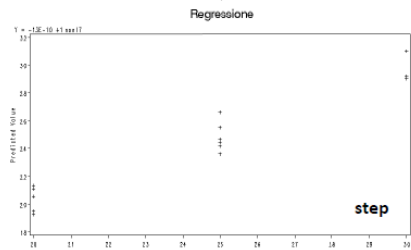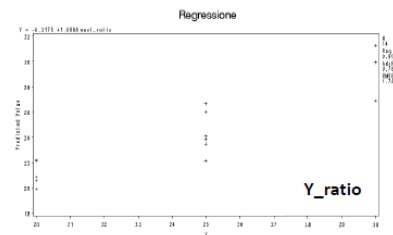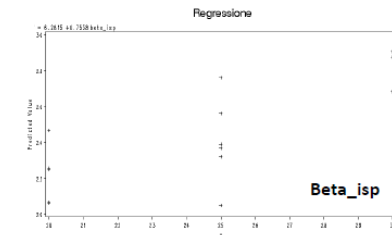






## Training

| Variable | N | Minimum | Maximum | Mean |
|----------|---|---------|---------|------|
| Y | 14 | 20.00 | 30.00 | 24.29 |
| beta_isp | 14 | 18.84 | 30.22 | 23.88 |
| y_ratio | 14 | 19.90 | 31.26 | 24.29 |
| y_step | 14 | 19.26 | 30.99 | 24.28 |
| residui_beta_isp | 14 | -4.37 | 6.16 | 0.40 |
| residui_ratio | 14 | -2.17 | 3.12 | 0.00 |
| residui_step | 14 | -1.62 | 1.39 | 0.01 |

Test 1

| Variable | N | Minimum | Maximum | Mean |
|---|---|---|---|---|
| Y | 27 | 20.00 | 30.00 | 24.44 |
| beta_isp | 27 | 17.35 | 34.81 | 24.43 |
| y_ratio | 27 | 17.82 | 42.65 | 25.67 |
| y_step | 27 | 18.79 | 31.47 | 23.80 |
| residui_beta_isp | 27 | -6.72 | 6.16 | 0.02 |
| residui_ratio | 27 | -12.65 | 3.12 | -1.23 |
| residui_step | 27 | -1.62 | 7.30 | 0.64 |

Test 2

| Variable | N | Minimum | Maximum | Mean |
|---|---|---|---|---|
| Y | 26 | 20.00 | 30.00 | 24.23 |
| beta_isp | 26 | 17.35 | 34.81 | 24.40 |
| y_ratio | 26 | 17.82 | 42.65 | 25.48 |
| y_step | 26 | 18.79 | 31.47 | 23.84 |
| residui_beta_isp | 26 | -6.72 | 6.16 | -0.17 |
| residui_ratio | 26 | -12.65 | 3.12 | -1.25 |
| residui_step | 26 | -1.62 | 6.05 | 0.39 |



Test 3
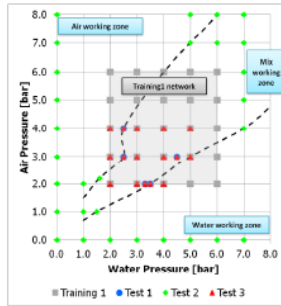
| Variable | N | Minimum | Maximum | Mean |
|---|---|---|---|---|
| Y | 27 | 20.00 | 30.00 | 24.44 |
| beta_isp | 27 | 17.35 | 34.81 | 24.43 |
| y_ratio | 27 | 17.82 | 42.65 | 25.67 |
| y_step | 27 | 18.79 | 31.47 | 23.80 |
| residui_beta_isp | 27 | -6.72 | 6.16 | 0.02 |
| residui_ratio | 27 | -12.65 | 3.12 | -1.23 |
| residui_step | 27 | -1.62 | 7.30 | 0.64 |

| Beta_isp | | | | | | | | R-Square | 0.5776 |
|---|---|---|---|---|---|---|---|---|---|
| Variable | DF | Parameter Estimate | Standard Error | t Value | Pr > \|t\| | Standardized Estimate | Variance Inflation | Adj R-Sq | 0.5424 |
| Intercept | 1 | 6.28151 | 4.49865 | 1.4 | 0.1879 | 0 | 0 | | |
| beta_isp | 1 | 0.7538 | 0.18608 | 4.05 | 0.0016 | 0.76001 | 1 | | |

| y_ratio | | | | | | | | R-Square | 0.8017 |
|---|---|---|---|---|---|---|---|---|---|
| Variable | DF | Parameter Estimate | Standard Error | t Value | Pr > \|t\| | Standardized Estimate | Variance Inflation | Adj R-Sq | 0.7852 |
| Intercept | 1 | -0.21752 | 3.55032 | -0.06 | 0.9522 | 0 | 0 | | |
| nonl_ratio | 1 | 1.00879 | 0.14484 | 6.96 | <.0001 | 0.89537 | 1 | | |

| step | | | | | | | | R-Square | 0.9347 |
|---|---|---|---|---|---|---|---|---|---|
| Variable | DF | Parameter Estimate | Standard Error | t Value | Pr > \|t\| | Standardized Estimate | Variance Inflation | Adj R-Sq | 0.9292 |
| Intercept | 1 | -1.31E-09 | 1.87333 | 0 | 1 | 0 | 0 | | |
| nonl7 | 1 | 1 | 0.07631 | 13.1 | <.0001 | 0.96679 | 1 | | |

$$Beta\_isp = 29.378 Q_a^{-0.081738} \left( \frac{Q_w}{Q_a} \right)^{0.044316}$$

$$Nonl\_ratio = a Q_a^{b} \left( \frac{Q_w}{Q_a} \right)^{c}$$

| Parameter | Estimate |
|---|---|
| a | 44.1146 |
| b | -0.3619 |
| c | -0.1386 |

$$nonl_7 = a + \exp(e + c P_a^2 + d P_a + f P_a P_w^2 + g P_a P_w + h P_w)$$

| Parameter | Estimate |
|---|---|
| a | 18.781 |
| c | -0.0997 |
| d | 0.3564 |
| e | 0.5295 |
| f | -0.0154 |
| g | -0.00169 |
| h | 0.5962 |

200
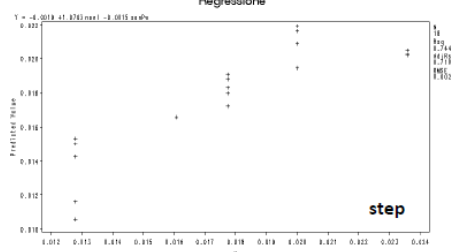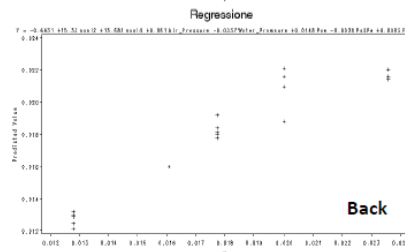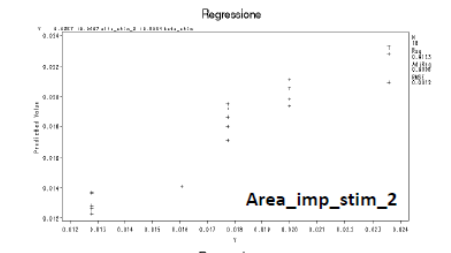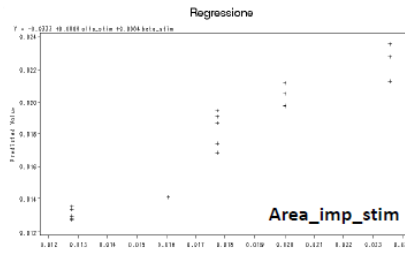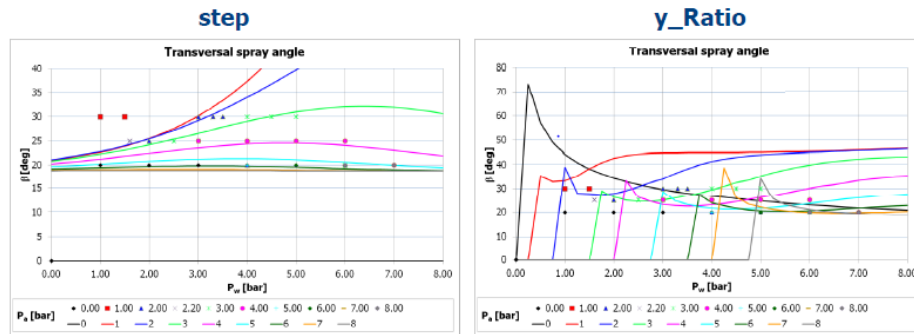
| Variable | N | Minimum | Maximum | Mean |
|---|---|---|---|---|
| Y | 14 | 0.0128 | 0.0236 | 0.0178 |
| y_back | 14 | 0.0142 | 0.0236 | 0.0196 |
| y_step | 14 | 0.0105 | 0.0220 | 0.0178 |
| Area_imp_stim | 14 | 0.0127 | 0.0235 | 0.0178 |
| Area_imp_stim_2 | 14 | 0.0123 | 0.0232 | 0.0178 |
| y_area_calcolata_stim | 14 | 0.0122 | 0.0247 | 0.0171 |
| residui_area_calcolata | 14 | -0.0012 | 0.0010 | 0.0000 |
| residui_back | 14 | -0.0036 | 0.0005 | -0.0018 |
| residui_step | 14 | -0.0025 | 0.0034 | 0.0000 |
| residui_Area_imp_stim | 14 | -0.0017 | 0.0023 | 0.0000 |
| residui_Area_imp_stim_2 | 14 | -0.0018 | 0.0026 | 0.0000 |

Training
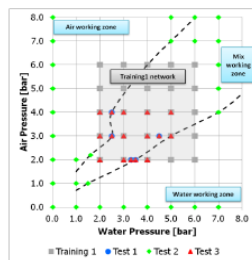
| Variable | N | Minimum | Maximum | Mean |
|---|---|---|---|---|
| Y | 4 | 0.0178 | 0.0236 | 0.0221 |
| y_back | 4 | 0.0188 | 0.0236 | 0.0224 |
| y_step | 4 | 0.0181 | 0.0210 | 0.0201 |
| Area_imp_stim | 4 | 0.0171 | 0.0238 | 0.0209 |
| Area_imp_stim_2 | 4 | 0.0169 | 0.0237 | 0.0208 |
| y_area_calcolata_stim | 4 | 0.0173 | 0.0251 | 0.0226 |
| residui_area_calcolata | 4 | -0.0015 | 0.0005 | -0.0005 |
| residui_back | 4 | -0.0011 | 0.0001 | -0.0002 |
| residui_step | 4 | -0.0004 | 0.0031 | 0.0020 |
| residui_Area_imp_stim | 4 | -0.0002 | 0.0021 | 0.0012 |
| residui_Area_imp_stim_2 | 4 | -0.0001 | 0.0024 | 0.0014 |

Test 1

| | | | | Back | | | | |
|---|---|---|---|---|---|---|---|---|
| Variable | DF | Parameter Estimate | Standard Error | t Value | Pr > \|t\| | Standardized Estimate | Variance Inflation | |
| Intercept | 1 | -0.69311 | 0.28486 | -2.43 | 0.0353 | 0 | 0 | |
| nonl2 | 1 | 15.32973 | 5.72136 | 2.68 | 0.0231 | 12.09961 | 2126.72491 | |
| nonl4 | 1 | 13.68501 | 6.38144 | 2.14 | 0.0576 | 11.48895 | 2993.2672 | |
| Air_Pressure | 1 | 0.06104 | 0.02486 | 2.46 | 0.034 | 22.0191 | 8388.42905 | |
| Water_Pressure | 1 | -0.02372 | 0.00699 | -3.4 | 0.0068 | -7.74692 | 542.86643 | |
| Paw | 1 | 0.01484 | 0.00409 | 3.63 | 0.0046 | 35.20335 | 9811.0159 | |
| Pa2Pw | 1 | -0.00383 | 0.00096428 | -3.97 | 0.0026 | -61.29854 | 24855 | |
| Pa3Pw | 1 | 0.00031754 | 0.0000747 | 4.25 | 0.0017 | 31.47649 | 5718.94801 | |

| R-Square | 0.9041 |
|---|---|
| Adj R-Sq | 0.837 |

| | | | | Step | | | |
|---|---|---|---|---|---|---|---|
| Variable | DF | Parameter Estimate | Standard Error | t Value | Pr > \|t\| | Standardized Estimate | Variance Inflation |
| Intercept | 1 | -0.0019 | 0.00306 | -0.62 | 0.5437 | 0 | 0 |
| nonl | 1 | 1.07032 | 0.16203 | 6.61 | <.0001 | 0.89918 | 1.08859 |
| senPw | 1 | -0.00154 | 0.00098771 | -1.56 | 0.1398 | -0.21223 | 1.08859 |

| R-Square | 0.7447 |
|---|---|
| Adj R-Sq | 0.7106 |

$$nonl = (a + bP_a)sinh^{-1}(P_w^{c+d*P_a} - (eP_a^2 + fP_a + g)) + hP_a^2 + iPa + l$$

| Parameter | Estimate |
|---|---|
| a | 0.0298 |
| b | 0.000446 |
| c | 0.000041 |
| d | 0.000011 |
| e | -0.00182 |
| f | 0.00564 |
| g | 0.2141 |
| h | -0.0004 |
| i | 0.000231 |
| l | 0 |

$$nonl_2 = a + P_w^b + P_a^c$$

| Parameter | Estimate |
|---|---|
| a | -1.9749 |
| b | 0.00165 |
| c | -0.0081 |

$$nonl_4 = a + \tan(P_a^2 + cP_a + d)$$

| Parameter | Estimate |
|---|---|
| a | -0.1381 |
| b | -0.00034 |
| c | 0.000385 |
| d | 0.1584 |

| | | | | area_imp_stim | | | |
|---|---|---|---|---|---|---|---|
| Variable | DF | Parameter Estimate | Standard Error | t Value | Pr > \|t\| | Standardized Estimate | Variance Inflation |
| Intercept | 1 | -0.03333 | 0.00404 | -8.25 | <.0001 | 0 | 0 |
| F1 | 1 | 0.00062388 | 0.00007036 | 8.87 | <.0001 | 0.71608 | 1.29281 |
| F2 | 1 | 0.00044637 | 0.00009348 | 4.78 | 0.0002 | 0.38564 | 1.29281 |

| R-Square | 0.9243 |
|---|---|
| Adj R-Sq | 0.9142 |

\

| | | | | Area_imp_stim_2 | | | |
|---|---|---|---|---|---|---|---|
| Variable | DF | Parameter Estimate | Standard Error | t Value | Pr > \|t\| | Standardized Estimate | Variance Inflation |
| Intercept | 1 | -0.03565 | 0.00466 | -7.66 | <.0001 | 0 | 0 |
| F3 | 1 | 0.00068121 | 0.00008398 | 8.11 | <.0001 | 0.73147 | 1.3911 |
| F2 | 1 | 0.0003919 | 0.00010438 | 3.75 | 0.0019 | 0.33858 | 1.3911 |

| R-Square | 0.9123 |
|---|---|
| Adj R-Sq | 0.9006 |

| | | | | Parameter Estimates | | | |
|---|---|---|---|---|---|---|---|
| Variable | DF | Parameter Estimate | Standard Error | t Value | Pr > \|t\| | Standardized Estimate | Variance Inflation |
| Intercept | 1 | -0.00000549 | 0.00106 | -0.01 | 0.996 | 0 | 0 |
| area_calcolat a_stim | 1 | 0.25029 | 0.01515 | 16.52 | <.0001 | 0.97873 | 1 |

| R-Square | 0.9579 |
|---|---|
| Adj R-Sq | 0.9544 |

nonl_ok_F1=(79.4787-1.2217*Pa)*arsinh(Pw**(0.00254+0.000315*Pa)-(0.00461*Pa2-0.0786*Pa-0.0661))+0.1898*Pa2-4.9382*Pa;
**F1**=-5367.60123

```
+73.25731*nonl_ok_F1
+159.87308*Air_Pressure
+5.34187*Air_Pressure2
-0.03034*Water_Pressure3 ;
nonl7_ok_F2=20+exp((-1.2554*Pa2-0.6685*Pa+5.9508-0.1828*PaPw2+2.7649*Paw-3.6614*PW));
F2=0.76024+0.97142*nonl7_ok_F2;
nonl3_ok=62.4065+tan(29.3820+0.5*(-131.2*tanh(((Pa)/2))));
nonl4_ok=66.5202+tan(-0.1853*Pa2-1.3307*Pa-2.4769);
F3=-48.08765
+2.73410*nonl3_ok
-1.25258*nonl4_ok
-0.06485*Water_Pressure3
+3.71997*Water_Pressure
+0.41596*Paw ;
```
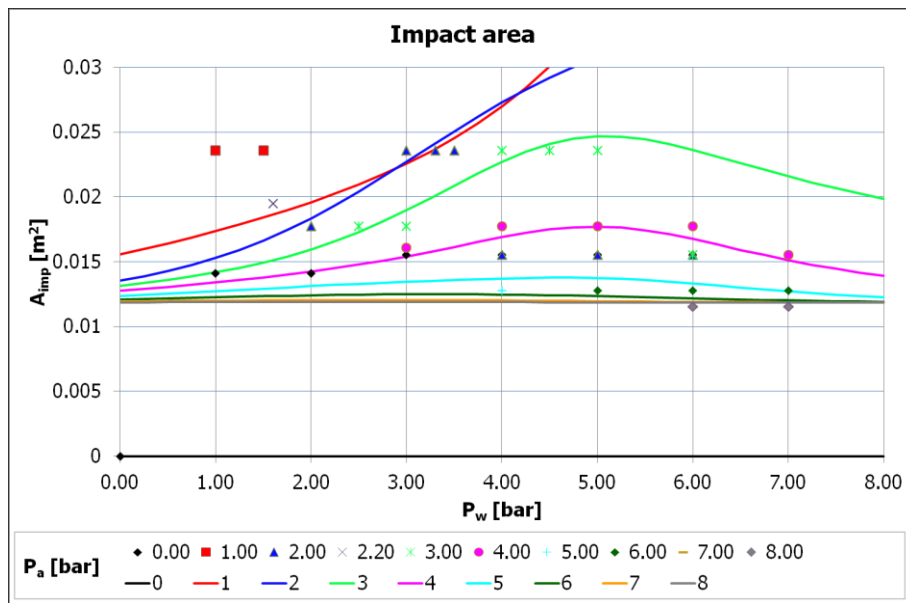


## Sauter mean diameter (D32)

Sauter mean diameter (D32) is an average of water drop size. It can be defined as the diameter of a drop having the same volume/surface area ratio as the entire spray.

D32(μm)=225.8



F_ratio
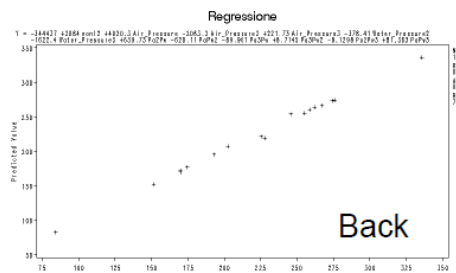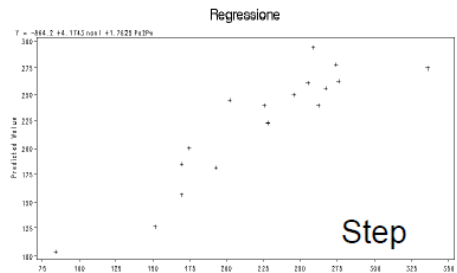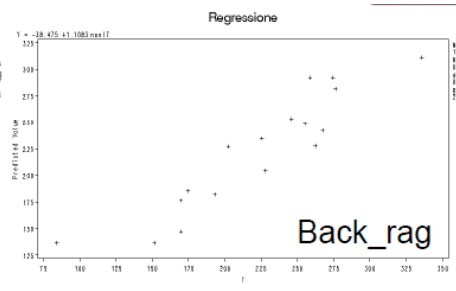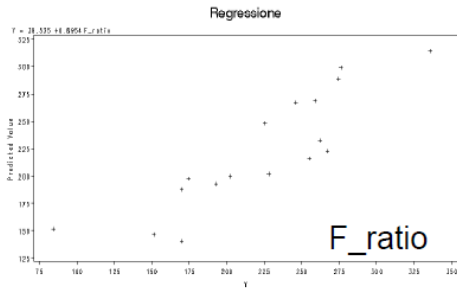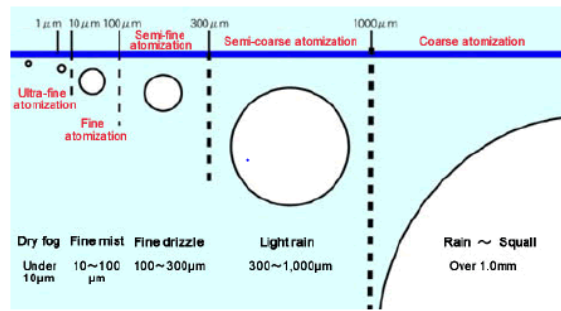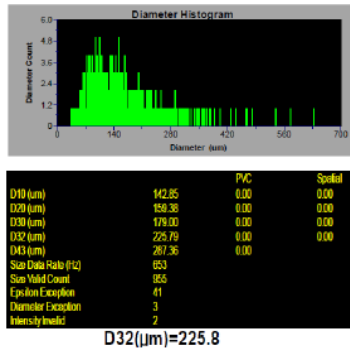


Back_rag



Step



Back

## Training

| Variable | N | Minimum | Maximum | Mean |
|---|---|---|---|---|
| Y | 17 | 84.33 | 335.73 | 222.10 |
| y_back | 17 | 119.96 | 373.16 | 258.70 |
| y_step | 17 | 103.09 | 293.12 | 221.56 |
| back_rag | 17 | 135.63 | 310.65 | 221.53 |
| y_f_ratio | 17 | 141.02 | 313.93 | 222.09 |
| residui_f_ratio | 17 | -67.20 | 44.84 | 0.00 |
| residui_back | 17 | -53.93 | -7.91 | -36.60 |
| residui_step | 17 | -42.22 | 61.48 | 0.54 |
| residui_back_rag | 17 | -51.30 | 35.58 | 0.56 |

## Test 4
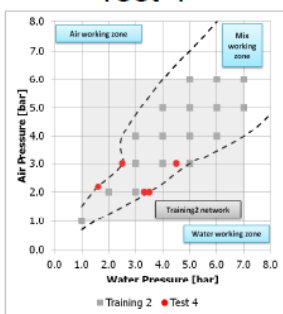


| Variable | N | Minimum | Maximum | Mean |
|---|---|---|---|---|
| Y | 5 | 129.92 | 353.70 | 256.11 |
| y_back | 5 | 247.56 | 415.44 | 326.25 |
| y_step | 5 | 207.12 | 270.25 | 246.54 |
| back_rag | 5 | 182.48 | 311.11 | 253.39 |
| y_f_ratio | 5 | 157.79 | 370.21 | 268.64 |
| residui_f_ratio | 5 | -39.64 | 6.28 | -12.53 |
| residui_back | 5 | -128.86 | -29.48 | -70.14 |
| residui_step | 5 | -77.20 | 83.45 | 9.57 |
| residui_back_rag | 5 | -52.56 | 44.81 | 2.72 |

**Test 1**

| Variable | N | Minimum | Maximum | Mean |
|---|---|---|---|---|
| Y | 4 | 129.92 | 353.70 | 282.94 |
| y_back | 4 | 258.78 | 415.44 | 345.92 |
| y_step | 4 | 207.12 | 270.25 | 251.68 |
| back_rag | 4 | 182.48 | 311.11 | 268.29 |
| y_f_ratio | 4 | 169.56 | 370.21 | 296.35 |
| residui_f_ratio | 4 | -39.64 | 6.28 | -13.41 |
| residui_back | 4 | -128.86 | -29.48 | -62.99 |
| residui_step | 4 | -77.20 | 83.45 | 31.26 |
| residui_back_rag | 4 | -52.56 | 44.81 | 14.65 |

**Test 2**

| Variable | N | Minimum | Maximum | Mean |
|---|---|---|---|---|
| Y | 9 | 54.06 | 270.33 | 184.73 |
| y_back | 9 | -245.54 | 304.82 | 189.02 |
| y_step | 9 | -14.41 | 293.12 | 188.14 |
| back_rag | 9 | 137.14 | 291.16 | 215.32 |
| y_f_ratio | 9 | 127.41 | 339.42 | 203.96 |
| residui_f_ratio | 9 | -78.10 | 44.84 | -19.23 |
| residui_back | 9 | -133.56 | 299.60 | -4.29 |
| residui_step | 9 | -77.18 | 68.47 | -3.41 |
| residui_back_rag | 9 | -83.08 | 27.14 | -30.59 |

**Test 3**

| Variable | N | Minimum | Maximum | Mean |
|---|---|---|---|---|
| Y | 12 | 129.92 | 353.70 | 249.19 |
| y_back | 12 | 219.64 | 415.44 | 299.94 |
| y_step | 12 | 156.75 | 274.25 | 237.98 |
| back_rag | 12 | 146.63 | 311.11 | 242.79 |
| y_f_ratio | 12 | 141.02 | 370.21 | 254.52 |
| residui_f_ratio | 12 | -39.64 | 28.88 | -5.33 |
| residui_back | 12 | -128.86 | -29.48 | -50.76 |
| residui_step | 12 | -77.20 | 83.45 | 11.21 |
| residui_back_rag | 12 | -52.56 | 44.81 | 6.39 |
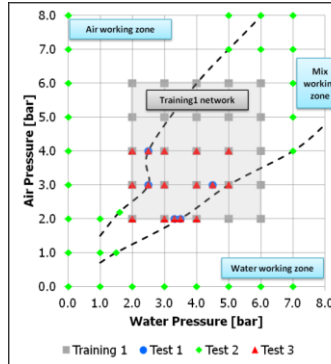


**F_ratio**

| Variable | DF | Parameter Estimate | Standard Error | t Value | Pr > \|t\| | Standardized Estimate | Variance Inflation |
|---|---|---|---|---|---|---|---|
| Intercept | 1 | 38.53497 | 27.16453 | 1.42 | 0.1765 | 0 | 0 |
| F_ratio | 1 | 0.89535 | 0.12762 | 7.02 | <.0001 | 0.87546 | 1 |

| R-Square | 0.7664 |
|---|---|
| Adj R-Sq | 0.7509 |

**back_rag**

| Variable | DF | Parameter Estimate | Standard Error | t Value | Pr > \|t\| | Standardized Estimate | Variance Inflation |
|---|---|---|---|---|---|---|---|
| Intercept | 1 | -38.47457 | 29.47473 | -1.31 | 0.2114 | 0 | 0 |
| nonl7 | 1 | 1.10829 | 0.12278 | 9.03 | <.0001 | 0.91899 | 1 |

| R-Square | 0.8445 |
|---|---|
| Adj R-Sq | 0.8342 |

**Step**

| Variable | DF | Parameter Estimate | Standard Error | t Value | Pr > \|t\| | Standardized Estimate | Variance Inflation |
|---|---|---|---|---|---|---|---|
| Intercept | 1 | -864.19505 | 138.26506 | -6.25 | <.0001 | 0 | 0 |
| nonl | 1 | 4.17429 | 0.52278 | 7.98 | <.0001 | 2.592 | 8.51474 |
| Pa2Pw | 1 | 1.76245 | 0.25531 | 6.9 | <.0001 | 2.24088 | 8.51474 |

| R-Square | 0.8267 |
|---|---|
| Adj R-Sq | 0.802 |

**Back**

| Variable | DF | Parameter Estimate | Standard Error | t Value | Pr > \|t\| | Standardized Estimate | Variance Inflation |
|---|---|---|---|---|---|---|---|
| Intercept | 1 | -344437 | 41436 | -8.31 | 0.0011 | 0 | 0 |
| nonl2 | 1 | 2084.00326 | 250.32205 | 8.33 | 0.0011 | 3003.67058 | 142660286 |
| Air_Pressure | 1 | 4920.3429 | 662.42243 | 7.43 | 0.0018 | 122.3251 | 297240 |
| Air_Pressure2 | 1 | -2063.17848 | 286.18025 | -7.21 | 0.002 | -392.47936 | 3248152 |
| Air_Pressure3 | 1 | 221.72532 | 33.05537 | 6.71 | 0.0026 | 273.25137 | 1818759 |
| Water_Pressure2 | 1 | -378.41367 | 54.10403 | -6.99 | 0.0022 | -92.14406 | 190221 |
| Water_Pressure3 | 1 | -1622.40191 | 194.12379 | -8.36 | 0.0011 | -2921.95512 | 133962964 |
| Pa2Pw | 1 | 639.73292 | 83.92193 | 7.62 | 0.0016 | 813.39385 | 12478212 |
| PaPw2 | 1 | -620.11135 | 75.48329 | -8.22 | 0.0012 | -898.54138 | 13110992 |
| Pa3Pw | 1 | -89.96067 | 12.668 | -7.1 | 0.0021 | -705.12967 | 10805522 |
| Pa3Pw2 | 1 | 8.71446 | 1.22123 | 7.14 | 0.002 | 451.15853 | 4380928 |
| Pa2Pw3 | 1 | -8.12981 | 1.05323 | -7.72 | 0.0015 | -483.5145 | 4300352 |
| PaPw3 | 1 | 81.36272 | 9.84641 | 8.26 | 0.0012 | 833.28266 | 11145159 |

| R-Square | 0.9964 |
|---|---|
| Adj R-Sq | 0.9854 |

$$F\_ratio = 23175 \left( \frac{Q_w}{Q_a} \right)^{0.1787}$$

$$nonl_7 = a + \exp(e + cP_a^2 + dP_a + fP_aP_w^2 + gP_aP_w + hP_w)$$

| Parameter | Estimate |
|---|---|
| a | -680.2 |
| c | 0.00772 |
| d | -0.0782 |
| e | 6.8572 |
| f | 0.000965 |
| g | -0.0146 |
| h | 0.0715 |

$$nonl = (a + bP_a)\sinh^{-1}(P_w^{c+d*P_a} - (eP_a^2 + fP_a + g)) + hP_a^2 + iPa + l$$

| Parameter | Estimate |
|---|---|
| a | 826.2 |
| b | -21.6555 |
| c | 0.00118 |
| d | 0.0152 |
| e | -0.0143 |
| f | 0.0694 |
| g | -2.8686 |
| h | -6.8302 |
| i | 58.8086 |
| l | -1430.9 |

$$nonl_2 = a + P_w^b + P_w^b$$

| Parameter | Estimate |
|---|---|
| a | 162.9 |
| b | 2.8879 |
| c | -1.2495 |

The "F_Ratio" formulation has the minor residuals and a trend more close to the expected physical behavior.
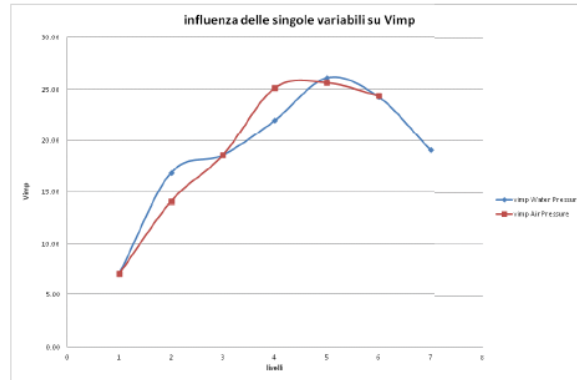
## Impact velocity: Vimp



**Velocity Mean(m/s)=23.58**



* purely indicative picture

| livelli | Water Pressure | Air Pressure | vimp Water Pressure | vimp Air Pressure |
|---|---|---|---|---|
| 1 | 1.00 | 1.00 | 7.09 | 7.09 |
| 2 | 2.00 | 2.00 | 16.83 | 14.09 |
| 3 | 3.00 | 3.00 | 18.57 | 18.55 |
| 4 | 4.00 | 4.00 | 21.99 | 25.16 |
| 5 | 5.00 | 5.00 | 26.15 | 25.68 |
| 6 | 6.00 | 6.00 | 24.31 | 24.41 |
| 7 | 7.00 | | 19.07 | |
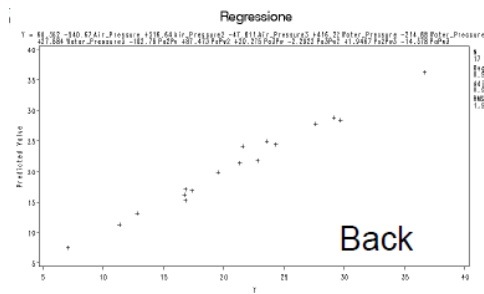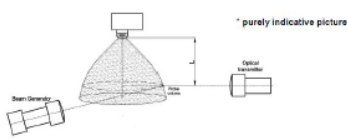


Back
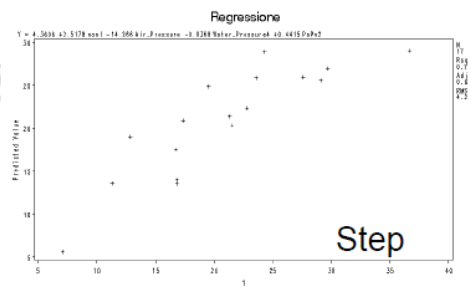


Step
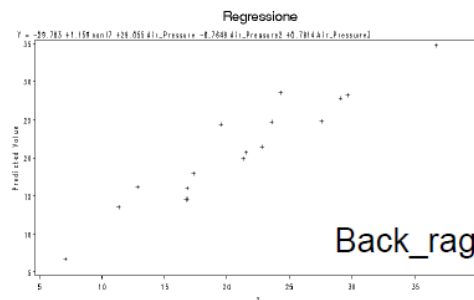


Back_rag

Training

| Variable | N | Minimum | Maximum | Mean |
|---|---|---|---|---|
| Y | 17 | 7.09 | 36.67 | 20.89 |
| y_step | 17 | 5.63 | 28.97 | 20.87 |
| y_back | 17 | 7.60 | 36.29 | 20.92 |
| back_rag | 17 | 6.76 | 34.61 | 20.84 |
| residui_step | 17 | -6.12 | 7.70 | 0.03 |
| residui_back | 17 | -2.58 | 1.57 | -0.02 |
| residui_back_rag | 17 | -4.83 | 2.84 | 0.06 |

Test 4
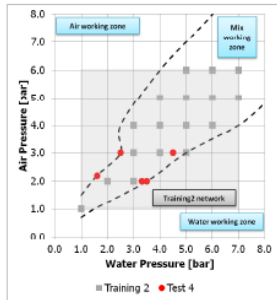
| Variable | N | Minimum | Maximum | Mean |
|---|---|---|---|---|
| Y | 5 | 11.51 | 20.08 | 13.96 |
| y_step | 5 | 13.08 | 19.92 | 16.39 |
| y_back | 5 | 5.79 | 27.47 | 13.36 |
| back_rag | 5 | 12.80 | 20.99 | 16.35 |
| residui_step | 5 | -5.82 | 0.38 | -2.42 |
| residui_back | 5 | -7.39 | 6.57 | 0.61 |
| residui_back_rag | 5 | -7.23 | -0.44 | -2.39 |



Test 1

| Variable | N | Minimum | Maximum | Mean |
|---|---|---|---|---|
| Y | 4 | 11.77 | 20.08 | 14.58 |
| y_step | 4 | 13.08 | 19.92 | 16.51 |
| y_back | 4 | 5.79 | 27.47 | 14.04 |
| back_rag | 4 | 12.80 | 20.99 | 15.76 |
| residui_step | 4 | -5.82 | 0.38 | -1.94 |
| residui_back | 4 | -7.39 | 6.57 | 0.54 |
| residui_back_rag | 4 | -2.06 | -0.44 | -1.18 |

Test 2

| Variable | N | Minimum | Maximum | Mean |
|---|---|---|---|---|
| Y | 9 | 6.50 | 26.58 | 17.46 |
| y_step | 9 | 4.87 | 23.79 | 14.88 |
| y_back | 9 | -454.44 | 48.10 | -83.21 |
| back_rag | 9 | 4.98 | 54.37 | 25.59 |
| residui_step | 9 | -4.36 | 13.41 | 2.58 |
| residui_back | 9 | -41.60 | 476.39 | 100.67 |
| residui_back_rag | 9 | -32.42 | 2.30 | -8.13 |

Test 3
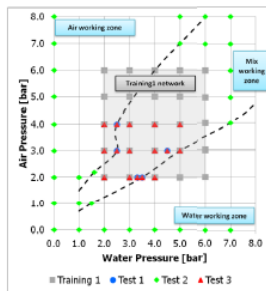
| Variable | N | Minimum | Maximum | Mean |
|---|---|---|---|---|
| Y | 12 | 11.34 | 29.10 | 18.14 |
| y_step | 12 | 13.08 | 25.84 | 18.84 |
| y_back | 12 | 5.79 | 28.81 | 17.95 |
| back_rag | 12 | 12.80 | 27.76 | 18.32 |
| residui_step | 12 | -5.82 | 3.55 | -0.70 |
| residui_back | 12 | -7.39 | 6.57 | 0.19 |
| residui_back_rag | 12 | -2.22 | 2.18 | -0.18 |

**back_rag**

| Variable | DF | Parameter Estimate | Standard Error | t Value | Pr > |t| | Standardized Estimate | Variance Inflation |
|---|---|---|---|---|---|---|---|
| Intercept | 1 | -29.78294 | 9.21634 | -3.23 | 0.0072 | 0 | 0 |
| nonl7 | 1 | 1.15896 | 0.16803 | 6.9 | <.0001 | 1.0364 | 2.64354 |
| Air_Pressure | 1 | 29.05488 | 8.71347 | 3.33 | 0.0059 | 5.8997 | 366.50553 |
| Air_Pressure2 | 1 | -8.76493 | 2.73722 | -3.2 | 0.0076 | -13.61819 | 2117.5721 |
| Air_Pressure3 | 1 | 0.78143 | 0.25267 | 3.09 | 0.0093 | 7.86557 | 757.27193 |

| R-Square | 0.8975 |
|---|---|
| Adj R-Sq | 0.8633 |

**Step**

| Variable | DF | Parameter Estimate | Standard Error | t Value | Pr > |t| | Standardized Estimate | Variance Inflation |
|---|---|---|---|---|---|---|---|
| Intercept | 1 | 4.36056 | 4.85644 | 0.9 | 0.3869 | 0 | |
| nonl | 1 | 2.51775 | 0.92054 | 2.74 | 0.0181 | 1.88384 | 23.1692 |
| Air_Pressure | 1 | -14.26631 | 7.21666 | -1.98 | 0.0715 | -2.89683 | 104.87122 |
| Water_Pressure4 | 1 | -0.03678 | 0.01348 | -2.73 | 0.0183 | -3.84934 | 97.23871 |
| PaPw2 | 1 | 0.44148 | 0.18095 | 2.44 | 0.0312 | 5.22475 | 223.96953 |

| R-Square | 0.7543 |
|---|---|
| Adj R-Sq | 0.6724 |

**Back**

| Variable | DF | Parameter Estimate | Standard Error | t Value | Pr > |t| | Standardized Estimate | Variance Inflation |
|---|---|---|---|---|---|---|---|
| Intercept | 1 | 60.36223 | 21.95853 | 2.75 | 0.0514 | 0 | 0 |
| Air_Pressure | 1 | -540.67404 | 150.12266 | -3.6 | 0.0227 | -109.78586 | 214737 |
| Air_Pressure2 | 1 | 316.63942 | 78.95149 | 4.01 | 0.016 | 491.96669 | 3477396 |
| Air_Pressure3 | 1 | -47.81118 | 10.51659 | -4.55 | 0.0104 | -481.2461 | 2589508 |
| Water_Pressure | 1 | 416.22414 | 130.3408 | 3.19 | 0.0331 | 95.77976 | 207896 |
| Water_Pressure2 | 1 | -214.88367 | 63.30087 | -3.39 | 0.0274 | -427.36076 | 3662637 |
| Water_Pressure3 | 1 | 27.68445 | 7.55914 | 3.66 | 0.0215 | 407.23185 | 2857251 |
| Pa2Pw | 1 | -102.76124 | 26.43158 | -3.89 | 0.0177 | -1067.14197 | 17411014 |
| PaPw2 | 1 | 87.4728 | 23.84335 | 3.67 | 0.0214 | 1035.21872 | 18401147 |
| Pa3Pw | 1 | 20.27543 | 4.55662 | 4.45 | 0.0112 | 1298.00674 | 19664882 |
| Pa3Pw2 | 1 | -2.2922 | 0.50308 | -4.56 | 0.0104 | -969.24202 | 10457377 |
| Pa2Pw3 | 1 | 1.94675 | 0.44901 | 4.34 | 0.0123 | 945.64689 | 10993682 |
| PaPw3 | 1 | -14.57829 | 3.66244 | -3.98 | 0.0164 | -1219.45049 | 21689411 |

| R-Square | 0.9827 |
|---|---|
| Adj R-Sq | 0.9308 |

$$nonl = (a + bP_a)\sinh^{-1}(P_w^{c+d*P_a} - (eP_a^2 + fP_a + g)) + hP_a^2 + iP_a + l$$

| Parameter | Estimate |
|---|---|
| a | -3.9816 |
| b | 10.4833 |
| c | -0.3251 |
| d | 0.0396 |
| e | 0.00984 |
| f | -0.0208 |
| g | -0.2244 |
| h | -0.7289 |
| i | 1.1178 |
| l | -1.1322 |

$$nonl_7 = a + \exp(e + cP_a^2 + dP_a + fP_aP_w^2 + gP_aP_w + hP_w)$$

| Parameter | Estimate |
|---|---|
| a | 10.5441 |
| c | -0.6059 |
| d | 1.4707 |
| e | 1.647 |
| f | -0.071 |
| g | 1.2631 |
| h | -2.6717 |

The "Back_rag" formulation has the minor residuals and a trend more close to the expected physical behavior.
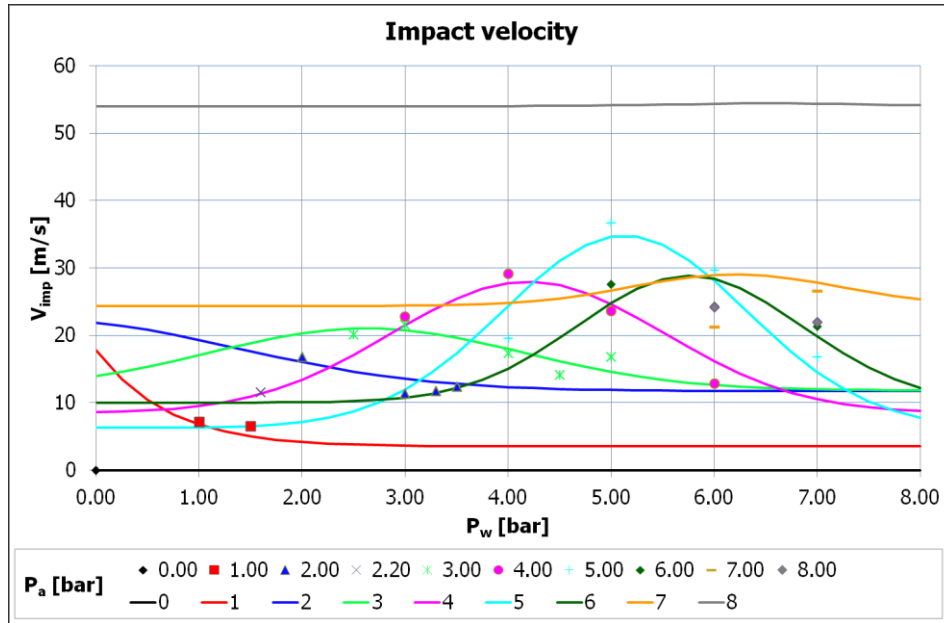
## Conclusion

The data analysis showed that the network of experimental points is sparse. Furthermore, with the exception of water and air flow rate, the sample data is not balanced (in some cases is heavily unbalanced). In these conditions the mathematical law presents more accuracy in the zone of greater data densification and more residual in the other zones.

Several mathematical laws able to predict the heat transfer coefficient (HTC) behavior of nozzle atomizer have been identified. These equations are based on the available data set within the temperature and pressures ranges:

$200 \leq Twall \leq 1000$ ºC,

$Pa \leq 4.0$ bar,

$Pw \leq 5.0$ bar.

# References

[1] SS Sahay, G Mohapatra, GE Totten. Overview of Pearlitic Rail Steel: Accelerated Cooling, Quenching, Microstructure, and Mechanical Properties. Journal of ASTM International, 2009, 6(7).

[2] HA Aglan. Fatigue Crack Growth and Fracture Behavior of Bainitic Rail Steels. U.S. Department of Transportation, Federal Railroad administration, September 2011.

[3] RK Steele. Steel Alloys with Lower Bainite Microstructures for Use in Railroad Cars and Track. Department of Transportation, Federal Railroad administration, January 2002.

[4] Intercritically Annealed Fe-1.5Mn-0.06C Steels", Materials Science and Engineering, Vol.A129, 1990

[5] I. Garcia, A.J. DeArdo. "Formation of Austenite in 1.5 Mn Steels", Metallurgical

[6] J. Huang, W.J. Poole, M. Miltzer. "Austenite Formation during Intercritical Annealing", Metallurgical and Materials Transactions, Vol. 35A, 2004

[7] H.K.D.H. Bhadeshia. "The Mechanism of Bainitic formation in Steels", Acta Metallurgica, Vol. 14,1980.

[8] H.K.D.H. Bhadeshia. "The Bainite Transformation in Steels", Metallurgical Transactions, Vol. 21A, 1990.

[9] N. DeCristofaro, R. Kaplow, W.S. Owen. "The Kinetics of Carbon Clustering in Martensite", Metallurgical Transaction A, Vol. 9A, 1978.

[10] V. Erhukimovitch, J. Baram. "Nucleation and Growth Transformation Kinetics", Physical Review B, Vol. 51, No. 10, 1995.

[11] Kempen, F. Sommer, E.J. Mittemeijer. "Determination and Interpretation of Isothermal and Non-Isothermal Transformation Kinetics, the Effective Activation Energies in Terms of Nucleation and Growth", Ph.D Thesis Institut for Metallkunde Der Universitat Stuttgart, 2001

[12] H.K.D.H. Bhadeshia, J. L. Lee. "A Methodology for the Prediction of Time-Temperature-Transformation Diagrams", Materials Science and Engineering, Vol. A171, 1993.

[13] T. Rèti, M. Gergely, P. Tardy. "Mathematical Treatment of Non-Isothermal Transformations", Materials Science and Technology, Vol. 3, 1987.

[14] A.A. Gorni. "Steel Forming and Heat Treating Hand Book", TU www.gorni.eng.brUT.

[15] I.A. Wierzsyllowski. "The Effect of the Thermal Path to Reach Isothermal Temperature on Transformation Kinetics", Metallurgical Transactions A, Vol. 22A, 1991

[16] M. Lusk, H.J. Jou. "On the Rule of Additivity in Phase Transformation Kinetics", Metallurgical and Materials Transaction A, Vol. 28A, 1987.

[17] T. Rèti, I. Felde. "A Non-Linear Extension of the Additivity Rule", Computational Materials Science, Vol. 15, 1999.

[18] T.T. Pham, E.B. Hawbolt, J.K. Brimacombe. "Predicting the Onset of Transformation under Non-Continuous Cooling Conditions", Metallurgical and Materials Transactions A, Vol. 26A, 1987.

[19] M.B. Kuban, R. Jayaraman, E.B. Hawbolt, J.K. Brimacombe. "An Assessment of the Additivity Principle in Predicting Continuous Cooling Austenite to Pearlite Transformation Kinetics Using Isothermal Transformation Data", Metallurgical Transactions A, Vol. 17A, 1986.

[20] R.G. Kamat, L.C. Brown, E.B. Hawbolt, J.K. Brimacombe. "The Principle of Additivity and the Preutectoid Ferrite Transformation", Metallurgical Transactions A, Vol. 23A, 1992.

[21] S. Serajzadeh. "Modelling of Temperature History and Phase Transformations during Cooling of steel", Journal of Materials Processing Technology, Vol. 146, 2004.

[22] C. Verdi, A. Visintin. "A Mathematical Model of the Austenite-Pearlite Transformation in Plain Carbon Steel based on the Scheils' Additivity Rule", Acta Metallurgica, Vol. 35, 1987.

[23] E.A. Wilson, S.F. Medina. "Application of Koistinen and Marburger's Athermal equation for Volume Fraction of Martensite to Diffusional Transformations obtained on Continuous Cooling 0.13% C High Strength Low Alloy Steel", Mater. Sci. Technol., Vol. 16, 2000.

[24] J.Z. Zhao, C. Mesplont, B.C. De Cooman. "Quantitative Analysis of the Dilatation during an Isothermal Decomposition of Austenites", Materials Science and Engineering A, Vol. A332, 2002.

[25] S.F. Medina, M.I. Vega, M. Chapa. "Critical Cooling temperatures and Phase transformation Kinetics in Structural Steels Determined by Mean Flow Stress and Dilatometry", Materials Science and Technology, Vol. 16, 2000.

[26] T.A. Kop, J. Sietsma, S. van der Zwaag. "Anisotropic Dilatation Behavior during Transformation of Hot Rolled Steel Showing Banded Structure", Materials Science and Technology, Vol. 17, 2001.

[27] J.Z. Zhao, C. Mesplont, B.C. De Cooman. "Calculation of the Phase Transformation Kinetics from a Dilatation Curve", Journal of Materials Processing Technology, Vol. 129, 2002.

[28] O. Grong, O.R. Myhr. "Additivity and Isokinetic Behavior in Relation

to Diffusion controlled Growth", Acta Mater., Vol. 48, 2000.

[29] J.S. Ye, H.B. Chang, T.Y. Hsu. "On the Application of the Additivity Rule In Pearlitic Transformation in Low alloy Steel", Metallurgical and Materials Transactions, Vol. 34A, 2003.

[30] F. J. Humphreys and M. Hatherly. Recrystallization and Related Annealing Phenomena. Pergamon Press, Oxford, 1995.

[31] D. Hull. Introduction to Dislocations. Pergamon Press, Oxford, 1st edition, 1965.

[32] W. Charnock and J. Nutting. The effect of Carbon and Nickel upon the stacking fault energy of iron. Metal Science, 1: 123-127, 1967.

[33] M. Cartmill. Softening during the Hot Deformation of Steels. Ph.D Thesis, Deakin University, Melbourne, 2006.

[34] J. Lin, D. Balint, and M. Pietrzyk. Microstructure Evolution in Metal Forming Processes. Woodhead, Cambridge, 2012.

[35] J. J. Jonas, C. M. Sellars, and W. J. Mcg. Tegart. Strength and structure under hotworking conditions. Metallurgical Reviews, 14: 1-24, 1969.

[36] E. Nes. Modelling of work hardening and stress saturation in FCC metals. Progress in Materials Science, 41: 129-193, 1997.

[37] C. M. Sellars. Recrystallization of metals during hot deformation. Philosophical Transactions of the Royal Society A: Mathematical, Physical and Engineering Sciences, 288: 147-158, 1978.

[38] K. H. J. Buschow. Encyclopedia of Materials Science and Technology. Elsevier, Amsterdam, 2001.

[39] R. Doherty, H. Mcqueen, T. Mcnelley, W. King, M. Kassner, D. Jensen, J. Jonas, F. Humphreys, D. Hughes, and A. Rollett. Current issues in recrystallization: A review Materials Science and Engineering: A, 238: 219-274, 1997.

[40] T. Sakai. Dynamic recrystallization microstructures under hot working conditions. Journal of Materials Processing Technology, 53: 349-361, 1995.

[41] E. I. Poliak and J. J. Jonas. Initiation of dynamic recrystallization in constant strain rate hot deformation. ISIJ International, 43: 684-691, 2003.

[42] S. F. Medina and C. A. Hernandez. General expression of the Zener-Hollomon parameter as a function of the chemical composition of low alloy and microalloyed steels. Acta Materialia, 44: 137-148, 1996.

[43] W. F. Hosford and R. M. Caddell. Metal Forming: Mechanics and Metallurgy. Prentice-Hall, Englewood Cliffs, N.J., 1983.

[44] J. J. Jonas, X. Quelennec, L. Jiang, and É. Martin. The Avrami

kinetics of dynamic recrystallization. Acta Materialia, 57: 2748-2756, 2009.

[45] W. P. Sun and E. B. Hawbolt. Comparison between static and metadynamic recrystallization. An application to the hot rolling of steels. ISIJ International, 37: 1000-1009, 1997.

[46] E. Palmiere and B. Wynne. *Thermomechanical Processing of Metals*. Class lectures, The University of Sheffield, 2013.

[47] T. Gladman. *The Physical Metallurgy of Microalloyed Steels*. Maney, London, 2002.

[48] J. Kliber, R. Fabik, I. Vitez, and K. Drozd. Hot forming recrystallization kinetics in steel. *Metalurgija*, 49: 67-71, 2010.

[49] S. H. Zahiri, S. M. Byon, S.-I. Kim, Y. Lee, and P. D. Hodgson. Static and metadynamic recrystallization of interstitial free steels during hot deformation. *ISIJ International*, 44: 1918-1923, 2004.

[50] M. R. Cartmill, M. R. Barnett, S. H. Zahiri, and P. D. Hodgson. An analysis of the transition between strain dependent and independent softening in austenite. *ISIJ International*, 45: 1903-1908, 2005.

[51] EE Magel. Rolling Contact Fatigue: A Comprehensive Review. U.S. Department of Transportation, Federal Railroad Administration, November 2011.

[52] B Bramfitt. A Metallurgical Perspective of the Role of Rail Steel in the Growth of America. Iron & Steel Technology, 2011.

[53] X Zhan, S Wang. Research on the improvement of rail head hardening technology on railway. Proceedings of the Eastern Asia Society for Transportation Studies, 2005, 5, 263 – 271.

[54] DIN EN 13674. Railway applications - Track - Rail - Part 1: Vignole railway rails 46 kg/m and above, 2011.

[55] TB/T 2344. Hot-rolled steel rails for railway. National Standards of the People's Republic of China, 2012.

[56] GOST R 51685. Railway Rails - General specifications. National Standards of the Russian federation, 2011.

[57] P. Carlone, G. Palazzo and R. Pasquino, "Finite element analysis of the steel quenching process: Temperature field and solid–solid phase change," Computers and Mathematics with Applications, 2010.

[58] Seong-Hoon Kang; Yong-Taek Im, "Three-dimensional thermo-elastic–plastic finite element modeling of quenching process of plain-carbon steel in couple with phase transformation," International Journal of Mechanical Sciences, 2007.

[59] K.J.Bathe, Finite Element Procedures in Engineering Analysis, New Jersey: Prentice-Hall, Inc., 1982.

[60] C.Mapelli, "Modello curve CCT TTT," Politecnico di Milano, 2015.

[61] J., Miettinen, "Calculation of Solidification-Related Thermophysical
[62] Properties for Steels," METALLURGICAL AND MATERIALS
TRANSACTIONS B VOLUME 28B, 1997.

[63] British Iron and Steel Research Association, "Physical Costants of
some Commercial Steel at Elevated Temperatures," 1953.

[64] I.Tamura, H.Sekine, T.Tanaka, C.Ouchi, Mathematical
Thermomechanical processing of High–strength Low-alloy Steels,
Butterworths, London 1988.

[65]  Steel heat treatment handbook ed. George E. Totten, p.595

[66] p. 53 Optical microscopy of carbon steel, Samuels ASM

[67] Acciai e leghe non ferrose - Nicodemi - p.69 - C<0.8

[68] Modelling of CCT diagrams..- Journal of Materials processing
Technology 192-193 (2007) 504-510

[69] ISIJ vol.43 n.12 del 2003 page 2018

[70] ISIJ vol.44 n.9 del 2004 page 1608

[71] ISIJ vol.42 n.8 del 2002 page 901

[72] ISIJ vol.34 n.11 del 1994 page 919

[73] P.Payson, C. H. Savage. Trans. ASM, 33:261-281, 1944.

[74] R.A. Grange, H.M. Stewart. Trans. AIME, 167:467-494, 1945.

[75] A.E. Nehrenberg. Trans. AIME, 167:494-501,1945.

[76] W. Steven, A. G. Haynes. JISI, 183:349-359,1956.

[77] K.W. Andrews. JISI, 203:721-727, 1965.

[78] Steels metallurgy and applications pp.11 3° edition- D.T.
LLEWELLYN - R.C: HUDD. Pp.44-45

[79]Ouchi et.al. ISIJ int. Vol. 22del 1982, page 222.

[80] Carlos Salaroli de Araujo et. Al. TMP 2008, paper 41.

[81] M. El Mehtedi et al., Proc. of 2nd Inter. Conf. on TMP of Steels, pp.
243

[82] T.M.Maccagno, J.J. Jonas et. Al., ISIJ Int.36 (1996) 720-728.

[83] I.P. Kemp, J. Iron Making Steel Making 17 (1990) 139-143.

[84] W. Lehnert, N.D. Cuong, ISIJ Int. 32 (1995) 1100-1108.

[85] Y. Lee et.al. Mat. Sci. Eng A336 (2002) 177-189.

[86] Y. Lee et al., J. Mater. Proc. Tech. 81 (2000) 87-96.

[87] Z. Wusatowski, Fundamentals of Rolling, Pergamon Press, London, 1969, 107-109.

[88] P.D. Hodgson, R.K. Gibbs: ISIJ Int. 32 (1992), 1329.

[89] C.M. Sellars, Mater. Sci. Technol. 6 (1990), 1072.

[90] F. Boratto, et. Al., Proc. Int. Conf. Physical Metallurgy of TMP of steels (THERMEC'08) (1998) Tokyo, 519.